UNIVERSITY OF CALIFORNIA SAN DIEGO

Metal Oxide Nanoparticles in Complex Environments: Characterization,

Implications and Biomolecule-Nanoparticle Interactions

A dissertation submitted in partial satisfaction of the requirements for the degree

Doctor of Philosophy

in

Nanoengineering

by

Irem Bahanur Ustunol

Committee in charge:

Professor Vicki H. Grassian, Chair
Professor Yi Chen
Professor Jesse V. Jokerst
Professor Ratnesh Lal
Professor Jeffrey D. Rinehart

2021

The dissertation of Irem Bahanur Ustunol is approved, and it is acceptable in quality and form for publication on microfilm and electronically:

_____

_____

_____

_____

_____
Chair

University of California San Diego

2021

DEDICATION

This dissertation is dedicated to my beloved mother for her unfailing love and

encouragement from day one.

EPIGRAPH

It always seems impossible until it's done.

Nelson Mandela

TABLE OF CONTENTS

LIST OF FIGURES

LIST OF TABLES

xviii

LIST OF SCHEMES

ACKNOWLEDGMENTS

Throughout graduate school and writing this dissertation, I have received a great deal of support and assistance from many people.

I would first like to express my deepest gratitude to my advisor, Dr. Vicki H. Grassian. Your expertise was invaluable for my studies and research, and I am very grateful for the opportunity to be a part of the Grassian group for the past four years. You consistently encouraged my participation in academic platforms and allowed me to represent our group on multiple occasions. Your steadfast support in these endeavors enabled me to return to the group with distinguished awards and become a true scientist. I have learned and grown so much during this journey, and I thank you immensely for your guidance and mentorship.

I would also like to acknowledge all of my esteemed committee members. Dr. Rathneswar Lal, your remarkably positive attitude has had a profound impact on my career path. Dr. Jesse Jokerst, Dr. Yi Chen, and Dr. Jeffrey Rinehart thank you for your guidance and insightful comments that fostered my growth and improved my research.

I would like to acknowledge my previous advisor, Dr. Sadik Esener, and our department graduate coordinator, Dana Jimenez. You both always believed in me and supported my efforts to complete this Ph.D. journey.

Lastly, I would like to thank my friends in San Diego, especially Deniz and Kunal Mehta. Kunal, you are a remarkable friend. I had enjoyed all the time we spent together, and I will always appreciate you allowing me to vent when I needed it the most. I admire your selflessness and am grateful for the support you have given me over the last five years.

Chapter 6, in full, is reproduced with permission from Taylor & Francis: Gonzalez-Pech, N. I.; Stebounova, L. V.; Ustunol, I. B.; Park, J. H., Renee Anthony, T.; Peters, T. M.; Grassian, V. H. Size, Composition, Morphology, and Health Implications of Airborne Incidental Metal-Containing Nanoparticles. *J. Occup. Environ. Hyg.* **2019,** 16, 6, 387-399. The dissertation author was the investigator and author of this paper. The dissertation author conducted electron microscopy and energy dispersive X-Ray (EDS) analyses.

Appendix A, in full, is reproduced with permission from Elsevier: Ustunol, I. B.; Gonzalez-Pech, N. I.; Grassian, V. H. pH-dependent Adsorption of α-Amino Acids, Lysine, Glutamic Acid, Serine, and Glycine, on TiO_2 Nanoparticle Surfaces. *J. Colloid Interface Sci.* **2019**, 554, 362-375. The dissertation author was the primary investigator and author of this paper.

VITA

2012   B.S. in Chemical Engineering – Yildiz Technical University, Turkey

2013   B.S. in Business Administration – Anadolu University, Turkey

2016   M.S. in Nanoengineering – University of California San Diego

2021   Ph.D. in Nanoengineering – University of California San Diego

PUBLICATIONS

1.   **Ustunol, I. B**.; Gonzalez-Pech, N. I. & Grassian, V. H. pH-Dependent Adsorption of α-Amino Acids, Lysine, Glutamic Acid, Serine, and Glycine, on TiO_2 Nanoparticle Surfaces, *J. Colloid Interf. Sci*. **2019,** 554, 362-375.

2.   Gonzalez-Pech, N. I.; Stebounova, L. V.; **Ustunol, I. B**.; Park, J. H.; Anthony, T. R.; Peters, T. M. & Grassian, V. H. Size, composition, morphology and health implications of airborne incidental metal-containing nanoparticles, *J. Occup. Environ. Hyg.* **2019**, 16(6), 387-399.

3.   **Ustunol, I. B**.; Coward, E.; Quirk, E. & Grassian, V.H. Interaction of Beta-Lactoglobulin and Bovine Serum Albumin with Iron Oxide (α-Fe_2O_3) Nanoparticles in the Presence and Absence of Pre-Adsorbed Phosphate (In preparation for submission)

4.   **Ustunol, I. B**.; Quirk, E.; Coward, E. & Grassian, V.H. Polar Amino Acid Interactions with α-Fe_2O_3 Nanoparticles: Effects of pH and Nanoparticle Type onto Adsorption. (In preparation for submission)

FIELDS OF STUDY

Major Field: Nanoengineering (Biomedical Nanotechnology)

Professor Vicki H. Grassian

ABSTRACT OF THE DISSERTATION

Metal Oxide Nanoparticles in Complex Environments: Characterization,

Implications and Biomolecule-Nanoparticle Interactions

by

Irem Bahanur Ustunol

Doctor of Philosophy in Nanoengineering

University of California San Diego, 2021

Professor Vicki H. Grassian, Chair

Nanoscience and nanotechnology are research areas that have shown great promise towards addressing clean and sustainable energy, environmental protection, and human health. Metal oxide nanoparticles are widely used in various applications, including removing pollutants from contaminated water, tracking cancer cell growth, targeted drug delivery. These nanoparticles are highly reactive, and their abundance in the environment brings potential concerns to their exposure, leading to increased interactions with biomolecules that have impactful environmental and health effects. Ecological systems have multi-components, including natural organic matter, oxyanions, and biological macromolecules; biological systems also contain complexity as proteins and nutrients can all be found at the nanomaterial-water interface upon nanoparticle exposure. Although significant research has been pursued on the surface transformations of metal oxide nanoparticles, multi-component adsorption kinetics, changes in adsorbate structure, and the impacts on the nanomaterial properties in complex environments remain unclear.

Once nanoparticles are introduced in complex aqueous biological and environmental systems, proteins adsorb onto their surfaces and form a dynamic layer termed "corona." Newly occurred corona may change the nanoparticle interfacial state and its biological and ecological identity. If altered, the new identity influences the nanoparticle fate within the surrounding complex media. Details of protein and amino acid (building block of proteins) interactions with nanoparticles and substantial structural change on nanoparticle surfaces remain unclear.

These processes can be affected by various factors due to the complexities of nano-bio surface interactions. Therefore, it is necessary to study multiple parameters individually, and a systematic study on the impacts of influential factors on the adsorption at the nano-bio interface is strongly desired.

The research presented in this dissertation pursues a greater understanding of metal oxide nanoparticle characterizations, implications, and biomolecule-nanoparticle interactions from studies of amino acid and protein adsorption. Nanoparticle- and environmental-related factors, including effects of pH, nanoparticle-type, biomolecule concentration, pre-adsorbed phosphate and lipopolysaccharides, and nanoparticle production in a workplace environment (occupational health study), were investigated. We studied the influencing factors of the complex environment individually to examine each aspect in detail. Attenuated Total Reflectance-Fourier Transform Infrared Spectroscopy (ATR-FTIR), as well as various microscopic and spectroscopic tools, were employed to help better understand the impact of these factors.

In this dissertation, adsorption of α-amino acids, lysine, glutamic acid, glycine, and serine, onto TiO_2 nanoparticles in buffered solutions was determined. The predominant molecular surface species and the adsorption affinity were highly pH-dependent. Adsorption of lysine and glycine were increased proportionally with changes in pH, whereas glutamic acid adsorption decreased with increasing pH. We attributed these differences to the functional groups of different species and the TiO_2 surface charge at each pH.

Furthermore, the effects of nanoparticle type and amino acid concentration on the mechanisms of amino acids, lysine, aspartic acid, and arginine, adsorption on α-Fe_2O_3 nanoparticles were investigated. The detailed chemistry in the adsorption processes implied the formation of outer-sphere and inner-sphere complex differences between different nanomaterials. Combined *in-situ* ATR-FTIR and curve-fitting provides insights and a greater understanding of changes in secondary structures of bovine serum albumin (BSA) and βeta-lactoglobulin (β-LG) upon adsorbed onto α-Fe_2O_3 nanoparticles in the presence and absence of co-adsorbed phosphate. The results indicated that structural changes were time-dependent, and the existence of pre-adsorbed phosphate influenced adsorption and desorption kinetics. An additional part of this work showed that pre-adsorbed lipopolysaccharide additionally played a role in the interaction of Immunoglobulin G (IgG) adsorbed onto α-Fe_2O_3 nanoparticles. In agreement with the β-LG adsorption, a significant change in Amide I/II ratio was observed for adsorbed IgG, indicating changes in the protein secondary structure compared to the solution phase. Deconvolution analyses revealed that the α-helix content of the adsorbed IgG was higher than the unbound conformation in the presence of lipopolysaccharides.

Moreover, to complement our understanding of protein and amino acid adsorption, we also investigated airborne nanoparticle presence in different production sites in an occupational health study. Identified nanoparticles in these settings were characterized by two forms: sub-micrometer fractal-like agglomerates from activities such as welding; and super-micrometer particles (nanoparticle collectors) with nanoparticles coagulated on their surfaces.

These agglomerates were proposed to affect deposition and transport inside the respiratory system. The respirable incidental nanoparticles would have corresponding health implications regarding their primary and/or secondary sites of uptake.

Overall, the research in this dissertation provides essential insights into understanding the behavior of metal oxide nanoparticles in complex environments. Studies on amino acid and protein adsorption, along with the detailed characterization of the nano-bio interface with spectroscopic and microscopic methods, allowed us to understand the effects of a multitude of influences on biomolecule-nanoparticle surface interactions.

Chapter 1   Introduction

1.1   Nanoscience and Significance of Metal Oxide Nanoparticles

"Nanoscience" or "nanotechnology" refers to science and engineering performed to control and manipulate matter on a scale less than 100 nm to improve material properties.[1] Nanotechnology offers excellent opportunities for making superior materials for a wide range of applications.[2,3] There are "bottom-up" and "top-down" approaches that have been used in nanotechnology to assemble nanostructures, materials, and devices.[1] These approaches allow nanomaterials to attain unique properties compared to their bulk sizes, including but not limited to the large surface area, magnetic characteristics, light absorbance capacity, high chemical reactivity, and long-term adsorbent stability.[4] Among nanomaterials, metal oxide nanoparticles consist a large percentage that has been used in cosmetics,[5–7] energy,[8–10] antibacterial/microbial applications,[11,12] optics and electronics,[13] materials,[14] food processing,[15] and biomedical applications.[4,16] The use cases of metal oxide nanoparticles are broad. The potential uncontrolled release of these nanomaterials into the environment brings concerns about their adverse impacts on the environment and human health.[17] However, there is little known about metal oxide nanoparticles in terms of their environmental fate, transformation, and toxicity.

1.2   Environmental and Human Exposure to Metal Oxide Nanoparticles

Metal oxide nanoparticles could be released into natural ecosystems through intentional or unintentional pathways[18] and be sourced as atmospheric or terrestrial.[19] Intentional nanoparticles are synthesized/engineered in a controlled manner and could have

uniform properties. Three emission scenarios are generally considered: (i) release during nanoparticle/nano-enabled device production; (ii) release during use; and (iii) release at waste handling (after disposal of nanoparticle-containing products).[18,20] Whereas unintentional or anthropogenic metal oxide nanoparticles could be produced as byproducts of human activities (i.e., combustion) or natural reactions.[18,21]

Pathway and Sources for Metal Oxide Nanoparticles

Incidental
- Byproducts of human activities
- Poorly controlled size and shape

Intentional
- Specifically designed and synthesized
- Precisely controlled size and shape

Transformation in the Environment

Physical Transformations
Aggregation
Adsorption
Deposition

Biologically Mediated
Biodistribution
Bioturbation

Macromolecule Interactions
H-Binding
Electrostatic interaction
Ligand exchange

Chemical Transformations
Dissolution
ROS production
Redox reactions

Figure 1.1: Pathways and transformation of metal oxide nanoparticles in the environment.

Released metal oxide nanoparticles could go through various physicochemical processes in the environment (Fig 1.1)[20–22] as macromolecule interactions, biodistribution, reactive oxygen species production, aggregation, ligand binding reaction, etc.[21,22] The interplay between the nanoparticles and these processes determines the fate and the toxicological potential,[23] in fact, nanoparticles could negatively impact the environment and human health.[24] Therefore, several studies on the NanoEHS (environmental health and safety) and molecular-level interactions between nanoparticles sorbates exist.[25–27] Despite

the comprehensive research efforts and available information on metal oxide nanoparticle emission, there is a lack of studies on the environmentally and biologically relevant complex media.[28] Biomolecule-nanoparticle complexes are highly heterogeneous, and their interactions consequently remain poorly understood. A detailed understanding of nanoparticle interaction with the environment could provide a safer use of engineered nanoparticles with minimal hazardous impact on the environment.

Environmentally abundant metal oxide nanoparticles could enter the human body through various exogenous and endogenous pathways:[17,19] pulmonary routes, oral ingestion, dermal contact, or intravenous injection from biomedical applications.[29] Upon introducing biological fluids, metal oxide nanoparticles can undergo interactions with biomolecules, and adsorbed biomolecules could impact nanoparticles' identity and environmental fate.[29] Depending on the size of nanoparticles entered the body; they could deposit on primary tissues or translocate to secondary sites. Oral ingested nanoparticles can subsequently travel into the gastrointestinal (GI) tract. Larger sized inhaled nanoparticles could deposit the section of the lungs (1–30 μm, and the submicron particles (< 1 μm) and nanoparticles (< 100 nm) penetrate deeply into the alveolar region, where removal mechanisms may be insufficient.[19] In fact, ultrafine nanoparticles could penetrate the lungs' deeper level,[30] disrupt cell-type-specific cytoskeleton,[31] and accumulate in the brain tissue bypassing the blood-brain barrier.[32] Secondary site depositions would increase the adverse health effects due to particle tissue and particle–cell interactions.[33,34]

1.3   Overview of Selected Nanoparticles

In this dissertation, aqueous phase biomolecule adsorption studies were performed with two different nanoparticles: titanium dioxide (anatase, TiO_2) and Fe(III)-oxide (hematite, α-Fe_2O_3).

1.3.1 TiO_2 Nanoparticles

TiO_2 is one of the most highly manufactured and widely used nanoparticles globally in surface science as a model semiconductor and versatile metal oxide compound.[35–39] The annual production of TiO_2 exceeds four million tons per year, and it has found many applications in the pharmaceutical industry, cosmetics, food processing.[40,41] TiO_2 has a unique bandgap structure that allows TiO_2 to be a promising catalyst for water splitting and solar energy conversion.[8,42] In addition to the photocatalytic properties of TiO_2, it has applications in the environmental and energy fields, self-cleaning surfaces, air/water purification systems.[43] In the biomedical field, titanium is used as a well-known implant material for dentistry.[44] Upon exposure to oxygen, the titanium surface will oxidize and form a layer of TiO_2; therefore, the biocompatibility of TiO_2 becomes critically important. There has been an increasing interest in TiO_2 interactions with biomolecules (i.e., amino acids and proteins) to improve material performance and better to understand biological component-surface interactions at the molecular level.[45–51] Studying amino acid and protein interactions with TiO_2 surfaces contributes to determining surface species and nanoparticle's new physical identity. The results can provide insights into the complex biomolecule adsorption mechanism and structural changes upon adsorption.

TiO$_2$ exists in nature in different crystalline forms, anatase, rutile, akaogiite, and brookite. At elevated temperatures (400 to 1200° C), anatase could transform into the rutile phase.[52] This phase transformation and its kinetics depend on multiple factors, including the morphological and chemical properties of TiO$_2$ and the specific heating methods.[52] Anatase TiO$_2$ has shown higher photocatalytic activity than rutile due to its larger bandgap, more efficient charge transport, and different surface properties.[53,54] The anatase and rutile forms are often used in the industry. However, anatase TiO$_2$ showed superior toxicity as inducing DNA damage and increasing protein nitration in the presence of ultraviolet illumination.[55,56] Despite the existing NanoEHS studies, there is still a gap in a complete evaluation of toxicological effects and biocompatibility of anatase TiO$_2$ in terms of interactions with the biological systems and the environment. Nanoscale anatase TiO$_2$ is selected in this research to analyze biomolecule-nanoparticle interactions.

1.3.2   α-Fe$_2$O$_3$ Nanoparticles

Iron oxide – i.e., Fe(III)-oxide (hematite) form – is present in terrestrial and marine systems and are among the most common minerals on most soils and sediments.[57–60] Iron oxides are significant sinks of a range of environmental elements, including organic compounds.[61] α-Fe$_2$O$_3$ is a thermodynamically stable mineral surface with high surface enthalpies, which promote strong water adsorption and interaction with ions.[61] Due to its high surface reactivity, thermodynamic stability, and subsequent adsorption capacity, it is a suitable sorbent for organic compounds and contaminants.[62–64] Iron oxide nanoparticles and their bio-inorganic hybrid forms are used in various applications, including coatings, cosmetics, catalysis, drug delivery, and environmental remediation.[65–67] Additionally, they

are also being studied for their potential use in imaging environmental sub-surfaces, detecting hydrocarbons in rocks near oil fields, sensing contaminants in waterways, and targeting various environmental interfaces for pollution treatment.[68] An exciting application of adsorption onto α-Fe_2O_3 is removing hazardous chemicals from aqueous environments. For instance, the arsenic-hematite compounds can be removed from their environment by reducing the amount of toxic arsenic in the system.[69] α-Fe_2O_3 nanoparticles can also regulate uranium quantities in contaminated environments. By adsorption of uranium onto these nanoparticles, uranium(VI) is reduced to less mobile and more easily separable form of uranium(IV).[70] These applications make iron oxide nanoparticles very useful in maintaining the quality of environmental systems. It is beneficial to understand the specific mechanisms involved with a substance's adsorption onto the nanoparticle surface.

In biological systems, abundant α-Fe_2O_3 nanoparticles is a suitable surface for biomolecule interactions, impacting nano-bio complex environmental fate and nutritional element lifecycles.[71] α-Fe_2O_3-biomolecule adsorption studies suggest that the hematite phase is highly reactive, and iron promotes the preservation of organic matter in sediments.[59] α-Fe_2O_3 exposure promoted adverse impacts on *Escherichia Coli* bacterial cells.[73] α-Fe_2O_3 nanoparticles are more toxic than microscale particles due to their strong interfacial physicochemical interactions with the cells revealed insight into size-dependent toxicity mechanisms.[74] Despite the widespread occurrence of biomolecule-hematite complexes in natural and industrial systems, the kinetics, structure, and persistence of protein and amino acid adsorption – particularly in heterogeneous aqueous matrices – are

not fully understood. Structural changes resulting from the adsorption of biomolecules onto α-Fe_2O_3 mineral surfaces may alter their functions and other environmental interactions.

1.4   Chemical Complexity at the Nano-Bio Interface

The "nano-bio" interface constitutes the kinetics and thermodynamic exchanges, dynamic physicochemical interactions between nanomaterial surfaces and the surfaces of biological components.[75] These components can be proteins, amino acids, membranes, phospholipids, endocytic vesicles, organelles, DNA, and biological fluids. Furthermore, aqueous environmental and biological systems consist of naturally-occurring assemblies of salts, nutrients, oxyanions, and heterogeneous organic compounds with varying molecular weights, which may compete for bridge or aggregate with biological components in solution.[76] While the understanding of nanoparticle behavior and biomolecule interactions has advanced in model systems, the experimental design often does not account for aqueous systems' natural complexity. Since there are complexity and heterogeneity of environmental and biological systems, understanding the biomolecule orientation and interaction in water and ion-containing systems and their dynamics in response to external stimuli within the aqueous systems is needed. Therefore, processes that could occur at nano-bio interfaces remain the subject of constant fascination for researchers.

1.5   Nano-Bio Surface Interactions

Understanding the impacts of nanoparticles on environmental and biological systems is essential for the safe use of nanotechnology and nanomaterial design for

biological applications. Interaction of a biomolecule with nanoparticle surface depends on adsorption affinity, diffusion kinetics, and solution chemistry as compounds dynamically compete, co-adsorb, and scaffold on the nanoparticle surface.[77–80] In this dissertation, the adsorption of proteins and amino acids onto TiO_2 and α-Fe_2O_3 nanoparticles were studied.

1.5.1 Protein Adsorption and Bio- and Eco-Corona Formation

Proteins and amino acids play an essential role in many environmental and biological processes.[81] The sequence of amino acids was found to influence peptide binding and protein adsorption.[82] Thus, studying amino acid and protein interactions with nanoparticle surfaces contribute to our understanding of nanoparticles' fate in the complex biological and environmental *milieu*. When nanoparticles interact with biological fluids, proteins create a dynamic coating termed "corona," and it determines the nanoparticle identity and influences physiological and environmental responses to the nanoparticles.[83–85] In biological systems, this dynamic layer is termed the "protein corona" [76,82,86], whereas it is termed "eco-corona" in the environment.[87] Depending on the binding affinities of protein onto the nanoparticle surfaces; the corona can be classified as "soft" or "hard." Soft corona contains the proteins that adsorb rapidly but reversibly to the nanoparticle surface. Hard corona proteins interact with surfaces slowly but irreversibly.[85,88] The formation of corona can influence cellular uptake, inflammation, aggregation, toxicity, and transformation of nanoparticles in complex environments. Furthermore, the nanoparticle surface can induce structural changes in adsorbed protein molecules, affecting the nanoparticle's overall bio-reactivity.[80]

1.5.2 Structural Changes of Proteins Upon Adsorption

The composition of protein surfaces and protein structural flexibility determines both the affinity and specificity of protein-nanoparticle interactions and plays an essential role in regulating surface-driven modifications to their secondary structure.[89] The interactions between nanoparticles and biomolecules requires the same principles as those between colloidal particles.[75] Enthalpic and entropic driving forces govern protein adsorption onto nanoparticle surfaces, including hydrophobic interactions, electrostatic forces, and entropy-driven binding. Still, they require special consideration for events occurring at the nanoscale.[75,85,90] Hydrophobicity minimizes the non-polar amino acids' exposure in the protein structure toward the hydrophilic aqueous media.[91] Thus, proteins tend to undergo conformational changes to enable the maximum interaction of their non-polar parts on the surface. If the nanoparticle surface is charged, electrostatic attractions can drive the protein adsorption from the polypeptide backbones of the protein.[92] However, proteins can adsorb with high flexibility and low conformation stability even under electrostatic repulsion, and this is majorly entropy-driven binding owing to the structural rearrangement of proteins upon adsorption.[93] For instance, bovine serum albumin (BSA) was found on negatively charged surfaces at pH higher than its isoelectric point.[93,94] This means that both the protein and the nanoparticle surface are negatively charged, and electrostatic repulsion exists. However, the adsorption that occurred was explained as BSA unfolding upon adsorption exhibits a maximal number of positively charged lateral chains (i.e., lysine residues) towards the nanoparticle surface.[93,94]

Nanoparticle surface-induced protein conformational changes could impact the downstream protein-protein interactions, cellular signaling, and DNA transcription.[80] DNA transcription is crucial for enzymes, as enzyme activity loss can happen due to the conformational changes in the protein active site, which interacts with the nanoparticle surface.[80] Such conformational changes can increase the accessibility of the enzyme active site for its substrate.[80] RNAse and lysozyme retained their native structures on silica nanoparticles, whereas albumin and lactoperoxidase underwent irreversible conformational changes.[95]

There are different levels in a protein structure as primary, secondary, tertiary, and quaternary.[9697] Primary structure contains the sequence of amino acids along with the polypeptide chains. Secondary protein structure has the α-helices and β-strands (including β-sheets and β-turns). These conformations are formed due to the twisting and folding of polypeptide chains driven by the hydrogen bonding between amino acid groups. The three-dimensional arrangement of a protein is considered the tertiary structure, and it is a further result fold of the polypeptide chain and corresponding secondary structure. Lastly, multiple tertiary structures associate could from protein quaternary structure. In this dissertation, "conformational change" or "structural change" is referred to as secondary structural rearrangement of the proteins upon adsorption on nanoparticle surfaces. The secondary structure of proteins was analyzed to investigate the surface-induced conformational change of protein upon adsorption using spectroscopic methods.

1.5.3 Parameters Governing Biomolecule-Nanoparticle Interactions

The nano-bio interface contains three dynamically interacting components: (i) the nanoparticle surface; (ii) a solid-liquid interface; (iii) the contact zone of the solid-liquid interface with biological substrates.[75] Surface characteristics of nanoparticles are mainly determined by their physicochemical composition and morphology, and nano-bio interactions occur when the particles interact with components in the surrounding medium. Details of protein interaction with nanoparticles and respective structural changes on nanoparticle surfaces remain unclear as these processes can be affected by various factors. Many factors could affect protein-nanoparticle surface interactions and the structure of adsorbed proteins on particle surfaces. These factors can be classified into three major categories: (i) nanoparticle-related factors (i.e., elemental composition, porosity, size, surface chemistry, crystallization); (ii) biomolecule-related factors (i.e., protein and amino acid species, dimension, molecular weight, isoelectric point, conformation stability), and (iii) surrounding medium-related (i.e., ionic strength, pH, the composition of the medium, environmental temperature).[98] Due to the complexities of nano-bio interactions, it is necessary to study various parameters individually.

1.6 Dissertation Motivation and Objectives

The overall objective of the research presented in this dissertation was the determination of fate and transformation of metal oxide nanoparticles in complex environments from amino acid and protein adsorption studies. In the present dissertation, biomolecule-nanoparticle surface interactions were investigated, focusing on the effects of pH, nanoparticle type, amino acid concentration, pre-adsorbed phosphate, and

lipopolysaccharides, and finally, nanoparticle production site (occupational health study). The influencing factors were individually studied in the following five chapters to investigate each aspect to better understand how different factors could affect biomolecule adsorption, structure in solution, and adsorbed on nanoparticle surfaces. All projects were conducted both macroscopically and at the nanoscale to understand the fundamentals governing the biomolecule-nanoparticle interactions. In Chapter 2, the experimental methods were used to achieve the research objectives, and the details of the experimental protocols are outlined. Instrumental techniques are classified into three sections: (i) nanoparticle physicochemical characterization, (ii) nanoparticle–nanoparticle interactions and aggregation studies, and (iii) aqueous phase biomolecule surface adsorption.

The research work presented in chapter 3 is about the investigation of pH-dependent amino acid adsorption on TiO_2 nanoparticles. The selected amino acids were lysine, glutamic acid, serine, and glycine as representative biomolecules in complex biological and environmental systems. The primary aim of this chapter is to uncover in detail how pH impacts amino acids speciation and adsorption onto nanoparticle surfaces. *In-situ* Attenuated total reflectance-Fourier Transform Infrared (ATR-FTIR) spectroscopy was used to monitor amino acid adsorbates by probing the spectral changes during the adsorption process. Zeta-potential analyses and dynamic light scattering methods were employed to analyze the impact of surface coverage on TiO_2 physicochemical properties.

In chapter 4, pH-dependent adsorption of arginine, aspartic acid, and lysine on α-Fe_2O_3 nanoparticles were investigated to uncover the effects of nanoparticle type and amino acid concentration on surface interactions. ATR-FTIR spectroscopy was used to

probe the spectral changes. The principles obtained from pH-dependent amino acid adsorption in chapter 3 were used to explain molecular level details of amino acids' adsorption mechanisms onto α-Fe_2O_3 nanoparticles.

Chapter 5 of the dissertation includes adsorption of the proteins of bovine serum albumin (BSA), β-lactoglobulin (β-LG), and immunoglobulin (IgG) onto α-Fe_2O_3 nanoparticles in the presence and absence of pre-adsorbed phosphate and lipopolysaccharides (LPS). ATR-FTIR spectroscopy was combined with curve fitting (deconvolution) analyses to provide an understanding of *real-time* biomolecule-nanoparticle surface interactions and protein conformational changes in a multi-component environment. To identify the effects of phosphate and LPS on the protein adsorption and desorption experiments, kinetics analyses from the ATR-FTIR spectra were further performed by looking at Amide I and II peak intensities. This chapter explains the fundamental mechanisms involved in protein adsorption/desorption in a multi-component, more complex aqueous environment.

Chapter 6 is aimed to complement our understanding of protein and amino acid adsorption studies. In this chapter, elemental and morphological analyses of airborne nanoparticles were performed in different production sites in an occupational health study. The dissertation author conducted electron microscopy and energy-dispersive X-Ray analyses (EDX) to identify the produced nanoparticles in these settings. Characterized particle agglomerates were in two forms: sub-micrometer fractal-like and super-micrometer particles (nanoparticle collectors). The agglomerates with nanoparticles coagulated on their surfaces proposed to affect deposition and transport inside the human

respiratory system. This chapter aimed to show that the incidental nanoparticles would have corresponding health implications regarding their pulmonary site of uptakes.

The conclusions and future directions of this research are given in Chapter 7. These studies will collectively provide essential insights into understanding the behavior of metal oxide nanoparticles in complex environments. The results from the studies on amino acid and protein adsorption, along with the detailed characterization of the nano-bio interface with spectroscopic and microscopic methods, contribute towards the growing database on the potential environmental and health implications of metal oxide nanoparticles.

1.7 References

(1) Subramani, K.; Elhissi, A.; Subbiah, U.; Ahmed, W. Introduction to Nanotechnology. In *Nanobiomaterials in Clinical Dentistry*; **2019**. https://doi.org/10.1016/B978-0-12-815886-9.00001-2.

(2) Paul, D. R.; Robeson, L. M. Polymer Nanotechnology: Nanocomposites. *Polymer*. **2008**. https://doi.org/10.1016/j.polymer.2008.04.017.

(3) Misra, R.; Acharya, S.; Sahoo, S. K. Cancer Nanotechnology: Application of Nanotechnology in Cancer Therapy. *Drug Discovery Today*. **2010.** https://doi.org/10.1016/j.drudis.2010.08.006.

(4) Ali, A.; Zafar, H.; Zia, M.; ul Haq, I.; Phull, A. R.; Ali, J. S.; Hussain, A. Synthesis, Characterization, Applications, and Challenges of Iron Oxide Nanoparticles. *Nanotechnology, Science and Applications*. Dove Medical Press Ltd August 19, **2016**, pp 49–67. https://doi.org/10.2147/NSA.S99986.

(5) Nohynek, G. J.; Dufour, E. K.; Roberts, M. S. Nanotechnology, Cosmetics and the Skin: Is There a Health Risk? In *Skin Pharmacology and Physiology*; **2008**. https://doi.org/10.1159/000131078.

(6) Lu, P. J.; Huang, S. C.; Chen, Y. P.; Chiueh, L. C.; Shih, D. Y. C. Analysis of Titanium Dioxide and Zinc Oxide Nanoparticles in Cosmetics. *J. Food Drug Anal.* **2015**. https://doi.org/10.1016/j.jfda.2015.02.009.

(7) Dréno, B.; Alexis, A.; Chuberre, B.; Marinovich, M. Safety of Titanium Dioxide

Nanoparticles in Cosmetics. *Journal of the European Academy of Dermatology and Venereology*. **2019**. https://doi.org/10.1111/jdv.15943.

(8)   Ye, L.; Zhang, Y.; Zhang, X.; Hu, T.; Ji, R.; Ding, B.; Jiang, B. Sol-Gel Preparation of SiO2/TiO2/SiO 2-TiO2 Broadband Antireflective Coating for Solar Cell Cover Glass. *Sol. Energy Mater. Sol. Cells* **2013**. https://doi.org/10.1016/j.solmat.2012.12.037.

(9)   Sun, X.; Xu, X.; Song, G.; Tu, J.; Li, L.; Yan, P.; Zhang, W.; Hu, K. Preparation of MgF2/SiO2 Coating with Broadband Antireflective Coating by Using Sol–Gel Combined with Electron Beam Evaporation. *Opt. Mater. (Amst).* **2020**. https://doi.org/10.1016/j.optmat.2020.109739.

(10)   Mao, Q.; Zeng, D.; Xu, K.; Xie, C. Fabrication of Porous TiO2-SiO2 Multifunctional Anti-Reflection Coatings by Sol-Gel Spin Coating Method. *RSC Adv.* **2014**. https://doi.org/10.1039/c4ra10424b.

(11)   Stoimenov, P. K.; Klinger, R. L.; Marchin, G. L.; Klabunde, K. J. Metal Oxide Nanoparticles as Bactericidal Agents. *Langmuir* **2002**. https://doi.org/10.1021/la0202374.

(12)   Dizaj, S. M.; Lotfipour, F.; Barzegar-Jalali, M.; Zarrintan, M. H.; Adibkia, K. Antimicrobial Activity of the Metals and Metal Oxide Nanoparticles. *Materials Science and Engineering C*. **2014.** https://doi.org/10.1016/j.msec.2014.08.031.

(13)   Vaseem, M.; Umar, A.; Hahn, Y. *ZnO Nanoparticles : Growth, Properties, and Applications*; **2010.**

(14)   Li, W.; Troyer, L. D.; Lee, S. S.; Wu, J.; Kim, C.; Lafferty, B. J.; Catalano, J. G.; Fortner, J. D. Engineering Nanoscale Iron Oxides for Uranyl Sorption and Separation: Optimization of Particle Core Size and Bilayer Surface Coatings. *ACS Appl. Mater. Interfaces* **2017**, *9* (15), 13163–13172. https://doi.org/10.1021/acsami.7b01042.

(15)   Chen, X. X.; Cheng, B.; Yang, Y. X.; Cao, A.; Liu, J. H.; Du, L. J.; Liu, Y.; Zhao, Y.; Wang, H. Characterization and Preliminary Toxicity Assay of Nano-Titanium Dioxide Additive in Sugar-Coated Chewing Gum. *Small* **2013**. https://doi.org/10.1002/smll.201201506.

(16)   Nosrati, H.; Salehiabar, M.; Bagheri, Z.; Rashidzadeh, H.; Davaran, S.; Danafar, H. Preparation, Characterization, and Evaluation of Amino Acid Modified Magnetic Nanoparticles: Drug Delivery and MRI Contrast Agent Applications. *Pharm. Dev. Technol.* **2018**. https://doi.org/10.1080/10837450.2018.1536995.

(17)   Vlachogianni, T.; Valavanidis, A. Nanomaterials: Environmental Pollution, Ecological Risks and Adverse Health Effects. *Nano Sci. Nano Technol.* **2014**.

(18)   Bundschuh, M.; Filser, J.; Lüderwald, S.; McKee, M. S.; Metreveli, G.;
        Schaumann, G. E.; Schulz, R.; Wagner, S. Nanoparticles in the Environment:
        Where Do We Come from, Where Do We Go To? *Environmental Sciences
        Europe*. **2018**. https://doi.org/10.1186/s12302-018-0132-6.

(19)   Gupta, R.; Xie, H. Nanoparticles in Daily Life: Applications, Toxicity and
        Regulations. *J. Environ. Pathol. Toxicol. Oncol.* **2018**.
        https://doi.org/10.1615/JEnvironPatholToxicolOncol.2018026009.

(20)   Tolaymat, T.; El Badawy, A.; Genaidy, A.; Abdelraheem, W.; Sequeira, R.
        Analysis of Metallic and Metal Oxide Nanomaterial Environmental Emissions. *J.
        Clean. Prod.* **2017**. https://doi.org/10.1016/j.jclepro.2016.12.094.

(21)   Amde, M.; Liu, J. fu; Tan, Z. Q.; Bekana, D. Transformation and Bioavailability of
        Metal Oxide Nanoparticles in Aquatic and Terrestrial Environments. A Review.
        Environmental Pollution. 2017. https://doi.org/10.1016/j.envpol.2017.06.064.

(22)   Simeonidis, K.; Mourdikoudis, S.; Kaprara, E.; Mitrakas, M.; Polavarapu, L.
        Inorganic Engineered Nanoparticles in Drinking Water Treatment: A Critical
        Review. *Environmental Science: Water Research and Technology*. **2016**.
        https://doi.org/10.1039/c5ew00152h.

(23)   Dale, A. L.; Casman, E. A.; Lowry, G. V.; Lead, J. R.; Viparelli, E.; Baalousha, M.
        Modeling Nanomaterial Environmental Fate in Aquatic Systems. *Environ. Sci.
        Technol.* **2015**. https://doi.org/10.1021/es505076w.

(24)   Bhatt, I.; Tripathi, B. N. Interaction of Engineered Nanoparticles with Various
        Components of the Environment and Possible Strategies for Their Risk
        Assessment. *Chemosphere*. **2011.**
        https://doi.org/10.1016/j.chemosphere.2010.10.011.

(25)   Lee, J.; Mahendra, S.; Alvarez, P. J. J. Nanomaterials in the Construction Industry:
        A Review of Their Applications and Environmental Health and Safety
        Considerations. *ACS Nano*. **2010**. https://doi.org/10.1021/nn100866w.

(26)   Shi, H.; Magaye, R.; Castranova, V.; Zhao, J. Titanium Dioxide Nanoparticles: A
        Review of Current Toxicological Data. *Particle and Fibre Toxicology*. **2013**.
        https://doi.org/10.1186/1743-8977-10-15.

(27)   Liu, G.; Gao, J.; Ai, H.; Chen, X. Applications and Potential Toxicity of Magnetic
        Iron Oxide Nanoparticles. *Small*. **2013**. https://doi.org/10.1002/smll.201201531.

(28)   von der Kammer, F.; Ferguson, P. L.; Holden, P. A.; Masion, A.; Rogers, K. R.;
        Klaine, S. J.; Koelmans, A. A.; Horne, N.; Unrine, J. M. Analysis of Engineered
        Nanomaterials in Complex Matrices (Environment and Biota): General
        Considerations and Conceptual Case Studies. *Environmental Toxicology and
        Chemistry*. **2012.** https://doi.org/10.1002/etc.723.

(29) Auría-Soro, C.; Nesma, T.; Juanes-Velasco, P.; Landeira-Viñuela, A.; Fidalgo-Gomez, H.; Acebes-Fernandez, V.; Gongora, R.; Parra, M. J. A.; Manzano-Roman, R.; Fuentes, M. Interactions of Nanoparticles and Biosystems: Microenvironment of Nanoparticles and Biomolecules in Nanomedicine. *Nanomaterials*. **2019.** https://doi.org/10.3390/nano9101365.

(30) Miller, M. R.; Raftis, J. B.; Langrish, J. P.; McLean, S. G.; Samutrtai, P.; Connell, S. P.; Wilson, S.; Vesey, A. T.; Fokkens, P. H. B.; Boere, A. J. F.; Krystek, P.; Campbell, C. J.; Hadoke, P. W. F.; Donaldson, K.; Cassee, F. R.; Newby, D. E.; Duffin, R.; Mills, N. L. Inhaled Nanoparticles Accumulate at Sites of Vascular Disease. *ACS Nano* **2017**, *11* (5), 4542–4552. https://doi.org/10.1021/acsnano.6b08551.

(31) Ispanixtlahuatl-Meráz, O.; Schins, R. P. F.; Chirino, Y. I. Cell Type Specific Cytoskeleton Disruption Induced by Engineered Nanoparticles. *Environmental Science: Nano*. **2018.** https://doi.org/10.1039/c7en00704c.

(32) Maher, B. A.; Ahmed, I. A. M.; Karloukovski, V.; MacLaren, D. A.; Foulds, P. G.; Allsop, D.; Mann, D. M. A.; Torres-Jardón, R.; Calderon-Garciduenas, L. Magnetite Pollution Nanoparticles in the Human Brain. *Proc. Natl. Acad. Sci. U. S. A.* **2016**. https://doi.org/10.1073/pnas.1605941113.

(33) Bakand, S.; Hayes, A.; Dechsakulthorn, F. Nanoparticles: A Review of Particle Toxicology Following Inhalation Exposure. *Inhalation Toxicology*. **2012**. https://doi.org/10.3109/08958378.2010.642021.

(34) Blank, M. D.; Disharoon, S.; Eissenberg, T. Comparison of Methods for Measurement of Smoking Behavior: Mouthpiece-Based Computerized Devices versus Direct Observation. *Nicotine Tob. Res.* **2009**. https://doi.org/10.1093/ntr/ntp083.

(35) Jomini, S.; Clivot, H.; Bauda, P.; Pagnout, C. Impact of Manufactured TiO_2 Nanoparticles on Planktonic and Sessile Bacterial Communities. *Environ. Pollut.* **2015**. https://doi.org/10.1016/j.envpol.2015.03.022.

(36) Fei Yin, Z.; Wu, L.; Gui Yang, H.; Hua Su, Y. Recent Progress in Biomedical Applications of Titanium Dioxide. *Physical Chemistry Chemical Physics*. **2013**. https://doi.org/10.1039/c3cp43938k.

(37) Sunada, K.; Watanabe, T.; Hashimoto, K. Studies on Photokilling of Bacteria on TiO 2 Thin Film. *J. Photochem. Photobiol. A Chem.* **2003**. https://doi.org/10.1016/S1010-6030(02)00434-3.

(38) Farshbaf Dadjour, M.; Ogino, C.; Matsumura, S.; Nakamura, S.; Shimizu, N. Disinfection of Legionella Pneumophila by Ultrasonic Treatment with TiO_2. *Water Res.* **2006**. https://doi.org/10.1016/j.watres.2005.12.047.

(39)   Markowska-Szczupak, A.; Ulfig, K.; Morawski, A. W. The Application of Titanium Dioxide for Deactivation of Bioparticulates: An Overview. *Catalysis Today*. **2011**. https://doi.org/10.1016/j.cattod.2010.11.055.

(40)   Ziental, D.; Czarczynska-Goslinska, B.; Mlynarczyk, D. T.; Glowacka-Sobotta, A.; Stanisz, B.; Goslinski, T.; Sobotta, L. Titanium Dioxide Nanoparticles: Prospects and Applications in Medicine. *Nanomaterials*. 2020. https://doi.org/10.3390/nano10020387.

(41)   Carp, O.; Huisman, C. L.; Reller, A. Photoinduced Reactivity of Titanium Dioxide. *Progress in Solid State Chemistry*. **2004**. https://doi.org/10.1016/j.progsolidstchem.2004.08.001.

(42)   Beranek, R. (Photo)Electrochemical Methods for the Determination of the Band Edge Positions of TiO 2-Based Nanomaterials. *Advances in Physical Chemistry*. **2011**. https://doi.org/10.1155/2011/786759.

(43)   Thomas, C. R.; George, S.; Horst, A. M.; Ji, Z.; Miller, R. J.; Peralta-Videa, J. R.; Xia, T.; Pokhrel, S.; Mädler, L.; Gardea-Torresdey, J. L.; Holden, P. A.; Keller, A. A.; Lenihan, H. S.; Nel, A. E.; Zink, J. I. Nanomaterials in the Environment: From Materials to High-Throughput Screening to Organisms. *ACS Nano* **2011**. https://doi.org/10.1021/nn1034857.

(44)   Özcan, M.; Hämmerle, C. Titanium as a Reconstruction and Implant Material in Dentistry: Advantages and Pitfalls. *Materials (Basel).* **2012**. https://doi.org/10.3390/ma5091528.

(45)   Pegueroles, M.; Tonda-Turo, C.; Planell, J. A.; Gil, F. J.; Aparicio, C. Adsorption of Fibronectin, Fibrinogen, and Albumin on TiO2: Time-Resolved Kinetics, Structural Changes, and Competition Study. *Biointerphases* **2012**. https://doi.org/10.1007/s13758-012-0048-4.

(46)   Begonja, S.; Rodenas, L. A. G.; Borghi, E. B.; Morando, P. J. Adsorption of Cysteine on TiO2 at Different PH Values: Surface Complexes Characterization by FTIR-ATR and Langmuir Isotherms Analysis. *Colloids Surfaces A Physicochem. Eng. Asp.* **2012**. https://doi.org/10.1016/j.colsurfa.2012.03.064.

(47)   Köppen, S.; Bronkalla, O.; Langel, W. Adsorption Configurations and Energies of Amino Acids on Anatase and Rutile Surfaces. *J. Phys. Chem. C* **2008**. https://doi.org/10.1021/jp803354z.

(48)   Costa, D.; Savio, L.; Pradier, C. M. Adsorption of Amino Acids and Peptides on Metal and Oxide Surfaces in Water Environment: A Synthetic and Prospective Review. *Journal of Physical Chemistry B*. **2016**. https://doi.org/10.1021/acs.jpcb.6b05954.

(49)   Szieberth, D.; Maria Ferrari, A.; Dong, X. Adsorption of Glycine on the Anatase

(101) Surface: An Ab Initio Study. *Phys. Chem. Chem. Phys.* **2010**. https://doi.org/10.1039/c004155f.

(50) Ustunol, I. B.; Gonzalez-Pech, N. I.; Grassian, V. H. PH-Dependent Adsorption of α-Amino Acids, Lysine, Glutamic Acid, Serine and Glycine, on TiO2 Nanoparticle Surfaces. *J. Colloid Interface Sci.* **2019**. https://doi.org/10.1016/j.jcis.2019.06.086.

(51) Givens, B. E.; Xu, Z.; Fiegel, J.; Grassian, V. H. Bovine Serum Albumin Adsorption on SiO2 and TiO2 Nanoparticle Surfaces at Circumneutral and Acidic PH: A Tale of Two Nano-Bio Surface Interactions. *J. Colloid Interface Sci.* **2017**. https://doi.org/10.1016/j.jcis.2017.01.011.

(52) Hanaor, D. A. H.; Sorrell, C. C. Review of the Anatase to Rutile Phase Transformation. *Journal of Materials Science*. **2011**. https://doi.org/10.1007/s10853-010-5113-0.

(53) Luttrell, T.; Halpegamage, S.; Tao, J.; Kramer, A.; Sutter, E.; Batzill, M. Why Is Anatase a Better Photocatalyst than Rutile? - Model Studies on Epitaxial TiO$_2$ Films. *Sci. Rep.* **2015**. https://doi.org/10.1038/srep04043.

(54) Liu, L.; Zhao, H.; Andino, J. M.; Li, Y. Photocatalytic CO$_2$ Reduction with H$_2$O on TiO$_2$ Nanocrystals: Comparison of Anatase, Rutile, and Brookite Polymorphs and Exploration of Surface Chemistry. *ACS Catal.* **2012**. https://doi.org/10.1021/cs300273q.

(55) Iswarya, V.; Bhuvaneshwari, M.; Alex, S. A.; Iyer, S.; Chaudhuri, G.; Chandrasekaran, P. T.; Bhalerao, G. M.; Chakravarty, S.; Raichur, A. M.; Chandrasekaran, N.; Mukherjee, A. Combined Toxicity of Two Crystalline Phases (Anatase and Rutile) of Titania Nanoparticles towards Freshwater Microalgae: Chlorella Sp. *Aquat. Toxicol.* **2015**. https://doi.org/10.1016/j.aquatox.2015.02.006.

(56) Dorier, M.; Brun, E.; Veronesi, G.; Barreau, F.; Pernet-Gallay, K.; Desvergne, C.; Rabilloud, T.; Carapito, C.; Herlin-Boime, N.; Carrière, M. Impact of Anatase and Rutile Titanium Dioxide Nanoparticles on Uptake Carriers and Efflux Pumps in Caco-2 Gut Epithelial Cells. *Nanoscale* **2015**. https://doi.org/10.1039/c5nr00505a.

(57) Cornell, R. M.; Schwertmann, U. Introduction to the Iron Oxides. In *The Iron Oxides*; **2003**. https://doi.org/10.1002/3527602097.ch1.

(58) Hochella, M. F.; Lower, S. K.; Maurice, P. A.; Penn, R. L.; Sahai, N.; Sparks, D. L.; Twining, B. S. Nanominerals, Mineral Nanoparticles, and Earth Systems. *Science*. **2008**. https://doi.org/10.1126/science.1141134.

(59) Theng, B. K. G.; Yuan, G. Nanoparticles in the Soil Environment. *Elements* **2008**. https://doi.org/10.2113/gselements.4.6.395.

(60) Keller, A. A.; McFerran, S.; Lazareva, A.; Suh, S. Global Life Cycle Releases of

Engineered Nanomaterials. *J. Nanoparticle Res.* **2013**. https://doi.org/10.1007/s11051-013-1692-4.

(61)   Barreto, M. S. C.; Elzinga, E. J.; Alleoni, L. R. F. The Molecular Insights into Protein Adsorption on Hematite Surface Disclosed by In-Situ ATR-FTIR/2D-COS Study. *Sci. Rep.* **2020**, *10* (1), 1–13. https://doi.org/10.1038/s41598-020-70201-z.

(62)   Cornell, R. M.; Schwertmann, U. *The Iron Oxides*; **2003**. https://doi.org/10.1002/3527602097.

(63)   Schwaminger, S. P.; Fraga-García, P.; Selbach, F.; Hein, F. G.; Fuß, E. C.; Surya, R.; Roth, H. C.; Blank-Shim, S. A.; Wagner, F. E.; Heissler, S.; Berensmeier, S. Bio-Nano Interactions: Cellulase on Iron Oxide Nanoparticle Surfaces. *Adsorption* **2017**. https://doi.org/10.1007/s10450-016-9849-y.

(64)   Waychunas, G. A.; Kim, C. S.; Banfield, J. F. Nanoparticulate Iron Oxide Minerals in Soils and Sediments: Unique Properties and Contaminant Scavenging Mechanisms. In *Journal of Nanoparticle Research*; **2005**. https://doi.org/10.1007/s11051-005-6931-x.

(65)   Bolisetty, S.; Vallooran, J. J.; Adamcik, J.; Mezzenga, R. Magnetic-Responsive Hybrids of Fe3O4 Nanoparticles with β-Lactoglobulin Amyloid Fibrils and Nanoclusters. *ACS Nano* **2013**. https://doi.org/10.1021/nn401988m.

(66)   Mudunkotuwa, I. A.; Grassian, V. H. The Devil Is in the Details (or the Surface): Impact of Surface Structure and Surface Energetics on Understanding the Behavior of Nanomaterials in the Environment. *Journal of Environmental Monitoring*. **2011**. https://doi.org/10.1039/c1em00002k.

(67)   Limo, M. J.; Sola-Rabada, A.; Boix, E.; Thota, V.; Westcott, Z. C.; Puddu, V.; Perry, C. C. Interactions between Metal Oxides and Biomolecules: From Fundamental Understanding to Applications. *Chemical Reviews*. **2018.** https://doi.org/10.1021/acs.chemrev.7b00660.

(68)   Li, W.; Liu, D.; Wu, J.; Kim, C.; Fortner, J. D. Aqueous Aggregation and Surface Deposition Processes of Engineered Superparamagnetic Iron Oxide Nanoparticles for Environmental Applications. *Environ. Sci. Technol.* **2014**, *48* (20), 11892–11900. https://doi.org/10.1021/es502174p.

(69)   Wang, S.; Gao, B.; Zimmerman, A. R.; Li, Y.; Ma, L.; Harris, W. G.; Migliaccio, K. W. Removal of Arsenic by Magnetic Biochar Prepared from Pinewood and Natural Hematite. *Bioresour. Technol.* **2015**. https://doi.org/10.1016/j.biortech.2014.10.104.

(70)   Shuibo, X.; Chun, Z.; Xinghuo, Z.; Jing, Y.; Xiaojian, Z.; Jingsong, W. Removal of Uranium (VI) from Aqueous Solution by Adsorption of Hematite. *J. Environ. Radioact.* **2009**. https://doi.org/10.1016/j.jenvrad.2008.09.008.

(71)   Lalonde, K.; Mucci, A.; Ouellet, A.; Gélinas, Y. Preservation of Organic Matter in Sediments Promoted by Iron. *Nature* **2012**. https://doi.org/10.1038/nature10855.

(72)   Lalonde, K.; Mucci, A.; Ouellet, A.; Gélinas, Y.; Ge, Y. Iron Promotes the Preservation of Organic Matter in Sediments. *Nature* **2012**.

(73)   Zhang, W.; Hughes, J.; Chen, Y. Impacts of Hematite Nanoparticle Exposure on Biomechanical, Adhesive, and Surface Electrical Properties of Escherichia Coli Cells. *Appl. Environ. Microbiol.* **2012**. https://doi.org/10.1128/AEM.00193-12.

(74)   Qu, C.; Qian, S.; Chen, L.; Guan, Y.; Zheng, L.; Liu, S.; Chen, W.; Cai, P.; Huang, Q. Size-Dependent Bacterial Toxicity of Hematite Particles. *Environ. Sci. Technol.* **2019**. https://doi.org/10.1021/acs.est.9b00856.

(75)   Nel, A. E.; Mädler, L.; Velegol, D.; Xia, T.; Hoek, E. M. V.; Somasundaran, P.; Klaessig, F.; Castranova, V.; Thompson, M. Understanding Biophysicochemical Interactions at the Nano-Bio Interface. *Nature Materials*. **2009**. https://doi.org/10.1038/nmat2442.

(76)   Fadare, O. O.; Wan, B.; Liu, K.; Yang, Y.; Zhao, L.; Guo, L.-H. Eco-Corona vs Protein Corona: Effects of Humic Substances on Corona Formation and Nanoplastic Particle Toxicity in Daphnia Magna. *Environ. Sci. Technol.* **2020**. https://doi.org/10.1021/acs.est.0c00615.

(77)   Kleber, M.; Sollins, P.; Sutton, R. A Conceptual Model of Organo-Mineral Interactions in Soils: Self-Assembly of Organic Molecular Fragments into Zonal Structures on Mineral Surfaces. *Biogeochemistry* **2007**. https://doi.org/10.1007/s10533-007-9103-5.

(78)   Coward, E. K.; Ohno, T.; Sparks, D. L. Direct Evidence for Temporal Molecular Fractionation of Dissolved Organic Matter at the Iron Oxyhydroxide Interface. *Environ. Sci. Technol.* **2019**. https://doi.org/10.1021/acs.est.8b04687.

(79)   Leinemann, T.; Preusser, S.; Mikutta, R.; Kalbitz, K.; Cerli, C.; Höschen, C.; Mueller, C. W.; Kandeler, E.; Guggenberger, G. Multiple Exchange Processes on Mineral Surfaces Control the Transport of Dissolved Organic Matter through Soil Profiles. *Soil Biol. Biochem.* **2018**. https://doi.org/10.1016/j.soilbio.2017.12.006.

(80)   Saptarshi, S. R.; Duschl, A.; Lopata, A. L. Interaction of Nanoparticles with Proteins: Relation to Bio-Reactivity of the Nanoparticle. *J. Nanobiotechnology* **2013**. https://doi.org/10.1186/1477-3155-11-26.

(81)   Alberts, B.; Bray, D.; Johnson, A.; Lewis, J.; Raff, M.; Roberts, K.; Walter, P.; Protein Structure and Function. In *Essential Cell Biolog*; **2018.** https://doi.org/10.1201/9781315815015-4.

(82)   Settanni, G.; Zhou, J.; Suo, T.; Schöttler, S.; Landfester, K.; Schmid, F.;

Mailänder, V. Protein Corona Composition of Poly(Ethylene Glycol)-and Poly(Phosphoester)-Coated Nanoparticles Correlates Strongly with the Amino Acid Composition of the Protein Surface. *Nanoscale* **2017**. https://doi.org/10.1039/c6nr07022a.

(83) Rabe, M.; Verdes, D.; Seeger, S. Understanding Protein Adsorption Phenomena at Solid Surfaces. *Advances in Colloid and Interface Science*. **2011**. https://doi.org/10.1016/j.cis.2010.12.007.

(84) Casals, E.; Pfaller, T.; Duschl, A.; Oostingh, G. J.; Puntes, V. Time Evolution of the Nanoparticle Protein Corona. *ACS Nano* **2010**. https://doi.org/10.1021/nn901372t.

(85) Lynch, I.; Dawson, K. A. Protein-Nanoparticle Interactions. *Nano Today*. **2008**. https://doi.org/10.1016/S1748-0132(08)70014-8.

(86) Cedervall, T.; Lynch, I.; Lindman, S.; Berggård, T.; Thulin, E.; Nilsson, H.; Dawson, K. A.; Linse, S. Understanding the Nanoparticle-Protein Corona Using Methods to Quntify Exchange Rates and Affinities of Proteins for Nanoparticles. *Proc. Natl. Acad. Sci. U. S. A.* **2007**. https://doi.org/10.1073/pnas.0608582104.

(87) Nasser, F.; Constantinou, J.; Lynch, I. Nanomaterials in the Environment Acquire an "Eco-Corona" Impacting Their Toxicity to Daphnia Magna—a Call for Updating Toxicity Testing Policies. *Proteomics*. **2020.** https://doi.org/10.1002/pmic.201800412.

(88) Mahmoudi, M.; Lynch, I.; Ejtehadi, M. R.; Monopoli, M. P.; Bombelli, F. B.; Laurent, S. Protein-Nanoparticle Interactions: Opportunities and Challenges. *Chemical Reviews*. **2011**. https://doi.org/10.1021/cr100440g.

(89) Hagemans, D.; van Belzen, I. A. E. M.; Luengo, T. M.; Rüdiger, S. G. D. A Script to Highlight Hydrophobicity and Charge on Protein Surfaces. *Front. Mol. Biosci.* **2015**. https://doi.org/10.3389/fmolb.2015.00056.

(90) Norde, W. My Voyage of Discovery to Proteins in Flatland ...and Beyond. *Colloids and Surfaces B: Biointerfaces*. **2008**. https://doi.org/10.1016/j.colsurfb.2007.09.029.

(91) Kang, Y.; Li, X.; Tu, Y.; Wang, Q.; Ågren, H. On the Mechanism of Protein Adsorption onto Hydroxylated and Nonhydroxylated TiO2 Surfaces. *J. Phys. Chem. C* **2010**. https://doi.org/10.1021/jp1037156.

(92) Van Der Veen, M.; Norde, W.; Stuart, M. C. Electrostatic Interactions in Protein Adsorption Probed by Comparing Lysozyme and Succinylated Lysozyme. *Colloids Surfaces B Biointerfaces* **2004**. https://doi.org/10.1016/j.colsurfb.2004.02.005.

(93)   Norde, W.; Anusiem, A. C. I. Adsorption, Desorption and Re-Adsorption of Proteins on Solid Surfaces. *Colloids and Surfaces* **1992**. https://doi.org/10.1016/0166-6622(92)80122-I.

(94)   Larsericsdotter, H.; Oscarsson, S.; Buijs, J. Structure, Stability, and Orientation of BSA Adsorbed to Silica. *J. Colloid Interface Sci.* **2005**. https://doi.org/10.1016/j.jcis.2005.03.064.

(95)   Turci, F.; Ghibaudi, E.; Colonna, M.; Boscolo, B.; Fenoglio, I.; Fubini, B. An Integrated Approach to the Study of the Interaction between Proteins and Nanoparticles. *Langmuir* **2010**. https://doi.org/10.1021/la904758j.

(96)   Rose, G. D. Secondary Structure in Protein Analysis. In *Encyclopedia of Biological Chemistry*; **2004**. https://doi.org/10.1016/b0-12-443710-9/00613-x.

(97)   Banaszak, L. J. Introduction to Protein Structure. In *Foundations of Structural Biology*; **2000**. https://doi.org/10.1016/b978-012077700-6/50001-8.

(98)   Pulido-Reyes, G.; Leganes, F.; Fernández-Piñas, F.; Rosal, R. Bio-Nano Interface and Environment: A Critical Review. *Environmental Toxicology and Chemistry*. **2017**. https://doi.org/10.1002/etc.3924.

Chapter 2   Experimental Methods

A variety of experimental methods and techniques were used in the research presented in this dissertation. These techniques provide insights into the detailed behavior of metal oxide nanoparticles in complex environmental or biological environments. Using physicochemical characterization tools that allowed for extensive macro- to nano-scale analyses, this dissertation aims to contribute to a conceptual framework for understanding the fate and implications of biomolecule-nanoparticle interactions from amino acid and protein adsorption studies. The details of the experimental methods utilized are described within the respective chapters. A summary of the experimental techniques used in this dissertation is shown in Table 2.1. The specific experimental designs were tailored case by case for each project to investigate the different aspects of the research.

Table 2.1: Experimental techniques used in this dissertation to probe nanoparticle physicochemical characterization, nanoparticle–nanoparticle interactions and aggregation, and aqueous-phase biomolecule adsorption to mineral surfaces.

	Techniques	Data Provided
Nanoparticle Physicochemical Characterization	Scanning Electron Microscopy (SEM)	Nanoparticle morphology (i.e., size, shape) and thin-film thickness measurements.
	Energy Dispersive X-Ray Spectroscopy (EDX)	Elemental mapping analyses of airborne nanoparticles.
	Transmission Electron Microscopy (TEM)	Nanoparticle morphology (i.e., size, shape) measurements, and aggregation state analyses.
	Brunauer-Emmett-Teller (BET) Analyzer	Specific surface area measurements of nanoparticles, including pore size and pore volume analyses.
	Powder X-Ray Diffraction (XRD)	Crystalline phase identification of nanoparticles.
Nanoparticle–Nanoparticle Interactions and Aggregation Studies	Dynamic Light Scattering (DLS)	Colloidal stability, hydrodynamic diameter, aggregation behavior, and aggregation kinetics of nanoparticles.
	Zeta Potential Analysis (ξ-potential)	Nanoparticle surface charge and stability as a function of pH, concentration, and functionalization in aqueous environments.
Aqueous Phase Biomolecule Surface Adsorption	Attenuated Total Reflection Fourier Transform Infrared Spectroscopy (ATR-FTIR)	Molecular-level characterization of biomolecule-nanoparticle interactions as a function of pH, concentration, and type of adsorbed molecules.

2.1 Nanoparticle Physiochemical Characterization

2.1.1 Scanning Electron Microscopy (SEM)

Scanning Electron Microscopy (SEM) is designed to analyze solid objects' surfaces by utilizing a beam of focused electrons of relatively low energy as an electron probe scanned over the sample.[1,2] The signals from the interaction of the electrons and sample surface produce secondary, backscattered, diffracted backscattered electrons, X-ray photons, etc. A teardrop-shaped electron–solid matter interaction volume with respective limits to the depths where each signal type can be emitted or detected are shown in Fig. 2.1. When an electron beam interacts with the specimen, the action stimulates the emission of high-energy backscattered electrons and low-energy secondary electrons from the specimen's surface. In SEM imaging, secondary electrons and backscattered electrons are mostly used. As the energy of secondary electrons is usually low (< 50 eV), the mean free path is limited in solid matter, and beams can escape from the surface after beam electrons have ejected them from atoms in the sample.[3,4] Backscattered electrons emerge from the specimen with a large fraction of the incident energy intact after experiencing scattering and deflection by the electric fields of the atoms in the sample.[3] The signals are then captured in a detector to provide direct information about the surface features.
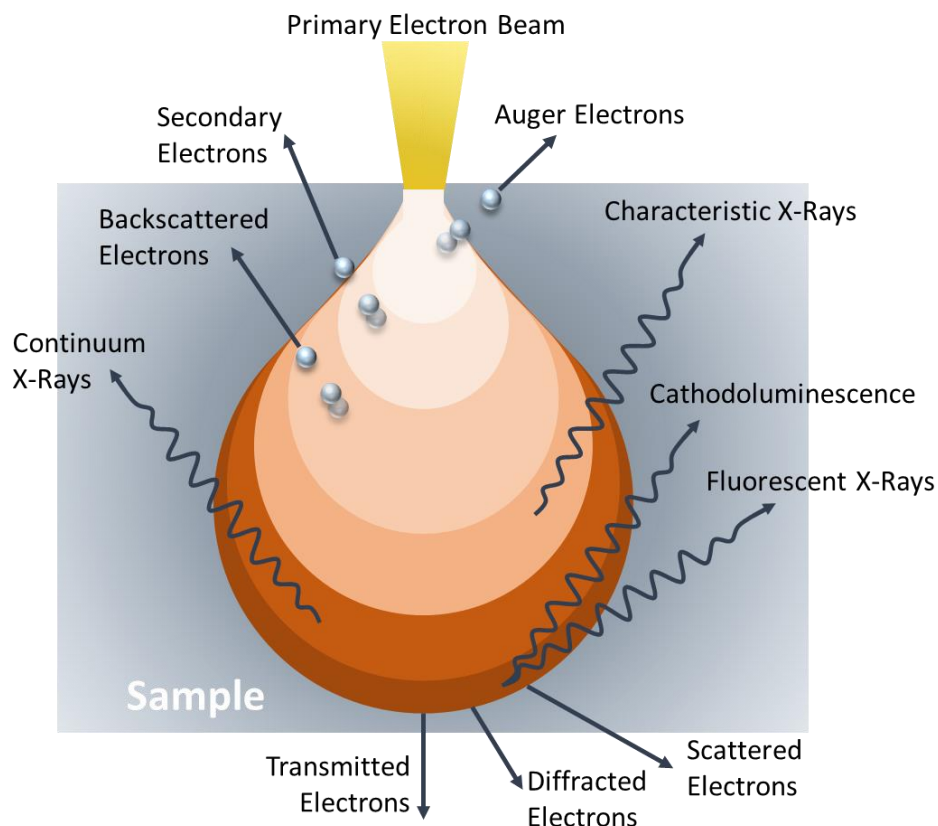
Figure 2.1: Different types of signals generated with electron–matter interaction volume.

For this work, SEM was primarily used to image nanoparticle morphology (i.e., size, shape) and acquire thin film thickness measurements of TiO_2 and $\alpha\text{-}Fe_2O_3$ nanoparticles. The thickness of the nanoparticle thin film over an internal reflection element (IRE) is crucial for ATR-FTIR measurements to understand the interaction and adsorption of molecules on the nanoparticle surface. Combining various detectors and beam generation systems within an SEM chamber has been very useful for different applications in nano and material science.[5] In addition to traditional SEM, Field Emission SEM (FE-SEM) was employed for thin-film thickness measurements. Compare with conventional SEM, this technique differs from producing clearer, less electrostatically

distorted images. FE-SEM was used to create improved spatial resolution images at low potentials (1-3 kV for this study). To simulate a film preparation on the crystal, the ATR crystal was initially covered with 16 silicon wafers (5x5 mm each). 1 mL of 3 mg/mL TiO_2 and 5 mg/mL α-Fe_2O_3 nanoparticle suspensions were deposited on the IRE and dried overnight. The wafers were then placed on cross-section sample holders to image the thickness of the films. The FE-SEM results showed that both α-Fe_2O_3 and TiO_2 nanoparticle films were ~3 µm (Fig. 2.2).
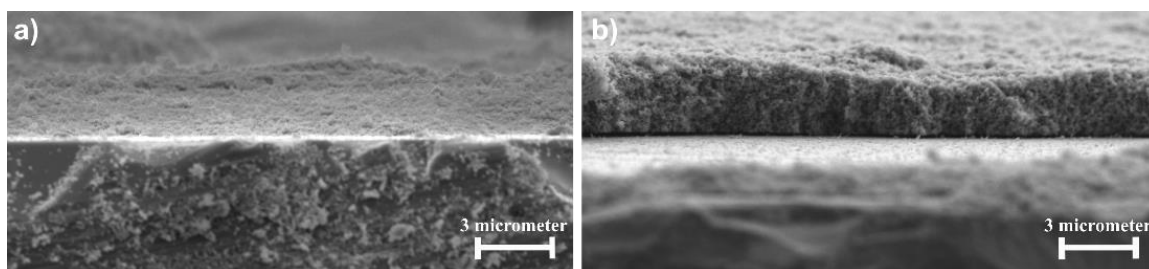
Figure 2.2: Cross-sectional FE-SEM images for a) α-Fe_2O_3 and b) TiO_2 nanoparticle thin films over silicon wafers.

2.1.2 Energy Dispersive X-Ray Spectroscopy (EDX)

Energy-dispersive X-ray spectroscopy (EDX) is an analytical tool used for the elemental analysis or chemical characterization of a sample.[6] The method relies on the interaction between X-ray excitation and sample composition. The characterization capability of EDX is based on the fundamental principle that each element has a unique atomic structure allowing for a unique set of peaks on its X-ray spectrum.[6]

When a high-energy beam of charged electrons or protons, or a beam of X-rays, is focused onto the sample, it stimulates X-rays' emission. Briefly, every atom in its ground state has electron shells bound to the nucleus. When the electron beam interacts with the specimen, an electron can eject from its inner-shell, creating a hole in its ground state. An

outer electron, a high-energy electron, fills the gap, and the difference in the energy is released as an X-ray.[1] In EDX, the number and energy of the X-rays emitted from a specimen can be measured. The difference between the energy levels of two shells is element-specific, allowing the elemental composition of the specimen to be determined.[6,7] EDX can be used for elemental analysis of the specimen surface while obtaining color-coded elemental mapping from SEM images. In this dissertation, EDX was used to analyze the elemental composition of airborne metal-containing particles collected on substrates from Microorifice Uniform Deposit Impactor (MOUDI)[8] stages at the machining center site and the foundry site. The details of these experiments are explained in Chapter 7 of the dissertation.

2.1.3   Transmission Electron Microscopy (TEM)

Transmission Electron Microscopy (TEM) provides molecular-level resolution images, and it is widely used in nanomaterial characterization.[9] TEM leverages the advantages of accelerated electron beam transmission (by the high voltage electric field) through a specimen, allowing for imaging of the internal as well as external features of material by analyzing morphology, composition, and crystal structure.[10]

Both SEM and TEM present unique advantages when compared to the other. In this dissertation, TEM was used to measure the size and size distribution of individual nanoparticles and analyze d-spacing to assess exposed facets of surface planes. Before imaging, diluted nanoparticle suspensions in MilliQ water were sonicated for 2 minutes. A 10 µL droplet from the sonicated suspension was then deposited on a formvar/carbon-coated 100-mesh copper grid and kept inside a dry (H_2O-less) air chamber until dried.

Images of the nanoparticles were taken by a JEOL JEM-1400 Plus transmission electron microscopy (TEM) at 80 kV. The acquired TEM images were processed using ImageJ software that allowed for lattice spacing measurements and size distributions.

2.1.4   Powder X-Ray Diffraction (XRD)

Crystalline phase characterization of the nanoparticles was completed using powder X-ray diffraction (XRD). XRD is a technique based on the constructive interference of monochromatic X-rays and a long-range-ordered, crystalline sample. In this method, an electron cloud movement is created by the incident X-ray waves interacting with an atom on the crystal surface. Re-radiation of the same frequency waves creates elastic scattering. The diffracted waves can then interfere to produce a diffraction maximum at certain incident angles, and specifically, constructive interference (and a diffracted ray), when conditions satisfy Bragg's Law, as shown in Equation 2.1:[11]

$$2d \sin\theta = n \lambda \qquad\qquad\qquad \text{(Eq. 2.1)}$$

where d is the interplanar distance of the crystal; θ is the angle of incidence; λ is the wavelength of the incident X-rays, and n is a positive integer representing the order of the diffraction. Samples rich in Fe could create fluorescence[12] under the incident Cu K_α beam from Cu XRD anodes, resulting in polychromatic radiation and an elevated background. This heightened background occurs because the $K\alpha$ line of Fe emitted radiation (6.40 keV) is close to the Cu K_α (8.04 keV). Fe-derived radiation will be detected, which would not affect peak position or intensity but increase the background. Two different types of XRD anodes (Mo and Cu) were used in this dissertation to eliminate this issue. The crystalline phase of TiO_2 nanoparticles was determined with a D8 ADVANCE Bruker powder XRD

using Cu K_α radiation at $\lambda=1.54184$ Å. Whereas, the crystalline phase of α-Fe_2O_3 nanoparticles was determined using an APEX II Ultra diffractometer equipped with a CCD-based area detector, using Mo K_α radiation at $\lambda= 0.71073$ Å.

2.1.5 Brunauer–Emmett–Teller (BET) Surface Area Measurements

Specific surface area (SSA) was calculated by Brunauer-Emmett-Teller (BET) analysis using a multi-point N_2-BET isotherm approach. A Quantachrome Nova 4200e surface analyzer was used for SSA and pore size measurements. Prior to nanoparticle loading, empty borosilicate sample tubes were weighed. Powdered nanoparticles were then placed in sample tubes and degassed at the desired temperature and time to remove any pre-adsorbed (impurities) molecules from the sample surface. After degassing, the sample's accurate mass was obtained by subtracting the initial sample tube mass from the total mass. N_2 adsorption-desorption isotherms in the relative pressure range (P/P_0) of 0.05-0.95 were used to determine SSA. The BET equation used for the calculations is shown in Equation 2.2:[13]

$$\frac{1}{W\left[\left(\frac{P_o}{P}\right)-1\right]} = \frac{1}{W_m C} + \frac{C-1}{W_m C}\left(\frac{P}{P_o}\right) \qquad \text{(Eq. 2.2)}$$

here, W is the weight of the adsorbed N_2 gas; W_m is the weight of the adsorbate constituting a monolayer, C is the BET constant, and P and P_o are the equilibrium and saturation pressures.

2.2   Nanoparticle–Nanoparticle Interactions and Aggregation Studies

2.2.1   Dynamic Light Scattering (DLS) for Hydrodynamic Diameter

Surface chemistry of nanoparticles plays a crucial role in their physicochemical behavior within complex environmental and biological processes, some of which can be seen in Fig. 2.3. In an aqueous environment, surface chemistry can affect adsorbate affinity to the surface.[14,15] A detailed understanding of nanoparticles' surface chemistry can help to

understand the relationships between nanoparticle structure, nanoparticle, and sorbate chemical activity. Hydrodynamic size indicates how nanoparticles behave in a liquid environment,[16] and one of the most critical factors determining distribution kinetics.[17] When characterizing nanoparticles, it reflects the size of the colloids in solution and includes surface coatings.[18] Upon adsorption of the molecules to nanoparticle surfaces, hydrodynamic size could change due to surface modifications. Determining the changes in hydrodynamic size for bare and biomolecule-coated nanoparticles is an important factor as most applications of nanomaterials occur in solutions. In this dissertation, nanoparticles' hydrodynamic sizes were measured using Dynamic Light Scattering (DLS), which enables us to investigate the correlation of particle sizes with physiological responses in a continually changing, dynamic state, where molecules adsorb onto the particle forming coronas.
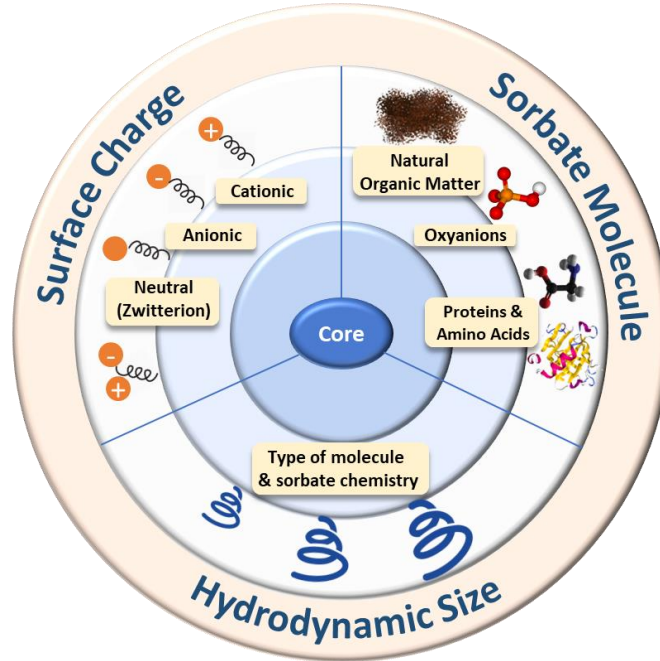
Figure 2.3: Surface chemistry parameters of nanoparticles that impact their environmental and biological fate in complex aqueous systems.

In an aqueous suspension, nanoparticles undergo Brownian motion due to the random collisions with the solvent and diffusion. The diffusion of particles is impacted by multiple factors and can be described by the Stokes-Einstein equation (Equation 2.3):

$$D = \frac{k_B T}{3\pi\eta d}$$
(Eq. 2.3)

where D is the diffusion coefficient, k_B is the Boltzmann constant, T is the absolute temperature, η is the viscosity, and d is the hydrodynamic diameter.

DLS quantitatively investigates the nanoparticle aggregation state in the aqueous milieu. When a laser beam is directed to the nanoparticle suspension, the beam scatters due to Brownian motion. The intensity fluctuates as a function of time and is then monitored and analyzed by autocorrelation functions in the instrument. The time decay in the correlation functions is a result of the hydrodynamic size of particles. To reduce their

surface free energy, nanoparticles tend to aggregate in an aqueous medium; therefore, it is essential to consider the hydrodynamic size of these nanoparticles. It is a more realistic depiction of their behavior compared to the calculated or observed size determined by electron microscopy imaging.

Hydrodynamic sizes of bare and amino acid-coated TiO_2 and α-Fe_2O_3 nanoparticles were investigated using a Beckman Coulter Delsa Nano submicron particle analyzer. A nanoparticle stock suspension was sonicated for 2 min, and aliquots were added to prepared amino acid solutions to reach final nanoparticle concentrations of 0.03 g/L and 0.01 g/L for TiO_2 and α-Fe_2O_3, respectively. These target concentration values were substantially more dilute than those used in ATR-FTIR experiments to increase light scattering efficiency.[19] Prior to nanoparticle addition, amino acid solutions were filtered through 0.2 µm syringe filters (Acrodisc, PALL) to remove any dust that could potentially distort the analysis.

2.2.2 Zeta Potential Analysis for Surface Charge Measurements

Nanoparticles in aqueous environments have charged surfaces. Zeta potential can be defined as the electric potential at the "slipping plane" or the interface which separates the mobile fluid from the fluid that remains attached to the nanoparticle surface, as shown by the schematic in Fig. 2.4.[20] In here, a negatively-charged nanoparticle surface is illustrated. Once the oppositely charged ions in the aqueous medium are attracted to the nanoparticle surface, they create ion clusters and ionized layers. Those ions strongly bonded to the surface is defined as the "stern layer." The layer between the stern layer and

slipping place is termed as the "diffuse layer." The diffuse layer and the stern layer together are referred to as the "electrical double layer."

In this work, Zeta-potential measurements were carried out with a Malvern Instruments Zetasizer Nano instrument. Samples were prepared following the same method for DLS measurements (section 2.2.1). Triplicate measurements were taken with 120 seconds equilibrium time given between each repetition. Zeta-potential results were fit to a Gaussian model and the mean values were reported.
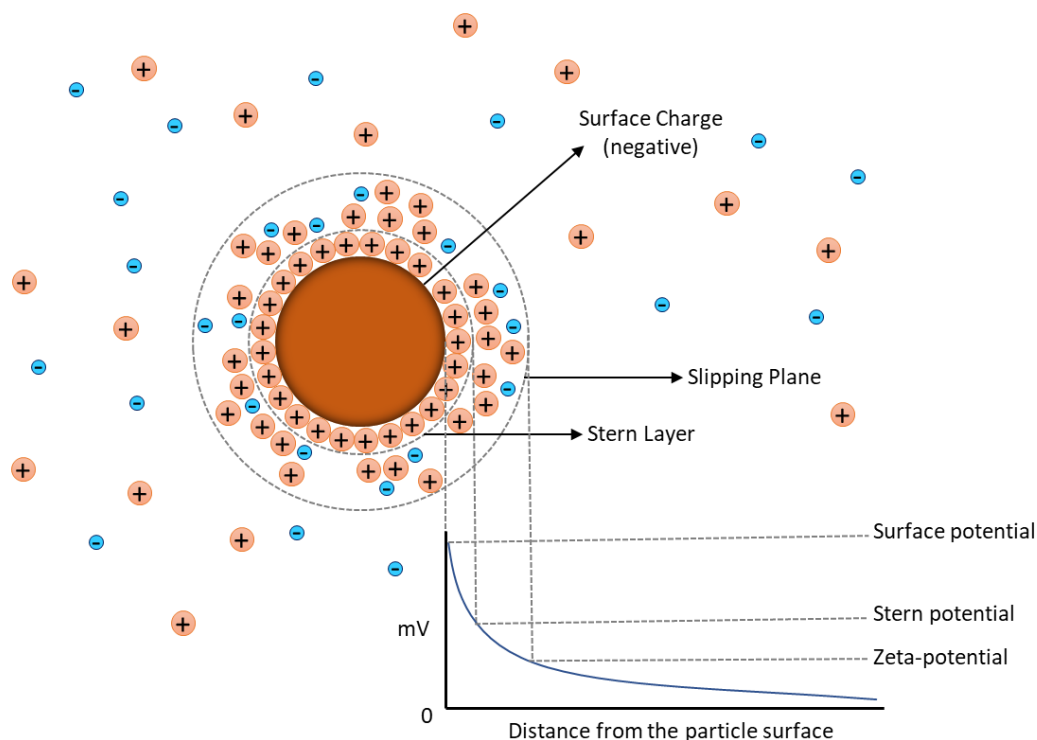
Figure 2.4: Schematic showing the zeta-potential concept and the respective charge layers.

2.3 Aqueous Phase Biomolecule Surface Adsorption

2.3.1 Attenuated Total Reflectance–Fourier Transform Infrared (ATR-FTIR) Spectroscopy

Infrared (IR) spectroscopy and Fourier transform infrared (FTIR) spectroscopy are highly established techniques for solid-phase characterization. Attenuated total reflection Fourier transform infrared (ATR-FTIR) spectroscopy has been developed to probe the molecular structure of, and interactions between, solid-phase compounds.[21] A schematic representation of an ATR-FTIR experimental setup is shown in Fig. 2.5. Spectra are obtained from the absorbance of the evanescent wave from IR active moieties in the interfacial region. Therefore, ATR is a sensitive technique to probe the interfacial region rather than the bulk sample, even in the presence of strong absorbing solvents, like water. These features make ATR-FTIR applicable to real-time *in-situ* analyses of the adsorption kinetics and molecular structural changes associated with adsorption.
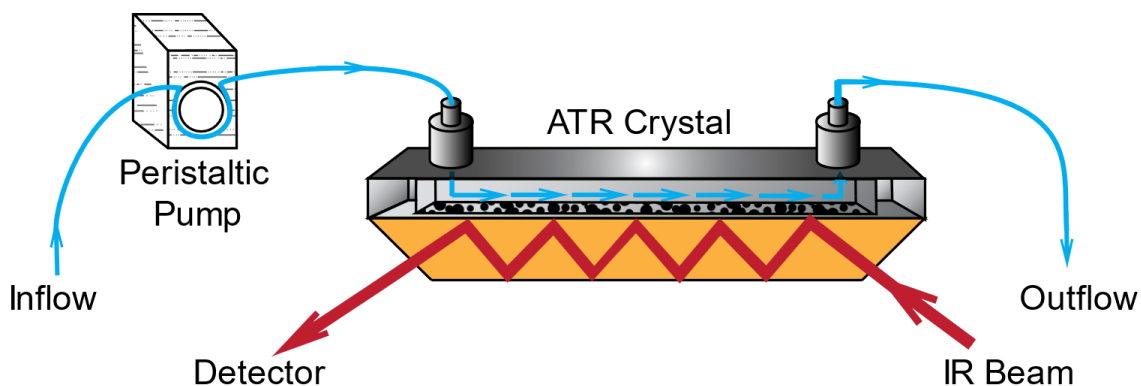
Figure 2.5:   Schematic representation of ATR-FTIR experimental setup.

In this technique, an infrared light beam is directed at an internal reflection element (IRE) at an incidence angle (θ). Total reflectance occurs at the interface of two materials

with different optical refractive indices.[21] The material with a higher refractive index (optically dense) is the IRE, while the one with the lower refractive index (optically rare) is the sample medium. At the point of reflection, an evanescent wave is generated below the sample. This field has a certain penetration depth (d_p), which depends on the properties of the materials involved and their respective refractive indices and is a measure of how far the evanescent wave extends into the sample. More specifically, the penetration depth is a result of the IR beam energy being absorbed by the molecule, due to the excitation from the ground vibrational energy level to a higher energy level. The difference within vibrational frequency changes provides information that allows for the study of molecular-level interactions of nanoparticles on liquid-solid interfaces, including the chemical and structural changes that occur during adsorption. The parameters involved in calculating the penetration depth are given by Equation 2.4:[21]

$$d_p = \frac{\lambda}{2\pi n_1 \sqrt{\left[sin^2\theta - (\frac{n_2}{n_1})^2 \right]}} \qquad \text{(Eq. 2.4)}$$

where λ is the wavelength, n_1 is the refractive index of the IRE, and n_2 is the refractive index of the sample medium in direct contact with the IRE.

In this dissertation, ATR-FTIR spectra were collected using a horizontal flow cell with an Amorphous Material Transmitting Infrared Radiation (AMTIR) crystal in a Thermo−Nicolet iS10 FTIR spectrometer equipped with an MCT-A detector. This crystal was selected because of its high chemical resistance in acidic and neutral environments and larger penetration depth compared to other IREs such as ZnSe and Ge. ATR-FTIR spectra were recorded across various time intervals suited to the research questions of each study.

1 mL aliquots from either 1.5 mg/mL TiO_2 or 5 mg/mL $\alpha\text{-}Fe_2O_3$ suspensions were deposited on the AMTIR crystal and dried overnight to form a thin film. Initially, pH adjusted MilliQ water (or buffer solution) water was flushed over the nanoparticle thin film for a desired amount of time to eliminate loosely bound particles, followed by a collection of a background spectrum. Spectra of adsorbates bound on nanoparticle surfaces were then acquired by subtracting the background spectrum from the time-dependent spectra. To determine surface-induced conformational changes of adsorbates, solution-phase spectra of the desired biomolecule were also collected.

2.4   References

(1)   JEOL. Scanning Electron Microscope A To Z. *Serv. Adv. Technol.* **2006**. https://doi.org/10.1017/S1431927605507797.

(2)   Joy, D. C. Introduction to the Scanning Electron Microscope. In *Microscopy and Microanalysis*; **2003**. https://doi.org/10.1017/s1431927603447788.

(3)   Goldstein, J. I.; Newbury, D. E.; Michael, J. R.; Ritchie, N. W. M.; Scott, J. H. J.; Joy, D. C. *Scanning Electron Microscopy and X-Ray Microanalysis*; **2017**. https://doi.org/10.1007/978-1-4939-6676-9.

(4)   Gomer, R. Field, Thermionic, and Secondary Electron Emission Spectroscopy. *J. Colloid Interface Sci.* **1984**. https://doi.org/10.1016/0021-9797(84)90229-7.

(5)   Zhou, W.; Apkarian, R.; Wang, Z. L.; Joy, D. Fundamentals of Scanning Electron Microscopy (SEM). In *Scanning Microscopy for Nanotechnology: Techniques and Applications*; **2007**. https://doi.org/10.1007/978-0-387-39620-0_1.

(6)   Nasrollahzadeh, M.; Atarod, M.; Sajjadi, M.; Sajadi, S. M.; Issaabadi, Z. Plant-Mediated Green Synthesis of Nanostructures: Mechanisms, Characterization, and Applications. In *Interface Science and Technology*; **2019.** https://doi.org/10.1016/B978-0-12-813586-0.00006-7.

(7)   Erdman, N.; Bell, D. C.; Reichelt, R. Scanning Electron Microscopy. In *Springer Handbooks*; **2019**. https://doi.org/10.1007/978-3-030-00069-1_5.

(8)   Marple, V. A.; Rubow, K. L.; Behm, S. M. A Microorifice Uniform Deposit

Impactor (Moudi): Description, Calibration, and Use. *Aerosol Sci. Technol.* **1991**. https://doi.org/10.1080/02786829108959504.

(9)   Smith, D. J. CHAPTER 1: Characterization of Nanomaterials Using Transmission Electron Microscopy. In *RSC Nanoscience and Nanotechnology*; **2015**. https://doi.org/10.1039/9781782621867-00001.

(10)   Wen, J. G. Transmission Electron Microscopy. In *Practical Materials Characterization*; **2014**. https://doi.org/10.1007/978-1-4614-9281-8_5.

(11)   Cantor, B.; Cantor, B. Bragg's Law. In *The Equations of Materials*; **2020.** https://doi.org/10.1093/oso/9780198851875.003.0002.

(12)   Chavan, T. A.; Ajith, N.; Periyamana Sankaran nampoothiri, R. D.; Swain, K. K. Energy Dispersive X-Ray Fluorescence Determination of Fe in Solid Powder Samples: A Quality Improvement Perspective. *X-Ray Spectrom.* **2019**. https://doi.org/10.1002/xrs.3023.

(13)   Brunauer, S.; Emmett, P. H.; Teller, E. Adsorption of Gases in Multimolecular Layers. *J. Am. Chem. Soc.* **1938**. https://doi.org/10.1021/ja01269a023.

(14)   Nam, J.; Won, N.; Bang, J.; Jin, H.; Park, J.; Jung, S.; Jung, S.; Park, Y.; Kim, S. Surface Engineering of Inorganic Nanoparticles for Imaging and Therapy. *Advanced Drug Delivery Reviews*. **2013**. https://doi.org/10.1016/j.addr.2012.08.015.

(15)   Nasser, F.; Constantinou, J.; Lynch, I. Nanomaterials in the Environment Acquire an "Eco-Corona" Impacting Their Toxicity to Daphnia Magna—a Call for Updating Toxicity Testing Policies. *Proteomics*. **2020**. https://doi.org/10.1002/pmic.201800412.

(16)   Gittings, M. R.; Saville, D. A. The Determination of Hydrodynamic Size and Zeta Potential from Electrophoretic Mobility and Light Scattering Measurements. *Colloids Surfaces A Physicochem. Eng. Asp.* **1998**. https://doi.org/10.1016/S0927-7757(98)00207-6.

(17)   Yang, L.; Kuang, H.; Zhang, W.; Aguilar, Z. P.; Xiong, Y.; Lai, W.; Xu, H.; Wei, H. Size Dependent Biodistribution and Toxicokinetics of Iron Oxide Magnetic Nanoparticles in Mice. *Nanoscale* **2015**. https://doi.org/10.1039/c4nr05061d.

(18)   Maguire, C. M.; Rösslein, M.; Wick, P.; Prina-Mello, A. Characterisation of Particles in Solution–a Perspective on Light Scattering and Comparative Technologies. *Science and Technology of Advanced Materials*. **2018**. https://doi.org/10.1080/14686996.2018.1517587.

(19)   Lowry, G. V.; Hill, R. J.; Harper, S.; Rawle, A. F.; Hendren, C. O.; Klaessig, F.; Nobbmann, U.; Sayre, P.; Rumble, J. Guidance to Improve the Scientific Value of

Zeta-Potential Measurements in NanoEHS. *Environ. Sci. Nano* **2016**. https://doi.org/10.1039/c6en00136j.

(20)   Bhattacharjee, S. DLS and Zeta Potential - What They Are and What They Are Not? *Journal of Controlled Release*. **2016**. https://doi.org/10.1016/j.jconrel.2016.06.017.

(21)   Mudunkotuwa, I. A.; Minshid, A. Al; Grassian, V. H. ATR-FTIR Spectroscopy as a Tool to Probe Surface Adsorption on Nanoparticles at the Liquid-Solid Interface in Environmentally and Biologically Relevant Media. *Analyst*. **2014**. https://doi.org/10.1039/c3an01684f.

Chapter 3   pH-Dependent Adsorption of α-Amino Acids, Lysine, Glutamic Acid, Serine and Glycine, on TiO₂ Nanoparticle Surfaces

3.1   Abstract

TiO₂ nanoparticles (NPs) are widely used in different applications, and potential exposure to these NPs raises concerns about their impact on human health. In contact with biological fluids, proteins adsorb onto NPs to create a protein corona. Protein adsorption is highly dependent on the affinity between exterior amino acid residues and the NP surface. Thus, studying amino acids adsorption onto NPs can provide insight into protein corona formation. Herein, the pH-dependent adsorption of α-amino acids onto TiO₂ NPs in buffered solutions is described. Methods include attenuated total reflectance-Fourier transform infrared (ATR-FTIR) spectroscopy to analyze molecular interactions and dynamic light scattering (DLS) to measure changes in size and zeta-potential upon adsorption. Since pH determines the surface charge and functionality, and the predominant molecular species, the adsorption affinity is highly pH dependent. Adsorption of lysine and glycine increases proportionally with changes in pH, whereas glutamic acid adsorption decreases with increasing pH. Serine shows the highest adsorption at its isoelectric point. These differences are attributed to the different speciation of the functional groups within the amino acids and the TiO₂ surface charge at each pH. Analyzing the pH-dependent adsorption of amino acids can provide a better understanding of biomolecule-surface interactions in *in vivo* and different biological *milieu*.

3.2   Introduction

In the last few decades, the increased use of NPs has led to concerns about their impact on human health and the environment.[1-4] This leads to intentional or unintentional exposure to NPs through pulmonary routes, oral ingestion, dermal contact or intravenous injection for biomedical applications.[5] As soon as NPs interact with biological fluids, competitive adsorption of different proteins and biological components creates a dynamic coating on the NP surface. This layer is termed the "protein corona", and it determines the NP biological identity and influences physiological and therapeutic responses to NPs.[6, 7] Contingent upon their biological identity, NPs can deposit on primary tissues or translocate to secondary sites. Furthermore, they can disrupt cell type-specific cytoskeleton,[5] accumulate in regions of the lungs[8] or even aggregate in the brain.[9]

TiO$_2$ has been widely used in surface science studies as a model semiconductor metal oxide.[10-12] There has been rising interest in TiO$_2$ interactions with proteins and amino acids to improve the *in situ* material performance and better understand biological component-surface interactions at the molecular level.[13, 14] Amino acids adsorption on NPs has been reported in numerous theoretical and experimental studies.[15-25] These studies conclude that the sequence of amino acids influences peptide bonding and protein corona formation. Studying amino acid interactions with NP surfaces contributes to our understanding of the "new biological identity" of NPs in biological *milieu*. The results of these studies can provide insight into the formation of protein corona, as well as protein secondary structural changes upon adsorption in potentially a predictable way.
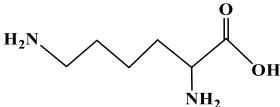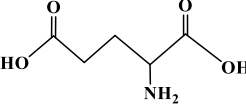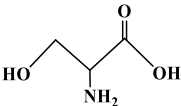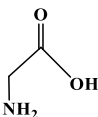
In aqueous environments, amino acids adsorb onto oxide NP surfaces on different surface sites. Hydroxyl groups are often involved in these interactions.[20] For amino acids, carboxylate groups can displace surface hydroxyl groups and directly bind to titanium sites at the surface.[26] For example, carboxylate groups play an essential role in cysteine adsorption.[27, 28] pH-dependent adsorption studies of cysteine onto TiO_2 have shown that adsorption is through electrostatic interactions and/or carboxylate coordination onto the surface.[23, 29] A molecular dynamics (MD) study[16] concluded that adsorption probabilities of arginine and aspartic acid (at pH values where these amino acids are charged) on TiO_2 NPs were significantly higher than aromatic and non-polar residues. Serine demonstrated weaker adsorption, but results were still higher than adsorption of less polar amino acids. However, physiological conditions such as pH and ionic strength were not considered in that study. In fact, the pH in different regions of the human body varies quite a bit. It is acidic in the stomach (pH = 1.5–4), neutral in the blood (pH = 7.35–7.45) and slightly alkaline in some parts of the duodenum and the intestines (pH = 7–8).[30-32] Thus, understanding the pH-dependent mechanisms of amino acid adsorption is essential. A recent study correlated the protein corona formation with the amino acid sequence of the protein exterior,[33] suggesting that protein adsorption behavior onto NP surfaces is related to amino acid interactions.

The primary aim of this study is to uncover in detail how pH affects amino acids speciation and their adsorption onto TiO_2 NPs. ATR-FTIR spectroscopy is used for *in situ* monitoring of amino acid adsorbates by probing the spectral changes during the adsorption process. Furthermore, the impact of surface coverage on NP physicochemical properties is analyzed using a DLS instrument and zeta-potential measurements. The size and surface

43

charge of NPs can impact living organisms and play an important role in how the human body responds to exposure and/or detoxifies NPs.[34-36] Therefore, the findings of this current study provide molecular level detail of the pH-dependent adsorption mechanisms of amino acids onto TiO_2 NPs. The insights from these studies contribute to elucidate specifics of the protein corona formation and aides in further understanding of biomolecule-surface interactions.

Table 3.1: Amino acids used in this study including their side chain characteristics, molecular structures, logarithmic dissociation constants (pKa), and isoelectric points (pHIEP) at 25 °C.

Amino Acid (Abbreviation)	Side Chain Characteristics	Molecular Structure	pK_a			pH_{IEP}
			pK_{a_1}	pK_{a_2}	pK_{a_3}	
Lysine (Lys, K)	polar positively charged		2.15	9.16	10.67	9.47
Glutamic Acid (Glu, E)	polar negatively charged		2.16	4.15	9.58	3.22
Serine (Ser, S)	polar neutral		2.13	9.05	–	5.68
Glycine (Gly, G)	non-polar neutral		2.34	9.58	–	6.06
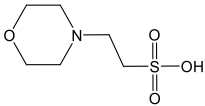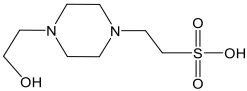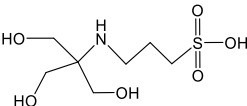
3.3   Materials and Methods

3.3.1   Materials

TiO$_2$ NPs were purchased from Nanostructured and Amorphous Materials Inc. L-lysine (>98.5%) and glycine (>98.5%) were purchased from Fisher Scientific, Inc. L-

glutamic acid (>99%) and L-serine (>99%) were purchased from Acros Organics. Characteristics of the amino acids used in this study are listed in Table 3.1. 2-(N-morpholino)-ethane sulfonic acid (MES) and 4-(2-hydroxyethyl)-1-piperazineethanesulfonic acid (HEPES) were obtained from Fisher Scientific Inc., and tris(hydroxymethyl)methylamino propane sulfonic acid (TAPS) from Spectrum Chemical. Table 3.2 presents the selected buffers used to maintain a stable pH throughout the adsorption experiments. Solutions were prepared with MilliQ water (Millipore, resistance = 18.2 MΩ·cm at 25 °C). pH was adjusted using hydrochloric acid (HCl) and sodium hydroxide (NaOH) solutions from Fisher Scientific, Inc. Ionic strength was maintained at 50 mM with addition of sodium chloride (NaCl) (Fisher Scientific, Inc.). All chemicals were used without purification.

Table 3.2:   Selected buffers used for experiments and their different pH ranges.

Buffer Common Name (Chemical Formula)	Molecular Structure	Applicable pH Range	Selected pH
MES ($C_6H_{13}NO_4S$)		5.5 – 6.7	6.0
HEPES ($C_8H_{18}N_2O_4S$)		6.8 – 8.2	7.4
TAPS ($C_7H_{17}NO_6S$)		7.7 – 9.1	9.0

3.3.2   Nanoparticle Characterization

The crystalline phase of TiO_2 NPs was determined with a D8 ADVANCE Bruker powder X-Ray diffractometer (XRD) using Cu K_α radiation at λ=1.54184 Å (40 kV, 40

mA). A 20 µL droplet from sonicated TiO_2 suspension (0.03 g/L) was placed on formvar/carbon coated 100-mesh copper grid (Electron Microscopy Sciences) and dried overnight. Images of the TiO_2 NPs were taken by a JEOL JEM-1400 Plus transmission electron microscopy (TEM) at 80 kV. Size distribution of more than 100 NPs was analyzed with an ImageJ software and results were fit to a Gaussian model. A Quantachrome Nova 4200e analyzer was used for surface area measurements from BET (Brunauer−Emmett−Teller) N_2 adsorption isotherms. Prior to analysis, TiO_2 NPs were degassed overnight at 120º C. Measurements were run in triplicate and the average value was reported. A Zeiss Sigma 500 field emission scanning electron microscopy (FE-SEM) was used to determine the morphology of the thin film. A horizontal 45º beveled faces amorphous material transmitting infrared radiation (AMTIR) crystal (PIKE Technologies) was initially covered with 16 silicon wafers, 5x5 mm each (TED Pella, Inc.). 1 mL NP suspension (1.5 mg/mL TiO_2 in MilliQ water) was deposited on the wafers and dried overnight. The wafers were then placed on 90º sample holders and images were taken under 3 kV beam current.

3.3.3   ATR-FTIR Spectroscopy

ATR-FTIR spectra were collected using a horizontal flow cell with an AMTIR crystal in a Thermo−Nicolet iS10 FTIR spectrometer equipped with an MCT-A detector (Fig. 3.1a). Spectra were recorded every 5 min at 4 cm^{-1} resolution. pH was controlled by dissolving amino acids in corresponding 25 mM buffered solutions (except for pH 2, a buffer was not used) and adjusted to 2, 6, 7.4, and 9. Amino acid solution spectra were collected for 100 mM concentration. For adsorption studies, 5 mM amino acid solutions

(much lower concentration than solution phase only studies) were used in order to prevent contributions from solution phase species to the spectrum. 1.5 mg/mL TiO_2 NP suspension was deposited on the AMTIR crystal and dried overnight to form a thin film (Fig. 3.1b). The solution flow rate over the film was then fixed ~1 mL/min. Initially, MilliQ water was flushed for 10 min to eliminate loosely bound particles and then buffer solution was introduced for 30 min followed by collection of a background spectrum. Finally, 5 mM amino acid solution was flushed for 1 h and the background spectrum was subtracted from the results to remove any buffer contributions from the spectrum.

3.3.4   Dynamic Light Scattering and Zeta-Potential Measurements

Hydrodynamic sizes of bare and amino acid adsorbed TiO_2 NPs were investigated using a Beckman Coulter Delsa Nano submicron particle analyzer. TiO_2 NPs stock suspension was sonicated for 2 min, and aliquots were added to 5 mM amino acid solutions. The final concentration (0.03 g/L) was much more diluted than ATR-FTIR experiments to increase the efficiency of light scattering.[37, 38] Prior to the addition of NPs, the solutions were filtered through 0.2 µm pore size syringe filters (Acrodisc, PALL) to remove any dust that could potentially distort the analysis and give erroneous results. Zeta-potential measurements were carried out with a Malvern Instruments Zetasizer Nano instrument. Samples were prepared following the same method for DLS measurements without buffers. Triplicate measurements were taken with 120 s equilibrium time between each repetition. Zeta-potential and number distribution of the hydrodynamic diameter results were fit to a Gaussian model and the mean values were reported.

47

3.4   Results and Discussion

3.4.1   Nanoparticle Characterization

Cross-sectional FE-SEM image of the corresponding TiO_2 NPs thin film shows a thickness of ~1.5 µm (Fig. 3.1b). The spectrum of the film suggests there is minimal contributions of organic compounds on the film surface (Fig. 3.1b insert). The peaks at 800 cm^{-1} and 905 cm^{-1} are associated with the TiO_2 lattice vibrations.[39] Hydroxylated TiO_2 NP surfaces have a broad 3400 cm^{-1} peak corresponding to O–H stretching vibration [v(O−H)], and the 1640 cm^{-1} peak represents H_2O bending mode [δ(H_2O)].[40]
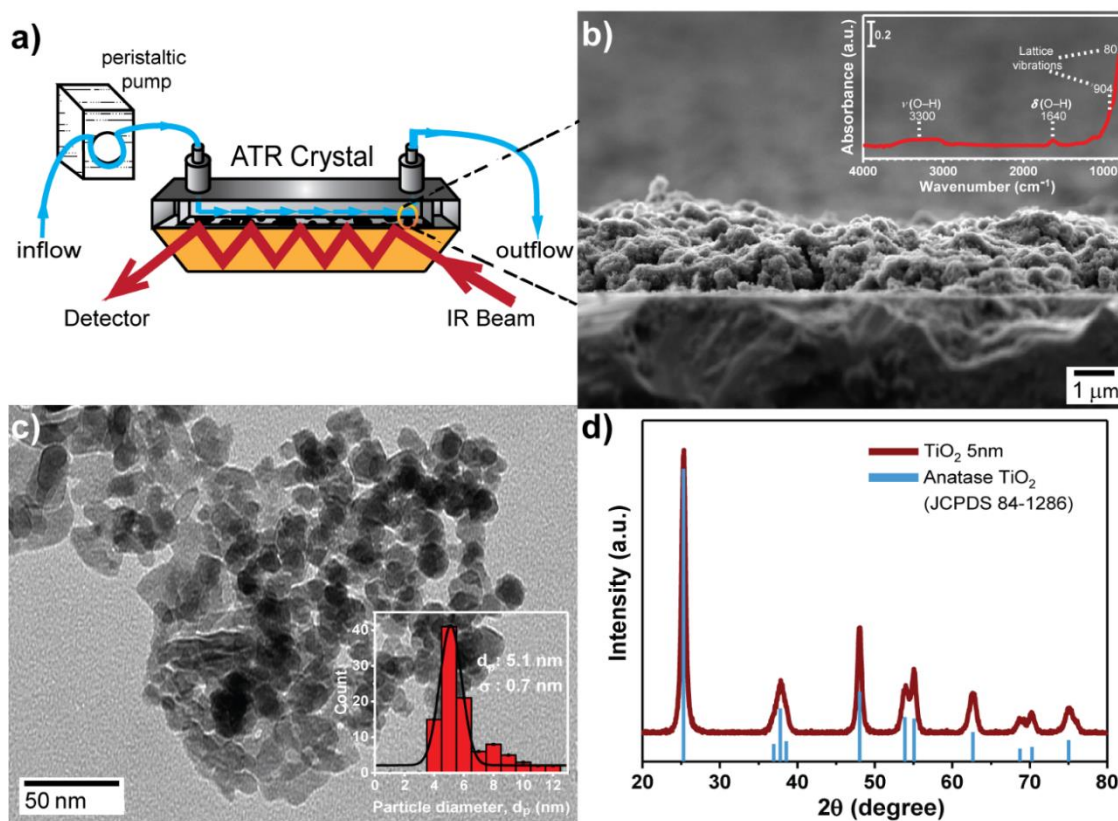
Figure 3.1: TiO_2 NPs thin film used in amino acid adsorption. (a) Schematic representation of the ATR-FTIR set-up; (b) FE-SEM image and the respective ATR-FTIR spectrum (insert) of the film; (c) TEM image and the size distribution analysis (insert); and (d) XRD data of TiO_2 NPs.

Size analysis of the particles in the TEM image shows the mean TiO_2 NP diameter is 5 ± 1 nm and NPs exhibit spherical morphology (Fig. 3.1c). XRD pattern in Fig. 3.1d identifies that NPs are entirely anatase, and the average surface area from BET analysis is 110 ± 3 m^2/g (Fig. A1). This is much lower than the calculated geometric area (308 m^2/g) for anatase TiO_2, based on bulk weighted density of 3.9 m^2/g, and indicates that NPs are aggregated.

3.4.2 Effects of pH on Lys and Glu Solution ATR-FTIR Spectra

In the aqueous phase, amino acids coexist as different species; protonated (cation), neutral (zwitterion) and deprotonated (anion) forms. The molar distribution of these different species can be determined using the Henderson−Hasselbalch approximation as follows (Eq. 3.1):[41]

$$pH = pK_a + \log \frac{[A^-]}{[HA]} \quad \text{(Eq 3.1)}$$

where pK_a is the logarithmic dissociation constant of the weak acid; [HA] is the molarity of the weak acid and $[A^-]$ is the molarity of the conjugate base at a certain pH.[42] The pH-dependent amino acid speciation can be summarized in a speciation plot as seen in Fig. 3.2 for Lys and Glu at different pH values, the solution spectra is also shown in the Fig. 3.2. Each spectrum includes the subtraction of appropriate buffered solution spectrum. The emergence and disappearance of vibrational peaks often times are obscured by overlap of neighboring peaks or interpreted as peak shifts.[43] To better observe all vibrational peaks, local minimum values from the second derivatives of the ATR-FTIR spectra were found via an OMNIC 9.0 software (Thermo Fisher) and used for assignments.

a) Lysine
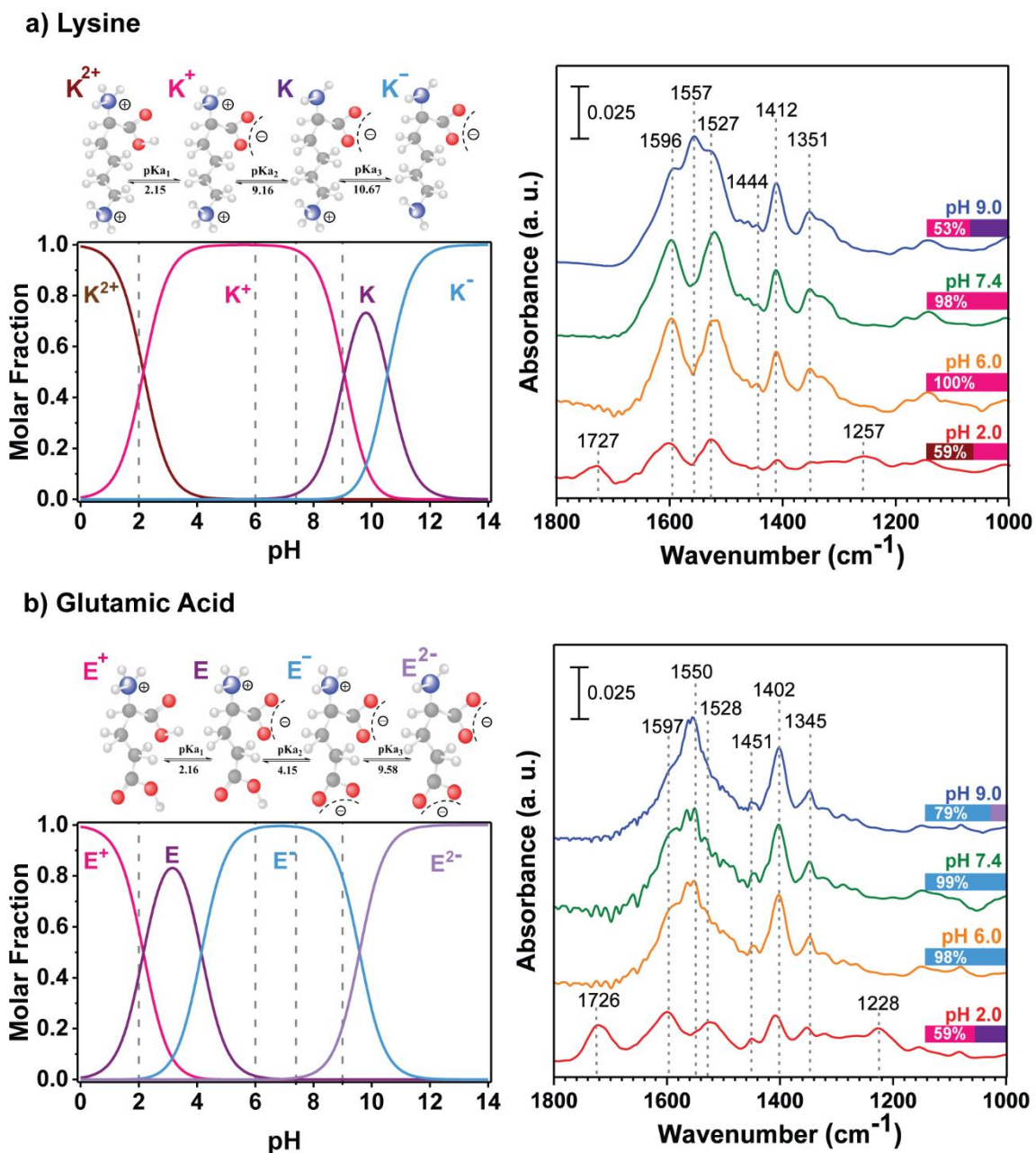
b) Glutamic Acid

Figure 3.2: pH-dependent amino acid speciation diagram with the corresponding structures (left) and the solution ATR-FTIR spectra as a function of pH (right). Spectra are shown for 100 mM (a) lysine and (b) glutamic acid solutions. The bars represent speciation percentages at each pH.

Lys has two amine groups in the structure and protonation species are represented as dication (K^{2+}), monocation (K^+), zwitterion (K), and monoanion (K^-). According to the Lys speciation distribution results at pH 2, ca. 60% the species is K^{2+} and the remaining

(40%) is K^+ (Fig. 3.2a left). The prominent carboxylic acid stretches at 1727 cm^{-1} and 1257 cm^{-1} are referred to ν(C=O) and ν(C−OH), respectively (Fig. 3.2a right). These peaks disappear with increasing pH due to deprotonation of carboxylic acid to form carboxylate ion.[21] Since Lys speciation is almost entirely K^+ in the pH range of ~3.7−7.5, the spectrum at pH 7.4 is identical to the one at pH 6. Carboxylate contributions to the spectra is seen by the asymmetric ν_{as}(COO⁻) and symmetric ν_s(COO⁻) stretching modes. The two modes show stronger peak intensities at these pH values in comparison to pH 2 due to carboxylate formation.[24, 43]

Table 3.3: Vibrational modes for solution phase and adsorbed lysine as a function of pH.

Vibrational Modes [a]	Vibrational Frequency (cm⁻¹)								
	pH 2		pH 6		pH 7.4		pH 9		Literature (Solution) [21, 43-49]
	Solution	Adsorbed	Solution	Adsorbed	Solution	Adsorbed	Solution	Adsorbed	
ν(C=O)	1727	1724	-	-	-	-	-	1740	1730-1733
δ_{as}(NH₃⁺)	1621	1621	1621	1615	1621	1621	1621	1621	1620-1634
ν_{as}(COO⁻)	1596	1599	1595	1593	1595	1592	1599	1598	1584-1608
ν_{sc}(NH₂)	-	1558	-	1558	1547	1547	1557	1564	1559
δ_s(NH₃⁺)	1528/1512	1528/1512	1527/1512	1521/1506	1528/1512	1527/1513	1527/1515	1527/1512	1521-1527
δ(CH₂)	1476/1461/ 1444	1484/1462/ 1442	1477/1461/ 1442	1473/1458/ 1446	1478/1462/ 1442	1476/1461/ 1443	1477/1463/ 1445	1478/1461/ 1443	1445-1476
ν_s(COO⁻)	1412	1416/1402	1413	1417/1397	1413	1413/1400	1412	1413/1401	1396-1414
ω(CH₂)/δ(CH)	1353/1332	1352/1331	1354/1327	1348/1320	1356/1332	1347/1321	1354/1310	1347/1321	1311-1352
ν(C−OH)	1257	1242	-	-	-	-	-	1236	1237-1255

[a] ν_s/ν_{as}: symmetric/asymmetric stretches; δ_s/δ_{as}: symmetric/asymmetric bends; ν_{sc}: scissor; and ω: wag vibrations.

ATR-FTIR spectral changes are observed under basic conditions as well. At pH 9, 53% of Lys speciation is K^+ and the remaining (47%) is K. The peak correspondent with the asymmetric bending mode of protonated amine $[\delta_{as}(NH_3^+)]$ overlaps with the ν_{as}(COO⁻) peak at 1599 cm^{-1}.[44] The deprotonated amine peak associated with the scissor motion at

1557 cm^{-1} [v_{sc}(NH$_2$)] begins to appear while the δ_{as}(NH$_3^+$) decreases.[44] A summary of Lys peak assignments is listed in Table 3.3.[21, 43-49]

Glu consists of two carboxyl groups with the following protonation species present in solution: monocation (E$^+$), zwitterion (E), monoanion (E$^-$), and dianion (E^{2-}). At pH 2, ca. 60% of the speciation is E$^+$ and the remaining (40%) is E (Fig. 3.2b left). Carboxylic acid groups are present on both species. The corresponding vibrations of v(C=O) and v(C−OH) appear at 1726 cm^{-1} and 1228 cm^{-1}, respectively (Fig. 3.2b right). The v_{as}(COO$^-$) peak at 1597 cm^{-1} and the v_s(COO$^-$) peak at 1410 cm^{-1} together confirm the presence of α-carboxylate (attached to α-carbon) in the zwitterion E. Glu solution spectra at pH 6 and pH 7.4 show similar features since only monoanion E$^-$ species is present. At these pH values, the amine group is protonated and differentiates the two carboxylate vibrations.[50] The v_{as}(COO$^-$) of α-carboxylate peak at 1598 cm^{-1} gets broadened as a result of H-bonding with the amine group, and another v_{as}(COO$^-$) peak at 1550 cm^{-1} appears for the distal-carboxylate group (as part of the side chain). Formation of the distal-carboxylate causes an increase in the v_s(COO$^-$) peak intensity at ~1402 cm^{-1}. Additionally, increase in pH causes the occurrence of the v_{as}(COO$^-$) peaks for α- and distal-carboxylate at very similar wavenumbers.[50] Thus, the shoulder at 1597 cm^{-1} gets narrower and v_{as}(COO$^-$) peak at 1552 cm^{-1} is present at high intensity at pH 9. In contrast to the Lys solution spectrum at this pH, there is no significant v_{sc}(NH$_2$) peak observed for Glu spectrum due to overlapping with the v_{as}(COO$^-$) peak. Glu peak assignments are summarized in Table 3.4.[21, 43-50]

Table 3.4: Vibrational modes for solution phase and adsorbed glutamic acid as a function of pH.

Vibrational Modes [a]	Vibrational Frequency (cm^{-1})								Literature (Solution) [21, 43-50]
	pH 2		pH 6		pH 7.4		pH 9		
	Solution	Adsorbed	Solution	Adsorbed	Solution	Adsorbed	Solution	Adsorbed	
ν(C=O)	1726	1722	-	-	-	-	-	1744	1712-1728
δ_{as}(NH$_3^+$)	1621	1621	1621	1621	1628	1621	1621	1621	1583-1635
ν_{as}(COO$^-$)	1597	1597/1546	1597/1547	1598/1552	1598/1550	1596/1552	1595/1552	1595/1551	1537-1560
δ_s(NH$_3^+$)	1527	1522	1527	1522	1530	1534	1527	1534	1520-1540
δ(CH$_2$)	1462/1451	1451	1462/1451/1442	1453	1465/1446	1467/1451/1443	1462/1451/1443	1462/1451/1442	1440-1454
ν_s(COO$^-$)	1410	1423/1404	1401	1424/1403	1402	1424/1402	1401	1401	1400-1417
ω(CH$_2$)/δ(CH)	1351/1320	1345/1321	1351/1320	1346/1325	1348/1322	1345/1326	1346/1325	1346/1325	1323-1350
ν(C−OH)	1228	1219	-	-	-	-	-	-	1205-1253

[a] ν_s/ν_{as}: symmetric/asymmetric stretches; δ_s/δ_{as}: symmetric/asymmetric bends; ν_{sc}: scissor; and ω: wag vibrations.

3.4.3 Carboxylate Binding Modes and pH-dependence of TiO$_2$ Nanoparticle Surfaces

Possible carboxylate binding modes on TiO$_2$ NPs are illustrated in Scheme 3.1.[52-55] Electrostatic interactions (as seen in Scheme 3.1a) and H-bonding (as seen in Scheme 3.1b-c) are shown. Monodentate, bidentate bridging, and bidentate chelating are the metal coordinated carboxylate binding modes (as seen in Scheme 3.1d-f).[51, 52] Bridging oxygen atoms of TiO$_2$ surface are coordinated to two in-plane titanium atoms.[51] Monodentate mode (as seen in Scheme 3.1d) involves binding between a single Ti^{4+} ion and an oxygen atom from carboxylate, whereas bidentate bridging (as seen in Scheme 3.1e) involves carboxylate binding onto two neighboring Ti^{4+} ions by two oxygen atoms.[51, 53] Both of the oxygen atoms from carboxylate bind to one single Ti^{4+} ion for bidentate chelating (as seen in Scheme 3.1f). Inner-sphere complexes along with the outer-sphere coordination, where

the water molecule is between the surface and adsorbate, play important roles to understand

adsorption mechanisms.[54, 55]
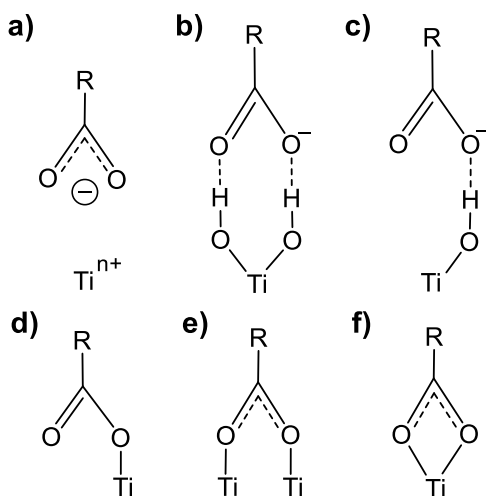
Scheme 3.1: Possible binding modes of carboxylate group onto TiO_2 NPs. (a) Electrostatic attraction; (b) double H-bonding; (c) single H-bonding; (d) monodentate (ester-like linkage); (e) bidentate bridging and (f) bidentate chelating.

Vibrational frequencies change depending on adsorbate coordination to NP surfaces.[47, 51] Carboxylate interactions can be characterized in part by the wavenumber splitting of the asymmetric and symmetric stretching modes ($\Delta v_{as-s} = \Delta v_{as} - \Delta v_s$). A large change in the Δv_{as-s} value of adsorbate compared to the value of uncoordinated species suggests a strong interaction with the NP surface.[15, 20, 23] If the difference is not significant enough, it is generally concluded that the bonding is not strong or chemisorption is not involved.[56] The difference in Δv_{as-s} values between the ionic (free aqueous) state and the bidentate bridging are very similar to distinguish, and H-bonds are known to affect the stability of ionic bonds.[51] An *ab initio* study[53] of acetate interactions with Na^+, Mg^{2+} and Ca^{2+} ions and water molecule showed that Δv_{as-s} value for double H-bonded carboxylate was smaller than the one of free acetate ion, but larger than the one of bidentate bridging.

According to Deacon's rule, Δv_{as-s} values for metal coordinated carboxylate binding modes follow the order: Δv_{as-s}(monodentate) $> \Delta v_{as-s}$(ionic) $> \Delta v_{as-s}$(bidentate bridging) $> \Delta v_{as-s}$ (bidentate chelating).[52-55] Considering the order and the existing studies, it is suggested that the Δv_{as-s} values for H-bonds are close to that for the ionic state. The observed Δv_{as-s} values are listed in Table A1. TiO_2 surfaces are known to have amphiphilic properties with both hydrophobic and hydrophilic sites. Hydrophilic sites can rapidly hydroxylate and form surface hydroxyl groups with changing pH. [14, 42] The protonation/deprotonation of the hydroxyl groups and the charge state of the surface can be controlled by solution pH as follows:[39, 57, 58]

$$\equiv Ti-OH + H^+ \rightarrow \equiv TiOH_2^+ \qquad (Eq.\ 3.2)$$

$$\equiv Ti-OH + OH^- \rightarrow \equiv TiO^- + H_2O \qquad (Eq.\ 3.3)$$
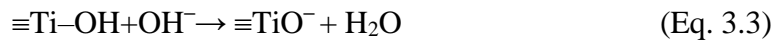
At pH values below the point zero charge (pH_{PZC}) of TiO_2, hydroxyl sites protonate, and the surface gains a net positive charge (Eq. 2). At pH values above the pH_{PZC}, it is expected to see deprotonation, and surface gains a net negative charge due to reaction with OH^- ions (Eq. 3.3).[29]

3.4.4   ATR-FTIR Analysis of Lys and Glu Adsorption as a Function of pH

Lys and Glu adsorbate spectra as a function of time are shown in Fig. 3.3. Although the experiments were conducted for 1 h, data are shown until the 20 min mark because adsorption reaches equilibrium at ~20 min, and no spectral changes are visible after this time. The dashed lines represent the spectra of 5 mM amino acid solutions used in the

adsorption studies. The importance of the carboxyl and amine groups during adsorption is clear when comparing the solution and adsorbate spectra (Fig. A2). Vibrational assignments for adsorbate spectra were based on the solution spectra. Effects of pH on adsorption is not only observed in the spectral features, but also in the peak intensities that correlate to the amount of adsorbed amino acids.

Lys adsorbate spectra at pH 2 shows two overlapping peaks of $v_{\mathrm{s}}(COO^-)$ at 1416 cm^{-1} and 1402 cm^{-1}, indicating the interaction between the carboxylate groups and the NP surface (Fig. 3.3a).[21] The observed $v(C=O)$ peak at 1724 cm^{-1} suggests the presence of protonated carboxylic acid groups. As previously discussed,[47] changes in the bandwidth for adsorbed $v_{\mathrm{s}}(COO^-)$ possibly reflect the heterogeneity in the hydration sphere and/or heterogeneity in the molecular interactions with the surface. This observation also refers to occurrence of multiple $\Delta v_{\mathrm{as-s}}$ values for amino acid adsorbate, which confirms that different states or orientations are present on the NP surfaces.[20] The $\Delta v_{\mathrm{as-s}}$ values for adsorbed Lys at pH 2 are 183 cm^{-1} and 197 cm^{-1}, while the uncoordinated Lys $\Delta v_{\mathrm{as-s}}$ value is 184 cm^{-1}. Displacement of surface hydroxyl groups and direct binding to Ti^{4+} ions are favorable in acidic conditions.[26] Changes in the $\Delta v_{\mathrm{as-s}}$ value from free species to the coordinated adsorbate are suggestive of surface hydroxyl group displacement and carboxylate adsorption. Thus, an increase of 13 cm^{-1} in $\Delta v_{\mathrm{as-s}}$ is due to the asymmetry in carboxylate stretch upon adsorption, confirming the mode of monodentate ①, as seen in Scheme 3.2a.[46] A decrease in $\Delta v_{\mathrm{as-s}}$ value can be concluded as a result of bidentate bridging ②; however, this change is not significant and could refer to double H-bonding of the carboxylate ③ to the hydroxylated TiO$_2$ NP surface ($\equiv$TiOH$_2^+$), as seen in Scheme 3.2a.
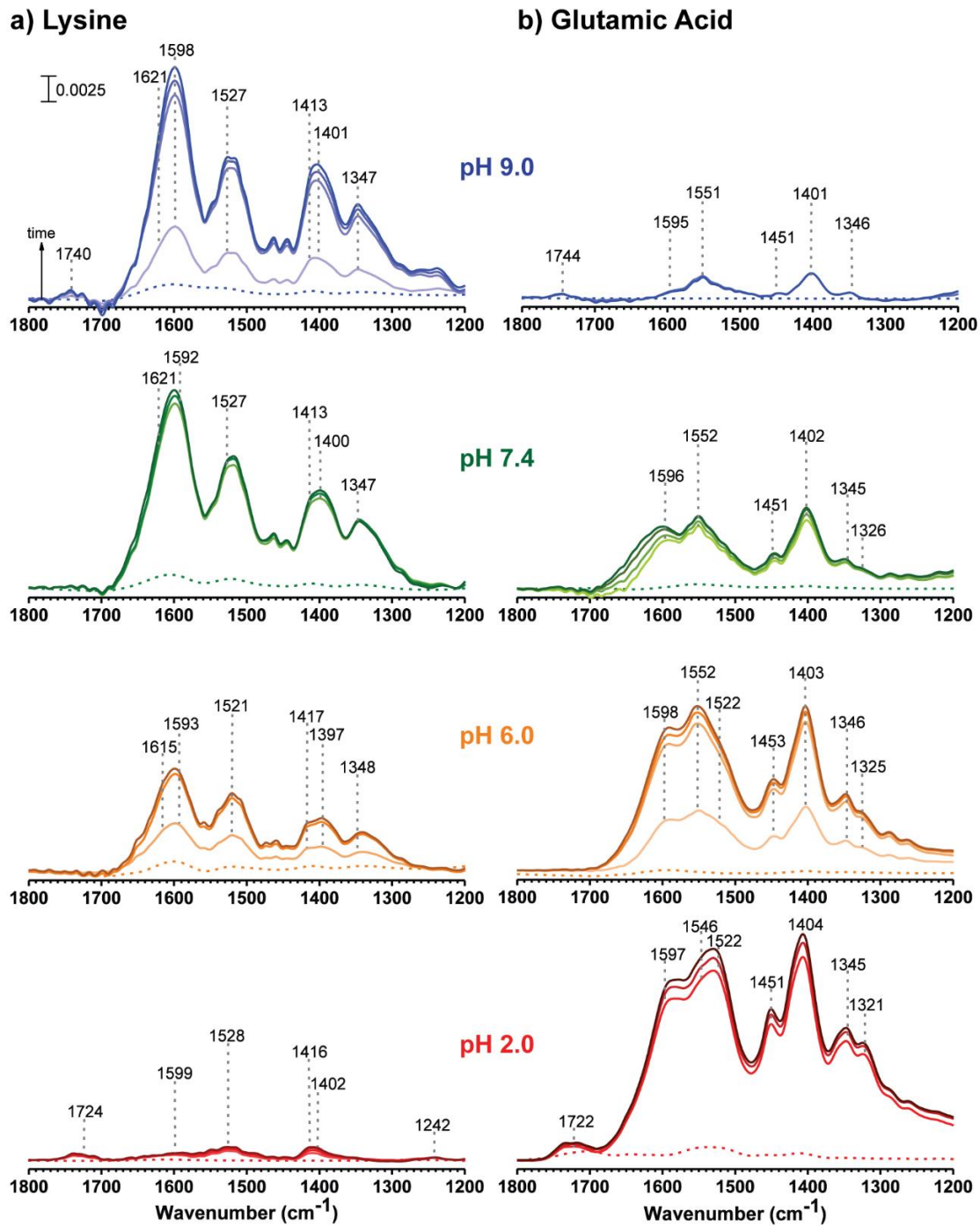
Figure 3.3: ATR−FTIR spectra of adsorbed (a) lysine and (b) glutamic acid onto TiO_2 NPs at different pH values as a function of time. Spectra were collected for 20 min at 5 min intervals. The dashed line shows the contribution from solution (5 mM) used for adsorption.

For Lys adsorbate spectra at pH 6 and pH 7.4, there is a drastic decrease in the $\delta_s(NH_3^+)$ peak intensity compared to solution phase, suggesting the interactions from protonated amine group to the TiO$_2$ NP surfaces. An increase in Δv_{as-s} value from free K$^+$ species is pointed to be a result of monodentate configuration. Moreover, the $v_s(COO^-)$ peak is broadened and a decrease in Δv_{as-s} value indicates the bidentate bridging. At pH 6 ($\approx$ pH$_{PZC}$ of the TiO$_2$ NPs, see Fig. 3.6), surface is monoprotonated ($\equiv$Ti–OH) and has a neutral charge. The shoulder is ~1635 cm^{-1} conceivably associated with the interfacial water. Inner-sphere complexes are energetically favorable on the surface, and outer-sphere complexes are known to initiate their formation. [24, 51] The high absorbance intensity of the spectra at pH 6 and pH 7.4 is suggested to be results of outer-sphere complexes. Thus, changes in Δv_{as-s} value for Lys adsorbate may indicate that double ③ and single H-bonding ④ configurations are also possible on the surface, as seen in Scheme 3.2a. In addition, an increase in pH from 6 to 7.4 enhances dehydroxylation, causing the NP surface to acquire a slightly negative charge ($\equiv$TiO$^-$).[24] For this reason, electrostatic attractions ⑤ are likely between the TiO$_2$ NP surfaces and the protonated amine group in K$^+$ species at pH 7.4, as seen in Scheme 3.2a. The higher peak intensities at pH 7.4 in comparison to pH 6 is explained by this phenomenon.
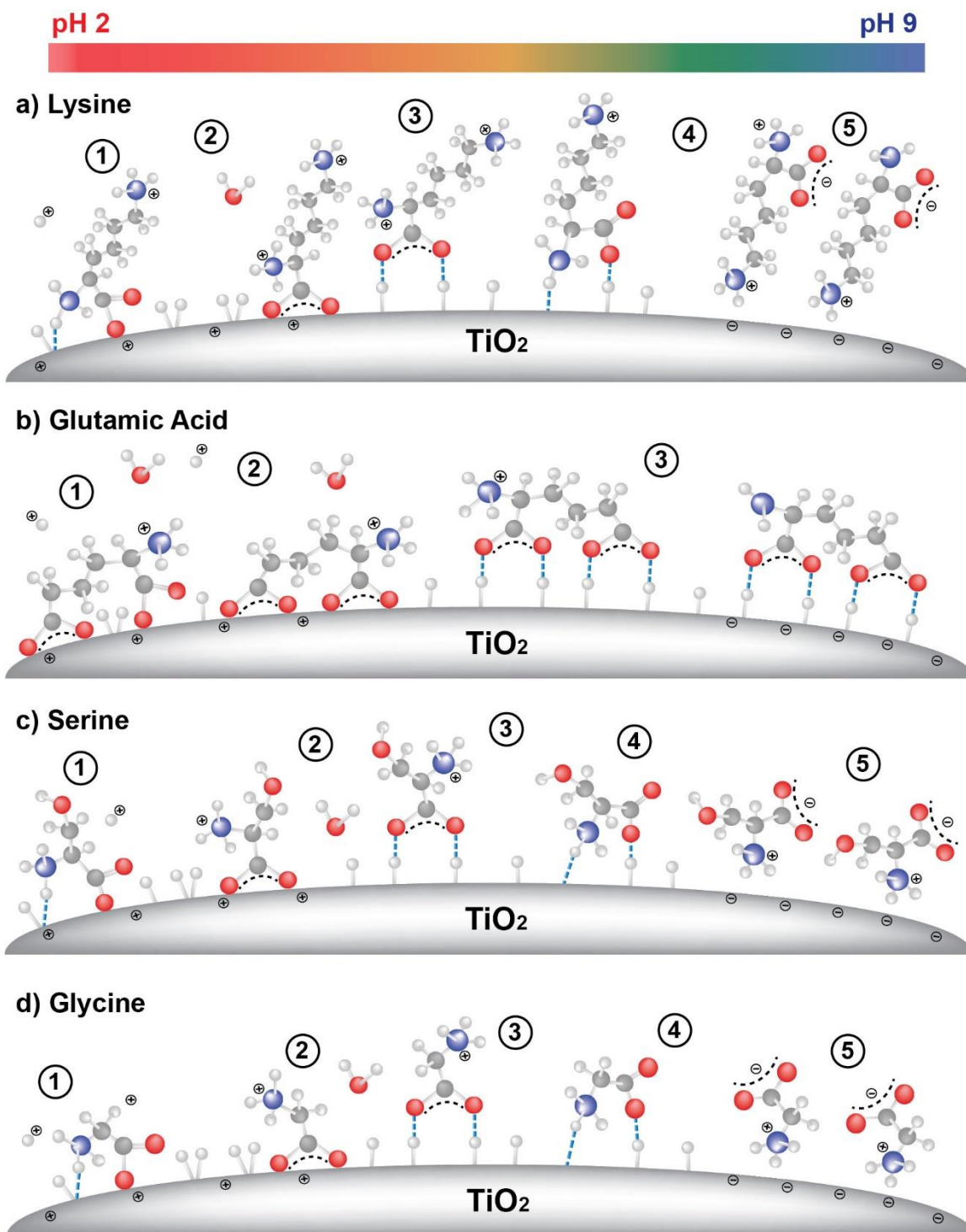
Scheme 3.2: pH-dependent conformations of adsorbed amino acids onto TiO_2 NPs. Surface charge and amino acid speciation change as a function of pH. Atoms are colored as oxygen (red), nitrogen (dark blue), carbon (grey), and hydrogen (white).

A notable change for Lys adsorbate spectrum at pH 9 is that the $v_{sc}(NH_2)$ peak at 1557 cm^{-1} is not observed while a new peak at 1740 cm^{-1} is associated with proton transfer from the amine group the carboxylate assisted potentially through an intermolecular process involving the surface hydroxyl groups.[21] At this pH, dehydroxylation of the TiO$_2$ NP surfaces increases even more. Protonated amine groups in K$^+$ and K are then attracted to the negative TiO$_2$ surface through electrostatic interactions with K$^+$ species showing a higher affinity. It is important to note that α-amine group in the Lys structure is in close proximity to the carboxylate group, and the possibility electrostatic interactions through this site onto negative TiO$_2$ NP surfaces can be excluded. Therefore, interactions are expected to occur through distal-amine group side chain. Although we propose that at pH 9 dominant interactions of Lys to the TiO$_2$ NP surface are through electrostatic attractions, there are slight changes in Δv_{as-s} values. These may indicate that double and single H-bonding from carboxylate sites are also possible with some of the remaining surface hydroxyl groups.

Glu preferably adsorbed on anatase (101) and rutile (100) TiO$_2$ active faces in bridging configurations and H-bonds.[17] Moreover, Glu showed higher coverage onto TiO$_2$ at pH values where there were strong electrostatic attractions to the surface.[50] The different peak intensities, associated with the surface coverage, are notable for Glu adsorption (Fig. 3.3b). When pH increases, electrostatic repulsion between the negatively charged NP surface and anionic Glu species increases. This causes a significant decrease in surface coverage; similar to what was observed for citric acid (a tricarboxylic acid) adsorption on TiO$_2$ NP surfaces.[59] In comparison to Glu solution spectrum at pH 2, the $v(C=O)$ peak diminishes in intensity and the bandwidth gets broadened, suggesting protonated surface

species and a weakening of the C=O bond due to interaction with the surface.[21] Multiple $v_s(COO^-)$ peaks in the adsorbate spectrum displays that there are different coordination modes coexist on the surface. A peak appears at 1546 cm^{-1} for $v_{as}(COO^-)$ with a corresponding high intensity $v_s(COO^-)$ peak at 1404 cm^{-1}, presumably associated with the distal-carboxylate. This can be deduced from the observed differentiation of carboxylate asymmetric stretches at higher pH values in the solution spectra (Fig 2b). Thus, Glu interactions with the surface happen in where both of the α- and distal-carboxylates are present together.[21, 50] At pH 2, Glu solution spectrum has only one asymmetric carboxylate stretch which tentatively comes from the α-carboxylate (see Table 3.4). The solution phase value for Δv_{as-s} is 187 cm^{-1}, whereas on the surface it is 174 cm^{-1} and 193 cm^{-1}. Therefore, it is proposed that α-carboxylate possibly adsorbs onto the surface in monodentate ① and bidentate bridging ② modes, as seen in Scheme 3.2b. The appearing distal-carboxylate $v_{as}(COO^-)$ peak indicates that this group coordinates to the surface in bidentate bridging mode.

At pH 6 and pH 7.4, adsorbate spectra of Glu resemble the solution spectra, and there is no significant increase in the Δv_{as-s} value observed. In fact, it is decreased ~20 cm^{-1} in comparison to solution phase. This can be explained as adsorbed carboxylates have higher symmetry in the structure. Therefore, we suggest that Glu adsorbs onto the surface in bidentate bridging mode from both of the carboxylates. Furthermore, one of the Δv_{as-s} values remains stable for both carboxylates, indicating double H-bonding ③, as seen in Scheme 3.2b. Electrostatic repulsion is possible through deprotonated carboxylate species to the negative TiO_2 NP surfaces at pH 7.4, which is seen by a decrease in the peak intensity.

At pH 9, the least surface coverage of Glu is observed due to gradually increasing electrostatic repulsion as pH increases. Despite the electrostatic repulsion, there is still some amount of Glu adsorbed on the TiO_2 NP surfaces. This is because of double H-bonding configuration to the surface hydroxyl groups, and the observed high intensity of the $v_s(COO^-)$ peak also support this assumption. Similar to Lys adsorption at pH 9, a new peak at 1744 cm^{-1} is associated with proton transfer from the amine groups to the carboxylates.[21]

The pH-dependent adsorption behavior of Glu is notably different from that of Lys. In fact, it displays distinctly opposite behavior, as shown in Fig. 3.3. Peak intensities of the Glu adsorbate spectra are much greater under acidic conditions. On the contrary, Lys adsorbate spectra have higher peak intensities under basic conditions. At pH 2, Glu (consists of E^+ and E species) shows the highest adsorption from strong carboxylate interactions to the positively charged TiO_2 NP surfaces. At pH 9, Lys (consists of K^+ and K species) exhibits the highest adsorption due to strong electrostatic attractions to the negatively charged TiO_2 NP surfaces. Both of the Lys and Glu have their zwitterionic forms in the speciation closer to where they show the highest adsorption results through different adsorption mechanisms (Fig. 3.2). Combinations of amine and carboxylate group interactions take place on pH-dependent adsorption mechanisms.

3.4.5 Effects of pH on Ser and Gly Solution ATR-FTIR Spectra

Ser has a polar uncharged alcohol side chain and two pK_a values associated with the three possible protonation species: monocation (S^+), zwitterion (S) and monoanion (S^-) as seen in Fig. 3.4a left. Alcohol group vibrations are observed in the solution spectra (Fig. 3.4a right). The $\nu(C-OH)$ and $\delta(C-OH)_{alcohol}$ modes are coupled in the spectral region extending from 1000 cm^{-1} to 1420 cm^{-1}.[45] In particular, the peak ~1054 cm^{-1} is associated with the bending mode of the alcohol group [$\delta(OH)_{alcohol}$], and increases in intensity with increasing pH as a result of changing structures of Ser from cationic to anionic species.[49]
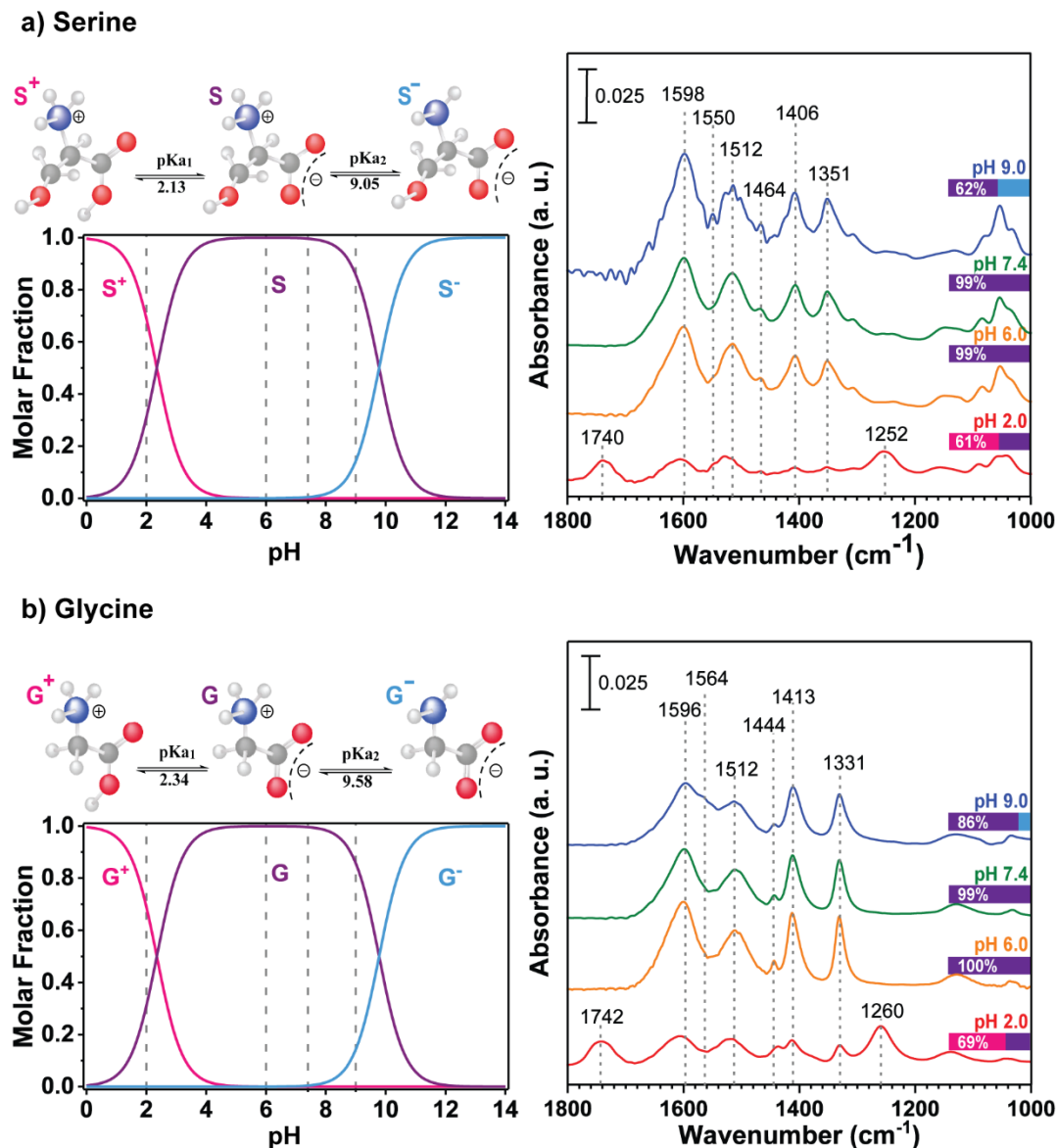
Figure 3.4: pH-dependent amino acid speciation diagram with the corresponding structures (left) and the solution ATR-FTIR spectra as a function of pH (right). Spectra are shown for 100 mM (a) serine and (b) glycine solutions. The bars represent the speciation percentages at each pH.

At pH 2, ca. 60% of Ser speciation is S^+ and the remaining (40%) is S (Fig. 3.4a left). Carboxylic acid stretches at 1740 cm^{-1} [v(C=O)] and 1252 cm^{-1} [v(C−OH)] are from the monocation S^+ species (Fig. 3.4a right). The v(C−OH) peak is anticipated to diminish in intensity and eventually reach unresolvable levels at high pH values. However, the peak

does not completely disappear, due to the fact that it couples to the δ(C−OH)$_{alcohol}$ vibration.[21,48] The peaks at 1596 cm^{-1} and 1411 cm^{-1} are assigned as the v_{as}(COO$^-$) and v_s(COO$^-$) vibrations in S species, respectively.[43] At pH 6 and pH 7.4, Ser solution phase spectra vibrational appearances are identical. When pH is increased to 9, amine group deprotonates, and the 1550 cm^{-1} peak is referred to v_{sc}(NH$_2$).[21] Peak assignments for Ser are summarized in Table 3.5.[20, 44, 45, 60, 61]

Table 3.5: Vibrational modes for solution phase and adsorbed serine as a function of pH.

Vibrational Modes [a]	Vibrational Frequency (cm^{-1})								Literature (Solution) 20, 44, 45, 60, 61
	pH 2		pH 6		pH 7.4		pH 9		
	Solution	Adsorbed	Solution	Adsorbed	Solution	Adsorbed	Solution	Adsorbed	
v(C=O)	1740	1738	-	-	-	-	-	-	1735
δ_{as}(NH$_3^+$)	1621	1621	1621	1621	1622	1622	1621	1621	1602-1621
v_{as}(COO$^-$)	1596	1595	1598	1599	1598	1597	1597	1595	1599-1621
v_{sc}(NH$_2$)	-	-	-	-	-	-	1550	-	1561
δ_s(NH$_3^+$)	1512	1512	1512	1512	1515	1513	1512	1512	1517-1531
δ(CH$_2$)	1463	1462	1463	1462	1464	1462	1462	1462	1450-1470
v_s(COO$^-$)	1411	1413/1403	1406	1412/1390	1405	1409/1391	1406	1412/1391	1407-1409
ω(CH$_2$)/δ(CH)	1353	1344	1353	1339	1353	1350	1353	1353	1318-1375
v(C−OH)/ δ(C−OH)$_{alcohol}$	1252	1242	1236	1242	1235	1240	1235	1229	1236-1251
δ(OH)$_{alcohol}$	1061	1058	1055	1045	1054	1059	1054	1060	1053-1066

[a] v_s/v_{as}: symmetric/asymmetric stretches; δ_s/δ_{as}: symmetric/asymmetric bends; v_{sc}: scissor; and ω: wag vibrations.

The vibrational assignments of Gly are useful to define the vibrational modes for other amino acids, since Gly is the simplest molecular structure. Gly exhibits three protonation species as monocation (G$^+$), zwitterion (G), and monoanion (G$^-$) which are shown in Fig. 3.4b left. The v(C=O) peak at 1742 cm^{-1} and v(C−OH) peak at 1260 cm^{-1} are from carboxylic acid stretches in G$^+$ species (Fig. 3.4b right).[21, 48] The two high intensity peaks at 1596 cm^{-1} and 1411 cm^{-1} refer to v_{as}(COO$^-$) and v_s(COO$^-$) vibrations, respectively.[48] At pH 6 and pH 7.4, zwitterion G is the only protonation form present in the

speciation. A similar observation was made for all the other amino acids solution spectra as there is no spectral change observed in Gly solution at these pH values. At pH 9, the 1564 cm^{-1} peak is assigned as $v_{sc}(NH_2)$ for deprotonated amine group in the monoanion, G$^-$. The decreasing peak intensity of $\delta_{as}(NH_3^+)$ coupled with the $v_{as}(COO^-)$ gives the appearance of a peak shift with increasing the pH from 2 to 9.[43] A summary of the Gly peak assignments is listed in Table 3.6.[43-48, 60, 62-64]

Table 3.6: Vibrational modes for solution phase and adsorbed glycine as a function of pH.

Vibrational Modes ^{a}	Vibrational Frequency (cm^{-1})								Literature (Solution) 43-48, 60, 62-64
	pH 2		pH 6		pH 7.4		pH 9		
	Solution	Adsorbed	Solution	Adsorbed	Solution	Adsorbed	Solution	Adsorbed	
$v(C=O)$	1742	1742	-	-	-	-	-	-	1740
$\delta_{as}(NH_3^+)$	1621	1627	1621	1622	1621	1622	1621	1621	1606-1654
$v_{as}(COO^-)$	1596	1598	1596	1596	1598	1595	1597	1596	1590-1620
$v_{sc}(NH_2)$	-	-	-	-	-	-	1564	1564	1561-1563
$\delta_s(NH_3^+)$	1512	1515	1512	1512	1512	1512	1512	1512	1508-1527
$\delta(CH_2)$	1439	1442	1443	1444	1443	1443	1443	1443	1435-1447
$v_s(COO^-)$	1411	1410/1380	1411	1414/1379	1413	1413/1380	1413	1412/1381	1378-1414
$\omega(CH_2)$	1331	1330	1331	1332	1331	1331	1331	1331	1332-1338
$v(C-OH)$	1260	1243	-	-	-	-	-	-	1258-1275

^{a} v_s/v_{as}: symmetric/asymmetric stretches; δ_s/δ_{as}: symmetric/asymmetric bends; v_{sc}: scissor; and ω: wagging vibrations.

3.4.6 ATR-FTIR Analysis of Ser and Gly Adsorption as a Function of pH.

Fig. 3.5 shows the adsorbate spectra of Ser and Gly onto TiO$_2$ NPs as a function of time. Ser adsorbate spectra have $\delta(C-OH)_{alcohol}$ peak ~1242 cm^{-1} at all pH values with a similar peak intensity, implying that alcohol group does not interact with the TiO$_2$ NP surfaces in our experimental conditions (Fig. 3.5a). At pH 2, $v(C=O)$ peak bandwidth gets broadened indicating a weaker C=O bond during Ser adsorption.[21] $v_s(COO^-)$ peak at 1413 cm^{-1} has the highest intensity suggesting a higher symmetry in the carboxylate structure.

$\Delta v_{\text{as-s}}$ value for Ser solution is 185 cm^{-1}; however, different $\Delta v_{\text{as-s}}$ values are observed on the surface as 182 cm^{-1} and 192 cm^{-1} due to the presence of multiple surface species. Increase in $\Delta v_{\text{as-s}}$ indicates monodentate binding ①, as seen in Scheme 3.2c. In addition, the shift in the $\Delta v_{\text{as-s}}$ value to a lower wavenumber suggests the presence of bidentate bridging mode ②, as seen in Scheme 3.2c. However, the decrease (3 cm^{-1}) alone is not significant enough to conclude the existence of chemisorption. Thus, one may suggest that double H-bonding ③ is seen on the surface as in Scheme 3.2c.

$\Delta v_{\text{as-s}}$ values for adsorbate Ser at pH 6 and pH 7.4 show reduction in comparison to solution phase. Thus, we propose that Ser binds to NP surface through bidentate bridging configuration at these pH values. Aside from this, there is also an increase in $\Delta v_{\text{as-s}}$ values, indicating carboxylate interactions occurs as well via monodentate binding. The reduction in the relative intensity of the $\delta_s(NH_3^+)$ peak at 1512 cm^{-1} displays the interactions from amine group to surface hydrogen ion.[17, 24] Higher peak intensities at neutral pH values (in comparison to pH 2) consequences of higher surface coverage as a result of H-bonding ③ – ④, as seen in Scheme 3.2c. At pH 9, Ser shows decreased surface coverage which can be observed in the change of the adsorbate spectra peak intensities. The reason behind this reduction requires further analysis in order to be explained.
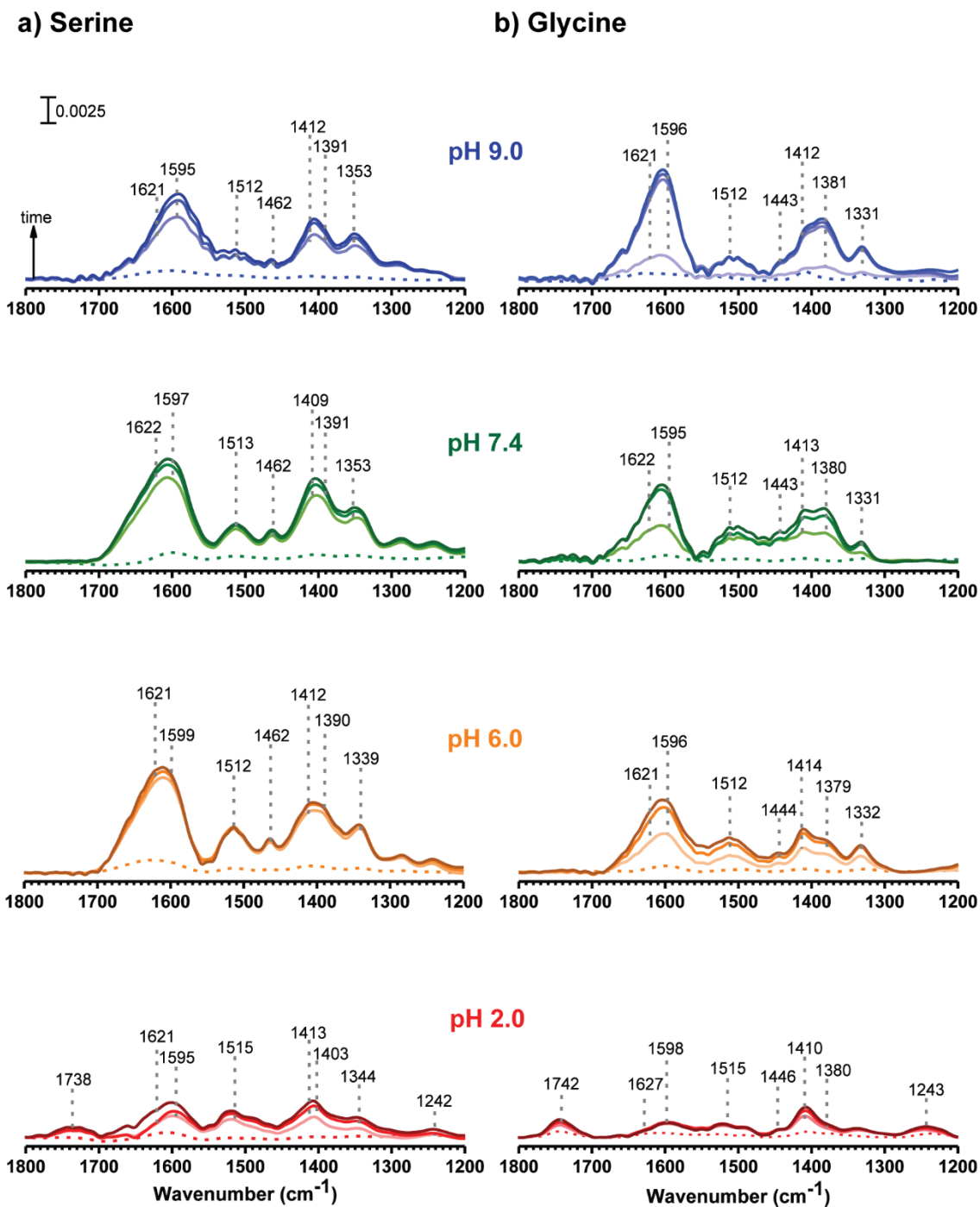
Figure 3.5: ATR−FTIR spectra of adsorbed (a) serine and (b) glycine onto TiO_2 NPs at different pH values as a function of time. Spectra were collected for 20 min at 5 min intervals. The dashed line shows the contribution from solution (5 mM) used for adsorption.

The increase in the Lys adsorption at pH 9 was explained as a result of electrostatic attractions. At basic conditions, the presence of positively charged molecules in the speciation is required to attract to the negative TiO_2 surface. According to the Henderson−Hasselbalch calculations at pH 9, protonated amine group is only present in zwitterion which is ca. 60% of the overall Ser speciation. Thus, the mean positive charge and the percentage of protonated amine group in the speciation are much lower when compared to Lys (53% K^+ and 47% K) and Gly (86% G). Thus, electrostatic attraction ⑤ could be less likely to the TiO_2 NP surfaces, as seen in Scheme 3.2c.

Gly adsorbate spectra at pH 2 has a high intensity $v_s(COO^-)$ peak at 1410 cm^{-1} (Fig. 3.5b). Δv_{as-s} value for Gly solution spectra is 185 cm^{-1}, which is similar to Ser solution at this pH. An increase in Δv_{as-s} value ~33 cm^{-1} indicates that Gly adsorbs to the NP surface in monodentate binding ①, as seen in Scheme 3.2d. A decrease in Δv_{as-s} value ~7 cm^{-1} suggests that bidentate bridging ② configuration is also present at pH 2, as seen in Scheme 3.2d. Gly adsorbate spectra have similar features at pH 6 and pH 7.4. Observed Δv_{as-s} values at these pH values were similar to one at pH 2. This supports that the modes of adsorption are same, and Gly carboxylate is in monodentate and bidentate bridging configurations on the TiO_2 NP surface. Compared to pH 2, there is a change in the amount of surface coverage as a result of hydroxyl group interactions at these pH values. In addition to the initially suggested modes, Gly could also displays double ③ and a single H-bonding ④, as seen in Scheme 3.2d. Due to the electrostatic attractions ⑤ from zwitterion Gly species to the surface, the peak intensities at pH 7.4 are higher than at pH 6, as seen in Scheme 3.2d. Gly adsorption on rutile TiO_2 surface in aqueous medium at pH 9 was previously performed,

and adsorption was not evidenced.[24] However, we observed a high amount of Gly adsorption at pH 9 onto anatase TiO_2 NPs. This is suggested to be a result of strong electrostatic attractions with a higher affinity of zwitterion to the surface, and H-bonding of carboxylates to the surface hydroxyl groups.

An overall summary of the pH-dependent changes in infrared peak intensities for amino acid adsorption behavior onto TiO_2 NPs is plotted in Fig. A3. The data can be understood in terms of the charges on the amino acids and NP surfaces along with specific molecular interactions that drive the adsorption process and cause changes (increases and decreases) in peak intensities. The normalized absorbance intensities at 1600 cm^{-1} from adsorbate spectra, along with the results from Fig. 3.3, clearly show the interesting adsorption behavior for charged residues. An MD study of amino acid adsorption onto negatively charged rutile TiO_2 NP surfaces in aqueous environment predicted the binding affinity of amino acids following the order as: arginine > lysine ~ aspartic acid > serine.[65] Our results show that compare to adsorption of neutral amino acids, adsorption of charged residues display larger changes due to pH. Total amino acid coverage onto TiO_2 NP surfaces changes notably as a function of pH. Lys and Gly exhibit similar adsorption trends; adsorption capacity increases with increasing pH. The difference in the peak intensities is a result of different affinities to the NP surfaces due to extra amine residue on Lys structure. Interestingly, Ser shows the highest adsorption capacity at pH 6, when solution pH is close to pH_{IEP} (see Table 3.1). The significantly different trend displayed by Ser can be the consequence of a different mean charge per unit molecule with changing pH. Comparable results on ferrihydrite surfaces was previously reported.[66] Ser showed gradually increased adsorption results from acidic to neutral pH values and decreasing results with higher pH.

3.4.7 Effects of the Amino Acid Adsorption on Hydrodynamic Size and Zeta-Potential

In aqueous solutions, NPs undergo various physicochemical transformations including aggregation and surface reconstruction to minimize their surface free energy.[40] These transformations impact the hydrodynamic sizes which are determined to be different than their initial states. Therefore, understanding the pH-dependent NP aggregation behavior is important, because it is highly correspondent to the biological responses.[67] According to DLS results in Fig. A4, measured hydrodynamic diameters are less than 1 μm, and the biggest aggregates are observed at ~pH_{PZC} of the TiO_2 NPs. The presence of amino acids does not change the aggregation size significantly. However, charged residues slightly increase the hydrodynamic sizes due to high surface coverages. Zeta-potential can be described as the electrical potential of the interface between the solution and the stationary layer of the ions attached to particle surface.[34] Electrostatic mobility in suspension is used to determine the zeta-potential, and the calculated results depend on various conditions such as: nanomaterial properties, solution features, and the selected theoretical model.[37] Eq. 3.4 shows the Smoluchowski model is applied to measure the zeta-potential of NPs.

$$\zeta = \mu \cdot \eta / (\varepsilon_0 \cdot \varepsilon_r) \qquad \text{(Eq. 3.4)}$$

where μ is the electrostatic mobility, $\eta = 8.90 \times 10^{-4}$ [Pa·s] is the viscosity of the solvent (water, 25 °C), $\varepsilon_0 = 8.85$ [pF/m] is the vacuum permittivity, and $\varepsilon_r = 78.54$ [pF/m] is the relative permittivity of water.[34, 37]
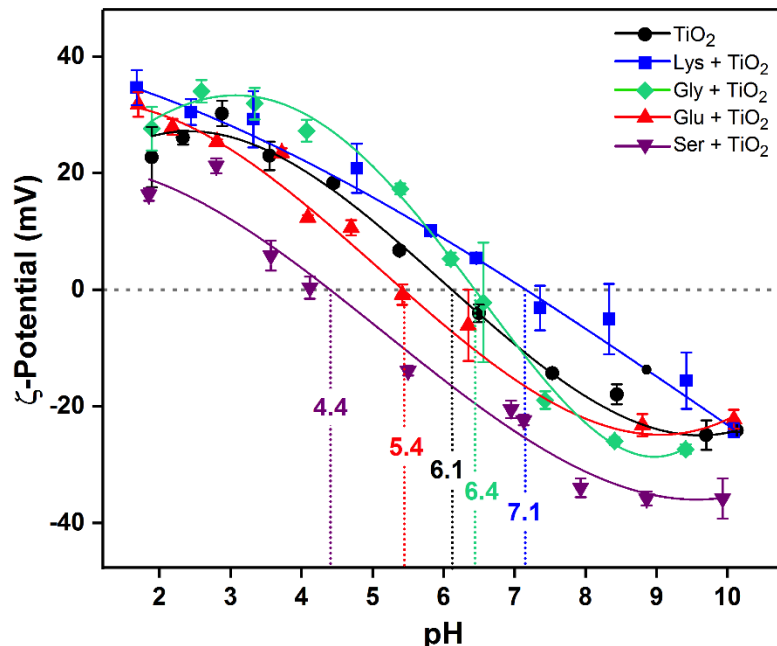
Figure 3.6: Changes in the zeta-potential upon amino acids adsorption onto TiO_2 NP surfaces. The corresponding pH_{IEP} values were determined by measuring the zeta-potential of bare and amino acid adsorbed TiO_2 NPs (0.03 g/L) as a function of pH. The solid lines represent polynomial fits of the distribution. The presence of glycine and lysine increases pH_{IEP} to 6.4 and 7.1, respectively; whereas, glutamic acid and serine adsorption decreases the pH_{IEP} to 5.4 and 4.4, respectively.

Changes in the zeta-potential measurements upon amino acids adsorption onto TiO_2 NPs are shown in Fig 3.6. The measured pH_{IEP} of bare TiO_2 NPs is 6.1, is consistent with literature values (~5.8−7.5).[51] At the pH_{IEP} (zero zeta-potential), repulsion between the NPs is minimized and they tend to aggregate. It is essential to note that the pH_{IEP} is not necessarily identical with the pH_{PZC}. At the pH_{PZC} (the surface has zero net charge), the adsorbed H^+ and OH^- ions are in equal amount. However, at the pH_{IEP}, other ions are also present on the surface and influence the charge state.[68] When the absolute value of the zeta-potential reaches prominent levels and pH is far from the pH_{IEP}, electrostatic repulsion is more dominant than Van der Waals forces. Therefore, strong electrostatic repulsive forces prevent the aggregation and NPs are closed to colloidal stability.[34, 37] Based on the results

from Fig. 3.6, ± 35 mV is the highest zeta-potential value measured. TiO_2 NPs are moderately stable in the low (<pH 2) and high (>pH 9) pH regions. This conclusion is also supported by the hydrodynamic size measurements; the smallest NP aggregation is observed in the presence of all of the amino acids at pH 2 and pH 9.

The hydroxylated TiO_2 surface contains two distinct types of hydroxyl groups, terminal and bridged hydroxyl sites.[39, 42] These sites are predominantly present on the chemically active face of the NP crystal structure, whereas the other crystal faces mostly include weakly bonded water molecules.[39] Shifts in the pH_{IEP} values are often times results of hydroxyl residual interactions and changes of the surface acidity. An increased acidity for arginine adsorption onto TiO_2 surface (71% anatase, 29% rutile) was previously observed as a negative shift in the pH_{IEP} value.[56] Measured pH_{IEP} values, where polynomial fits of the data points cross the zero zeta-potential, are listed in Fig. 3.6. The pH_{IEP} of Ser adsorbed TiO_2 NPs is 4.4 and pH_{IEP} of Gly adsorbed TiO_2 NPs is 6.4. The opposite direction of the shifts has been proposed to be a result of interactions with different surface hydroxyl groups,[42] whereby Ser interacts with the terminal hydroxyl and makes the TiO_2 NP surfaces more acidic and Gly (the smallest of the amino acids) potentially interacts with bridged hydroxyl groups. There is a positive shift in pH_{IEP} in the presence of Lys (pH_{IEP} = 7.1). A similar shift in pH_{IEP} for Lys adsorption on superparamagnetic iron oxide NPs has been seen previously.[22] It is implied that carboxyl groups of Lys interact with the surface where amine groups orient outward into the aqueous media, increasing the overall NP surface charge. In contrast to Lys, there is a negative shift in pH_{IEP} in the presence of Glu (pH_{IEP} = 5.4) due to the interaction of carboxylate groups with the NP surface and reduced net surface charge.

73

3.5   Conclusions and Implications

In the current study, we investigated effects of pH on amino acids adsorption onto TiO$_2$ NP surfaces. From the ATR-FTIR spectra, it is evident that solution pH significantly influences amino acid speciation and adsorption mechanisms. Depending on the predominant speciation and TiO$_2$ NP surface charge, adsorption involves a combination of carboxylate and amine group interactions. Gly and Lys reveal a similar trend of higher adsorption with increasing pH. In contrast, Glu adsorption decreases with increasing pH. Ser adsorption onto TiO$_2$ NPs surfaces is the highest around pH$_{IEP}$. In our experimental conditions, multiple surface species coexist at different pH values. Protonated surface species are present for all amino acids at pH 2. At pH 9, Lys and Glu adsorbate spectra have new peaks at 1740 cm^{-1} and 1744 cm^{-1}, respectively. As previously demonstrated in the example of histidine, this is a possible result of surface-induced deprotonation of the amine group and proton transfer to the carboxylate.[21]

Individual amino acid-NP studies provide great potential to design biocompatible materials. In fact, these single amino acid or small peptide interaction results can be used to model more complex systems. Adsorption studies of Glu on rutile and amorphous TiO$_2$ surfaces[69, 70] proposed that at high concentrations, distal-carboxylate group attaches to surface via bidentate chelating adsorption, possibly a mechanism which allows chiral-self organization. The current study covers a wider range of pH values including physiological and basic pH conditions. Additionally, chelating coordination would require a significant decrease in the $\Delta\nu_{as\text{-}s}$ value,[56] and this is not observed in these data for Glu at pH 2. Thus, it is suggested here that in fact both α- and distal-carboxylates of Glu are involved in the

interactions. Furthermore, density functional theory (DFT) and MD studies reported that zwitterion species have higher stability on TiO_2 surface and are present in adsorbed multilayers.[71-73] In general, we observed the highest adsorption (as indicated by the increase in the peak intensities) when amino acid speciation consists of zwitterion species. This can support our assumption that stability of surface species is related to the adsorption behavior, and potentially alters the total surface coverage. DLS results conclude that adsorption of amino acids changes NP aggregation and zeta-potential. Additionally, hydrodynamic sizes are greatest at ~pH_{PZC} of TiO_2 NPs. The presence of charged residues causes the most significant changes on zeta-potential measurements. Lys adsorption increases the pH_{IEP} value of the TiO_2 NPs, whereas Glu adsorption decreases the pH_{IEP} value. Ser and Gly interact with the surface from different surface hydroxyl groups.

Qiu et al. have used scanning tunneling microscopy (STM) to understand the adsorption behavior of Gly onto TiO_2 and results show that Gly adsorbs onto single crystal surface dissociatively as anionic (G^-) form.[74] Lerotholi et al. used X-Ray photoelectron spectroscopy (XPS) and suggested that only at low surface coverage, Gly surface species are present as anionic form. High surface coverage regime corresponds to existence of multilayers where zwitterion presents.[75] However, those experiments are conducted under highly controlled gas phase conditions. Biomolecular processes are highly dependent on the presence of aqueous environment and our results reveal that water molecules modify amino acid interactions. In addition, ionic strength and pH affect the physiological responses and need to be considered in experimental studies. At the pH values where solution spectra look identical, significant changes in the peak intensities are observed for

adsorption results since NP surface charge changes upon dehydroxylation. Higher surface coverages are explained as the possible results of H-bonding.

This study of pH-dependent amino acid adsorption in buffered solutions onto TiO_2 NP surfaces presents integration of different types of data, including ATR-FTIR spectroscopy and DLS measurements, to better understand adsorption processes. The findings of this work help to determine the surface species and possible insights into protein adsorption mechanisms and protein corona formation. Overall, the results provide valuable insights into the mechanisms of more complex aqueous biomolecule-surface interactions at different pH values and illuminate a detailed understanding of the human exposure to NPs.

3.6   Acknowledgements

Chapter 3, in full, is reproduced with permission from Elsevier: Ustunol, I. B.; Gonzalez-Pech, N. I.; Grassian, V. H. pH-dependent Adsorption of α-Amino Acids, Lysine, Glutamic Acid, Serine, and Glycine, on TiO_2 Nanoparticle Surfaces. *J. Colloid Interface Sci.* **2019**, 554, 362-375. The dissertation author was the primary investigator and author of this paper.

3.7 References

(1)   Fernández-García, M.; Rodriguez, J. A. Metal Oxide Nanoparticles. In *Encyclopedia of Inorganic and Bioinorganic Chemistry*, John Wiley & Sons Ltd, 2011.

(2)   Grassian, V. H.; O'Shaughnessy P, T.; Adamcakova-Dodd, A.; Pettibone, J. M.; Thorne, P. S. Inhalation Exposure Study of Titanium Dioxide Nanoparticles with a Primary Particle Size of 2 to 5 nm. *Environ. Health Persp.* **2007,** *115*(3), 397-402.

(3)   Sajid, M.; Ilyas, M.; Basheer, C.; Tariq, M.; Daud, M.; Baig, N.; Shehzad, F. Impact of Nanoparticles on Human and Environment: Review of Toxicity Factors, Exposures, Control Strategies, and Future Prospects. *Environ. Sci. Pollut. Res. Int.* **2015,** *22*(6), 4122-4143.

(4)   Ge, M.; Cao, C.; Huang, J.; Li, S.; Chen, Z.; Zhang, K. Q.; Al-Deyab, S. S.; Lai, Y. A Review of One-Dimensional TiO_2 Nanostructured Materials for Environmental and Energy Applications. *J. Mater. Chem. A* **2016,** *4*(18), 6772-6801.

(5)   Ispanixtlahuatl-Meráz, O.; Schins, R. P. F.; Chirino, Y. I. Cell Type Specific Cytoskeleton Disruption Induced by Engineered Nanoparticles. *Environ. Sci-Nano* **2018,** *5*(2), 228-245.

(6)   Monopoli, M. P.; Aberg, C.; Salvati, A.; Dawson, K. A. Biomolecular Coronas Provide the Biological Identity of Nanosized Materials. *Nat. Nanotechnol.* **2012,** *7*(12), 779-786.

(7)   Walkey, C. D.; Olsen, J. B.; Song, F.; Liu, R.; Guo, H.; Olsen, D. W.; Cohen, Y.; Emili, A.; Chan, W. C. Protein Corona Fingerprinting Predicts the Cellular Interaction of Gold and Silver Nanoparticles. *ACS Nano* **2014,** *8* (3), 2439-2455.

(8)   Miller, M. R.; Raftis, J. B.; Langrish, J. P.; McLean, S. G.; Samutrtai, P.; Connell, S. P.; Wilson, S.; Vesey, A. T.; Fokkens, P. H. B.; Boere, A. J. F.; Krystek, P.; Campbell, C. J.; Hadoke, P. W. F.; Donaldson, K.; Cassee, F. R.; Newby, D. E.; Duffin, R.; Mills, N. L. Inhaled Nanoparticles Accumulate at Sites of Vascular Disease. *ACS Nano* **2017,** *11*(5), 4542-4552.

(9)   Maher, B. A.; Ahmed, I. A. M.; Karloukovski, V.; MacLaren, D. A.; Foulds, P. G.; Allsop, D.; Mann, D. M. A.; Torres-Jardon, R.; Calderon-Garciduenas, L.

Magnetite Pollution Nanoparticles in the Human Brain. *P. Natl. Acad. Sci. USA* **2016,** *113*(39), 10797-10801.

(10)   Yin, Z. F.; Wu, L.; Yang, H. G.; Su, Y. H. Recent Progress in Biomedical Applications of Titanium Dioxide. *Phys. Chem. Chem. Phys.* **2013,** *15*(14), 4844-4858.

(11)   Sunada, K.; Watanabe, T.; Hashimoto, K. Studies on Photokilling of Bacteria on TiO$_2$ Thin Film. *J. Photoch. Photobio. A* **2003,** *156*(1-3), 227-233.

(12)   Dadjour, M. F.; Ogino, C.; Matsumura, S.; Nakamura, S.; Shimizu, N. Disinfection of Legionella Pneumophila by Ultrasonic Treatment with TiO$_2$. *Water Res.* **2006,** *40*(6), 1137-1142.

(13)   Szieberth, D.; Maria Ferrari, A.; Dong, X. Adsorption of Glycine on the Anatase (101) Surface: An ab Initio Study. *Phys. Chem. Chem. Phys.* **2010,** *12*(36), 11033-11040.

(14)   Nosaka, A. Y.; Tanaka, G.; Nosaka, Y. Study by Use of ^{1}H NMR Spectroscopy of the Adsorption and Decomposition of Glycine, Leucine, and Derivatives in TiO$_2$ Photocatalysis. *J. Phys. Chem. B* **2014,** *118*(27), 7561-7567.

(15)   Costa, D.; Savio, L.; Pradier, C. M. Adsorption of Amino Acids and Peptides on Metal and Oxide Surfaces in Water Environment: A Synthetic and Prospective Review. *J. Phys. Chem. B* **2016,** *120*(29), 7039-7052.

(16)   Liu, S.; Meng, X. Y.; Perez-Aguilar, J. M.; Zhou, R. An *in silico* Study of TiO$_2$ Nanoparticles Interaction with Twenty Standard Amino Acids in Aqueous Solution. *Sci. Rep.* **2016,** *6*, 37761.

(17)   Köppen, S.; Bronkalla, O.; Langel, W. Adsorption Configurations and Energies of Amino Acids on Anatase and Rutile Surfaces. *J. Phys. Chem. C* **2008,** *112*(35), 13600-13606.

(18)   Zhao, Y. L.; Wang, C. H.; Zhai, Y.; Zhang, R. Q.; Van Hove, M. A. Selective Adsorption of L-Serine Functional Groups on the Anatase TiO$_2$ (101) Surface in Benthic Microbial Fuel Cells. *Phys. Chem. Chem. Phys.* **2014,** *16*(38), 20806-20817.

(19)   Sowmiya, M.; Senthilkumar, K. Adsorption of Proline, Hydroxyproline and Glycine on Anatase (001) Surface: A First-Principle Study. *Theor. Chem. Acc.* **2015,** *135*(12).

(20)   Schwaminger, S. P.; García, P. F.; Merck, G. K.; Bodensteiner, F. A.; Heissler, S.; Günther, S.; Berensmeier, S. Nature of Interactions of Amino Acids with Bare Magnetite Nanoparticles. *J. Phys. Chem. C* **2015,** *119*(40), 23032-23041.

(21)   Mudunkotuwa, I. A.; Grassian, V. H. Histidine Adsorption on TiO_2 Nanoparticles: An Integrated Spectroscopic, Thermodynamic, and Molecular-Based Approach Towards Understanding Nano-Bio Interactions. *Langmuir* **2014,** *30*(29), 8751-8760.

(22)   Pušnik, K.; Peterlin, M.; Cigić, I. K.; Marolt, G.; Kogej, K.; Mertelj, A.; Gyergyek, S.; Makovec, D. Adsorption of Amino Acids, Aspartic Acid, and Lysine onto Iron-Oxide Nanoparticles. *J. Phys. Chem. C* **2016,** *120*(26), 14372-14381.

(23)   Begonja, S.; Rodenas, L. A. G.; Borghi, E. B.; Morando, P. J. Adsorption of Cysteine on TiO_2 at Different pH Values: Surface Complexes Characterization by FTIR-ATR and Langmuir Isotherms Analysis. *Colloid Surface A* **2012,** *403*, 114-120.

(24)   Ojamae, L.; Aulin, C.; Pedersen, H.; Kall, P. O. IR and Quantum-Chemical Studies of Carboxylic Acid and Glycine Adsorption on Rutile TiO_2 Nanoparticles. *J. Colloid Interface Sci.* **2006,** *296*(1), 71-78.

(25)   Feyer, V.; Plekan, O.; Tsud, N.; Chab, V.; Matolin, V.; Prince, K. C. Adsorption of Histidine and Histidine-Containing Peptides on Au (111). *Langmuir* **2010,** *26*(11), 8606-8613.

(26)   Schmidt, M.; Steinemann, S. G. XPS Studies of Amino-Acids Adsorbed on Titanium-Dioxide Surfaces. *Fresen J. Anal. Chem.* **1991,** *341*(5-6), 412-415.

(27)   Thomsen, L.; Wharmby, M. T.; Riley, D. P.; Held, G.; Gladys, M. J. The Adsorption and Stability of Sulfur Containing Amino Acids on Cu {531}. *Surf. Sci.* **2009,** *603*(9), 1253-1261.

(28)   Ataman, E.; Isvoranu, C.; Knudsen, J.; Schulte, K.; Andersen, J. N.; Schnadt, J. Adsorption of L-Cysteine on Rutile TiO_2 (110). *Surf. Sci.* **2011,** *605*(1-2), 179-186.

(29)   Lachheb, H.; Dappozze, F.; Houas, A.; Guillard, C. Adsorption and Photocatalytic Degradation of Cysteine in Presence of TiO_2. *J. Photoch. Photobio A* **2012,** *246*, 1-7.

(30)   Beasley, D. E.; Koltz, A. M.; Lambert, J. E.; Fierer, N.; Dunn, R. R. The Evolution of Stomach Acidity and its Relevance to the Human Microbiome. *PLoS ONE* **2015,** *10*(7), e01344116.

(31)   Schwalfenberg, G. K. The Alkaline Diet: Is there Evidence that an Alkaline pH Diet Benefits Health? *J. Environ. Public Health* **2012,** *2012*, 727630.

(32)   Koziolek, M.; Grimm, M.; Becker, D.; Iordanov, V.; Zou, H.; Shimizu, J.; Wanke, C.; Garbacz, G.; Weitschies, W. Investigation of pH and Temperature Profiles in the GI Tract of Fasted Human Subjects Using the Intellicap® System. *J. Pharm. Sci.* **2015,** *104* (9), 2855-2863.

(33)   Settanni, G.; Zhou, J.; Suo, T.; Schottler, S.; Landfester, K.; Schmid, F.; Mailander, V. Protein Corona Composition of Poly(ethyleneglycol) and Poly(phosphoester) coated Nanoparticles Correlates Strongly with the Amino Acid Composition of the Protein Surface. *Nanoscale* **2017,** *9*(6), 2138-2144.

(34)   Jastrzebska, A. M.; Kurtycz, P.; Olszyna, A.; Karwowska, E.; Miaskiewicz-Peska, E.; Zaleska-Radziwill, M.; Doskocz, N.; Basiak, D. The Impact of Zeta Potential and Physicochemical Properties of TiO_2-Based Nanocomposites on Their Biological Activity. *Int. J. Appl. Ceram. Tec.* **2015,** *12*(6), 1157-1173.

(35)   Yang, L.; Kuang, H.; Zhang, W.; Aguilar, Z. P.; Wei, H.; Xu, H. Comparisons of the Biodistribution and Toxicological Examinations After Repeated Intravenous Administration of Silver and Gold Nanoparticles in Mice. *Sci. Rep.* **2017,** *7*(1), 3303.

(36)   Ibrahim, K. E.; Al-Mutary, M. G.; Bakhiet, A. O.; Khan, H. A. Histopathology of the Liver, Kidney, and Spleen of Mice Exposed to Gold Nanoparticles. *Molecules* **2018,** *23*(8).

(37)   Lowry, G. V.; Hill, R. J.; Harper, S.; Rawle, A. F.; Hendren, C. O.; Klaessig, F.; Nobbmann, U.; Sayre, P.; Rumble, J. Guidance to Improve the Scientific Value of Zeta-Potential Measurements in nanoEHS. *Environ. Sci-Nano* **2016,** *3*(5), 953-965.

(38)   Schwegmann, H.; Feitz, A. J.; Frimmel, F. H. Influence of the Zeta Potential on the Sorption and Toxicity of Iron Oxide Nanoparticles on S. Cerevisiae and E. coli. *J. Colloid Interf. Sci.* **2010,** *347*(1), 43-48.

(39)   Connor, P. A.; Dobson, K. D.; McQuillan, A. J. Infrared Spectroscopy of the TiO_2/Aqueous Solution Interface. *Langmuir* **1999,** *15*, 2402-2408.

(40)   Mudunkotuwa, I. A.; Grassian, V. H., Biological and Environmental Media Control Oxide Nanoparticle Surface Composition: The Roles of Biological Components (Proteins and Amino Acids), Inorganic Oxyanions and Humic Acid. *Environ. Sci-Nano* **2015,** *2*(5), 429-439.

(41)   Po, H. N.; Senozan, N. M. The Henderson-Hasselbalch Equation: Its history and Limitations. *J. Chem. Educ.* **2001,** *78*(11), 1499-1503.

(42)   Tran, T. H.; Nosaka, A. Y.; Nosaka, Y. Adsorption and Photocatalytic Decomposition of Amino Acids in TiO_2 Photocatalytic Systems. *J. Phys. Chem. B* **2006,** *110*(50), 25525-25531.

(43)   Sebben, D.; Pendleton, P. Infrared Spectrum Analysis of the Dissociated States of Simple Amino Acids. *Spectrochim Acta A* **2014,** *132*, 706-712.

(44)   Wolpert, M.; Hellwig, P. Infrared Spectra and Molar Absorption Coefficients of the 20 Alpha Amino Acids in Aqueous Solutions in the Spectral Range from 1800 to 500 cm^{-1}. *Spectrochim Acta A* **2006,** *64*(4), 987-1001.

(45)   Barth, A. The Infrared Absorption of Amino Acid Side Chains. *Prog. Biophys. Mol. Biol.* **2000,** *74*(3-5), 141-173.

(46)   Roddick-Lanzilotta, A. D.; McQuillan, A. J. An in Situ Infrared Spectroscopic Investigation of Lysine Peptide and Polylysine Adsorption to TiO_2 from Aqueous Solutions. *J. Colloid Interface Sci.* **1999,** *217*(1), 194-202.

(47)   Roddick-Lanzilotta, A. D.; Connor, P. A.; McQuillan, A. J. An in Situ Infrared Spectroscopic Study of the Adsorption of Lysine to TiO_2 from an Aqueous Solution. *Langmuir* **1998,** *14*(22), 6479-6484.

(48)   Derbel, N.; Hernández, B.; Pflüger, F.; Liguier, J.; Geinguenaud, F.; Jaïdane, N.; Ben Lakhdar, Z.; Ghomi, M. Vibrational Analysis of Amino Acids and Short Peptides in Hydrated Media. I. ʟ-Glycine and ʟ-Leucine. *J. Phys. Chem. B* **2007,** *111*(6), 1470-1477.

(49)   Hernández, B.; Pflüger, F.; Adenier, A.; Nsangou, M.; Kruglik, S. G.; Ghomi, M. Energy Maps, Side Chain Conformational Flexibility, and Vibrational Features of Polar Amino Acids ʟ-Serine and ʟ-Threonine in Aqueous Environment. *J. Chem. Phys.* **2011,** *135*(5), 055101.

(50)   Roddick-Lanzilotta, A. D.; McQuillan, A. J. An in situ Infrared Spectroscopic
         Study of Glutamic Acid and of Aspartic Acid Adsorbed on TiO$_2$: Implications for
         the Biocompatibility of Titanium. *J. Colloid Interface Sci.* **2000,** *227*(1), 48-54.

(51)   Jayalath, S.; Wu, H.; Larsen, S. C.; Grassian, V. H. Surface Adsorption of
         Suwannee River Humic Acid on TiO$_2$ Nanoparticles: A Study of pH and Particle
         Size. *Langmuir* **2018,** *34*(9), 3136-3145.

(52)   Weng, Y. X.; Li, L.; Liu, Y.; Wang, L.; Yang, G. Z. Surface-Binding Forms of
         Carboxylic Groups on Nanoparticulate TiO$_2$ Surface Studied by the Interface-
         Sensitive Transient Triplet-State Molecular Probe. *J. Phys. Chem. B* **2003,**
         107(18), 4356-4363.

(53)   Nara, M.; Torii, H.; Tasumi, M. Correlation Between the Vibrational Frequencies
         of the Carboxylate Group and the Types of its Coordination to A Metal Ion: An
         ab Initio Molecular Orbital Study. *J. Phys. Chem.* **1996,** *100*(51), 19812-19817.

(54)   Qu, Q.; Geng, H.; Peng, R.; Cui, Q.; Gu, X.; Li, F.; Wang, M. Chemically
         Binding Carboxylic Acids onto TiO$_2$ Nanoparticles with Adjustable Coverage by
         Solvothermal Strategy. *Langmuir* **2010,** *26*(12), 9539-9546.

(55)   Uznanski, P.; Zakrzewska, J.; Favier, F.; Kazmierski, S.; Bryszewska, E.
         Synthesis and Characterization of Silver Nanoparticles from (Bis)alkylamine
         Silver Carboxylate Precursors. *J. Nanopart. Res.* **2017,** *19*(3), 121.

(56)   Li, L.; Feng, Y.; Liu, Y.; Wei, B.; Guo, J.; Jiao, W.; Zhang, Z.; Zhang, Q.
         Titanium Dioxide Nanoparticles Modified by Salicylic Acid and Arginine:
         Structure, Surface Properties and Photocatalytic Decomposition of p-Nitrophenol.
         Appl. Surf. Sci. **2016,** *363*, 627-635.

(57)   Langel, W.; Menken, L. Simulation of the Interface Between Titanium Oxide and
         Amino Acids in Solution by First Principles MD. *Surf. Sci.* **2003,** *538*(1-2), 1-9.

(58)   Gao, Q.; Xu, W.; Xu, Y.; Wu, D.; Sun, Y.; Deng, F.; Shen, W. Amino Acid
         Adsorption on Mesoporous Materials: Influence of Types of Amino Acids,
         Modification of Mesoporous Materials, and Solution Conditions. *J. Phys. Chem.
         B* **2008,** *112*(7), 2261-2267.

(59)   Mudunkotuwa, I. A.; Grassian, V. H. Citric Acid Adsorption on TiO$_2$
         Nanoparticles in Aqueous Suspensions at Acidic and Circumneutral pH: Surface
         Coverage, Surface Speciation, and its Impact on Nanoparticle-Nanoparticle
         Interactions. *J. Am. Chem. Soc.* **2010,** *132*(42), 14986-14994.

(60)   Quesada-Moreno, M. M.; Aviles-Moreno, J. R.; Marquez-Garcia, A. A.; Partal-Urena, F.; Gonzalez, J. J. L. L-Serine in Aqueous Solutions at Different pH: Conformational Preferences and Vibrational Spectra of Cationic, Anionic and Zwitterionic Species. *J. Mol. Struct.* **2013,** *1046*, 136-146.

(61)   Lambie, B.; Ramaekers, R.; Maes, G. Conformational Behavior of Serine: An Experimental Matrix-isolation FT-IR and Theoretical DFT(B3LYP)/6-31++G** Study. *J. Phys. Chem. A* **2004,** *108*(47), 10426-10433.

(62)   Max, J. J.; Trudel, M.; Chapados, C. Infrared Titration of Aqueous Glycine. *Appl. Spectrosc.* **1998,** *52*(2), 226-233.

(63)   Kumar, S.; Rai, A. K.; Singh, V. B.; Rai, S. B. Vibrational Spectrum of Glycine Molecule. *Spectrochim Acta A* **2005,** *61*(11-12), 2741-2746.

(64)   Meng, M.; Stievano, L.; Lambert, J. F. Adsorption and Thermal Condensation Mechanisms of Amino Acids on Oxide Supports. 1. Glycine on Silica. *Langmuir* **2004,** *20*, 914-923.

(65)   Sultan, A. M.; Hughes, Z. E.; Walsh, T. R. Binding Affinities of Amino Acid Analogues at the Charged Aqueous Titania Interface: Implications for Titania-Binding Peptides. *Langmuir* **2014,** *30*(44), 13321-13329.

(66)   Yang, Y.; Lohwacharin, J.; Takizawa, S. Analysis of Adsorption Processes of Dissolved Organic Matter (DOM) on Ferrihydrite Using Surrogate Organic Compounds. *Environ. Sci. Pollut. Res. Int.* **2017,** *24*(27), 21867-21876.

(67)   Jiang, J. K.; Oberdorster, G.; Biswas, P. Characterization of Size, Surface Charge, and Agglomeration State of Nanoparticle Dispersions for Toxicological Studies. *J. Nanopart. Res.* **2009,** *11*(1), 77-89.

(68)   Tschapek, M.; Wasowski, C.; Torressanchez, R. M. PZC and IEP of γ-Al$_2$O$_3$ and TiO$_2$. *J. Electroanal. Chem.* **1976,** *74* (2), 167-176.

(69)   Sverjensky, D. A.; Jonsson, C. M.; Jonsson, C. L.; Cleaves, H. J.; Hazen, R. M. Glutamate Surface Speciation on Amorphous Titanium Dioxide and Hydrous Ferric Oxide. *Environ. Sci. Technol.* **2008,** *42,* 6034-6039.

(70)   Parikh, S. J.; Kubicki, J. D.; Jonsson, C. M.; Jonnson C. L.; Hazen, R. M.; Serjensky, D. A; Sparks, D. L. Evaluating Glutamate and Aspartate Binding Mechanisms to Rutile (α-TiO$_2$) via ATR-FTIR Spectroscopy and Quantum Chemical Calculations. *Langmuir* **2011**, *27*, 5, 1778-1787.

(71)   Pantaleone, S. R.; Rimola, A.; Rimola Sodupe, M. Canonical, Deprotonated, or Zwitterionic? A Computational Study on Amino Acid Interaction with the TiO_2 (101) Anatase Surface. *J. Phys. Chem. C* **2017,** *121*, 14156-14165.

(72)   Tonner, R., Adsorption of Proline and Glycine on the TiO_2 (110) Surface: A Density Functional Theory Study. *Chemphyschem* **2010,** *11*(5), 1053-1061.73.

(73)   Monti, S.; Van Duin, A. C. T.; Kim, S. Y.; Barone, V. Exploration of the Conformational and Reactive Dynamics of Glycine and Diglycine on TiO_2: Computational Investigations in the Gas Phase and in Solution. *J. Phys. Chem. C* **2012**, *116*, 8, 5141-5150.

(74)   Qiu, T.; Barteau, M. A. STM Study of Glycine on TiO_2 (110) Single Crystal Surfaces. *J. Colloid Interface Sci.* **2006**, *303,* 229-235.

(75)   Lerotholi, T. J.; Kröger, E. A.; Knight, M. J.; Unterberger, W.; Hogan, K.; Jackson, D.C.; Lamont, C. L. A.; Woodruff, D. P. Adsorption Structure of Glycine on TiO_2 (110): A Photoelectron Diffraction Determination. *Surf. Sci*. **2009**, *603*, 2305-2311.

Chapter 4   Polar Amino Acid Interactions with α-Fe$_2$O$_3$ Nanoparticles: Effects of pH, Nanoparticle Type, and Amino Acid Concentration onto Adsorption

4.1   Abstract

Environmentally abundant nanoscale iron oxide could interact with biomolecules and consequently impact the environment and human health. In this study, polar amino acids, lysine (Lys), glutamic acid (Glu), aspartic acid (Asp), and arginine (Arg), adsorption onto α-Fe$_2$O$_3$ nanoparticles were investigated. Lys and Glu adsorption onto α-Fe$_2$O$_3$ as a function of pH was compared with the results from an earlier study of TiO$_2$ to determine the effect of different nanoparticle types on amino acid interactions. Attenuated total reflectance-Fourier transform infrared (ATR-FTIR) spectroscopy was used to probe amino acid side chain interactions with nanoparticles and determine surface species upon adsorption. Predominant speciation of the amino acids and the surface chemistry of α-Fe$_2$O$_3$ nanoparticles led to differences in adsorption mechanisms. Asp surface coverage onto α-Fe$_2$O$_3$ was higher in comparison to Arg. Lys and Glu showed a different trend of adsorption with changing pH. Nanoparticle type changed amino acid adsorption behavior onto surfaces. Amino acids showed a stronger amine group interaction and higher symmetry of carboxylate coordination on the α-Fe$_2$O$_3$ compared to TiO$_2$. These differences were attributed to the different speciation of the functional groups within the amino acids and the nanoparticle surface charge. The detailed chemistry in the adsorption processes implied the formation of outer-sphere and inner-sphere complex differences between different nanomaterials.

4.2   Introduction

Iron oxide nanoparticles have shown great promise for various environmental and biological applications, including removing pollutants from contaminated water,[1–3] tracking cancer cell growth,[4,5] and improving targeted drug delivery.[6] They attain interest due to their magnetic properties, light absorbance capacity, high chemical reactivity, and long-term adsorbent stability under most circumstances.[7] Many applications of nanoparticles rely on surficial reactions with chemical compounds they are exposed to,[8,9] particularly adsorption of molecules with useful characteristics.[6,9] Nanoparticle surfaces can be functionalized by molecules using a covalent modification strategy via synthesis or noncovalent modification complexation or adsorption process.[10] Amino acids –the building blocks of more complex protein molecules– are common adsorbates used to functionalize nanoparticles.[11] By studying amino acid adsorption, an understanding of the persistence and availability of such bio-essential compounds and predictive insight into how larger molecules (i.e., enzymes) might behave upon introduction to nanoparticle surfaces can be gained.[5,6] Consequently, amino acid interactions with nanoparticles have been studied to understand how the size, morphology, and surface chemistry of the nanoparticles change after adsorption occurs,[5] and how external factors –such as pH, ionic strength, and concentration– play a role in amino acid adsorption.[12,13]

Despite the abundant research efforts to characterize molecular-level interactions between nanoparticles and sorbates/ents, amino acid-nanoparticle complexes are highly heterogeneous and consequently remain poorly understood. Much of this ambiguity is rooted in the diversity of amino acids, nanoparticles, and environmental conditions present,

which affect complex formation kinetics, structure, and stability. For instance, nanoparticle concentration and composition in an aqueous environment have significantly impacted the adsorption extent.[14] High concentrations of nanoparticles led to a small shift in the total amount of glycine and glutamic acid adsorption. In contrast, a dilute concentration promoted adsorption by a factor of 3 to 4 and 1.5 to 6 times onto ZnO and TiO_2, respectively.[14] pH impacted adsorption density, as was exemplified with aspartic acid and lysine adsorption onto iron oxide.[12] In particular, at pH 2, 4, 7 –when amino acid suspension concentration was higher than 2 mg/mL– lysine showed higher surface coverage than aspartic acid on superparamagnetic iron oxide nanoparticles (SPION).[12] Agglomeration studies of iron oxide nanoparticles showed that the pH effect is more substantial than amino acid acidity.[15] While the adsorption reactions are generalized to Langmuir model kinetics[16], the impact of pH, concentration, and other parameters on reaction rates are still not well constrained. Of particular importance to biological systems, hematite (α-Fe_2O_3) is a ubiquitous and bio-incompatible oxide phase, found abundantly in soils and sediments globally.[5,17,18] Due to its prevalence in natural environments, biomolecules frequently interact with hematite, impacting nano-bio complex environmental fate and nutritional (N, P, S, and C) lifecycles.[18,19] Moreover, the research available on hematite-contaminant sorption suggests that these phases are highly reactive, and iron promotes the preservation of organic matter in sediments.[16] Ionic strength also plays a role in how molecules adsorb onto α-Fe_2O_3 surfaces, as higher ionic strength decreased the ratio of monodentate complexes observed.[20]
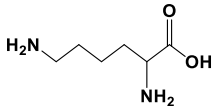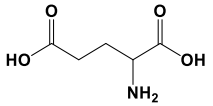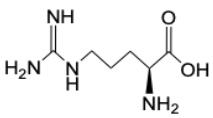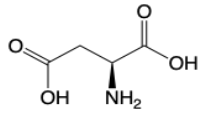
These previous studies confirm that iron oxide nanoparticles interact with biological and ecological systems frequently; however, little is known about the

interactions of amino acids and biological macromolecules at α-Fe_2O_3 surfaces. Biomolecule adsorption onto α-Fe_2O_3 suggests that when provoking the surface chemistry of the nanoparticles and the size-dependent orientation of the functional groups, it is expected to see different surface species of the amino acids upon adsorption. However, the exact patterns and mechanisms of these interactions still need to be investigated. Since the functional groups and polarity of amino acids are highly diverse, their adsorption behavior onto α-Fe_2O_3 cannot be generalized by studying one type of amino acid. Structural properties of amino acids impact adsorption mechanisms, structures, and dynamics, influencing mineral surface catalytic changes and stability.

This study examines the adsorption of polar amino acids, lysine, glutamic acid, aspartic acid, and arginine, onto α-Fe_2O_3 nanoparticle surfaces. These amino acids were selected due to their different functional groups and charge properties at physiological pH (Table 4.1).[21,22] The results from pH-dependent lysine and glutamic acid adsorption were compared to the results from an earlier study to assess the difference in amino acid adsorption mechanisms between the TiO_2 and α-Fe_2O_3 nanoparticles. Furthermore, the effect of arginine and aspartic acid concentration on the interactions was also investigated. A comprehensive comparison of amino acid adsorption behavior can promote a detailed understanding of how larger molecules may interact with nanoparticles. Here, Attenuated Total Reflectance Fourier Transform Infrared (ATR-FTIR) spectroscopy was used to analyze the surface interactions. The results of this study will add new perspectives to the body of literature available on nanoparticle-amino acid adsorption interactions, with an insight into the role of ubiquitous hematite phases in modulating amino acid cycling. In probing diverse amino acid behavior at the nanoscale iron interface, it is aimed to further

our understanding of complex nanoparticle-biomolecule interactions, and reactivity and dynamics of α-Fe$_2$O$_3$ as a sorbent in relevant environmental and biological systems. Subsequently, the results from this study can be used to inform a variety of projects, from environmental remediation applications to targeted drug treatment methods.

Table 4.1: The amino acids used in this study, including their side-chain characteristics, molecular structures, logarithmic dissociation constants (pK_a), and isoelectric points (pH$_{IEP}$) at 25 °C.

Amino Acid (Abbreviation)	Side Chain	Side Chain Characteristics	Molecular Structure	pK_a			pH$_{IEP}$
				pK_{a1}	pK_{a2}	pK_{a3}	
Lysine (Lys, K)	-(CH$_2$)$_4$ NH$_2$	Polar, Positively Charged (Acidic)		2.15	9.16	10.67	9.47
Glutamic Acid (Glu, E)	-(CH$_2$)$_2$ COOH	Polar, Negatively Charged (Basic)		2.16	4.15	9.58	3.22
Arginine (Arg, R)	-(CH$_2$)$_3$NH-C(NH)NH$_2$	Polar, Positively Charged (Acidic)		2.03	9.00	12.1	10.76
Aspartic Acid (Asp, D)	-CH$_2$ COOH	Polar, Negatively Charged (Basic)		1.95	3.71	9.66	2.85

4.3 Experimental Methods and Materials

4.3.1 Materials

α-Fe$_2$O$_3$ nanoparticles were purchased from Alfa Aesar, MA. Aspartic Acid (Sigma-Aldrich, MO), lysine (Fisher Scientific, Inc), glutamic acid (Acros Organics), and

arginine (Sigma-Aldrich, MO) were used as purchased without further purification; Table 4.1 shows their molecular structures and properties. The experiments' primary solvent was MilliQ water (Millipore, resistance = 18.2 MΩ.cm at 25 $^\circ$C). Throughout the experiments, the desired ionic strength was 10 mM for aspartic acid and arginine, 50 mM for lysine and glutamic acid, and adjusted with NaCl (Fisher Scientific, Inc.). There was no buffer solution involved in the adsorption experiments for aspartic acid and arginine. However, to better compare lysine and glutamic acid adsorption on α-Fe$_2$O$_3$ from the results of their adsorption on TiO$_2$, the same buffers in an earlier study were used.[13] HEPES [4-(2-hydroxyethyl)-1-piperazineethanesulfonic acid] were obtained from Fisher Scientific Inc. and TAPS [tris(hydroxymethyl)methylamino propane sulfonic acid] from Spectrum Chemical. Lysine and glutamic acid were dissolved in 25 mM HEPES buffer (for pH 7.4) and 25 mM TAPS buffer (for pH 9.0). There was no buffer for the experiments at pH 2.0, and the pH values for the experiments were achieved using HCl and NaOH solutions (Fisher Scientific, Inc.).

4.3.2 Nanoparticle Characterization

A JEOL JEM-1400 Plus transmission electron microscopy (TEM) at 80 kV was used to determine the size and morphology of the α-Fe$_2$O$_3$ nanoparticles. Nanoparticles were deposited on a formvar/carbon-coated 100-mesh copper grid (Electron Microscopy Sciences) for TEM imaging. Nanoparticle crystalline phase was determined using an APEX II Ultra diffractometer equipped with a CCD-based area detector, with MoKα radiation at λ= 0.71073 Å. Surface area and pore size measurements were performed using a Quantachrome Nova 4200e analyzer. Before analysis, samples were degassed for 6 hours

at 120 ºC, and the data from Brunauer-Emmett-Teller (BET) N2 adsorption and desorption were analyzed using 20 multipoint isotherms with partial pressures (P/Po) of 0.05-0.95.

A Malvern Instruments Zetasizer Nano instrument particle analyzer was used for zeta-potential measurements of bare α-Fe_2O_3 nanoparticles to determine the isoelectric point (pH_{IEP}). The procedure for collecting zeta-potential measurements was similar to the approach used previously[13] and is as follows: α-Fe_2O_3 nanoparticle stock suspension was sonicated for 2 mins, and 100 µL aliquots were added to 10 mM NaCl solutions at desired pH values. The α-Fe_2O_3 final concentration (0.01 g/L) of the resulting solution was significantly diluted to increase light scattering efficiency. Before nanoparticles' addition, solutions were filtered through 0.2 µm pore size syringe filters (Acrodisc, PALL) to remove any dust that could potentially distort the analysis. Triplicate measurements were taken (with 2 minutes interval) after 24 hours of solution preparation, and the mean values were reported.

4.3.3   ATR-FTIR Spectroscopy

A horizontal 45º angle of incidence Amorphous Material Transmitting Infrared Radiation (AMTIR) crystal (PIKE Technologies) in a Thermo–Nicolet iS10 FTIR spectrometer equipped with a mercury cadmium telluride (MCT-A) detector was used for the ATR-FTIR experiments. Spectra were collected in 5 min intervals at 4 cm^{-1} resolution with an average of 512 scans per spectrum. The background IR spectra of the MilliQ solution on the AMTIR crystal was subtracted from the final amino acid IR spectra. For solution-phase arginine and glutamic acid spectral collection, 5 mM and 25 mM concentrations of amino acid solutions were examined. A higher solution concentration

was not possible for aspartic acid to be prepared due to its low solubility compared to arginine. Thus, 25 mM amino acid spectra were used for aspartic acid and arginine solution peak assignments, and the results were used to identify adsorbate peaks. Lysine and glutamic acid solution-phase results were used from an earlier study (refer to Fig 3.2) and peak assignments were recorded in Table 4.3 and Table 4.4 accordingly. To study the adsorption/desorption of amino acids onto α-Fe$_2$O$_3$ nanoparticle surfaces, a 1 mL nanoparticle suspension from a 5 mg/mL stock solution was drop-cast onto the AMTIR crystal to create a thin film and was dried overnight. For arginine and aspartic acid adsorption: a flow system with a peristaltic pump was used to flow MilliQ solution (adjusted to desired pH 7.4) across the film for 20 minutes. This step aimed to eliminate loosely bound nanoparticles on the crystal and adjust the film surface charge accordingly. For lysine and glutamic acid: instead of MilliQ, 25 mM buffer solutions have flowed in this step. The final spectrum of the first flow (sampled after 30 minutes) was used as the background for data reprocessing. After the background spectrum collection, the inflow was switched to the amino acid solution (at a concentration of 1 mM or 5 mM), and the data were collected for 90 minutes.

4.4   Results and Discussion

4.4.1   Nanoparticle Characterization

Details of the characterization results can be seen in Fig. 4.1. Powder X-Ray Diffraction (XRD) and Transmission Electron Microscopy (TEM) results revealed that the nanoparticles are entirely hematite with ~5-20 nm diameters and have a high aggregation tendency with 110 m^2/g surface area. Zeta-potential is the electrical potential of the

interface between the solution and the stationary layer of the ions attached to the particle surface.[23] Changes in the zeta-potential measurements of α-Fe$_2$O$_3$ nanoparticles are shown in Fig 4.1c. The measured pH$_{IEP}$ was 6.0, and -36 mV and +25 mV were the lowest and highest zeta-potential values measured.
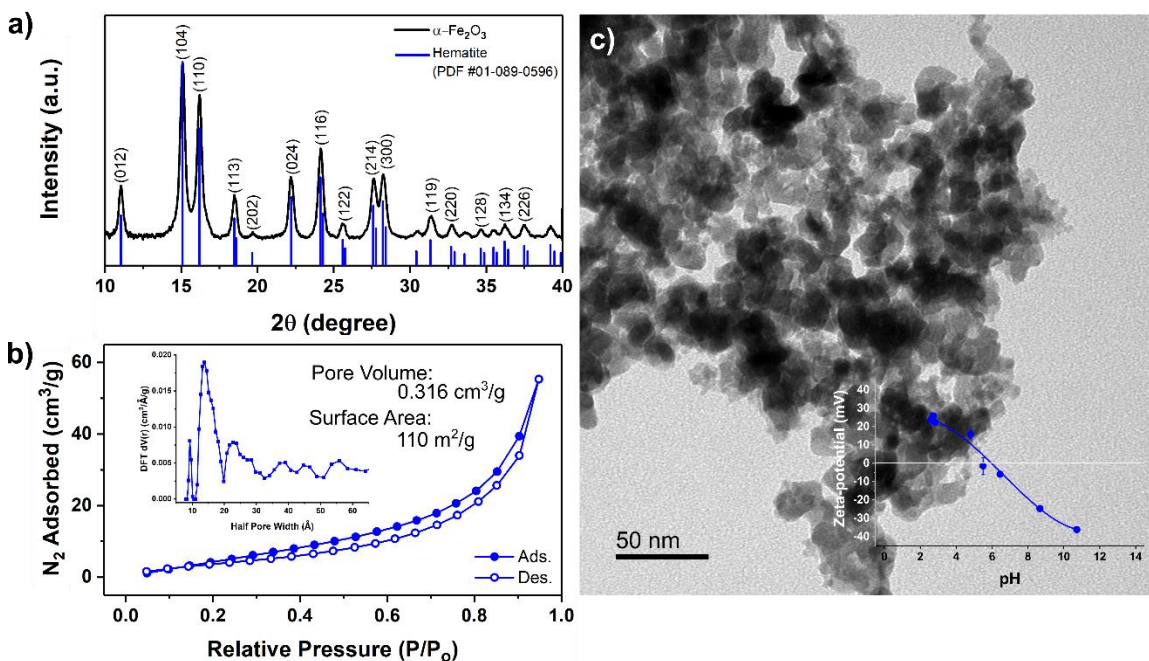
Figure 4.1: Characterization of α-Fe$_2$O$_3$ nanoparticles. (a) XRD pattern indicates that particles are hematite; (b) BET surface area measurement shows that particles have 110 m^2/g surface area, and (c) TEM image of the nanoparticles indicates high aggregation tendency of the nanoparticles.

4.4.2 Amino Acid Solution Phase ATR-FTIR Results

IR spectral resolution of lysine, glutamic acid, aspartic acid, and arginine side-chains are of interest for monitoring complex biomolecule (i.e., protein) activity.[24] The solvent-exposed carboxylic and amine groups make these amino acids versatile and highly reactive. Thus, these amino acids are often found in the active sites of proteins.[24] The molar distribution of arginine and aspartic acid species at a pH range from 0-14 was determined

using the Henderson−Hasselbalch approximation[25]. The results from these calculations can be seen in Fig. 4.2.
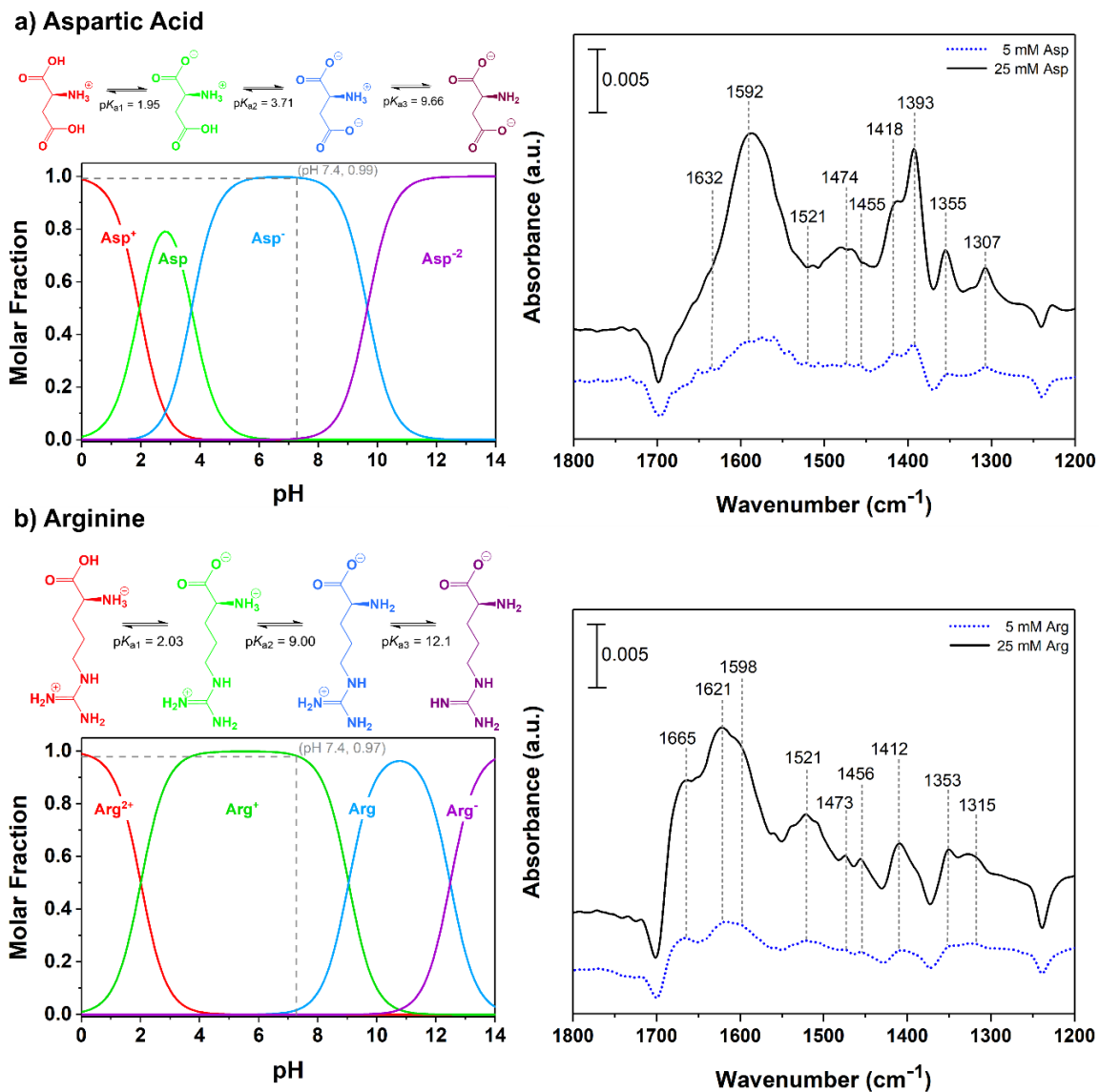
Figure 4.2: pH-dependent amino acid speciation diagram with the corresponding structures (left) and the solution ATR-FTIR spectra at pH 7.4 (right). Spectra are shown for 5 mM and 25 mM (a) aspartic acid and (b) arginine solutions. The molar fraction of the forms of amino acids present in the solution is computed via the Henderson-Hasselbalch equation.[25] The 25 mM amino acid solution spectra were used for peak assignments.

Aspartic acid has two carboxyl groups with the following protonation species present in solution: monocation (Asp$^+$), zwitterion (Asp), monoanion (Asp$^-$), and dianion (Asp^{-2}). According to the speciation plot in Fig. 4.2a, aspartic acid solution at pH 7.4 has a molar fraction of 0.99 Asp$^-$, with a small percentage of Asp^{-2}. In monoanion species, aspartic acid side-chains include two deprotonated carboxylate groups and one protonated amine group. The 25 mM aspartic acid solution spectrum was used to define the peaks of the solution spectra. The vibrational frequencies from the functional groups can be seen in the solution phase ATR-FTIR spectra in Fig. 4.2a. Here, each spectrum includes the subtraction of the appropriate pH-adjusted MilliQ solution spectrum. The vibrational peaks were determined from the local minimum values of the second derivatives via OMNIC 9.0 software (Thermo Fisher) and used for assignments Table 4.2.[26–28]

At pH 7.4, both carboxylic acid groups are deprotonated as carboxylate in aspartic acid. The C=O band of the COO$^-$ groups can be identified as it features absorption in a frequency region isolated from other side chains and appears due to stretching vibrations: the antisymmetric and the symmetric. The peak at 1592 cm^{-1} is assigned for v_{as}(COO$^-$) of α-carboxylate (attached to α-carbon). The amine group of aspartic acid is also protonated and differentiates the two carboxylate vibrations. Thus, the band for v_{as}(COO$^-$) of α-carboxylate is broadened due to H-bonding with the deprotonated amine group.[13] Additionally, the occurrence of the v_{as}(COO$^-$) peaks for α- and distal-carboxylate (as part of the side chain) are at very similar wavenumbers at this pH value.[27] The shoulder on the right side of the 1592 cm^{-1} peak appears for the distal-carboxylate group v_{as}(COO$^-$)

vibration.[13,27] 1418 cm^{-1} and 1393 cm^{-1} peaks are assigned as $v_s(COO^-)$ vibrations for α-

and distal-carboxylate, respectively.

Table 4.2: Vibrational modes for solution-phase and adsorbed phase aspartic acid and arginine at pH 7.4.[26–28]

	Vibrational Modes*	Vibrational Frequency (cm^{-1})			
		Experimental Values			
		Solution	1 mM Adsorbed on α-Fe$_2$O$_3$	5 mM Adsorbed on α-Fe$_2$O$_3$	Literature (Solution)
Aspartic Acid	$\delta_{as}(NH_3^+)$	1652	1651	1652	1618-1641
	$v_{as}(COO^-)$	1592/1556	1591/1559	1587/1557	1570-1598
	$\delta_s(NH_3^+)$	1521	1523	1520	1520-1532
	$\delta(CH_2)$	1474/1455	1475/1462	-	1456-1481
	$v_s(COO^-)$	1413/1393	1416/1392	1415/1393	1390-1421
	$\omega(CH_2)/\delta(CH)$	1355/1307	1353/1308	1351/1307	1306-1358
	$\delta(C-OH)$	1230	1229	1224	1221-1247
	Vibrational Modes*	Vibrational Frequency (cm^{-1})			
		Experimental Values			
		Solution	1 mM Adsorbed on α-Fe$_2$O$_3$	5 mM Adsorbed on α-Fe$_2$O$_3$	Literature (Solution)
Arginine	$\delta_{as}(NH_3^+)$	1621	1631	1632	1633
	$v_{as}(COO^-)$	1598	1582	1589	1574-1608
	$\delta_s(NH_3^+)$	1521	1519	1520	1516-1527
	$\delta(CH_2)$	1473/1446	1474/1450	1475/1452	1454-1475
	$v_s(COO^-)$	1412	1408	1405	1410-1414
	$\omega(CH_2)/\delta(CH)$	1353/1332	1352/1331	1350/1330	1325-1356
	$\delta(C-OH)$	1212	1230	1232	1212

^{a} v_s/v_{as}: symmetric/asymmetric stretches; δ_s/δ_{as}: symmetric/asymmetric bends; v_{sc}: scissor; and ω: wag vibrations.

Solution-phase arginine at pH 7.4 in Fig. 4.2b shows the pH-dependent molecular

structure. The amine groups are protonated, and the carboxylic acid group is deprotonated

to form a carboxylate ion. The arginine speciation is almost entirely Arg$^+$ at this pH.

Carboxylate contributions to the spectra are seen by the asymmetric $v_{as}(COO^-)$ and

symmetric $v_s(COO^-)$ stretching modes. The asymmetric stretch of the α-carboxylate, close to the cationic amine, is at 1598 cm^{-1}, and the symmetric stretching $v_s(COO^-)$ is at 1412 cm^{-1}. The $v_{as}(COO^-)$ band is broadened, presumably as a result of hydrogen bonding with the amine.[13] The peak correspondent with the asymmetric bending mode of protonated amine $\delta_{as}(NH_3^+)$ at 1621 cm^{-1} does not overlap and can be seen clearly. Symmetric $\delta_s(NH_3^+)$ deformation of the amine group also occurs at ~1521 cm^{-1}, and the peak at 1665 cm^{-1} is assigned as $v(C\text{-}N)$.[26] Amine absorptions of arginine are comparatively strong compared to aspartic acid as the arginine species contains an additional amine group in the side-chain. A summary of arginine peak assignments is listed in Table 4.2.[26–28]

Solution-phase lysine peak assignments were recorded from the earlier study[13] (refer to Fig 3.2) and a summary of lysine peak assignments is listed in Table 4.3.[26,29–31] Briefly, lysine contains two amine groups in its structure, and species are shown as dication (Lys^{2+}), monocation (Lys$^+$), zwitterion (Lys), and monoanion (Lys$^-$). At pH 2, the prominent carboxylic acid stretches at 1727 cm$^{-1,}$ and 1257 cm^{-1} are referred to $v(C=O)$ and $v(C\text{−}OH)$, respectively (Fig. 4.3a right). At pH 7.4, lysine speciation is entirely monocation (Lys$^+$). Deprotonated carboxylate group contributions to the IR spectra appear as the asymmetric $v_{as}(COO^-)$ and symmetric $v_s(COO^-)$ stretching modes at 1595 cm^{-1} 1413 cm^{-1}, respectively.[13] These two vibrational modes show stronger peak intensities when pH increases due to polar charged amino acid speciation.[29,32] The deprotonated amine peak associated with the scissor motion at 1557 cm^{-1} [$v_{sc}(NH_2)$] begins to appear while the $\delta_{as}(NH_3^+)$ decreases.[13]

Table 4.3: Vibrational modes for solution-phase and adsorbed lysine on different metal oxide nanoparticles as a function of pH.

Vibrational Modes [a]	Vibrational Frequency (cm^{-1})									
	pH 2			pH 7.4			pH 9.0			
	Solution	Adsorbed on TiO$_2$	Adsorbed on α-Fe$_2$O$_3$	Solution	Adsorbed on TiO$_2$	Adsorbed on α-Fe$_2$O$_3$	Solution	Adsorbed on TiO$_2$	Adsorbed on α-Fe$_2$O$_3$	Literature (Solution)
v(C=O)	1727	1724	-	-	-		-	1740	-	1730-1733
δ_{as}(NH$_3^+$)	1621	1621	1618	1621	1621	1626	1621	1621	1626	1620-1634
v_{as}(COO$^-$)	1596	1599	1595	1595	1592	1587	1599	1598	1583	1584-1608
v_{sc}(NH$_2$)	-	1558	1558	1547	1547	1559	1557	1564	1558	1559
δ_s(NH$_3^+$)	1528/1512	1528/1512	1520/1512	1528/1512	1527/1513	1521/1508	1527/1515	1527/1512	1520/1508	1521-1527
δ(CH$_2$)	1476/1461/1444	1484/1462/1442	1474/1460/1448	1478/1462/1442	1476/1461/1443	1474/1459/1442	1477/1463/1445	1478/1461/1443	1474/1459/1443	1445-1476
v_s(COO$^-$)	1412	1416/1402	1411	1413	1413/1400	1410/1397	1412	1413/1401	1397	1396-1414
ω(CH$_2$)/δ(CH)	1353/1332	1352/1331	1350/1327	1356/1332	1347/1321	1351/1320	1354/1310	1347/1321	1350/1309	1311-1352
v(C−OH)	1257	1242	-	-	-		-	1236	-	1237-1255

[a] v_s/v_{as}: symmetric/asymmetric stretches; δ_s/δ_{as}: symmetric/asymmetric bends; v_{sc}: scissor; and ω: wag vibrations.

Solution-phase glutamic acid peak assignments were also recorded from the earlier study[13] (refer to Fig 3.2). A summary of Glu peak assignments are summarized in Table 4.4.[13,26,27,29–31] Glu consists of two carboxyl groups with the following protonation species present in solution: monocation (Glu$^+$), zwitterion (Glu), monoanion (Glu$^-$), and dianion (Glu^{2-}). At pH 2, v_{as}(COO$^-$) at 1597 cm^{-1} and the v_s(COO$^-$) at 1410 cm^{-1} together confirm the presence of α-carboxylate in the zwitterion form. At pH 7.4, the amine group is protonated and differentiates the two carboxylate vibrations.[27] There is no significant v_{sc}(NH$_2$) peak observed at pH 9 spectrum due to overlapping with the v_{as}(COO$^-$) peak.[13]

Table 4.4: Vibrational modes for solution-phase and adsorbed glutamic acid on different metal oxide nanoparticles as a function of pH.

Vibrational Modes [a]	Vibrational Frequency (cm^{-1})									Literature (Solution)
	pH 2			pH 7.4			pH 9.0			
	Solution	Adsorbed on TiO$_2$	Adsorbed on α-Fe$_2$O$_3$	Solution	Adsorbed on TiO$_2$	Adsorbed on α-Fe$_2$O$_3$	Solution	Adsorbed on TiO$_2$	Adsorbed on α-Fe$_2$O$_3$	
v(C=O)	1726	1722	-	-	-	-	-	1744	-	1712-1728
δ_{as}(NH$_3^+$)	1621	1621	1622	1628	1621	1620	1621	1621	1622	1583-1635
v_{as}(COO$^-$)	1597	1597/1546	1584/1538	1598/1550	1596/1552	1583/1552	1595/1552	1595/1551	1583/1552	1537-1560
δ_s(NH$_3^+$)	1527	1522	1523	1530	1534	1544	1527	1534	1543	1520-1540
δ(CH$_2$)	1462/1451	1451	1448	1465/1446	1467/1451/1443	1478/1448	1462/1451/1443	1462/1451/1442	1475/1448	1440-1454
v_s(COO$^-$)	1410	1423/1404	1406	1402	1424/1402	1402	1401	1401	1402	1400-1417
ω(CH$_2$)/δ(CH)	1351/1320	1345/1321	1359/1316	1348/1322	1345/1326	1346//1315	1346/1325	1346/1325	1347/1316	1323-1350
v(C−OH)	1228	1219	-	-	-	-	-	-	-	1205-1253

[a] v_s/v_{as}: symmetric/asymmetric stretches; δ_s/δ_{as}: symmetric/asymmetric bends; v_{sc}: scissor; and ω: wag vibrations.

4.4.3 pH-Dependent Lysine and Glutamic Acid Adsorption onto α-Fe$_2$O$_3$ Nanoparticles: Effects of Nanoparticle Type

The pH-dependent adsorption behavior of glutamic acid and lysine onto α-Fe$_2$O$_3$ nanoparticle surfaces is notably different from each other, as shown in Fig. 4.3. The peak intensities of the lysine adsorbate spectra are much greater under basic conditions. On the contrary, glutamic acid adsorbate spectra have higher peak intensities under acidic conditions. A similar trend was observed for glutamic acid and lysine adsorption onto TiO$_2$ nanoparticles due to combinations of amine and carboxylate group interactions take place on pH-dependent adsorption mechanisms.[13]

Lysine adsorbate spectra at pH 2.0 show only one v_s(COO$^-$) peak at 1411 cm^{-1} on α-Fe$_2$O$_3$ nanoparticle surface different than its adsorption onto TiO$_2$ (Fig. 4.3a).[13] Unlike

its solution-phase, there was no observed v(C=O) peak on the hematite surface, suggesting the absence of a protonated carboxylic acid group on the surface. Vibrational frequencies could change upon adsorbate coordination to nanoparticle surfaces, and carboxylate group interactions can be characterized in part by the wavenumber splitting of the asymmetric and symmetric stretching modes ($\Delta v_{as-s} = \Delta v_{as} - \Delta v_s$).[33] The calculated results for Δv_{as-s} are recorded in Table 4.5. According to Deacon's rule, Δv_{as-s} values for metal coordinated carboxylate binding modes follow the order: Δv_{as-s}(monodentate) > Δv_{as-s}(ionic) > Δv_{as-s}(bidentate bridging) > Δv_{as-s} (bidentate chelating).[13,34] Considering this order and the existing studies, it was suggested that the Δv_{as-s} values for H-bonds are close to that for the ionic state.[13] The Δv_{as-s} value for adsorbed lysine at pH 2 is 184 cm^{-1} (see Table 4.5), which is the same as the uncoordinated Lys Δv_{as-s} value could refer to H-bonding of the carboxylate. The occurrence of a single Δv_{as-s} value for lysine adsorbate confirms a more symmetrical orientation; therefore, double H-bonding is present on the α-Fe$_2$O$_3$ surface.

For lysine adsorbate spectra at pH 7.4, there is a drastic decrease in the δ_s(NH$_3^+$) peak intensity compared to the solution-phase, suggesting the interactions from protonated amine group to the α-Fe$_2$O$_3$ nanoparticle surface. A similar observation was recorded lysine adsorption onto TiO$_2$.[13] The v_s(COO$^-$) peak is narrowed, and the Δv_{as-s} value for adsorbed lysine at pH 7.4 is 177 cm^{-1}. A decrease in Δv_{as-s} value from free K$^+$ species is pointed to be a result of bidentate bridging configuration. At pH 7.4 (> pH$_{IEP}$ of the α-Fe$_2$O$_3$ nanoparticle, see Fig. 4.1c), the surface is deprotonated and negatively charged, whereas lysine is mostly present at its Lys$^+$ species; thus, inner-sphere complexes are favorable, and

outer-sphere complexes are known to initiate their formation.[32] The higher absorbance intensity of the spectra at pH 7.4 compared to the one at pH 2.0 is suggested to result from outer-sphere complexes. Electrostatic attractions are likely to occur between the hematite surface and the protonated amine group in Lys$^+$ species at pH 7.4.

At pH 9, dihydroxylation of the hematite surface increases further. Protonated amine groups in K$^+$ and K are then attracted to the negatively charged α-Fe$_2$O$_3$ surface through electrostatic interactions. Similar to the lysine adsorption onto TiO$_2$ surface, v_{sc}(NH$_2$) peak at 1557 cm^{-1} is not observed, suggesting Lys$^+$ species are showing a higher affinity to the surface than K species. There is a significant change in Δv_{as-s} value (173 cm^{-1}) for the adsorbate lysine spectra compared to its free form, indicating bidentate bridging. Electrostatic interactions were expected to occur through the distal-amine group side chain as this group is farther in terms of molecular-proximity to the carboxylate group.

Table 4.5: Changes in the wavenumber splitting of symmetric and asymmetric carboxylate stretches for lysine and glutamic acid upon adsorption on TiO_2 and $\alpha\text{-}Fe_2O_3$ nanoparticles. The results from TiO_2 re-recorded from an earlier study.[13]

Vibrational Modes [a]	Vibrational Frequency Shift (cm^{-1}) ($\Delta v_{as\text{-}s}$)*								
	pH 2.0			pH 7.4			pH 9.0		
		Adsorbed			Adsorbed			Adsorbed	
	Solution	TiO_2	$\alpha\text{-}Fe_2O_3$	Solution	TiO_2	$\alpha\text{-}Fe_2O_3$	Solution	TiO_2	$\alpha\text{-}Fe_2O_3$
Lys	184	183/197	184	182	179/192	177	187	185/197	173
Glu α-carboxylate	187	174/193	178	196	172/194	181	194	194	181
Glu distal-carboxylate	-	123/142	132	148	128/150	150	151	150	150

($\Delta v_{as\text{-}s} = \Delta v_{as} - \Delta v_s$); v_{as}: asymmetric stretching and v_s: symmetric stretching vibrations.
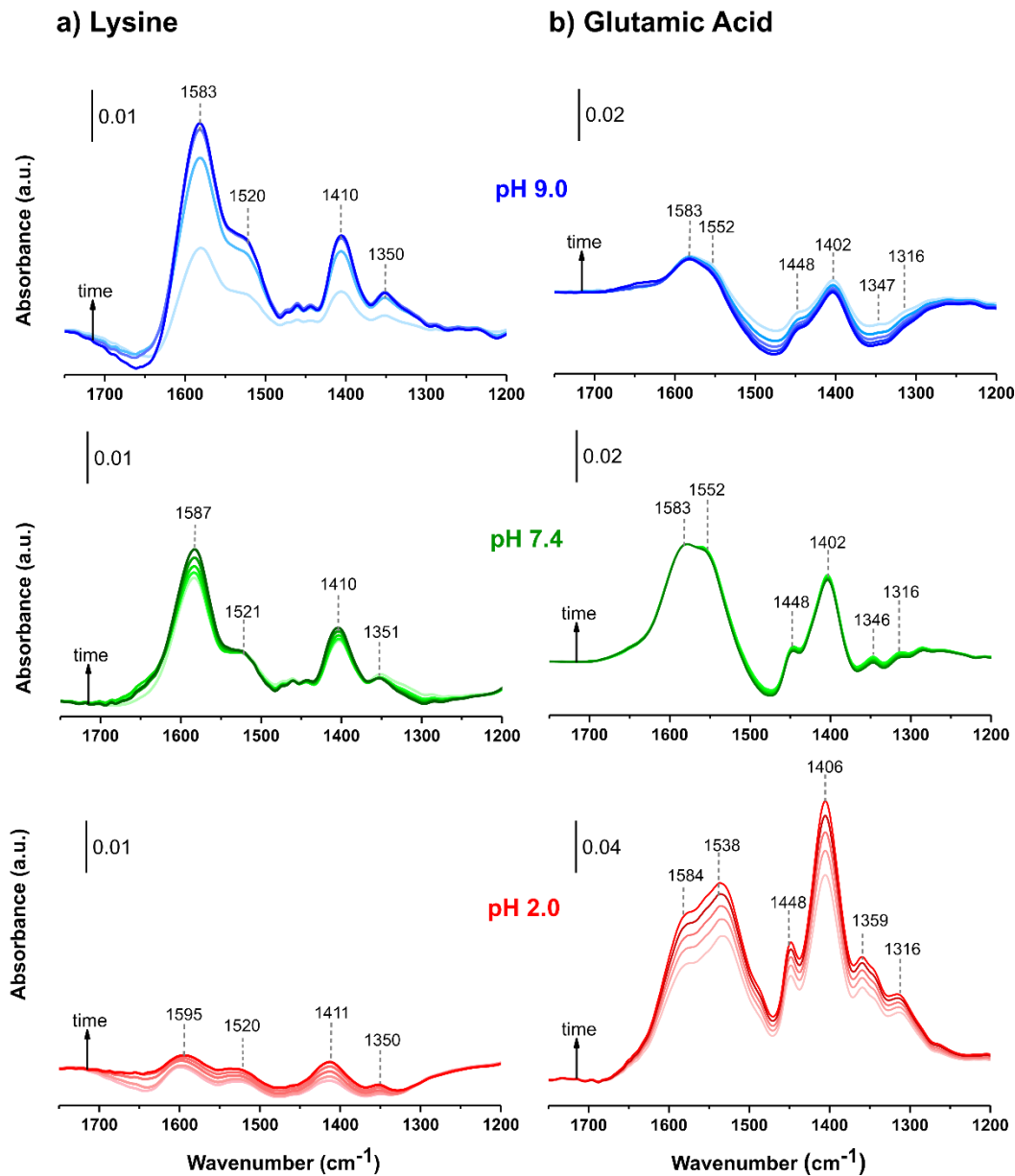
Figure 4.3: ATR−FTIR spectra of adsorbed (a) lysine and (b) glutamic acid onto α-Fe$_2$O$_3$ NPs at different pH values as a function of time. Spectra were collected for 20 min at 5 min intervals.

The difference in the peak intensities associated with glutamic acid's surface adsorption is notable (Fig. 4.3b). When pH increases from 2 to 9, electrostatic repulsion between the negatively charged nanoparticle surface and anionic species increases. This

causes a significant decrease in surface coverage, similar to what was observed for glutamic acid adsorption on TiO_2 nanoparticle surfaces.[13]

According to Fig 4.3b glutamic acid adsorbate spectra at pH 2, the $v(C=O)$ peak does not appear, indicating the weakening of the C=O bond due to interaction with the hematite surface.[16] The peak at 1538 cm^{-1} is for $v_{as}(COO^-)$ with a corresponding high-intensity $v_s(COO^-)$ peak at 1404 cm^{-1}, presumably associated with the distal-carboxylate.[13] The observed differentiation of carboxylate asymmetric stretches indicates glutamic acid interacts with the hematite surface with both of the α- and distal-carboxylates. At pH 2, glutamic acid solution spectrum has shown to have only one $v_{as}(COO^-)$ which tentatively comes from the α-carboxylate (see Table 4.4). Moreover, the solution-phase Δv_{as-s} value was 187 cm^{-1}, whereas, on the hematite surface this value was decreased to 178 cm^{-1} and a new Δv_{as-s} value was occurred for distal-carboxylate as 132 cm^{-1}. Therefore, it is proposed that both α- and distal-carboxylate possibly adsorb onto the surface in bidentate bridging.

At pH 7.4, electrostatic repulsion is possible through deprotonated carboxylate species to the negatively charged α-Fe_2O_3 nanoparticle surfaces, which can be seen by a decrease in the absorbance intensities compared to pH 2. A further decrease in the Δv_{as-s} value for α-carboxylate was observed ~15 cm^{-1} in comparison to solution phase. This can be explained as adsorbed α-carboxylate have higher symmetry in the structure.[13] Therefore, we suggest that at pH 7.4 glutamic acid adsorbs onto the hematite surface in bidentate bridging mode from α-carboxylate. Furthermore, the change in distal-carboxylate Δv_{as-s} value was minimal, indicating a single H-bonding. The least surface coverage of glutamic acid was observed at pH 9 due to gradually decreasing electrostatic attraction as pH

increases. Despite the electrostatic repulsion, some amount of glutamic adsorption onto hematite surfaces can be a result of double H-bonding configuration to the surface hydroxyl groups.

Overall, in comparison to lysine and glutamic acid adsorption onto TiO_2 nanoparticle surfaces, both amino acids have shown stronger amine group interaction on the α-Fe_2O_3. In most cases, Δv_{as-s} value was smaller for adsorbates on α-Fe_2O_3 indicating more symmetrical carboxylate coordination to the surface. Heterogeneity of the surface species was reduced as less variety in the Δv_{as-s} was observed onto Fe_2O_3 nanoparticles. Thus, it is shown here that nanoparticle type changes amino acid adsorption behavior and surface species.

4.4.4 Aspartic Acid and Arginine and Adsorption onto α-Fe_2O_3 Nanoparticles: Effects of Amino Acid Concentration

To determine the effects of amino acid concentration onto adsorption mechanisms and surface species, aspartic acid and arginine adsorption onto α-Fe_2O_3 nanoparticles was investigated. Fig. 4.4 shows the adsorbate spectra of 1 mM and 5 mM (a) aspartic acid and (b) arginine on α-Fe_2O_3 nanoparticles at pH 7.4 as a function of time. Solution peak assignments from Fig. 4.2 were used to determine the adsorbate vibrations in Fig. 4.4 as the adsorption plots shared similar peak values. However, the shape and wavenumber of infrared bands of adsorbate spectra varied between experiments when the adsorbate solution's concentration was changed. The emergence and disappearance of vibrational peaks were obscured by overlapped neighboring peaks or interpreted as peak shifts and used to indicate the changes in amino acid adsorption mechanisms.[29] By looking at the Fig

4.4, we can see the increase in the absorbance intensity when amino acid concentration increases from 1 mM to 5 mM. Aspartic acid surface coverage onto on α-Fe$_2$O$_3$ nanoparticles at pH 7.4 was higher than arginine.
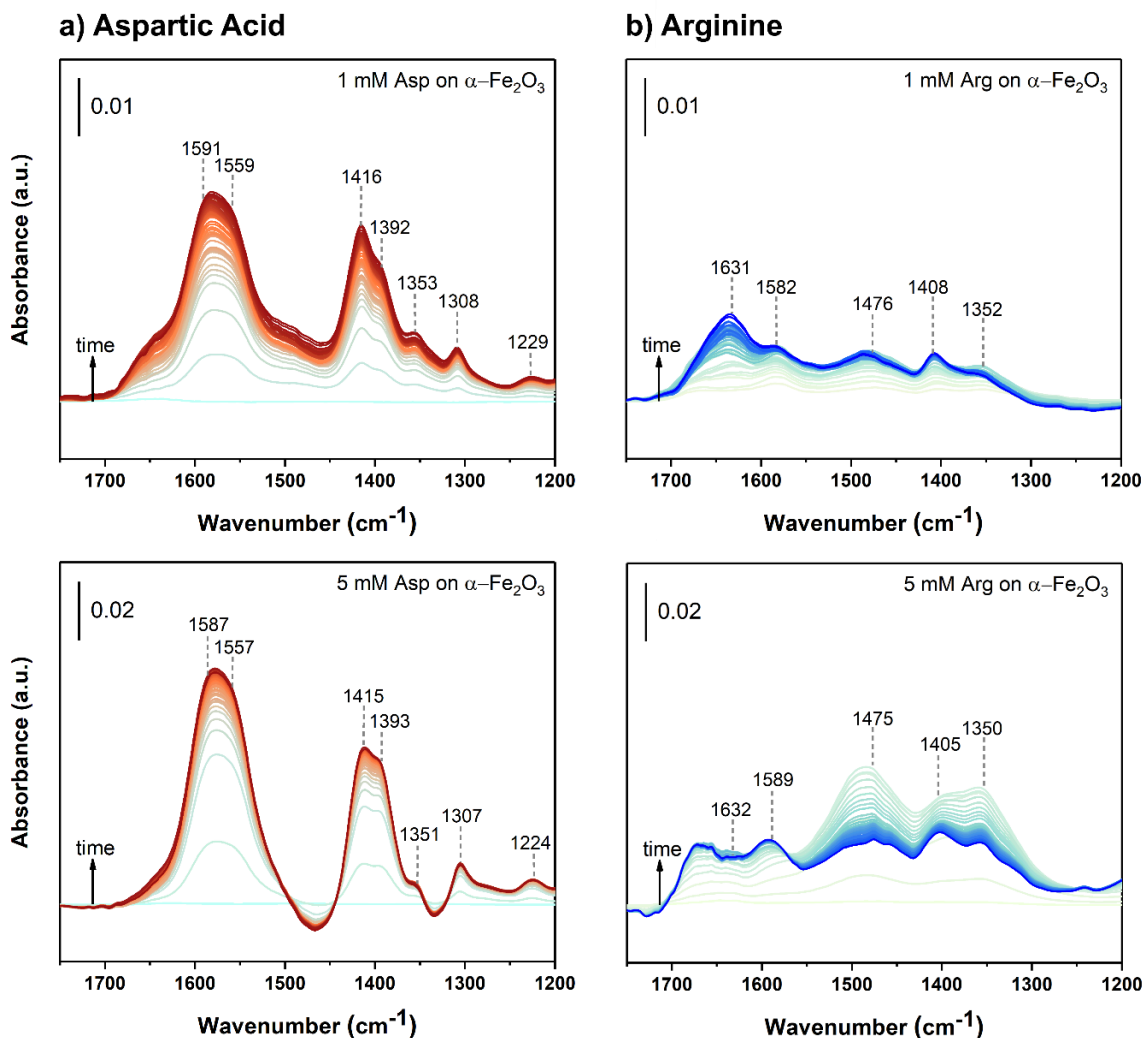
Figure 4.4: Adsorption spectra of 1 mM and 5 mM aspartic acid (a) and arginine (b) on α-Fe$_2$O$_3$ nanoparticles at pH 7.4 as a function of time. Darker color spectra indicate the data collection at a later time.

The spectrum of adsorbed aspartic acid (in Fig 4.4a) resembles that of solution spectrum at pH 7.4 with a change in the absorbance intensities of the v_s(COO$^-$) vibrations for distal- and α-carboxylate. For 1 mM aspartic acid adsorbate, the two carboxylate groups

are present spectra and the 1416 cm^{-1} and 1392 cm^{-1} peaks are assigned as $v_s(COO^-)$ for

α- and distal-carboxylate, respectively. The α-carboxylate $v_s(COO^-)$ at 1392 cm^{-1} has

higher absorbance intensity than the same vibration for distal-carboxylate, indicating the

carboxylate group interaction within the α-Fe$_2$O$_3$ preferably from the α-carboxylate.

Furthermore, the 1587 cm^{-1} and 1412 cm^{-1} peaks have the greatest change in absorbance

over time during both adsorption and desorption, compared to the other peaks. When the

concentration of aspartic acid increased, the peak values for $v_{as}(COO^-)$ and $v_s(COO^-)$

stretches did not change significantly indicating carboxylate binding modes to hematite

surface for aspartic acid remained same. However, the deprotonated amine group bending

modes diminished in intensity, could indicate an increase in H-bonding at higher

concentration. Δv_{as-s} value for α-carboxylate of aspartic acid reduced from 179 cm^{-1} to 172

cm^{-1} indicating a higher symmetry in the carboxylate structure. Outer-sphere complexes

are known to initiate energetically more favorable inner-sphere complexes on the surface.[13]

At pH 7.4 hematite surface is negatively charged. Higher surface coverage of aspartic acid

onto negatively charged surface explained as a result of outer-sphere complexes. As the

changes in Δv_{as-s} values were not as significant from the free species to adsorbate form

however total amino acid coverage is still higher, double H-bonding configurations from

distal-carboxylates are also possible on the α-Fe$_2$O$_3$ surface.

1 mM arginine adsorbate spectra at pH 7.4 shows a drastic decrease in the

$v_{as}(COO^-)$ peak intensity compared to solution phase, suggesting the interactions from

carboxylate group to α-Fe$_2$O$_3$ nanoparticle surfaces. Solution-phase Δv_{as-s} value for

Arginine was 186 cm^{-1}, this value lower to 174 cm^{-1} and 184 cm^{-1} for 1 mM and 5mM

adsorbate spectra, respectively. A decrease in $\Delta v_{\text{as-s}}$ value from free Arg^+ species is pointed to be a result of bidentate bridging configuration for lower concentration. However, when amino acid concentration increased H-Bonding is more favorable on the surface as the change in $\Delta v_{\text{as-s}}$ was less significant.

4.5   Conclusions

This study investigated the interactions between $\alpha\text{-Fe}_2\text{O}_3$ nanoparticles and the polar amino acids, lysine, glutamic acid, aspartic acid, and arginine. Comparing the pH-dependent adsorption of lysine and glutamic onto $\alpha\text{-Fe}_2\text{O}_3$ with an earlier study onto TiO_2 nanoparticles give us a better understanding of how nanoparticles, in general, interact with amino acids, and thus equips us to manage them as necessary for health and environmental protection. $\alpha\text{-Fe}_2\text{O}_3$ and TiO_2 nanoparticles are important metal oxides nanomaterials that are widely used in industry and consumer products. Their increased abundancy in the environment makes them easily accessible to come into contact with biological environments and ecosystems. This study shows that these two metal oxide nanoparticles could interact distinctively with the amino acids as a function of pH. Amino acid conformation differs on the two oxide surfaces compared to that of solution. Depending on the predominant speciation of amino acids and the surface charge of nanoparticles, adsorption involves a combination of carboxylate and amine group interactions. Lysine adsorption onto $\alpha\text{-Fe}_2\text{O}_3$ nanoparticles increased with increasing pH. In contrast, Glu adsorption decreased with increasing pH. Surface species were changing at different pH values. Furthermore, amino acid concentration was impacting the extend of adsorption. Aspartic acid showed higher surface coverage in comparison to arginine onto $\alpha\text{-Fe}_2\text{O}_3$

surface at pH 7.4. Moreover, a stronger H-bonding was occurred when aspartic acid concentration increased. The findings of this work help to determine the surface species and possible insights into more complex biomolecule (i.e., protein) adsorption mechanisms in aqueous environment. Overall, the results provide valuable insights into the mechanisms biomolecule-nanoparticle surface interactions on different metal oxide nanoparticles and illuminate a detailed understanding of their environmental and human exposure.

4.6   Acknowledgments

Chapter 4, in part, is currently being prepared for submission for publication of the material: Ustunol, I. B., Quirk, E.; Coward, E.; Grassian, V. H. Polar Amino Acid Interactions with α-Fe$_2$O$_3$ Nanoparticles: Effects of pH and Nanoparticle Type onto Adsorption. The dissertation author is the primary investigator and author of this material.

4.7   References

(1)   Pan, Z.; Li, W.; Fortner, J. D.; Giammar, D. E. Measurement and Surface Complexation Modeling of U(VI) Adsorption to Engineered Iron Oxide Nanoparticles. *Environ. Sci. Technol.* **2017**, *51* (16), 9219–9226. https://doi.org/10.1021/acs.est.7b01649.

(2)   Grabrucker, A. M.; Ruozi, B.; Belletti, D.; Pederzoli, F.; Forni, F.; Vandelli, M. A.; Tosi, G. Nanoparticle Transport across the Blood Brain Barrier. *Tissue Barriers* **2016**, *4* (1). https://doi.org/10.1080/21688370.2016.1153568.

(3)   Li, W.; Troyer, L. D.; Lee, S. S.; Wu, J.; Kim, C.; Lafferty, B. J.; Catalano, J. G.; Fortner, J. D. Engineering Nanoscale Iron Oxides for Uranyl Sorption and Separation: Optimization of Particle Core Size and Bilayer Surface Coatings. *ACS Appl. Mater. Interfaces* **2017**, *9* (15), 13163–13172. https://doi.org/10.1021/acsami.7b01042.

(4)   Antal, I.; Strbak, O.; Khmara, I.; Koneracka, M.; Kubovcikova, M.; Zavisova, V.; Kmetova, M.; Baranovicova, E.; Dobrota, D. MRI Relaxivity Changes of the Magnetic Nanoparticles Induced by Different Amino Acid Coatings. *Nanomaterials* **2020**, *10* (2). https://doi.org/10.3390/nano10020394.

(5)   Nosrati, H.; Salehiabar, M.; Bagheri, Z.; Rashidzadeh, H.; Davaran, S.; Danafar, H. Preparation, Characterization, and Evaluation of Amino Acid Modified Magnetic Nanoparticles: Drug Delivery and MRI Contrast Agent Applications. *Pharm. Dev. Technol.* **2018**, *23* (10), 1156–1167. https://doi.org/10.1080/10837450.2018.1536995.

(6)   Dutta, B.; Nema, A.; Shetake, N. G.; Gupta, J.; Barick, K. C.; Lawande, M. A.; Pandey, B. N.; Priyadarsini, I. K.; Hassan, P. A. Glutamic Acid-Coated Fe3O4 Nanoparticles for Tumor-Targeted Imaging and Therapeutics. *Mater. Sci. Eng. C* **2020**, *112*, 110915. https://doi.org/10.1016/j.msec.2020.110915.

(7)   Ali, A.; Zafar, H.; Zia, M.; ul Haq, I.; Phull, A. R.; Ali, J. S.; Hussain, A. Synthesis, Characterization, Applications, and Challenges of Iron Oxide Nanoparticles. *Nanotechnology, Science and Applications*. Dove Medical Press Ltd August 19, 2016, pp 49–67. https://doi.org/10.2147/NSA.S99986.

(8)   Fu, Q.; Cui, Z.; Xue, Y.; Zhu, J.; Guo, S. Size- and Shape-Dependence of the Thermodynamic Properties of Nanocrystals. *Mater. Chem. Phys.* **2017**, *202*, 177–183. https://doi.org/10.1016/j.matchemphys.2017.09.027.

(9)   Limo, M. J.; Sola-Rabada, A.; Boix, E.; Thota, V.; Westcott, Z. C.; Puddu, V.; Perry, C. C. Interactions between Metal Oxides and Biomolecules: From Fundamental Understanding to Applications. *Chemical Reviews*. 2018. https://doi.org/10.1021/acs.chemrev.7b00660.

(10)   Chandra Kanth, P.; Verma, S. K.; Gour, N. Functionalized Nanomaterials for Biomedical and Agriculture Industries. In *Handbook of Functionalized Nanomaterials for Industrial Applications*; 2020. https://doi.org/10.1016/b978-0-12-816787-8.00010-7.

(11)   Lin, T. Y.; Chen, D. H. One-Step Green Synthesis of Arginine-Capped Iron

Oxide/Reduced Graphene Oxide Nanocomposite and Its Use for Acid Dye Removal. *RSC Adv.* **2014**. https://doi.org/10.1039/c4ra03505d.

(12) Pušnik, K.; Peterlin, M.; Cigić, I. K.; Marolt, G.; Kogej, K.; Mertelj, A.; Gyergyek, S.; Makovec, D. Adsorption of Amino Acids, Aspartic Acid, and Lysine onto Iron-Oxide Nanoparticles. *J. Phys. Chem. C* **2016**, *120* (26), 14372–14381. https://doi.org/10.1021/acs.jpcc.6b03180.

(13) Ustunol, I. B.; Gonzalez-Pech, N. I.; Grassian, V. H. PH-Dependent Adsorption of α-Amino Acids, Lysine, Glutamic Acid, Serine and Glycine, on TiO2 Nanoparticle Surfaces. *J. Colloid Interface Sci.* **2019**. https://doi.org/10.1016/j.jcis.2019.06.086.

(14) Papina, J.; Godymchuk, A.; Kutukov, A.; Kuznetsov, D.; Baisalova, G. Amino Acids Adsorption in Differently Aged and Concentrated Aqueous Suspensions of ZnO and TiO 2 Nanoparticles. https://doi.org/10.1088/1742-6596/1145/1/012022.

(15) Godymchuk, A.; Papina, I.; Karepina, E.; Kuznetsov, D.; Lapin, I.; Svetlichnyi, V. Agglomeration of Iron Oxide Nanoparticles: PH Effect Is Stronger than Amino Acid Acidity. *J. Nanoparticle Res.* **2019**, *21* (10). https://doi.org/10.1007/s11051-019-4634-y.

(16) Mudunkotuwa, I. A.; Grassian, V. H. Histidine Adsorption on TiO2 Nanoparticles: An Integrated Spectroscopic, Thermodynamic, and Molecular-Based Approach toward Understanding Nano-Bio Interactions. *Langmuir* **2014**. https://doi.org/10.1021/la500722n.

(17) Theng, B. K. G.; Yuan, G. Nanoparticles in the Soil Environment. *Elements* **2008**. https://doi.org/10.2113/gselements.4.6.395.

(18) Barreto, M. S. C.; Elzinga, E. J.; Alleoni, L. R. F. The Molecular Insights into Protein Adsorption on Hematite Surface Disclosed by In-Situ ATR-FTIR/2D-COS Study. *Sci. Rep.* **2020**, *10* (1), 1–13. https://doi.org/10.1038/s41598-020-70201-z.

(19) Lalonde, K.; Mucci, A.; Ouellet, A.; Gélinas, Y. Iron Promotes the Preservation of Organic. No. 514.

(20) Johnston, C. P.; Chrysochoou, M. Mechanisms of Chromate Adsorption on Hematite. *Geochim. Cosmochim. Acta* **2014**, *138*, 146–157. https://doi.org/10.1016/j.gca.2014.04.030.

(21) Thurlkill, R. L.; Grimsley, G. R.; Scholtz, J. M.; Pace, C. N. PK Values of the Ionizable Groups of Proteins. *Protein Sci.* **2006**. https://doi.org/10.1110/ps.051840806.

(22) Pace, C. N.; Grimsley, G. R.; Scholtz, J. M. Protein Ionizable Groups: PK Values and Their Contribution to Protein Stability and Solubility. *Journal of Biological Chemistry*. 2009. https://doi.org/10.1074/jbc.R800080200.

(23)   Jastrzębska, A. M.; Kurtycz, P.; Olszyna, A.; Karwowska, E.; Miaškiewicz-Pęska, E.; Załęska-Radziwiłł, M.; Doskocz, N.; Basiak, D. The Impact of Zeta Potential and Physicochemical Properties of TiO2-Based Nanocomposites on Their Biological Activity. *Int. J. Appl. Ceram. Technol.* **2015**. https://doi.org/10.1111/ijac.12340.

(24)   Vieira Pinto, S. M.; Tasinato, N.; Barone, V.; Amadei, A.; Zanetti-Polzi, L.; Daidone, I. Modeling Amino-Acid Side Chain Infrared Spectra: The Case of Carboxylic Residues. *Phys. Chem. Chem. Phys.* **2020**. https://doi.org/10.1039/c9cp04774c.

(25)   Po, H. N.; Senozan, N. M. The Henderson-Hasselbalch Equation: Its History and Limitations. *J. Chem. Educ.* **2001**. https://doi.org/10.1021/ed078p1499.

(26)   Wolpert, M.; Hellwig, P. Infrared Spectra and Molar Absorption Coefficients of the 20 Alpha Amino Acids in Aqueous Solutions in the Spectral Range from 1800 to 500 Cm-1. *Spectrochim. Acta - Part A Mol. Biomol. Spectrosc.* **2006**, *64* (4), 987–1001. https://doi.org/10.1016/j.saa.2005.08.025.

(27)   Roddick-Lanzilotta, A. D.; McQuillan, A. J. An in Situ Infrared Spectroscopic Study of Glutamic Acid and of Aspartic Acid Adsorbed on TiO2: Implications for the Biocompatibility of Titanium. *J. Colloid Interface Sci.* **2000**. https://doi.org/10.1006/jcis.2000.6864.

(28)   Navarrete, J. T. L.; Hernández, V.; Ramírez, F. J. Ir and Raman Spectra of L-aspartic Acid and Isotopic Derivatives. *Biopolymers* **1994**. https://doi.org/10.1002/bip.360340810.

(29)   Sebben, D.; Pendleton, P. Infrared Spectrum Analysis of the Dissociated States of Simple Amino Acids. *Spectrochim. Acta - Part A Mol. Biomol. Spectrosc.* **2014**. https://doi.org/10.1016/j.saa.2014.05.026.

(30)   Barth, A. The Infrared Absorption of Amino Acid Side Chains. *Progress in Biophysics and Molecular Biology*. 2000. https://doi.org/10.1016/S0079-6107(00)00021-3.

(31)   Roddick-Lanzilotta, A. D.; McQuillan, A. J. An in Situ Infrared Spectroscopic Investigation of Lysine Peptide and Polylysine Adsorption to TiO2 from Aqueous Solutions. *J. Colloid Interface Sci.* **1999**. https://doi.org/10.1006/jcis.1999.6367.

(32)   Ojamäe, L.; Aulin, C.; Pedersen, H.; Käll, P. O. IR and Quantum-Chemical Studies of Carboxylic Acid and Glycine Adsorption on Rutile TiO2 Nanoparticles. *J. Colloid Interface Sci.* **2006**. https://doi.org/10.1016/j.jcis.2005.08.037.

(33)   Jayalath, S.; Wu, H.; Larsen, S. C.; Grassian, V. H. Surface Adsorption of Suwannee River Humic Acid on TiO2 Nanoparticles: A Study of PH and Particle Size. *Langmuir* **2018**. https://doi.org/10.1021/acs.langmuir.8b00300.

(34)   Nara, M.; Torii, H.; Tasumi, M. Correlation between the Vibrational Frequencies of the Carboxylate Group and the Types of Its Coordination to a Metal Ion: An Ab Initio Molecular Orbital Study. *J. Phys. Chem.* **1996**. https://doi.org/10.1021/jp9615924.

Chapter 5   Interaction of Proteins with Iron Oxide (α-Fe₂O₃) Nanoparticles in the Presence and Absence of Pre-Adsorbed Phosphate and Lipopolysaccharides

5.1   Abstract

Protein adsorption onto geochemical surfaces (mineral surfaces in complex aqueous environmental systems) is critical to the environmental fate and transport of biological compounds. However, adsorption kinetics, coverage, and conformation of biological macromolecules are poorly understood, particularly in the presence of ubiquitous oxyanions and endotoxins in environmental matrices. In this study, the adsorption of two proteins, beta-lactoglobulin (*β*-LG) and bovine serum albumin (BSA), onto hematite iron oxide (α-Fe₂O₃) nanoparticles was investigated in the presence and absence of phosphate. Immunoglobulin G (IgG) adsorption onto α-Fe₂O₃ was also investigated in the presence and absence of lipopolysaccharides (LPS). Using attenuated total reflectance-Fourier transform infrared (ATR-FTIR), our results show that phosphate occupied active sites and reduced protein surface coverage. Furthermore, the secondary structures of proteins when adsorbed onto α-Fe₂O₃ surfaces were substantially altered compared to their unbound conformations. When bound, *β*-LG conformation shifted to an increase in α-helix forms, whereas BSA transitioned from α-helix to β-sheet secondary structure upon adsorption. However, these differences were attenuated in the presence of adsorbed phosphate, slowing the kinetics of conformational changes during BSA and *β*-LG adsorption. The impact of pre-adsorbed phosphate on adsorption was, notably, protein-specific —*β*-LG exhibited a higher adsorption rate compared to BSA— and the former was partially reversible when phosphate was present. Pre-adsorbed LPS impacted IgG protein

secondary structure upon adsorption, and α-helix content of IgG was increased, and extended-chains content was reduced in the presence of LPS. Conformational changes could impact protein behavior, cycling, etc., as the protein domains are associated with different functions contributing to protein's overall role. Our results reveal the importance of phosphate on protein-mineral adsorption kinetics, conformation, and fate in complex aqueous systems.

5.2   Introduction

Nanoscale iron oxides, ubiquitous in terrestrial and marine soils and sediments,[1–4] are well-known sorbents of organic compounds and contaminants due to their high surface area and reactivity, thermodynamic stability, and subsequent adsorption capacity.[5–7] As such, iron oxide nanoparticles and their bio-inorganic hybrid forms are commonly used as a sorbent in coatings, cosmetics, catalysis, drug delivery, and environmental remediation applications.[8–10] Hematite (α-Fe_2O_3) is the most thermodynamically-stable iron oxide mineral, with surface terminations that have elevated free energies of formation and surface enthalpies promoting strong water adsorption and interaction with ions.[11,12] Despite this enhanced reactivity, adsorption dynamics and stability of many common molecules to α-Fe_2O_3, particularly in heterogeneous aqueous matrices, are not fully understood.

Proteins, an essential subset of biological macromolecules, play a vital role in environmental and biological processes.[13] Derived as byproducts of human activities and from secretion or lysis of microorganisms, roots, and fungi.[14,15] All proteins, including enzymes, bind to other molecules to perform their function and associate protein-mediated processes.[16] For instance, proteins attach to viruses or bacteria for destruction; the enzyme

115

hexokinase binds glucose and adenosine triphosphate (ATP) to catalyze their reaction.[15,16] Indeed, microbially-derived proteinaceous compounds are found to be abundant at mineral interfaces.[17,18] Most proteins have a high propensity for adsorption at solid-liquid interfaces due to their amphiphilic—both hydrophilic and hydrophobic—properties.[19] When proteins encounter nanoparticle interfaces in an aqueous environmental and biological *milieu*, proteins do not behave like rigid particles.[20] Instead, they can form a dynamic layer on nanoparticle surfaces once they are adsorbed.[21,22] In biological systems, this layer is termed the "*protein corona*"[23–25], whereas, in the environment, this layer is termed "*eco-corona*."[26] The formation of this corona can influence aggregation, reactivity, toxicity, and transformation of the minerals.[27] Moreover, adsorbed proteins can change their secondary conformation, mobility, and enzymatic activity.[28–31] Thus, amino acid and protein interactions at the aqueous-nanomaterial interfaces have been widely-investigated using various vibrational spectroscopic and computational methods.[32–36]

Previous studies of protein adsorption onto metal oxide nanoparticles, polymers, and other clay surfaces have demonstrated how perturbations in pH, temperature, protein concentration, and nanomaterial surface chemistry can significantly influence the adsorption kinetics, adsorbed protein assembly, and protein secondary structure.[19,33,37–40] Different structural units in a protein (i.e., α-helix, *β*-sheet) form the protein domains associated with different functions contributing to protein's overall role.[41] For instance, a recent study probed the kinetics and mechanisms of bovine serum albumin (BSA) adsorption onto hematite particles using two-dimensional correlation spectroscopy (2DCOS) of the attenuated total reflectance-Fourier transform infrared (ATR-FTIR) spectra.[28] The results revealed that an increase in the α-helix structure was observed during

the initial surface coverage of BSA. In contrast, α-helical structural loss happens at the later stage of the adsorption process. BSA adsorption on montmorillonite was also analyzed as a function of concentration.[33] At higher concentrations and surface coverage, BSA unfolding was found to be less pronounced, and a more compact, aggregated protein structure was present. Furthermore, a study of beta-lactoglobulin (β-LG) and BSA adsorption onto hydrophobic surfaces –combined with molecular dynamics (MD) simulations, quartz crystal microbalance (QCM), and atomic force microscopy (AFM)– suggested that proteins formed a rigid monolayer on the solid surfaces.[42] The isoelectric point (pH$_{IEP}$) of the protein-coated surface was similar to the pH$_{IEP}$ of the protein in solution at high surface coverage.[42] Upon adsorption of β-LG onto montmorillonite at acidic pH, modification of the interlayer space and a partial exfoliation of the clay mineral were also observed in addition to structural conformational changes of the protein.[37]
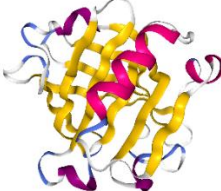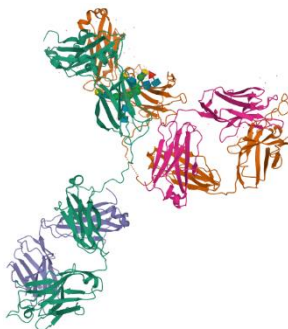
While our understanding of nanoparticle behavior and protein interactions has advanced in model systems, the experimental design often does not account for aqueous systems' natural complexity. Environmental and biological aqueous systems consist of naturally-occurring assemblies of salts, nutrients, oxyanions, endotoxins, and heterogeneous organic compounds with varying molecular weights, which may compete with, co-adsorb, or aggregate with proteins in solution.[24] As such, the adsorption of a biomolecule on the nanoparticle surface depends on adsorption affinity, diffusion kinetics, and solution chemistry as compounds dynamically compete, co-adsorb, and scaffold on the nanoparticle surface driven by their nano-size and large surface-to-mass ratio.[43–47]

Phosphate, a highly-abundant nutrient in aqueous soil and groundwater systems,[48] can impact protein surface adsorption.[30] Inorganic and organic phosphate compounds

117

accumulate in environmental systems, catalyzing harmful algal growth (eutrophication) and the proliferation of aquatic plants, and have been identified as pollutants of concern in groundwater.[49,50] Phosphate provides a pH-stable environment[51] and can itself adsorb onto nanoparticles,[52] occupying active sites on the surfaces.[53]

Bacterial lipopolysaccharides (LPS), large molecules of endotoxins, are present on the outer membrane of gram-negative bacteria and one of the most abundant bioactive molecules present in the environment and several body compartments. The human body limits the entrance of LPS through mucosal penetration; however, low-level LPS can be found in the plasma[54], and their content could increase in certain conditions.[55] LPS contains a lipid and a polysaccharide composed of O-antigen, its outer and inner core are joined by a covalent bond and works as a pathogen-associated molecular pattern.[56] It can activate macrophages and promote pro-inflammatory protein production.[56] Recently, studies on cell-based immunological tests were stated that LPS adsorbed nanoparticles could interfere with test results,[57] because LPS contamination could be overlooked or their adsorption could modulate the effects of LPS on immune cells. In fact, LPS adsorbed bio-corona of TiO_2 nanoparticles were found to activate selected pro-inflammatory transduction pathways.[56] Despite the ubiquitous presence of phosphate and LPS in environmental systems, the dynamics of protein adsorption onto iron oxide surfaces in the presence of these molecules are not well understood. Proteins adsorption onto nanoparticles in phosphate or LPS containing complex systems could alter protein conformational changes which would further impact protein binding capabilities and functions contributing to the overall role of a protein.

Table 5.1: Protein properties and crystal structures of BSA, β-LG, and IgG. Protein Data Base numbers of protein models are 4F5S, 1BEB, and 1HZH, respectively.[37,58]

	Bovine Serum Albumin (BSA)	β-Lactoglobulin (β-LG)	Immunoglobulin G (IgG)
Crystal Structure			
Number of Amino Acids	582	162	1331
Isoelectric Point (pH$_{IEP}$)	4.9	5.1	6.6
Molecular Mass (kDa)	68	18.4	151.6

To probe protein sorption under environmentally and biologically relevant conditions, β-LG and BSA were adsorbed to α-Fe$_2$O$_3$ nanoparticles in the presence and absence of phosphate at pH 6. These model proteins represent endmembers of protein size, flexibility, and native conformation.[59] β-LG is a small (162 amino acids), rigid protein and is considered to be a model for a 'hard' protein that does not experience significant structural alterations after adsorption onto surfaces (Table 5.1).[42] β-LG is a globular protein with a predominantly β-sheet structure[59] and one of the major allergens in cow's milk.[60] Thus, studies involving the denaturing conditions (pH and temperature) of β-LG have been investigated because of their relevance to food and dairy processing.[61] Additionally, the heat-induced aggregation of β-LG is also used as a model for fibril formation of neurodegenerative disease.[62] In comparison, BSA has a larger size (582 amino acids) and

is considered to be a 'soft' protein model, as it undergoes a conformational change upon surface adsorption.[30,39] It also differs from β-LG in that BSA mainly consists of α-helix in aqueous media in its crystal structure.[30,63] BSA is also used as a model protein in many studies due to its high abundance, low cost, and similarity to human serum albumin (HSA).[30] By comparing the adsorptive behavior of these two model proteins, we can begin to understand the structural and kinetics effects of phosphate pre-adsorption on protein surface interactions in aqueous systems. Furthermore, IgG was adsorbed to α-Fe_2O_3 nanoparticles in the presence and absence of LPS at pH 7.4. IgG is a relatively large protein with a molecular weight of about 153 kDa and made of four peptide chains. Its secondary structure largely consists of β-sheet structures whereas the α-helix content is relatively small.[64,65] By comparing the adsorptive behavior of these model proteins, we can begin to understand the structural and kinetics effects of phosphate and LPS pre-adsorption on protein surface interactions in aqueous systems.

To characterize aqueous-phase protein surface adsorption, ATR-FTIR spectroscopy was used. The information from these *in situ* analyses is intended to provide an understanding of real-time biomolecule-surface interactions in a multi-component environment. Solution-phase secondary structural analysis of these proteins in the Amide I region was compared to that of adsorbed proteins by deconvolution analysis to understand the conformational changes upon adsorption. Both Amide I (1600-1700 cm^{-1}) and Amide II (1500-1600 cm^{-1}) regions of the ATR-FTIR spectra are further analyzed to identify phosphate and LPS effects on the adsorption and desorption experiment kinetics of the proteins. This study provides a framework and conceptualization of fundamental mechanisms involved in protein adsorption/desorption in a multi-component, more

complex aqueous environment. It offers essential information on how interactions at the nano-geo-bio interface can change the conformation of biological molecules.

5.3 Materials and Experimental Methods

5.3.1 Materials

α-Fe_2O_3 nanoparticles were purchased from Alfa Aesar, MA. The lyophilized forms of β-LG ($\geq$90%), BSA ($\geq$99.5%), IgG ($\geq$99.5%), and LPS from *E.Coli* O111:B4 were purchased from Sigma-Aldrich. Characteristics of the proteins used in this study and their crystal structures are shown in Table 5.1. The phosphate buffer solution of 250 µM $Na_2HPO_4.H_2O$ (Fisher Scientific, Inc.) and 0.04 g L^{-1} LPS solutions were used for adsorption studies. The experiments to determine phosphate's effect were performed at pH 6, whereas the LPS study was conducted at pH 7.4. Solution pH values were adjusted by using hydrochloric acid (HCl), and sodium hydroxide (NaOH) solutions from Fisher Scientific, Inc. Solutions were prepared with Milli-Q water (Millipore, resistance = 18.2 MΩ.cm at 25 °C) and NaCl (Fisher Scientific, Inc.) was used to maintain 10 mM ionic strength through the experiments. All chemicals were used as received without further purification.

5.3.2 Nanoparticle Characterization

The size and morphology of the α-Fe_2O_3 nanoparticles were determined by a JEOL JEM-1400 Plus transmission electron microscopy (TEM) at 80 kV. For TEM imaging, a 10 µL droplet from a sonicated α-Fe_2O_3 nanoparticle suspension was deposited on a formvar/carbon-coated 100-mesh copper grid (Electron Microscopy Sciences) and kept inside a dry air chamber until it is completely dried. A high-resolution transmission

electron microscopy (HRTEM) instrument (JEOL-2800) was used to determine the exposed facet at 200 kV. The crystalline phase of nanoparticles was determined using an APEX II Ultra diffractometer equipped with a CCD-based area detector, using MoK_{α} radiation at $\lambda = 0.71073$ Å. 2D images from the APEX II detector were processed using DiffractEva software (Bruker). A Quantachrome Nova 4200e analyzer was used for surface area and pore size measurements from Brunauer-Emmett-Teller (BET) N_2 adsorption. Before analysis, samples were degassed for 8 hours at 120 ºC and the data were analyzed using a 15 multipoint isotherm with partial pressures (P/P_o) of 0.05-0.95.

5.3.3 ATR-FTIR Spectroscopy

ATR-FTIR spectra were collected using a horizontal 45º beveled faces amorphous material transmitting infrared radiation (AMTIR) crystal (PIKE Technologies) in a Thermo–Nicolet iS10 FTIR spectrometer equipped with a mercury cadmium telluride (MCT-A) detector. The MCT-A has a narrow band with a 650 cm^{-1} cutoff and offers high mid-IR sensitivity and more significant IR response for small amounts of energy reaching the detector. All spectra were recorded in 2-minute intervals at 4 cm^{-1} resolution, and an average of 128 scans was collected over a spectral range of 750-4000 cm^{-1}.

The primary solvent for all the solutions was 10 mM NaCl in Milli-Q water. Protein solutions were made immediately before analysis to maintain the desired pH throughout the experiment. Two phosphate solutions of 25 mM and 250 µM were prepared for solution-phase analysis and adsorption studies, respectively. Solution-phase spectra of the proteins were compared to those of protein adsorbates to observe any spectral changes that occurred upon adsorption onto α-Fe_2O_3. To obtain solution-phase protein spectra, native

BSA and β-LG were dissolved in the solvent to 5 mg mL^{-1} concentration. Native IgG was dissolved in the solvent to 0.2 mg mL^{-1}, and the same concentration of IgG was used for both solution-phase analysis and adsorption studies.

A high concentration of protein solution is needed to obtain a quality spectrum due to the low affinity of the protein for the ATR crystal surface. However, above the concentration of 5 mg mL^{-1}, gel-like solutions of β-LG were observed. Thus, this concentration was selected for the solution phase analysis for BSA and β-LG proteins. Aqueous protein spectra were collected using ATR-FTIR flow-cell crystal without an α-Fe$_2$O$_3$ coating. After collecting protein solution spectra, a background spectrum of each solvent was subtracted from the sample spectrum. To reduce the interference of water bands in the IR region at ~1640 cm^{-1} (H–O–H bending), which overlaps with the Amide I mode of the proteins (1600-1700 cm^{-1}), an atmospheric suppression correction was performed in the OMNIC 9 software (ThermoFisher).
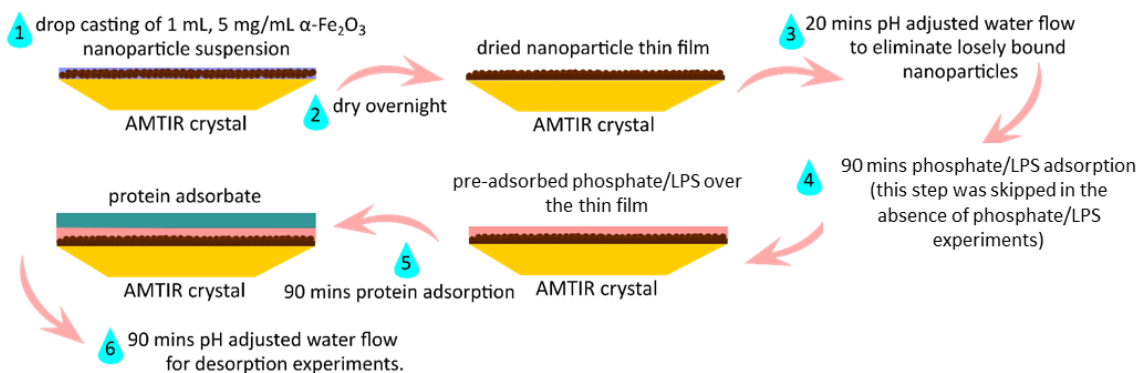
Scheme 5.1: The detailed schematic of the ATR-FTIR protein adsorption and desorption experimental steps in the study.

123

The methodology for surface adsorption and desorption reactions are detailed in Scheme 5.1. Briefly, experiments followed these steps: (1) α-Fe$_2$O$_3$ nanoparticles were drop cast on the AMTIR crystal by depositing 1 mL of 5 mg mL^{-1} nanoparticle suspension, and (2) dried overnight in a dry air chamber. After nanoparticle film preparation, (3) pH-adjusted Milli-Q water flowed at 0.5 ml min^{-1} over the thin film for 20 min to remove any loosely bound nanoparticles, to adjust nanoparticle surface charge, and to allow for background spectrum collection. Next, (4) phosphate buffer (or LPS solution) was introduced to the system for 90 min to create phosphate- or LPS-coated nanoparticles before protein flow. This step was omitted in the absence of phosphate/LPS experiments. (5) For BSA and β-LG, a 1 mg mL^{-1}; for IgG, a 0.2 mg mL^{-1} protein solution was flowed over the nanoparticle film surface for 90 min to induce adsorption. Following protein adsorption, (6) the protein-coated surface was again washed with the primary solvent for 90 min. The pH of the protein solutions was measured before and after the experiment to ensure stability throughout the adsorption experiments. Phosphate adsorption was confirmed by observing saturated adsorbed phosphate at ~90 min which was determined by plotting absorbance peak intensity for the adsorbed phosphate band (at 1040 cm^{-1}) during adsorption onto α-Fe$_2$O$_3$ (Fig. 5.4).

5.3.4   Computational Analysis of the ATR-FTIR Data

For quantitative analyses of absorbed protein secondary structures, ATR-FTIR solution conformation results were compared to those of the adsorbates over time. Selected spectra at 4 and 90 min of adsorption were isolated to compare protein secondary structure at low and high surface coverage. In the presence of pre-adsorbed phosphate, the additional

adsorption spectra at 46 min were also analyzed at the adsorption half-time to observe time-dependent conformational changes better. Before curve fitting, the Amide I band range (1600-1700 cm^{-1}) was extracted from each original time-dependent spectral series (Fig. 5.1). This range was baseline corrected to a linear-line, and the Amide 1 band range was normalized with the highest peak intensity to ensure that observed bands were due to protein adsorption rather than water. The second derivatives of the spectra were processed using Origin 2017 Suite (OriginLab Corporation, Northampton, Massachusetts, USA) to better observe all vibrational peaks. The local minimum values from the second derivatives of the ATR-FTIR spectra were used to identify each secondary component's band position and used for assignments. Curve fitting iterations to a Gaussian shape at the band positions were then performed to achieve the best composite results. Protein solution-phase secondary structural results and previous literature values[30,39,60] were used as a preliminary standard to fit the adsorbed protein spectra.
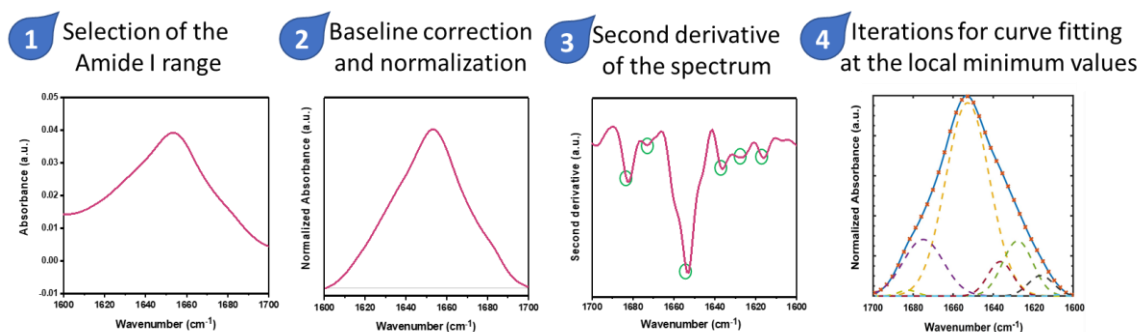
Figure 5.1: Process of curve fitting data analysis: (1) The Amide I band range from the raw data of protein adsorption experiment was extracted at a selected reaction time. (2) This range was baseline corrected to a linear-line and normalized the Amide 1 band range with the highest peak intensity. (3) The second derivatives of the spectra were processed, and the local minimum values were used to identify the band position of each secondary component. (4) The Amide I band was deconvolution into Gaussian curves were then performed to achieve the best composite results.

5.4 Results and Discussion

5.4.1 Nanoparticle Characterization

Fig. 5.2 shows the detailed physical characterization of iron oxide nanoparticles. XRD pattern in Fig. 5.2a identified that sampled nanoparticles were entirely hematite, with a specific surface area of 89 m^2 g^{-1} and average pore size of 0.247 cm^3 g^{-1} from Density Functional Theory (DFT) method calculations. TEM and HRTEM images of α-Fe_2O_3 nanoparticles (Fig. 5.2b-c) indicated that the particles had a high aggregation tendency and were approximately 5-20 nm in diameter, with the most exposed facet being the (104) surface plane.
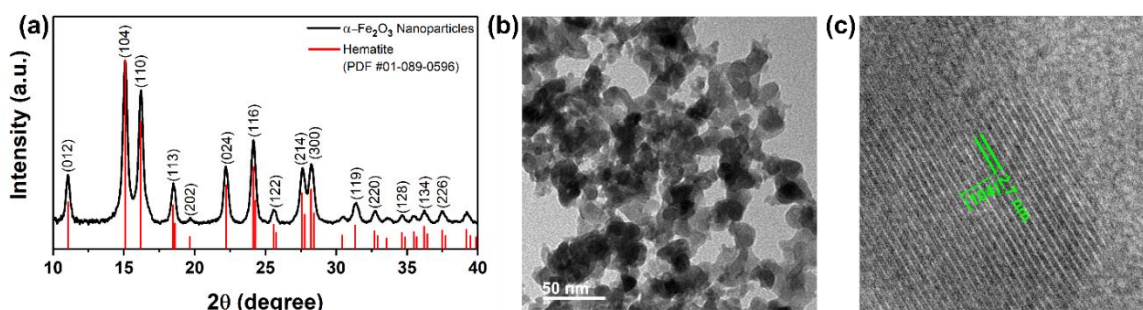
Figure 5.2:   Characterization of α-Fe_2O_3 nanoparticles. (a) XRD pattern indicates that particles are hematite; (b) TEM and (c) HRTEM images of the nanoparticles with exposed (104) facets.

5.4.2 ATR-FTIR Spectroscopy of Phosphate and LPS in Solution and Adsorbed on α-Fe_2O_3

Unbound and mineral-adsorbed phosphate were both examined via ATR-FTIR spectroscopy to determine vibrational frequency changes of phosphate and show the surface coverage before protein adsorption. The protonation state of phosphate can be seen in Fig. 3a. At pH 6, the molar fraction of phosphate is comprised of 0.94 $H_2PO_4^-$ and 0.06 HPO_4^{2-} species (Fig. 5.3b). The vibrations of these aqueous phosphate species can be seen

126

in the IR spectra in Fig. 5.3c. There are two primary phosphate vibrations identified: nondegenerate symmetric stretching (v_1) and triply degenerate symmetric stretching (v_3).[66,67] Due to asymmetry in the tetrahedral structure of $H_2PO_4^-$ species, the bands at 990 cm^{-1} and 1155 cm^{-1} appear from the split degenerate symmetric stretching (v_3). The band at 940 cm^{-1} indicates coexisting HPO_4^{2-} species, and the v_1 band is active at 878 cm^{-1}. The broad shoulder at ~1220 cm^{-1} represents bending mode [$\delta(POH)$] and is derived from $H_2PO_4^-$ species.[66,67]
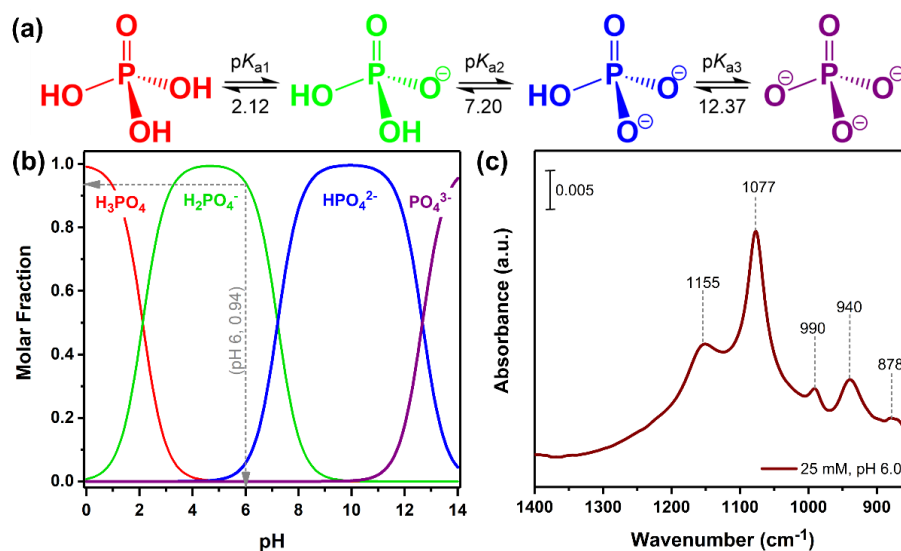
Figure 5.3: (a) Phosphate acid-base reaction equilibria where pKa1= 2.12, pKa2= 7.20, and pKa3= 12.37; (b) phosphate speciation diagram calculated using Henderson-Hasselbalch equation66 shows that 0.94 molar fraction of phosphate speciation at pH 6 is H2PO4-. (c) IR spectrum of aqueous phase phosphate (25 mM) in 10 mM NaCl solution at pH 6.

Adsorption and desorption spectra of phosphate were characterized as a function of interaction time (Fig. 5.4). Phosphate adsorption onto α-Fe$_2$O$_3$ surfaces is shown in Fig. 5.4a. The bands observed ~1098 cm^{-1} and 1040 cm^{-1} comprise sets of doublets derived from the phosphate ion's P-O stretching vibration.[69] The adsorption band region in Fig. 5.4a is notably broader, suggesting multiple adsorption bonding modes are co-occurring.

Notably, a large amount of phosphate irreversibly binds to the α-Fe$_2$O$_3$ surface, as the peak absorbance intensities do not return to baseline when desorbed with water at pH 6 (Fig. 5.4b). Normalized absorbance peak intensities of the adsorbed phosphate (band at 1040 cm^{-1}) during adsorption onto α-Fe$_2$O$_3$ (0-90 min) and desorption experiments (90-180 min) suggests that adsorbed phosphate is saturated on the α-Fe$_2$O$_3$ surface at ~90 min (Fig. 5.4c). This component of adsorbed phosphate may bond via inner-sphere complexation directly at the solid-solution interface.[66,70,71] Therefore, these data suggest that phosphate is forming a mixture of surface species and bonding modes, as is evidenced by multiple overlapping peaks in the phosphate region of the ATR-FTIR spectrum.[70,72] LPS adsorption was confirmed by observing adsorbate spectrum at ~60 min. Adsorbate spectra reveals similarities to its native protein structure based on the existing literature,[73] and 0.2 g L^{-1} LPS adsorbate spectra can be seen in Fig. 5.5. The peaks at 1642 cm^{-1} and 1544 cm^{-1} were assigned as Amide I and Amide II, respectively.
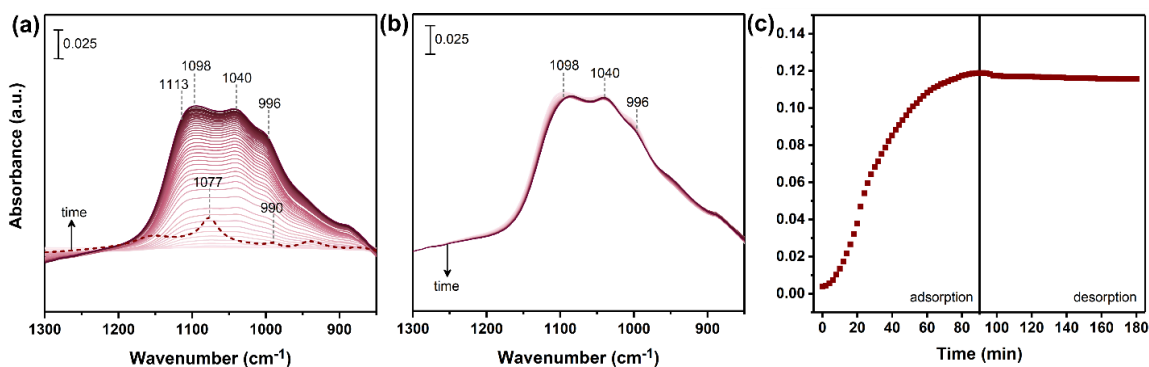
Figure 5.4: ATR-FTIR spectra of (a) 250 μM phosphate adsorption on α-Fe$_2$O$_3$ as function of time at pH 6; (b) Phosphate desorption from α-Fe$_2$O$_3$ with 10 mM NaCl as a f(time) at pH 6; (c) Normalized absorbance peak intensity for the adsorbed phosphate band (at 1040 cm^{-1}) during adsorption onto α-Fe$_2$O$_3$ (time 0-90 min) and desorption experiments (time 90-180 min) plotted as a f(time). The dashed line represents the spectrum of aqueous phase phosphate (25 mM) in 10 mM NaCl solution at pH 6. When phosphate desorbed, there no change to the adsorbed spectra corresponding to the irreversibility of phosphate surface adsorption.
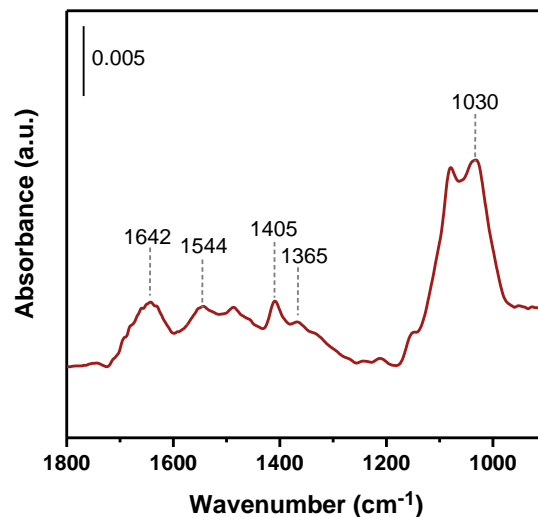
Figure 5.5: ATR-FTIR spectra of 0.2 g L^{-1} LPS adsorbate on α-Fe$_2$O$_3$ at pH 7.4 at 90 mins.

5.4.3 ATR-FTIR Spectroscopy of Proteins in Solution

ATR-FTIR spectra of BSA and β-LG solutions at pH 6 are shown in Fig. 5.6. Peak assignments from these solution-phase spectra were compared to adsorbed-phase spectra within the Amide I and II regions. The Amide I bands were centered at 1633 cm^{-1} and 1653 cm^{-1} for β-LG and BSA, respectively.[39,59] The Amide I band predominantly contains symmetric stretching of C=O, with contributions from out-of-phase C−N bending and in-plane N-H bending.[30,74] Amide II bands of the proteins were located at 1548 cm^{-1} and 1545 cm^{-1} for β-LG and BSA, respectively.[40,59,60,75] The Amide II and Amide III (1200-1350 cm^{-1}) regions consist of out-of-phase C−N stretching mode and out-of-phase in-plane N-H bending from the peptide backbone of the proteins.[74,76] The peaks observed at 1452 cm^{-1} and 1455 cm^{-1} were assigned to CH$_2$ scissoring, and 1400 cm^{-1} is derived from C−O carboxylate stretching. The peaks ranged ~1050 cm^{-1} for β-LG correspond to C−C and C−OH groups.[76,77] ATR-FTIR spectra of 0.2 g L^{-1} IgG in 10 mM NaCl solution at pH 7.4 can be seen in Fig 5.7. The peak at 1639 cm^{-1} is for the Amide I band; the 1549 cm^{-1} peak

is for the Amide II band of the protein. The peak at 1454 cm^{-1} is assigned to the CH$_2$ scissoring, and 1398 cm^{-1} is from C−O carboxylate stretching. These peak assignments were further used to compare the solution phase with the adsorbed phase spectra for the Amide I and II regions.
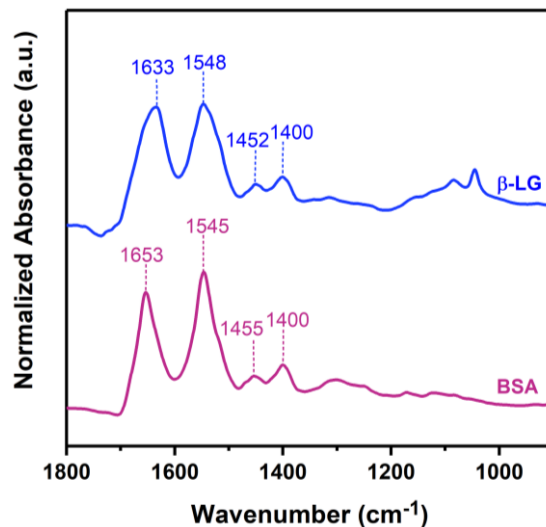
Figure 5.6: Normalized ATR-FTIR spectra of 5 mg mL^{-1} BSA and β-LG in 10 mM NaCl solution at pH 6. Spectra normalized by the Amide I band relative intensities. The peaks at 1633 cm^{-1} and 1653 cm^{-1} are for the Amide I bands; 1548 cm^{-1} and 1545 cm^{-1} peaks are for the Amide II bands of the proteins. The peaks at 1452 cm^{-1} and 1455 cm^{-1} are assigned to the CH$_2$ scissoring, and 1400 cm^{-1} is from C−O carboxylate stretching. These peak assignments were further used to compare the solution phase with the adsorbed phase spectra for the Amide I and II regions.
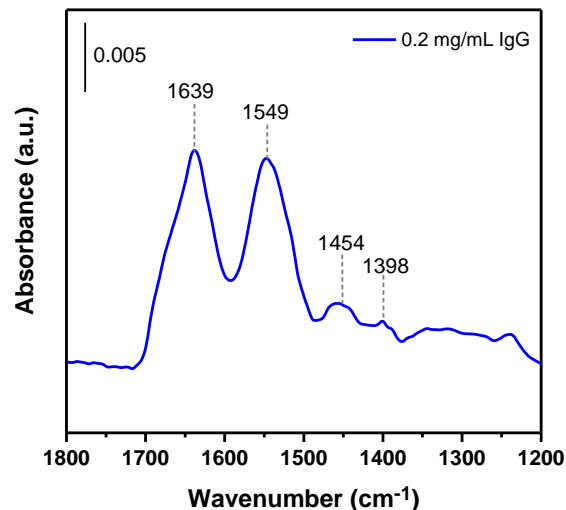
Figure 5.7: ATR-FTIR spectra of 0.2 g L^{-1} IgG in 10 mM NaCl solution at pH 7.4.

5.4.4 Effect of Phosphate and LPS on ATR-FTIR Spectroscopy of Proteins Adsorbed onto α-Fe$_2$O$_3$

ATR-FTIR is a powerful *in-situ* characterization method to monitor protein secondary conformational changes upon adsorption on nanoparticle surfaces.[78] Upon adsorption onto the nanoparticle surface, proteins form a well-organized layer that dictates the identity of the bio-nano complex.[79] These changes are essential for protein biological activity as they could create new binding sites on the protein structure, which determine the protein interactions with other ligands, change protein structure, and impact protein aggregation.[58,80,81] Furthermore, phosphate at mineral surfaces in complex aqueous environmental systems could potentially influence protein-nanoparticle interactions. Thus, to understand the impact of phosphate on protein adsorption, IR spectra were recorded with and without the presence of pre-adsorbed phosphate. To identify specific surface interactions causing frequency shifts and band shape differences, solution-phase spectral results (Fig. 5.6) were compared to those of adsorbed species (Fig. 5.8).

131

ATR-FTIR spectra of protein adsorption onto α-Fe$_2$O$_3$ over time (color scale) in the presence and absence of phosphate are shown in Fig. 5.8. The total surface coverage of the proteins decreased when phosphate was pre-adsorbed to the particle surface. This phenomenon was observed in the decreased intensity of the Amide I and Amide II peaks for proteins when phosphate is present, suggesting that phosphate competes with proteins for available nanoparticle surface area.
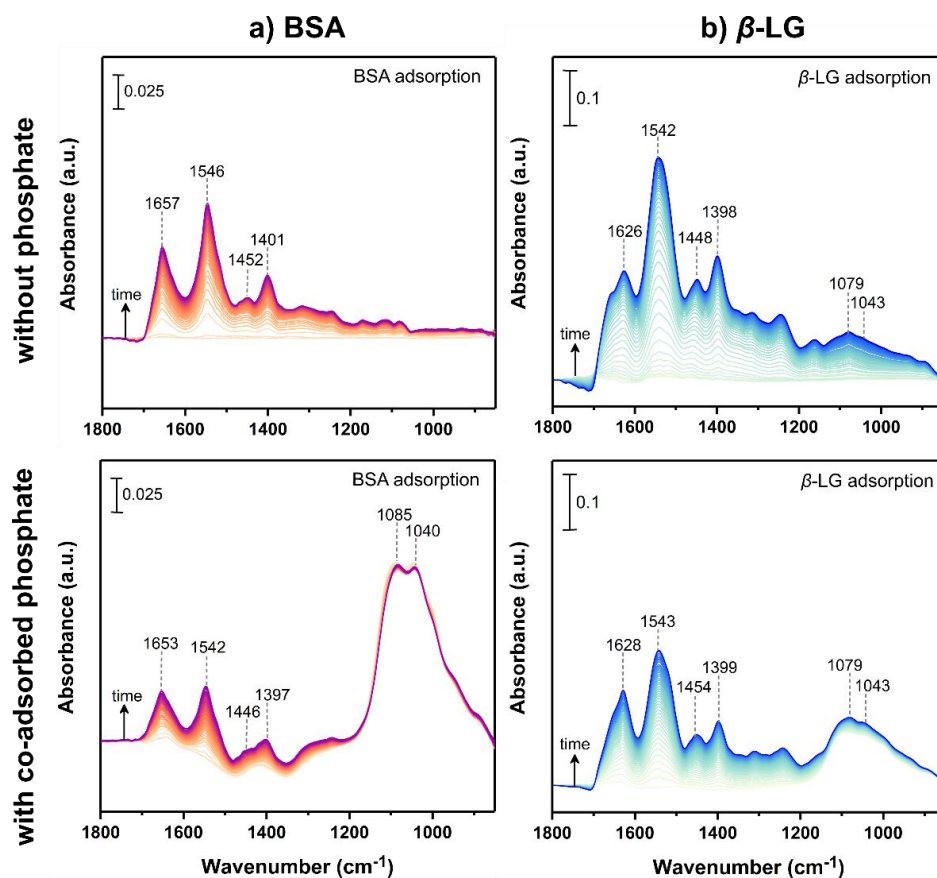
Figure 5.8: ATR-FTIR spectra of 1 mg/mL (a) BSA and (b) β-LG adsorption experiments on α-Fe$_2$O$_3$ without phosphate (top) and with pre-adsorbed phosphate (bottom) as a f(time) at pH 6. In the presence of phosphate, a fewer amount of protein is adsorbed on the nanoparticle surface. By comparing the solution phase with adsorbed phase spectra, shifts in the Amide I band of the spectra indicating the secondary structural changes of the proteins upon adsorption. The increase in the phosphate region ~1000 cm-1 stems from the β-LG solution contribution.

Compared to solution-phase spectra, peak shifting upon adsorption implicates inner-sphere complexation, secondary structural changes, and hydrogen bonding between the protein and nanoparticle surface.[75] Upon adsorption onto the nanoparticle surface, proteins underwent secondary structural changes, which can be observed by notable peak shifts for both BSA and β-LG Amide I and Amide II bands. The vibrational frequency assignments for these bands are shown in Table 5.2. During BSA adsorption onto the nanoparticle surface, frequency shifts in the peak location were minimal, indicating small protein structure changes.[76] Critically, the presence of pre-adsorbed phosphate affected β-LG adsorption onto the α-Fe_2O_3 surface, as suggested by smaller shifts in Amide I peaks from its position of solution-phase upon adsorption. The solution phase Amide I peak was at 1633 cm^{-1} for β-LG. This band showed a blue-shift upon adsorption to nanoparticle surfaces and was observed at 1626 cm^{-1} in the absence of phosphate. Shifts to lower wavenumbers in the Amide I band are indicative of increasing hydrogen bonds.[74] However, when there was pre-adsorbed phosphate on the nanoparticle surface, the observed decrease in band position was dampened. This observation suggests that pre-adsorbed phosphate may reduce the extent of protein secondary structural changes and prevent protein denaturation on the α-Fe_2O_3 surface. A similar result was previously observed during BSA adsorption onto TiO_2 surface under acidic conditions.[30]

Table 5.2: Vibrational frequencies for protein Amide I and Amide II peaks for the solution and adsorbed phase.

	Vibrational Frequency (cm^{-1})					
	BSA			β-LG		
	Solution Phase	Adsorbed on α-Fe$_2$O$_3$ (Δ)*	Adsorbed on phosphate-coated α-Fe$_2$O$_3$ (Δ)*	Solution Phase	Adsorbed on α-Fe$_2$O$_3$ (Δ)*	Adsorbed on phosphate-coated α-Fe$_2$O$_3$ (Δ)*
Amide I	1653	1657 (+5)	1653 (-0)	1633	1626 (-7)	1628 (-5)
Amide II	1545	1546 (+1)	1542 (-3)	1548	1542 (-6)	1543 (-7)

(Δ)* = Difference between adsorbed and solution phase vibrational frequency.

In addition to Amide band frequency shifts, band shape changes were also observed upon protein adsorption onto the α-Fe$_2$O$_3$ surface. For instance, when β-LG was adsorbed in the absence of phosphate, the spectral shoulder at 1640 cm^{-1} developed (Fig. 5.8b), hypothesized to be due to hydrogen bonding changes upon protein adsorption.[74] However, in the presence of phosphate, the band shape of β-LG Amide I resembled its native state, indicating phosphate constrained protein denaturation and secondary structural changes.[30] We observed no change in phosphate band intensities during sorption experiments; however, band shape changes were detected upon protein introduction indicating possible differences in surface phosphate species and adsorption modes during protein adsorption.
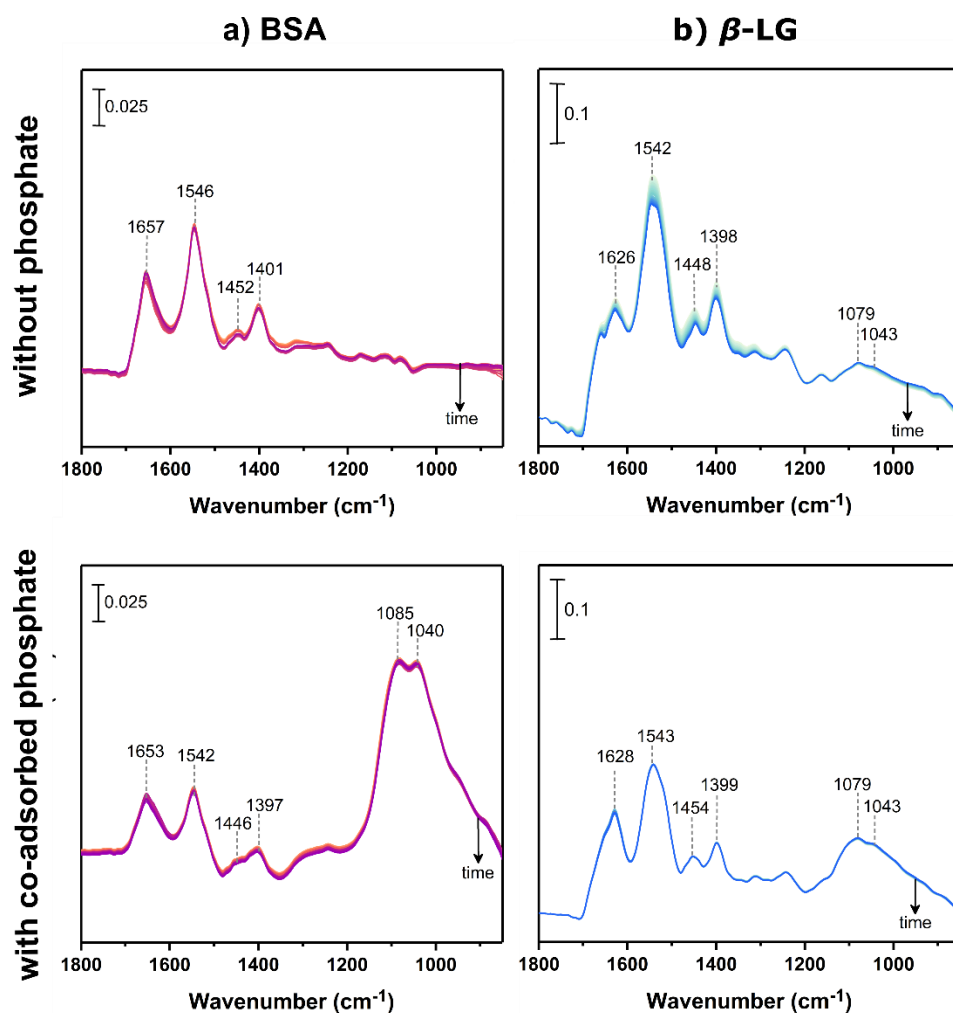
Figure 5.9: ATR-FTIR spectra of 1 mg/mL (a) BSA and (b) β-LG desorption experiments from α-Fe$_2$O$_3$ with 10 mM NaCl (in MilliQ) without phosphate (top) and with co-adsorbed phosphate (bottom) as a f(time) at pH 6.

Adsorbed proteins were also subjected to desorption experiments to determine their stability (Fig. 5.9). As seen in desorption spectra, BSA did not desorb from the α-Fe$_2$O$_3$ surface, indicating this protein is irreversibly adsorbed onto the surface, and pre-adsorbed phosphate did not impact the irreversibility of BSA adsorption significantly. However, partial reversibility was observed for *β*-LG in the absence of phosphate, and kinetics measurements were completed to investigate this distinction. Notably, the adsorption and desorption of BSA and *β*-LG were highly time-dependent. To understand the time-

dependency of secondary structural changes, adsorption kinetics, and changes to Amide I/II spectral ratios were further probed.

For the effect of pre-adsorbed LPS, IgG was absorbed onto hematite surfaces and the results of the protein adsorption in the presence and absence of LPS can be seen in Fig. 5.10. In the presence of LPS, a higher amount of protein is adsorbed on the nanoparticle surface. By comparing the solution phase with adsorbed phase spectra, shifts in the Amide I band and the change in the band shape was observed indicating the secondary structural changes of the proteins upon adsorption.
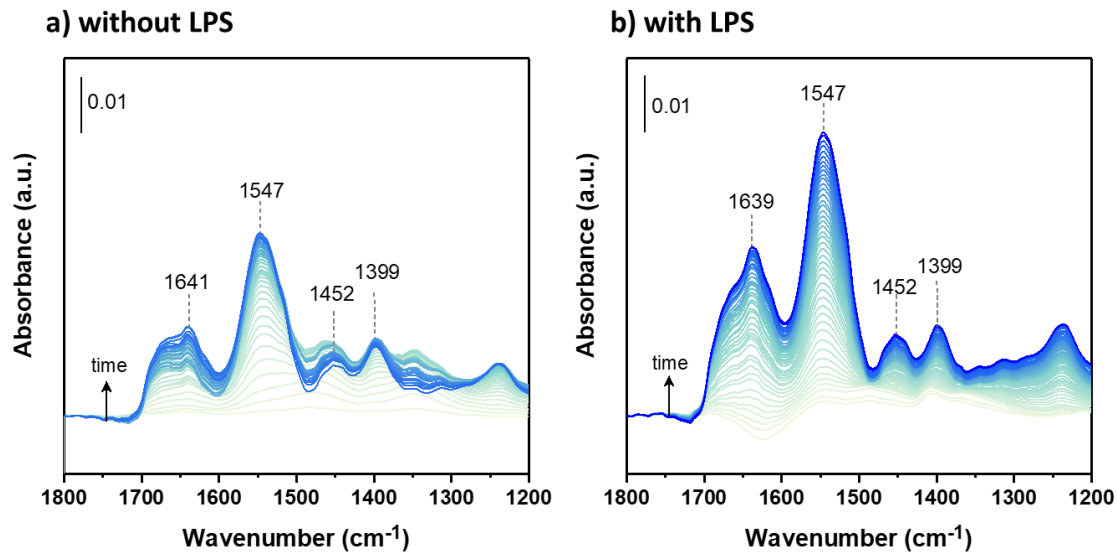
Figure 5.10: ATR-FTIR spectra of 0.2 mg/mL IgG adsorption experiments on α-Fe2O3 without LPS (a) and with pre-adsorbed LPS (b) as a f(time) at pH 7.4.

5.4.5 Adsorption Kinetics, Conformation Changes, and Reversibility of BSA and β-LG at the α-Fe₂O₃ Surface

The dynamic adsorption behavior of proteins on α-Fe$_2$O$_3$ nanoparticles in the presence and absence of phosphate are shown in Fig. 5.11 In kinetic isotherms analyses, the Amide II band was used rather than the Amide I or III regions to monitor and quantify protein adsorption, as this band is less sensitive to structural changes or potential aggregation, and to minimize water interference.[33,82] Peak intensities of the Amide II band absorbance for the adsorbed BSA and *β*-LG during adsorption onto α-Fe$_2$O$_3$ nanoparticles (0-90 min) and desorption (90-180 min) were examined as a function of time at pH 6 (Fig. 5.11). It is apparent that phosphate affected the total concentration of proteins adsorbed on the α-Fe$_2$O$_3$ nanoparticle surface. BSA alone reached saturation at ~0.2 absorbance units; however, in the presence of pre-adsorbed phosphate on the nanoparticle surface, saturation was reached at approximately 0.1 absorbance units, indicating phosphate occupies the active sites of the particle surface and reduced total protein coverage. α-Fe$_2$O$_3$ nanoparticles showed pH$_{IEP}$ near 6 (see Fig. 4.1 in Chapter 4), indicating a neutral charge and hydroxylic surface at the experimental pH value. In terms of sorbate reactivity, as both proteins were negatively charged at pH 6, we suggest that adsorption was altered through hydrogen bonding, and polar amino acid residues or other protein fragments may contribute to the adsorption process while electrostatic interactions were minimal.
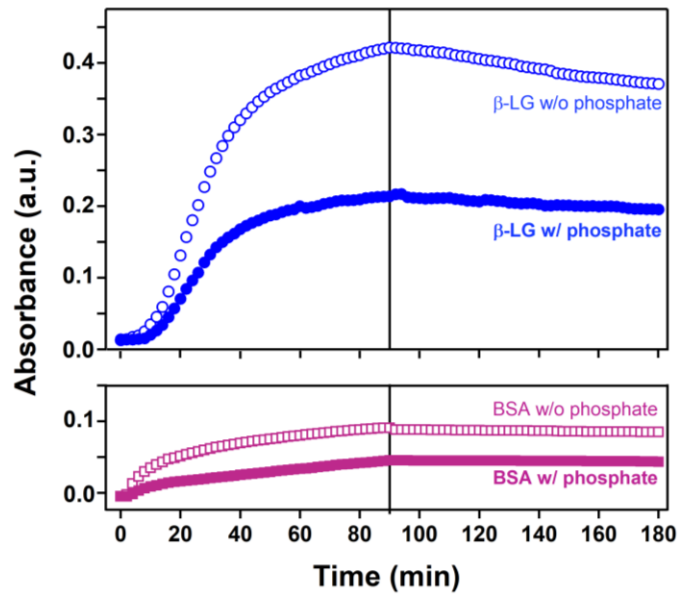
Figure 5.11: Absorbance intensities for the adsorbed BSA and β-LG for the Amide II peak height during adsorption onto α-Fe$_2$O$_3$ nanoparticles (0-90 min) and desorption (90-180 min) plotted as f(time) at pH 6. The solid and empty symbols represent the Amide II bands' peak heights in the presence and absence of pre-adsorbed phosphate, respectively. Kinetics results in this plot show the Difference in the total protein coverage on the nanoparticle surfaces. The adsorption rate of proteins is slowed in the presence of phosphate, β-LG absorbance intensity almost four times higher to BSA, as a possible result of the higher affinity of β-LG to the surface and its smaller size compared to BSA.

In addition to modulating surface coverage, phosphate influenced protein adsorption kinetics via protein-specific mechanisms. *β*-LG did not reach equilibrium when phosphate was absent, while equilibrium was achieved within 90 minutes when phosphate is present (Fig. 5.11). This observation was not as significant for BSA adsorption onto α-Fe$_2$O$_3$ surfaces. *β*-LG adsorbed onto surface ~4 times higher in comparison to BSA, as can be seen from the absorbance intensities in Fig. 5.11. Protein surface coverage could depend on the solution concentration in which the adsorbent is immersed and/or the molecular volume of the adsorbing protein (proportional to its molecular weight).[83] The Difference within the total absorbance was suggested to be a result of a higher affinity of *β*-LG to the

138

surface and its smaller size compared to BSA and controlled by water/surface interactions. Thus, the total surface coverage of BSA onto α-Fe$_2$O$_3$ surfaces was proposed to be less.

Adsorption isotherms onto α-Fe$_2$O$_3$ nanoparticles were protein-specific and, notably, phosphate did not impact the isotherm morphology. Kinetic analysis of BSA revealed Langmuir-type adsorption isotherms, similar to previous adsorption studies of BSA on oxides[39,84,85] and clay materials.[34,86] In contrast, a sigmoidal-shape (S-shape) adsorption curve for β-LG adsorption was achieved in our experimental conditions in Fig 5.11. An S-shape adsorption isotherm is often caused by lateral interactions between the adsorbed species and unrestricted monolayer-multilayer formation related to protein size.[83,87,88] Our replicate experiments resulted in consistent S-shape isotherms, confirming that aqueous phase β-LG adsorption to α-Fe$_2$O$_3$ nanoparticles forms multilayer structures.

To probe such disparate adsorption structures' stability, desorption experiments were carried out by flowing 10 mM NaCl at pH 6 over protein-α-Fe$_2$O$_3$ nanoparticle complexes. The desorption region in Fig. 5.9 shows that pre-adsorbed phosphate impacts protein adsorption reversibility and BSA adsorbed onto α-Fe$_2$O$_3$ surface irreversibly. Similar behavior was observed before in an earlier study; BSA adsorption reversibility on TiO$_2$ surface at pH 4 was influenced in the presence of co-adsorbed phosphate.[30] In the absence of phosphate, partial desorption for β-LG was observed, supporting the hypothesized result of multilayer formation for β-LG in the absence of pre-adsorbed phosphate. During multilayer adsorption, protein adsorbs to surfaces primarily through protein/surface interactions as higher-order layers are too distant from the adsorbent surface to be held by interaction forces in close-proximity this type of adsorption is mostly partially reversible.[83]

Real-time changes in the Amide I/II ratio provides insight into protein conformational changes during adsorption.[89] Therefore, this ratio was examined as a function of time during adsorption and desorption experiments (Fig. 5.12). In here, Adsorption experiments are done in the presence and absence of co-adsorbed phosphate. Desorption studies are done with NaCl solutions at pH 6. The solid and empty symbols represent the peak heights of the Amide II bands in the presence and absence of co-adsorbed phosphate, respectively. The figure indicates protein conformational changes happen in the earlier time points (before 20 mins) in the absence of phosphate, whereas the conformational change is slower in the presence of co-adsorbed phosphate (before 60 mins). We observed time-dependent protein conformational changes phosphate-driven impacts on the rate of such changes. Conformational changes occurred in the first 20 minutes of the reaction in the absence of phosphate yet took up to 60 minutes to appear in the presence of pre-adsorbed phosphate. Insights from this figure were used to select time points for secondary structural analysis at an early (4 min) and final time point (90min).
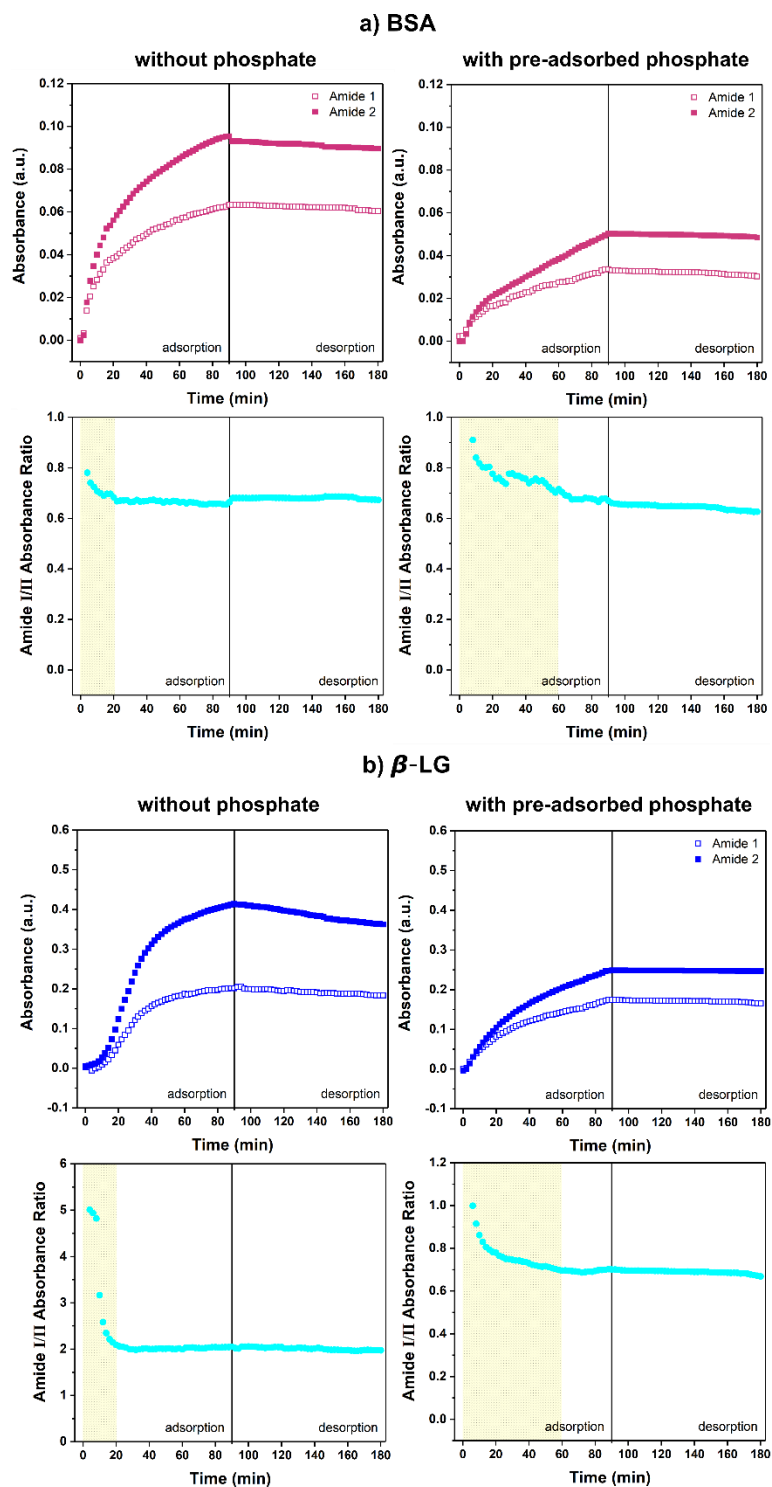
Figure 5.12: Ratio of the Amide I/II peak absorbance intensities for the adsorbed BSA and β-LG during adsorption onto α-Fe$_2$O$_3$ nanoparticles (0-90 min) and desorption (90-180 min) plotted as f(time) at pH 6.

5.4.6 Phosphate and LPS Effects on Secondary Structural Changes of The Proteins Adsorbed on α-Fe₂O₃ Nanoparticles

Protein secondary structures were investigated via analysis of the ATR-FTIR Amide I band, which is highly sensitive to protein conformational changes.[36] Protein solution ATR-FTIR spectra were deconvoluted into β-sheets, turns, α-helices, extended chains (short-segment chains connecting the α-helical segment), random coils, and side-chain moieties (Fig. 5.13). Vibrational frequencies (cm^{-1}) of the absorption peak centers associated with individual secondary structure components of the BSA and β-LG solutions after curve fitting are summarized in Table 5.3. The peak center positions were shifted ±3 cm^{-1} from the local minimum positions determined by the second derivative, and the coefficients of determination (R^2) were ≥ 0.9 for deconvolution fits.
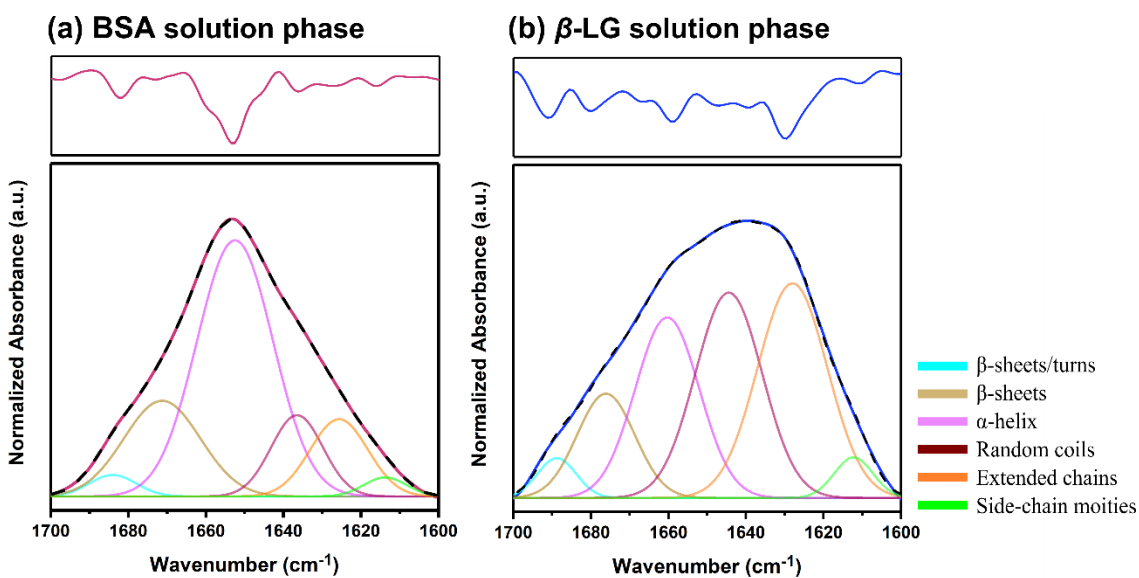
Figure 5.13: Background subtracted and normalized protein Amide I band for secondary structural analysis with curve fitting results for (a) BSA and (b) β-LG solutions at pH 6.0.

Table 5.3: Summarized vibrational frequencies (cm^{-1}) of the absorption peak centers associated with individual secondary structure components of the BSA and β-LG solutions after curve fitting.

	Secondary Structure	Solution Phase	Vibrational Frequency (cm^{-1})			
			Adsorbed on α-Fe$_2$O$_3$ (Δ)*		Adsorbed on phosphate-coated α-Fe$_2$O$_3$ (Δ)*	
			4 min	90 min	4 min	90 min
BSA	β-sheets	1684	1690	1690	1689	1683
	Turns	1671	1677	1677	1674	1671
	α-helices	1652	1659	1658	1658	1655
	Random coils	1636	1643	1645	1644	1642
	Extended chains	1625	1629	1631	1631	1630
	Side-chain moieties	1613	1612	1612	1612	1611
	Secondary Structure	**Solution Phase**	**4 min**	**90 min**	**4 min**	**90 min**
β-LG	β-sheets	1688	1695	1690	1691	1688
	Turns	1676	1676	1680	1683	1679
	α-helices	1660	1658	1658	1666	1661
	Random coils	1644	1650	1643	1647	1644
	Extended chains	1628	1635	1628	1629	1626
	Side-chain moieties	1612	1618	1612	1614	1611

(Δ)* = Difference between adsorbed and solution phase secondary structure content.

Earlier studies showed that *β*-LG structure is comprised of a short α-helix and eight strands of antiparallel *β*-sheets, which form a conical barrel.[37] In contrast, BSA is comprised solely of α-helix structures.[39] However, it is essential to note that reported variations are possible within ±10% among secondary structures distribution.[11] The curve fitting results for solution-phase protein conformational analyses, shown in Fig. 5.13, were aligned with previous findings,[39] as the dominant component of BSA solution-phase conformation at pH 6.0 was largely α-helix (52%), and of *β*-LG solution was primarily extended chains/β-sheets (49%).
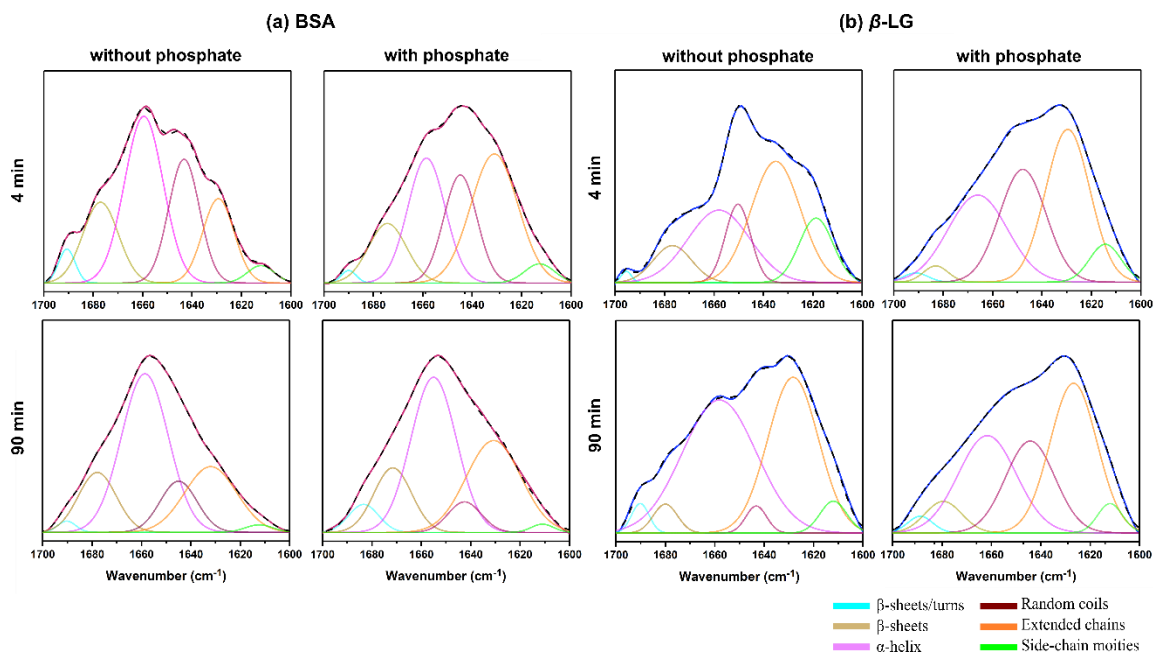
Figure 5.14: Background subtracted and normalized protein Amide I band for secondary structural analysis with curve fitting results for (a) BSA and (b) β-LG adsorbed on α-Fe$_2$O$_3$ nanoparticles in the presence and absence of pre-adsorbed phosphate at pH 6.0. The magenta and dark blue solid lines represent the original experimental spectrum, and the black dashed lines represent the cumulative fit. Component bands are given for intermolecular β-sheets/turns (cyan), β-sheets (green/brown), α-helices (fuchsia), random coils (dark red), short-segment chains connecting the α-helices (orange), side-chain moieties (lime).

To further our understanding of the effects of pre-adsorbed phosphate on adsorbed protein conformation, curve fitting analyses of the ATR-FTIR data at different time points (4 and 90 min) were performed and shown in Fig. 5.14. The deconvoluted integrated peak area of the overlapping peaks was fitted for relevant secondary components. The changes with varying conditions are reported in Table 5.4.[39,40,76,90,91] Critically, protein conformations changed upon adsorption, and phosphate presence affected these changes. During BSA adsorption in the absence of phosphate, a comparison of the IR spectra of the aqueous and adsorbed phase showed a distinct loss of α-helix content (↓9%) and a gain in the extended chains (↑18%). An unfolding process after BSA adsorption on metal oxides has been previously observed. [30,39] However, when phosphate was present, the loss of α-

144

helix content and gain in the extended chains were reduced. This suggests that pre-adsorbed phosphate inhibited BSA unfolding on the α-Fe$_2$O$_3$ nanoparticle surface. During β-LG adsorption in the absence of phosphate, curve-fitting analyses implicate increasing α-helix content (19→48%) and decreasing random coils (29→3%)This type of secondary structure shift could be the result of a higher exposition of hydrophilic groups of side-chains and protection of the hydrophobic core of the protein.[92]

Table 5.4: Secondary structural elements content (%) in the Amide I region determined via curve-fitting for solution phase (5 mg/mL) and after 90 min adsorption onto α-Fe$_2$O$_3$ and phosphate-coated α-Fe$_2$O$_3$.

	Secondary Structure	Solution Phase	Adsorbed on α-Fe$_2$O$_3$ (Δ)*		Adsorbed on phosphate-coated α-Fe$_2$O$_3$ (Δ)*	
			4 min	90 min	4 min	90 min
BSA	β-sheets/turns	3	3 (↓0)	5 (↑2)	1 (↓2)	1 (↓2)
	β-sheets	20	17 (↓3)	15 (↓5)	13 (↓7)	15 (↓15)
	α-helices	52	38 (↓14)	43 (↓9)	27 (↓25)	48 (↓4)
	Random coils	11	23 (↑12)	6 (↑5)	21 (↑10)	12 (↑1)
	Extended chains	12	15 (↑3)	30 (↑18)	35 (↑13)	22 (↑10)
	Side-chain moieties	2	4 (↑2)	1 (↑1)	3 (↑1)	2 (↓0)
	Secondary Structure	**Solution Phase**	**4 min**	**90 min**	**4 min**	**90 min**
β-LG	β-sheets/turns	4	1 (↓3)	3 (↑1)	1 (↓3)	2 (↓2)
	β-sheets	13	9 (↓4)	3 (↑10)	2 (↓11)	6 (↓7)
	α-helices	19	27 (↑8)	48 (↑19)	27 (↑8)	29 (↑9)
	Random coils	29	12 (↓17)	3 (↓26)	28 (↓1)	23 (↓6)
	Extended chains	32	37 (↑5)	39 (↑7)	35 (↑3)	36 (↑4)
	Side-chain moieties	3	14 (↑11)	4 (↑1)	7 (↑4)	4 (↑1)

(Δ)* = Difference between adsorbed and solution phase secondary structure content.

Less noticeable structural changes were observed during B-LG adsorption in the presence of phosphate, suggested by dampened increases in β-LG α-helix content. Conformational changes for the β-LG were more significant in comparison to the BSA in the absence of phosphate, as can be seen in Table 5.4. In a recent study,[28] an increase in α-

helix structure was observed in BSA adsorbed on hematite surfaces under increasing protein concentrations. Another study of *β*-LG adsorption on montmorillonite by Nuclear Magnetic Resonance (NMR) spectroscopy revealed that at high *β*-LG concentrations, significant secondary structural changes with a loss of β-sheet organization occurred.[37] Since *β*-LG likely adsorbed onto the mineral surface as a multilayer; this assembly may result in a more compact and aggregated protein structure.
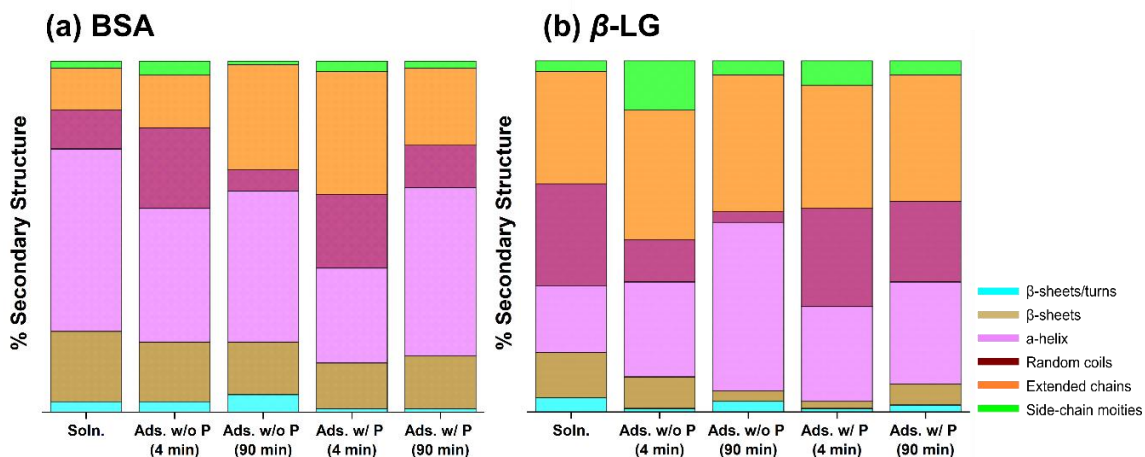
Figure 5.15: Summary bar plot of the secondary structural content (%) in (a) BSA and (b) β-LG determined via curve fitting in solution and after 4 and 90 mins of adsorption onto α-Fe$_2$O$_3$ and phosphate-coated α-Fe$_2$O$_3$ nanoparticle surfaces.

The temporal sequences of protein conformational changes were characterized by comparing early time point (4 min) curve fitting results with those from the final time point (90 min) (Table 5.4). In the absence of phosphate at 4 min, BSA appeared to unfold first into random coils (↑12%) followed by a loss of α-helices (↓14%). At 90 min, BSA unfolding of α-helices was reduced (↓9) with an increment to extended chains (↑18%). When pre-adsorbed phosphate was present during BSA adsorption, the protein first unfolded into random coils (↑10%) and extended chains (↑13%) simultaneously, followed by a loss of α-helices (↓25%). Overall, this corresponds to the conversion of more compact

α-helix forms into relatively disordered structures.[11] During *β*-LG adsorption in the absence of phosphate, similar to BSA, the increment of the α-helix fraction was more significant at low protein coverage (early time point) and protein denaturation slowed down at higher coverage (later time point). These results are in agreement with analyses of the Amide I/II ratio in Fig. 5.12. Summary bar plot of the secondary structural content (%) of proteins determined via curve fitting in solution and after adsorption onto α-Fe_2O_3 and phosphate-coated α-Fe_2O_3 nanoparticle can be seen in Fig. 5.15.

IgG conformational changes upon adsorbed onto α-Fe_2O_3 were characterized by curve fitting results with those from the final time point (90 min) (Figure 5.16). And the changes in the secondary components are recorded in Table 5.5. In the absence of LPS, IgG unfold into extended chains (↑4%) and β-turns (↑4%) with a loss of α-helices (↓8%). However, when pre-adsorbed LPS was present during IgG adsorption, the protein folded to α-helices with a (↑6%) of a gain. This corresponds to the conversion of more compact α-helix forms and ordered structure.
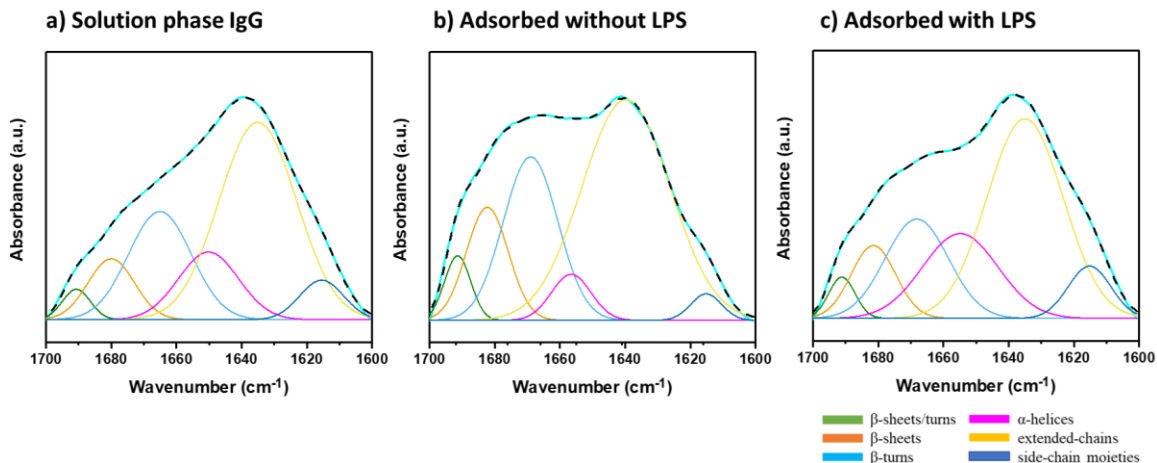
Figure 5.16: Background subtracted and normalized protein Amide I band for secondary structural analysis with curve fitting results for IgG solution and adsorbed on α-Fe$_2$O$_3$ nanoparticles in the presence and absence of pre-adsorbed LPS at pH 7.4. The solid cyan lines represent the original experimental spectrum, and the black dashed lines represent the cumulative fit.

Table 5.5: Secondary structural elements content of IgG (%) in the Amide I region determined via curve-fitting for solution phase (0.2 mg/mL) and after 90 min adsorption onto α-Fe$_2$O$_3$ and LPS-coated α-Fe$_2$O$_3$.

	Secondary Structure	**Solution Phase**	**Adsorbed on α-Fe$_2$O$_3$ (Δ)***	**Adsorbed on LPS-coated α-Fe$_2$O$_3$ (Δ)***
	β-sheets/turns	3	5 ($\uparrow$2)	3 ($\downarrow$0)
	β-sheets	9	12 ($\uparrow$3)	9 ($\downarrow$0)
IgG	β-turns	21	24 ($\uparrow$3)	18 ($\downarrow$3)
	α-helices	13	5 ($\downarrow$8)	19 ($\uparrow$6)
	Extended chains	48	52 ($\uparrow$4)	44 ($\downarrow$4)
	Side-chain moieties	6	2 ($\downarrow$4)	7 ($\uparrow$1)

(Δ)* = Difference between adsorbed and solution phase secondary structure content.

5.5   Conclusions

ATR-FTIR spectroscopic measurements in tandem with computational analyses demonstrate the critical impact of phosphate on protein adsorption kinetics, extent, conformation, and stability. Proteins underwent dynamic changes in their secondary conformation during adsorption on the hematite surface, and pre-adsorbed phosphate and

LPS prevented protein denaturation. Adsorption isotherms revealed that adsorption kinetics were protein-specific, as BSA exhibited Langmuir adsorption behavior, while contrastingly, *β*-LG showed sigmoidal-shape adsorption indicative of multilayer adsorption. From deconvolution analyses of the Amide I band for proteins, unfolding or refolding of adsorbed proteins was observed. While BSA unfolds into random coils and extended chains (followed by a loss of α-helices), *β*-LG was folding into α-helices. Likewise, *β*-LG, adsorbed IgG folded into α-helices in the presence of pre-adsorbed LPS. Protein conformational changes were sequential and time-dependent, and significant conformational changes occurred at low protein coverage. The potential impacts of pre-adsorbed components, at the mineral-water interface, to protein denaturation impacts protein behavior in environmental and biological systems. Multi-component adsorption kinetics can have significant roles in biogeochemical cycling. Changes in protein structures can be followed by a loss of activity. Thus, pre-adsorbed phosphate and LPS could potentially impact protein's function, ligand binding capability, and reactivity.

5.6   Acknowledgments

5.7   References

(1)   Cornell, R. M.; Schwertmann, U. Introduction to the Iron Oxides. In *The Iron Oxides*; 2003. https://doi.org/10.1002/3527602097.ch1.

(2)   Hochella, M. F.; Lower, S. K.; Maurice, P. A.; Penn, R. L.; Sahai, N.; Sparks, D. L.; Twining, B. S. Nanominerals, Mineral Nanoparticles, and Earth Systems. *Science*. 2008. https://doi.org/10.1126/science.1141134.

(3)   Theng, B. K. G.; Yuan, G. Nanoparticles in the Soil Environment. *Elements* **2008**. https://doi.org/10.2113/gselements.4.6.395.

(4)   Keller, A. A.; McFerran, S.; Lazareva, A.; Suh, S. Global Life Cycle Releases of Engineered Nanomaterials. *J. Nanoparticle Res.* **2013**. https://doi.org/10.1007/s11051-013-1692-4.

(5)   Cornell, R. M.; Schwertmann, U. *The Iron Oxides*; 2003. https://doi.org/10.1002/3527602097.

(6)   Schwaminger, S. P.; Fraga-García, P.; Selbach, F.; Hein, F. G.; Fuß, E. C.; Surya, R.; Roth, H. C.; Blank-Shim, S. A.; Wagner, F. E.; Heissler, S.; Berensmeier, S. Bio-Nano Interactions: Cellulase on Iron Oxide Nanoparticle Surfaces. *Adsorption* **2017**. https://doi.org/10.1007/s10450-016-9849-y.

(7)   Waychunas, G. A.; Kim, C. S.; Banfield, J. F. Nanoparticulate Iron Oxide Minerals in Soils and Sediments: Unique Properties and Contaminant Scavenging Mechanisms. In *Journal of Nanoparticle Research*; 2005. https://doi.org/10.1007/s11051-005-6931-x.

(8)   Bolisetty, S.; Vallooran, J. J.; Adamcik, J.; Mezzenga, R. Magnetic-Responsive Hybrids of Fe3O4 Nanoparticles with β-Lactoglobulin Amyloid Fibrils and Nanoclusters. *ACS Nano* **2013**. https://doi.org/10.1021/nn401988m.

(9)   Mudunkotuwa, I. A.; Grassian, V. H. The Devil Is in the Details (or the Surface): Impact of Surface Structure and Surface Energetics on Understanding the Behavior of Nanomaterials in the Environment. *Journal of Environmental Monitoring*. 2011. https://doi.org/10.1039/c1em00002k.

(10)   Limo, M. J.; Sola-Rabada, A.; Boix, E.; Thota, V.; Westcott, Z. C.; Puddu, V.; Perry, C. C. Interactions between Metal Oxides and Biomolecules: From Fundamental Understanding to Applications. *Chemical Reviews*. 2018. https://doi.org/10.1021/acs.chemrev.7b00660.

(11)   Barreto, M. S. C.; Elzinga, E. J.; Alleoni, L. R. F. The Molecular Insights into Protein Adsorption on Hematite Surface Disclosed by In-Situ ATR-FTIR/2D-COS Study. *Sci. Rep.* **2020**, *10* (1), 1–13. https://doi.org/10.1038/s41598-020-70201-z.

(12)   Mazeina, L.; Navrotsky, A. Enthalpy of Water Adsorption and Surface Enthalpy of Goethite (α-FeOOH) and Hematite (α-Fe2O3). *Chem. Mater.* **2007**. https://doi.org/10.1021/cm0623817.

(13)   Alberts, B.; Bray, D.; Johnson, A.; Lewis, J.; Raff, M.; Roberts, K.; Walter, P.; Protein Structure and Function. In *Essential Cell Biolog*; 2018. https://doi.org/10.1201/9781315815015-4.

(14)   Enzymes in the Environment: Activity, Ecology, and Applications. *Choice Rev. Online* **2002**. https://doi.org/10.5860/choice.40-1527.

(15)   Littlechild, J. A. Protein Structure and Function. In *Introduction to Biological and Small Molecule Drug Research and Development: Theory and Case Studies*; 2013. https://doi.org/10.1016/B978-0-12-397176-0.00002-9.

(16)   Alberts, B.; A, J.; Lewis J. Analyzing Protein Structure and Function. *Mol. Biol. Cell* **2002**.

(17)   Newcomb, C. J.; Qafoku, N. P.; Grate, J. W.; Bailey, V. L.; De Yoreo, J. J. Developing a Molecular Picture of Soil Organic Matter-Mineral Interactions by Quantifying Organo-Mineral Binding. *Nat. Commun.* **2017**. https://doi.org/10.1038/s41467-017-00407-9.

(18)   Moon, J.; Xia, K.; Williams, M. A. Consistent Proteinaceous Organic Matter

Partitioning into Mineral and Organic Soil Fractions during Pedogenesis in Diverse Ecosystems. *Biogeochemistry* **2019**. https://doi.org/10.1007/s10533-018-0523-1.

(19) Kim, J. T.; Weber, N.; Shin, G. H.; Huang, Q.; Liu, S. X. The Study of β-Lactoglobulin Adsorption on Polyethersulfone Thin Film Surface Using QCM-D and AFM. *J. Food Sci.* **2007**. https://doi.org/10.1111/j.1750-3841.2007.00344.x.

(20) Rabe, M.; Verdes, D.; Seeger, S. Understanding Protein Adsorption Phenomena at Solid Surfaces. *Advances in Colloid and Interface Science*. 2011. https://doi.org/10.1016/j.cis.2010.12.007.

(21) Casals, E.; Pfaller, T.; Duschl, A.; Oostingh, G. J.; Puntes, V. Time Evolution of the Nanoparticle Protein Corona. *ACS Nano* **2010**. https://doi.org/10.1021/nn901372t.

(22) Lynch, I.; Dawson, K. A. Protein-Nanoparticle Interactions. *Nano Today*. 2008. https://doi.org/10.1016/S1748-0132(08)70014-8.

(23) Cedervall, T.; Lynch, I.; Lindman, S.; Berggård, T.; Thulin, E.; Nilsson, H.; Dawson, K. A.; Linse, S. Understanding the Nanoparticle-Protein Corona Using Methods to Quntify Exchange Rates and Affinities of Proteins for Nanoparticles. *Proc. Natl. Acad. Sci. U. S. A.* **2007**. https://doi.org/10.1073/pnas.0608582104.

(24) Fadare, O. O.; Wan, B.; Liu, K.; Yang, Y.; Zhao, L.; Guo, L.-H. Eco-Corona vs Protein Corona: Effects of Humic Substances on Corona Formation and Nanoplastic Particle Toxicity in Daphnia Magna . *Environ. Sci. Technol.* **2020**. https://doi.org/10.1021/acs.est.0c00615.

(25) Settanni, G.; Zhou, J.; Suo, T.; Schöttler, S.; Landfester, K.; Schmid, F.; Mailänder, V. Protein Corona Composition of Poly(Ethylene Glycol)-and Poly (Phosphoester)-Coated Nanoparticles Correlates Strongly with the Amino Acid Composition of the Protein Surface. *Nanoscale* **2017**. https://doi.org/10.1039/c6nr07022a.

(26) Nasser, F.; Constantinou, J.; Lynch, I. Nanomaterials in the Environment Acquire an "Eco-Corona" Impacting Their Toxicity to Daphnia Magna—a Call for Updating Toxicity Testing Policies. *Proteomics*. 2020. https://doi.org/10.1002/pmic.201800412.

(27) Mei, N.; Hedberg, J.; Odnevall Wallinder, I.; Blomberg, E. Influence of Biocorona Formation on the Transformation and Dissolution of Cobalt Nanoparticles under Physiological Conditions. *ACS Omega* **2019**.

https://doi.org/10.1021/acsomega.9b02641.

(28) Liu, F.; Li, X.; Sheng, A.; Shang, J.; Wang, Z.; Liu, J. Kinetics and Mechanisms of Protein Adsorption and Conformational Change on Hematite Particles. *Environ. Sci. Technol.* **2019**. https://doi.org/10.1021/acs.est.9b02651.

(29) Nielsen, K. M.; Calamai, L.; Pietramellara, G. Stabilization of Extracellular DNA and Proteins by Transient Binding to Various Soil Components. In *Nucleic Acids and Proteins in Soil*; 2006. https://doi.org/10.1007/3-540-29449-x_7.

(30) Xu, Z.; Grassian, V. H. Bovine Serum Albumin Adsorption on TiO2 Nanoparticle Surfaces: Effects of Ph and Coadsorption of Phosphate on Protein-Surface Interactions and Protein Structure. *J. Phys. Chem. C* **2017**. https://doi.org/10.1021/acs.jpcc.7b07525.

(31) Satzer, P.; Svec, F.; Sekot, G.; Jungbauer, A. Protein Adsorption onto Nanoparticles Induces Conformational Changes: Particle Size Dependency, Kinetics, and Mechanisms. *Eng. Life Sci.* **2016**. https://doi.org/10.1002/elsc.201500059.

(32) Schmidt, M. P.; Martínez, C. E. Supramolecular Association Impacts Biomolecule Adsorption onto Goethite. *Environ. Sci. Technol.* **2018**. https://doi.org/10.1021/acs.est.7b06173.

(33) Schmidt, M. P.; Martínez, C. E. Kinetic and Conformational Insights of Protein Adsorption onto Montmorillonite Revealed Using in Situ ATR-FTIR/2D-COS. *Langmuir* **2016**. https://doi.org/10.1021/acs.langmuir.6b00786.

(34) Andersen, A.; Reardon, P. N.; Chacon, S. S.; Qafoku, N. P.; Washton, N. M.; Kleber, M. Protein-Mineral Interactions: Molecular Dynamics Simulations Capture Importance of Variations in Mineral Surface Composition and Structure. *Langmuir* **2016**. https://doi.org/10.1021/acs.langmuir.6b01198.

(35) Ustunol, I. B.; Gonzalez-Pech, N. I.; Grassian, V. H. PH-Dependent Adsorption of α-Amino Acids, Lysine, Glutamic Acid, Serine and Glycine, on TiO2 Nanoparticle Surfaces. *J. Colloid Interface Sci.* **2019**. https://doi.org/10.1016/j.jcis.2019.06.086.

(36) Roach, P.; Farrar, D.; Perry, C. C. Interpretation of Protein Adsorption: Surface-Induced Conformational Changes. *J. Am. Chem. Soc.* **2005**. https://doi.org/10.1021/ja042898o.

(37) Assifaoui, A.; Huault, L.; Maissiat, C.; Roullier-Gall, C.; Jeandet, P.; Hirschinger,

J.; Raya, J.; Jaber, M.; Lambert, J. F.; Cayot, P.; Gougeon, R. D.; Loupiac, C. Structural Studies of Adsorbed Protein (Betalactoglobulin) on Natural Clay (Montmorillonite). *RSC Adv.* **2014**. https://doi.org/10.1039/c4ra11607k.

(38) Kolman, K.; Makowski, M. M.; Golriz, A. A.; Kappl, M.; Pigłowski, J.; Butt, H. J.; Kiersnowski, A. Adsorption, Aggregation, and Desorption of Proteins on Smectite Particles. *Langmuir* **2014**. https://doi.org/10.1021/la502840s.

(39) Givens, B. E.; Xu, Z.; Fiegel, J.; Grassian, V. H. Bovine Serum Albumin Adsorption on SiO2 and TiO2 Nanoparticle Surfaces at Circumneutral and Acidic PH: A Tale of Two Nano-Bio Surface Interactions. *J. Colloid Interface Sci.* **2017**. https://doi.org/10.1016/j.jcis.2017.01.011.

(40) Sit, I.; Xu, Z.; Grassian, V. H. Plasma Protein Adsorption on TiO2 Nanoparticles: Impact of Surface Adsorption on Temperature-Dependent Structural Changes. *Polyhedron* **2019**. https://doi.org/10.1016/j.poly.2019.06.036.

(41) Basu, M. K.; Poliakov, E.; Rogozin, I. B. Domain Mobility in Proteins: Functional and Evolutionary Implications. *Brief. Bioinform.* **2009**. https://doi.org/10.1093/bib/bbn057.

(42) Pérez-Fuentes, L.; Drummond, C.; Faraudo, J.; Bastos-González, D. Adsorption of Milk Proteins (β-Casein and β-Lactoglobulin) and BSA onto Hydrophobic Surfaces. *Materials (Basel).* **2017**. https://doi.org/10.3390/ma10080893.

(43) Kleber, M.; Sollins, P.; Sutton, R. A Conceptual Model of Organo-Mineral Interactions in Soils: Self-Assembly of Organic Molecular Fragments into Zonal Structures on Mineral Surfaces. *Biogeochemistry* **2007**. https://doi.org/10.1007/s10533-007-9103-5.

(44) Coward, E. K.; Ohno, T.; Sparks, D. L. Direct Evidence for Temporal Molecular Fractionation of Dissolved Organic Matter at the Iron Oxyhydroxide Interface. *Environ. Sci. Technol.* **2019**. https://doi.org/10.1021/acs.est.8b04687.

(45) Leinemann, T.; Preusser, S.; Mikutta, R.; Kalbitz, K.; Cerli, C.; Höschen, C.; Mueller, C. W.; Kandeler, E.; Guggenberger, G. Multiple Exchange Processes on Mineral Surfaces Control the Transport of Dissolved Organic Matter through Soil Profiles. *Soil Biol. Biochem.* **2018**. https://doi.org/10.1016/j.soilbio.2017.12.006.

(46) Saptarshi, S. R.; Duschl, A.; Lopata, A. L. Interaction of Nanoparticles with Proteins: Relation to Bio-Reactivity of the Nanoparticle. *J. Nanobiotechnology* **2013**. https://doi.org/10.1186/1477-3155-11-26.

(47)   Vroman, L. Effect of Adsorbed Proteins on the Wettability of Hydrophilic and Hydrophobic Solids. *Nature* **1962**. https://doi.org/10.1038/196476a0.

(48)   Holtan, H.; Kamp-Nielsen, L.; Stuanes, A. O. Phosphorus in Soil, Water and Sediment: An Overview. *Hydrobiologia* **1988**. https://doi.org/10.1007/BF00024896.

(49)   Holman, I. P.; Whelan, M. J.; Howden, N. J. K.; Bellamy, P. H.; Willby, N. J.; Rivas-Casado, M.; McConvey, P. Phosphorus in Groundwater - An Overlooked Contributor to Eutrophication? *Hydrol. Process.* **2008**. https://doi.org/10.1002/hyp.7198.

(50)   Zhao, G.; Du, J.; Jia, Y.; Lv, Y.; Han, G.; Tian, X. The Importance of Bacteria in Promoting Algal Growth in Eutrophic Lakes with Limited Available Phosphorus. *Ecol. Eng.* **2012**. https://doi.org/10.1016/j.ecoleng.2012.02.007.

(51)   Wei, T.; Kaewtathip, S.; Shing, K. Buffer Effect on Protein Adsorption at Liquid/Solid Interface. *J. Phys. Chem. C* **2009**. https://doi.org/10.1021/jp806586n.

(52)   Huang, X. Intersection of Isotherms for Phosphate Adsorption on Hematite. *J. Colloid Interface Sci.* **2004**. https://doi.org/10.1016/j.jcis.2003.12.007.

(53)   Moulton, S. E.; Barisci, J. N.; McQuillan, A. J.; Wallace, G. G. ATR-IR Spectroscopic Studies of the Influence of Phosphate Buffer on Adsorption of Immunoglobulin G to TiO2. *Colloids Surfaces A Physicochem. Eng. Asp.* **2003**. https://doi.org/10.1016/S0927-7757(03)00078-5.

(54)   Guerville, M.; Boudry, G. Gastrointestinal and Hepatic Mechanisms Limiting Entry and Dissemination of Lipopolysaccharide into the Systemic Circulation. *American Journal of Physiology - Gastrointestinal and Liver Physiology*. 2016. https://doi.org/10.1152/ajpgi.00098.2016.

(55)   Kallio, K. A. E.; Hätönen, K. A.; Lehto, M.; Salomaa, V.; Männistö, S.; Pussinen, P. J. Endotoxemia, Nutrition, and Cardiometabolic Disorders. *Acta Diabetol.* **2015**. https://doi.org/10.1007/s00592-014-0662-3.

(56)   Bianchi, M. G.; Allegri, M.; Chiu, M.; Costa, A. L.; Blosi, M.; Ortelli, S.; Bussolati, O.; Bergamaschi, E. Lipopolysaccharide Adsorbed to the Bio-Corona of TiO2 Nanoparticles Powerfully Activates Selected pro-Inflammatory Transduction Pathways. *Front. Immunol.* **2017**. https://doi.org/10.3389/fimmu.2017.00866.

(57)   Oostingh, G. J.; Casals, E.; Italiani, P.; Colognato, R.; Stritzinger, R.; Ponti, J.;

Pfaller, T.; Kohl, Y.; Ooms, D.; Favilli, F.; Leppens, H.; Lucchesi, D.; Rossi, F.; Nelissen, I.; Thielecke, H.; Puntes, V. F.; Duschl, A.; Boraschi, D. Problems and Challenges in the Development and Validation of Human Cell-Based Assays to Determine Nanoparticle-Induced Immunomodulatory Effects. *Part. Fibre Toxicol.* **2011**. https://doi.org/10.1186/1743-8977-8-8.

(58)   Rodzik, A.; Pomastowski, P.; Sagandykova, G. N.; Buszewski, B. Interactions of Whey Proteins with Metal Ions. *International Journal of Molecular Sciences*. 2020. https://doi.org/10.3390/ijms21062156.

(59)   O'Loughlin, I. B.; Kelly, P. M.; Murray, B. A.; Fitzgerald, R. J.; Brodkorb, A. Concentrated Whey Protein Ingredients: A Fourier Transformed Infrared Spectroscopy Investigation of Thermally Induced Denaturation. *Int. J. Dairy Technol.* **2015**. https://doi.org/10.1111/1471-0307.12239.

(60)   Fang, Y.; Dalgleish, D. G. Conformation of β-Lactoglobulin Studied by FTIR: Effect of PH, Temperature, and Adsorption to the Oil-Water Interface. *J. Colloid Interface Sci.* **1997**. https://doi.org/10.1006/jcis.1997.5191.

(61)   Ehn, B. M.; Ekstrand, B.; Bengtsson, U.; Ahlstedt, S. Modification of IgE Binding during Heat Processing of the Cow's Milk Allergen β-Lactoglobulin. *J. Agric. Food Chem.* **2004**. https://doi.org/10.1021/jf0304371.

(62)   Krebs, M. R. H.; Devlin, G. L.; Donald, A. M. Amyloid Fibril-like Structure Underlies the Aggregate Structure across the PH Range for β-Lactoglobulin. *Biophys. J.* **2009**. https://doi.org/10.1016/j.bpj.2009.03.028.

(63)   Bouhekka, A.; Bürgi, T. In Situ ATR-IR Spectroscopy Study of Adsorbed Protein: Visible Light Denaturation of Bovine Serum Albumin on TiO 2. *Appl. Surf. Sci.* **2012**. https://doi.org/10.1016/j.apsusc.2012.08.017.

(64)   Buijs, J.; Norde, W.; Lichtenbelt, J. W. T. Changes in the Secondary Structure of Adsorbed IgG and F(Ab′)2 Studied by FTIR Spectroscopy. *Langmuir* **1996**. https://doi.org/10.1021/la950665s.

(65)   Giacomelli, C. E.; Bremer, M. G. E. G.; Norde, W. ATR-FTIR Study of IgG Adsorbed on Different Silica Surfaces. *J. Colloid Interface Sci.* **1999**. https://doi.org/10.1006/jcis.1999.6479.

(66)   Elzinga, E. J.; Sparks, D. L. Phosphate Adsorption onto Hematite: An in Situ ATR-FTIR Investigation of the Effects of PH and Loading Level on the Mode of Phosphate Surface Complexation. *J. Colloid Interface Sci.* **2007**. https://doi.org/10.1016/j.jcis.2006.12.061.

(67)   Tejedor-Tejedor, M. I.; Anderson, M. A. Protonation of Phosphate on the Surface of Goethite As Studied by CIR-FTIR and Electrophoretic Mobility. *Langmuir* **1990**. https://doi.org/10.1021/la00093a015.

(68)   Po, H. N.; Senozan, N. M. The Henderson-Hasselbalch Equation: Its History and Limitations. *J. Chem. Educ.* **2001**. https://doi.org/10.1021/ed078p1499.

(69)   Gong, W. A Real Time in Situ ATR-FTIR Spectroscopic Study of Linear Phosphate Adsorption on Titania Surfaces. *Int. J. Miner. Process.* **2001**. https://doi.org/10.1016/S0301-7516(01)00045-X.

(70)   Kubicki, J. D.; Paul, K. W.; Kabalan, L.; Zhu, Q.; Mrozik, M. K.; Aryanpour, M.; Pierre-Louis, A. M.; Strongin, D. R. ATR-FTIR and Density Functional Theory Study of the Structures, Energetics, and Vibrational Spectra of Phosphate Adsorbed onto Goethite. *Langmuir* **2012**. https://doi.org/10.1021/la303111a.

(71)   Arai, Y.; Sparks, D. L. ATR-FTIR Spectroscopic Investigation on Phosphate Adsorption Mechanisms at the Ferrihydrite-Water Interface. *J. Colloid Interface Sci.* **2001**. https://doi.org/10.1006/jcis.2001.7773.

(72)   Elzinga, E. J.; Sparks, D. L. Phosphate Adsorption onto Hematite: An in Situ ATR-FTIR Investigation of the Effects of PH and Loading Level on the Mode of Phosphate Surface Complexation. *J. Colloid Interface Sci.* **2007**. https://doi.org/10.1016/j.jcis.2006.12.061.

(73)   Barkleit, A.; Foerstendorf, H.; Li, B.; Rossberg, A.; Moll, H.; Bernhard, G. Coordination of Uranium(vi) with Functional Groups of Bacterial Lipopolysaccharide Studied by EXAFS and FT-IR Spectroscopy. *Dalt. Trans.* **2011**. https://doi.org/10.1039/c1dt10546a.

(74)   Barth, A. Infrared Spectroscopy of Proteins. *Biochimica et Biophysica Acta - Bioenergetics*. 2007. https://doi.org/10.1016/j.bbabio.2007.06.004.

(75)   Kim, J.; Doudrick, K. Emerging Investigator Series: Protein Adsorption and Transformation on Catalytic and Food-Grade TiO2 Nanoparticles in the Presence of Dissolved Organic Carbon. *Environ. Sci. Nano* **2019**. https://doi.org/10.1039/c9en00130a.

(76)   Givens, B. E.; Diklich, N. D.; Fiegel, J.; Grassian, V. H. Adsorption of Bovine Serum Albumin on Silicon Dioxide Nanoparticles: Impact of p H on Nanoparticle–Protein Interactions . *Biointerphases* **2017**. https://doi.org/10.1116/1.4982598.

(77)   Gbassi, G.; Yolou, F.; Sarr, S.; Atheba, P.; Amin, C.; Ake, M. Whey Proteins Analysis in Aqueous Medium and in Artificial Gastric and Intestinal Fluids. *Int. J. Biol. Chem. Sci.* **2012**. https://doi.org/10.4314/ijbcs.v6i4.38.

(78)   Mudunkotuwa, I. A.; Minshid, A. Al; Grassian, V. H. ATR-FTIR Spectroscopy as a Tool to Probe Surface Adsorption on Nanoparticles at the Liquid-Solid Interface in Environmentally and Biologically Relevant Media. *Analyst*. 2014. https://doi.org/10.1039/c3an01684f.

(79)   Yang, J.; Wang, B.; You, Y.; Chang, W. J.; Tang, K.; Wang, Y. C.; Zhang, W.; Ding, F.; Gunasekaran, S. Probing the Modulated Formation of Gold Nanoparticles-Beta-Lactoglobulin Corona Complexes and Their Applications. *Nanoscale* **2017**. https://doi.org/10.1039/c7nr02999c.

(80)   Thomson, A. J.; Gray, H. B. Bio-Inorganic Chemistry. *Current Opinion in Chemical Biology*. 1998. https://doi.org/10.1016/S1367-5931(98)80056-2.

(81)   Surewicz, W. K.; Mantsch, H. H. New Insight into Protein Secondary Structure from Resolution-Enhanced Infrared Spectra. *Biochimica et Biophysica Acta (BBA)/Protein Structure and Molecular*. 1988. https://doi.org/10.1016/0167-4838(88)90107-0.

(82)   Tsai, D. H.; Delrio, F. W.; Keene, A. M.; Tyner, K. M.; MacCuspie, R. I.; Cho, T. J.; Zachariah, M. R.; Hackley, V. A. Adsorption and Conformation of Serum Albumin Protein on Gold Nanoparticles Investigated Using Dimensional Measurements and in Situ Spectroscopic Methods. *Langmuir* **2011**. https://doi.org/10.1021/la104124d.

(83)   Parhi, P.; Golas, A.; Barnthip, N.; Noh, H.; Vogler, E. A. Volumetric Interpretation of Protein Adsorption: Capacity Scaling with Adsorbate Molecular Weight and Adsorbent Surface Energy. *Biomaterials* **2009**. https://doi.org/10.1016/j.biomaterials.2009.09.005.

(84)   Song, L.; Yang, K.; Jiang, W.; Du, P.; Xing, B. Adsorption of Bovine Serum Albumin on Nano and Bulk Oxide Particles in Deionized Water. *Colloids Surfaces B Biointerfaces* **2012**. https://doi.org/10.1016/j.colsurfb.2012.02.011.

(85)   Alkan, M.; Demirbaş, Ö.; Doğan, M.; Arslan, O. Surface Properties of Bovine Serum Albumin - Adsorbed Oxides: Adsorption, Adsorption Kinetics and Electrokinetic Properties. *Microporous Mesoporous Mater.* **2006**. https://doi.org/10.1016/j.micromeso.2006.07.007.

(86)   Barral, S.; Villa-García, M. A.; Rendueles, M.; Díaz, M. Interactions between

Whey Proteins and Kaolinite Surfaces. *Acta Mater.* **2008**. https://doi.org/10.1016/j.actamat.2008.02.009.

(87)   Scheufele, F. B.; Módenes, A. N.; Borba, C. E.; Ribeiro, C.; Espinoza-Quiñones, F. R.; Bergamasco, R.; Pereira, N. C. Monolayer-Multilayer Adsorption Phenomenological Model: Kinetics, Equilibrium and Thermodynamics. *Chem. Eng. J.* **2016**. https://doi.org/10.1016/j.cej.2015.09.085.

(88)   Buttersack, C. Modeling of Type IV and v Sigmoidal Adsorption Isotherms. *Phys. Chem. Chem. Phys.* **2019**. https://doi.org/10.1039/c8cp07751g.

(89)   Jackson, M.; Mantsch, H. H. Artifacts Associated with the Determination of Protein Secondary Structure by ATR-IR Spectroscopy. *Appl. Spectrosc.* **1992**. https://doi.org/10.1366/0003702924124862.

(90)   Dockal, M.; Carter, D. C.; Rüker, F. Conformational Transitions of the Three Recombinant Domains of Human Serum Albumin Depending on PH. *J. Biol. Chem.* **2000**. https://doi.org/10.1074/jbc.275.5.3042.

(91)   Park, Y. J.; Kim, K. H.; Lim, D. W.; Lee, E. K. Effects of PH and Protein Conformation on In-Solution Complexation between Bovine α-Lactalbumin and Oleic Acid: Binding Trend Analysis by Using SPR and ITC. *Process Biochem.* **2015**. https://doi.org/10.1016/j.procbio.2015.05.018.

(92)   Militello, V.; Casarino, C.; Emanuele, A.; Giostra, A.; Pullara, F.; Leone, M. Aggregation Kinetics of Bovine Serum Albumin Studied by FTIR Spectroscopy and Light Scattering. *Biophys. Chem.* **2004**. https://doi.org/10.1016/j.bpc.2003.09.004.

Chapter 6   Microscopic Analysis of Airborne Incidental Metal Containing Nanoparticles for Occupational Health

6.1   Abstract

There is great concern in the potential adverse health implications of engineered nanoparticles. However, there are many circumstances where the production of incidental nanoparticles, i.e., nanoparticles unintentionally generated as a side product of some anthropogenic process, is of even greater concern. In this study, metal-based incidental nanoparticles were measured in two different occupational settings, a machining center, and a foundry. Sample collection substrates were used for off-site analysis, including single-particle analysis using scanning electron microscopy and energy-dispersive X-ray spectroscopy. Between the two sites, there were similarities in the size and composition of the incidental nanoparticles as well as in the agglomeration and coagulation behavior of nanoparticles. In particular, incidental nanoparticles were identified in two forms: sub-micrometer fractal-like agglomerates from activities such as welding and super-micrometer particles with incidental nanoparticles coagulated to their surface herein called nanoparticle collectors. These agglomerates will affect deposition and transport inside the respiratory system of the respirable incidental nanoparticles and the corresponding health implications. The studies of incidental nanoparticles generated in occupational settings lay the groundwork on which occupational health and safety protocols should be built.

6.2   Introduction

The health implications of engineered nanoparticles (ENPs) have been discussed for over a decade in the environmental health and safety (EHS) field.[1] Efforts to develop a framework for evaluating EHS implications of ENPs and the corresponding risk assessments are currently in progress.[2-4] These risk assessments are usually based on property-driven or functional assay-rooted approaches that consider changes in the properties of nanoparticles (NPs) under relevant environmental conditions.[5] However, these approaches are difficult to apply to incidental nanoparticles (INPs) – nanoparticles unintentionally generated as a side product of anthropogenic processes – because they are often poorly characterized.

In recent years, there has been great interest in assessing the concentrations of nanoparticles to which workers are exposed during ENP production and product development.[6, 7] Such studies have resulted in correlations between higher concentrations with specific work activities[8, 9] and enabled the development of methodologies to better assess ENPs in the workplace.[10-12] This work has undoubtedly helped to improve occupational safety in nanotechnology industries.[13] However, the INPs generated in many occupations are not fully understood. Welding is one of the processes that generate high levels of INPs that are known to contain mostly iron (Fe) and manganese (Mn) oxides, among many other metals.[14] These particles are of great interest in terms of the health implications for welders due to the toxicity of Mn even at low levels of exposure.[15] Other activities, such as smelting[16, 17] or surface treatments,[18] have been reported to generate significant quantities of aluminum (Al) containing INPs. In general, any industrial process

that involves combustion or generation of metal fumes likely produce INPs.[(19-21)] It is therefore important to understand the nature of these INPs.

The health implications of airborne nanoparticles are not a new concern. For decades, epidemiological studies have associated particulate matter (PM) in air pollution with increases in mortality and the frequency of cardiovascular,[22-25] pulmonary,[26, 27] and neurological diseases.[28-30] Despite the fact that mechanisms by which PM causes adverse health effects have not been fully elucidated, several studies have linked them to the ability to trigger oxidative stress.[23, 25, 31] Stronger associations of PM exposure with adverse health effects have been found for ultrafine particles, i.e. nanoparticles in the ambient environment, rather than larger micron-sized particles.[24] This finding may be due in part to the fact that ultrafine particles possess a higher content of transition metals and organics than larger particles, making them prone to generate reactive oxygen species (ROS).[25, 32] Furthermore, ultrafine particles are usually generated by anthropogenic sources such as power plants, car exhausts, combustion, mining, and other industrial sources.[30]

Recently, Maher *et al*.[33] observed anthropogenic magnetite nanoparticles generated by combustion in the brains of humans from Mexico and England. This study confirms that nanoparticles can translocate from the respiratory tract to accumulate in the brain after inhalation, a hypothesis once solely based on results of experiments in mice.[34-36] Moreover, sufficient accumulation occurs even at relatively low PM concentrations (with peak values for roadside dust at ~40 µg/m^3) that can result in a neurodegenerative disease.[33] This finding motivated a thorough characterization of ultrafine particles, which have shown elevated concentrations of transition metals.[37-40] These studies become really relevant

considering magnetic INPs found in the brain contained traces of other transition metals including nickel (Ni), platinum (Pt), cobalt (Co) and possibly copper (Cu).[33]

Detailed size and composition characterization of INPs is required to better understand their potential implications. Off-site measurement techniques usually provide more detailed information about size and composition including lower detection and quantification limits; however, the implementation of on-site techniques not only decreases the time and cost of characterization compared to off-site analyses. Typical off-site analyses involve gravimetric analysis or digestion of samples deposited onto substrates.[41] These samples are collected on-site by aspirating a known volume of air through a substrate, in order to collect enough particle mass for further analyses. While methods for measuring particle concentrations and size distribution on-site are well established,[42] more detailed chemical analysis, including elemental analysis, on-site remains challenging. A rapid method to measure on-site the mass concentration of metal-containing PM by size and composition from 10 nm to 10 µm was recently reported. This method uses a nano micro-orifice uniform-deposit impactor (nano-MOUDI) to collect and separate particles by size and a field portable x-ray fluorescence (FP-XRF) to measure metal concentrations.[43] By using this non-destructive technique, the nano-MOUDI substrates can be used further for single particle analysis, including scanning electron microscopy (SEM), and energy-dispersive X-ray spectroscopy (EDS). A previous study demonstrated that single particle analysis can be used to distinguish airborne engineered nanomaterials from incidental particles.[44]

The present study aims to characterize and compare the composition, size and morphology of PM smaller than 10µm, with a special interest on the INPs generated in two

occupational settings. These sites were selected due to the significant concentration of Fe, Mn and Cu found during a recent assessment of INPs exposure levels.[45] A FP-XRF was employed for on-site chemical characterization of metal-containing aerosol.[43] An off-site single-particle analysis was then performed to characterize primary particle morphology, composition and agglomerate status of INPs found in these two settings. Implications of these findings and potential health effects are discussed.

6.3   Methods

6.3.1   Test Sites and Sampling Equipment

A heavy vehicle machining and assembly center and an iron foundry were selected based on the similarities in the composition of particulate matter: Fe, Cu and Mn that were detected in a preliminary study at both sites.[45] The machining center produces construction and forestry equipment. Metal and metal oxide PM including nanoparticles were generated by robotic and manual metal inert gas (MIG) welding as well as metal parts grinding at this site. The foundry manufactures ductile iron and grey iron metal parts, where PM monitoring was carried out during metal melting, metal pouring and grinding operations. In both locations, sampling was performed during three days using a field sampling cart placed in different areas of interest as described in detail previously.[45]

Size-resolved analysis of the INPs was carried out using the nano-MOUDI (Model 125-R, MSP Corporation, Shoreview, MN). The nano-MOUDI was operated at 10 L/min with 13 greased polycarbonate (PC) substrates (0.2 µm, 47 mm, Sterlitech Corporation, Kent, WA) as previously reported.[45] A mixed cellulose ester (MCE) filter (0.8 µm, 47 mm, Zefon International, Inc., Ocala, FL) was used as a backup filter in the last nano-MOUDI stage.

Table 6.1 shows the particle size ranges that each stage collects. Particles were collected onto transmission electron microscopy (TEM) grids (200-mesh carbon coated Ni grid, 01840N-F, Ted Pella Inc., CA) with an electrostatic precipitator (ESPnano model 100, DASH Connector Technology, Inc., WA).

Table 6.1: Size separation is done using a nano-MOUDI cascade impactor with the corresponding stages.

Stage	d_{50}, nm	Midpoint diameter (d_i), nm	Substrate material
1	10000	15000	Polycarbonate
2	5600	7800	Polycarbonate
3	3200	4400	Polycarbonate
4	1800	2500	Polycarbonate
5	1000	1400	Polycarbonate
6	560	780	Polycarbonate
7	320	440	Polycarbonate
8	180	250	Polycarbonate
9	100	140	Polycarbonate
10	59	79.5	Polycarbonate
11	32	45.5	Polycarbonate
12	18	25	Polycarbonate
13	10	14	Polycarbonate
14 Final filter	<10	6	Mixed cellulose ester (MCE)

For the machining center, sampling was carried out 6h/day on average. Day 1 sampling occurred near a robotic welding area, Day 2 sampling was near a manual

welding and grinding areas, and Day 3 sampling was between the manual and robotic welding areas. For both types of welding, an ER70S-3 wire was used; the material safety data sheet (MSDS) reports elemental concentrations of 95.31% Fe, 1.85% Mn, 0.5% Cu, 0.15% C, 1.15% Si, 0.035% S, 0.025% P, 0.15% Ni, 0.15% Cr, 0.03% V, 0.15% Mo. In the foundry, sampling was carried out 8h/day on average. The field measurement cart was positioned in the grinding area on Day 1, and in the hot metal melting/pouring area for days 2 and 3. Ductile iron was produced on the first two days, while grey iron was produced on the third day. Although exact alloy compositions were proprietary information, the alloys met specifications for American Society for Testing and Materials (ASTM) grey iron and ductile iron designations. With Fe as the matrix, base composition for grey iron may range from 3.0 to 3.5% C, 0.6 to 0.9% Mn, 1.3 to 1.8% Si, together with relatively minor components of P and S. Ductile iron base composition is expected to range from 3.0 to 4.0% C, 0.1 to 1.0% Mn, 1.8 to 3.0% Si, with also P and S as relatively minor components.

6.3.2 Electron Microscopy Analysis

Particles collected on TEM grids were imaged by TEM (JEOL-1230, JEOL Ltd., Japan) and images were analyzed by ImageJ software (version 1.50i, NIH, USA). PC substrates from nano-MOUDI Stages 3, 5, 7, 9 and 11 collected during Day 1 at the machining center site and during Day 2 at the foundry site were analyzed by SEM. In order to minimize charging effects, the PC substrates were coated with Iridium (K575X Sputter Coater, Quorum Technologies Ltd, UK) for 7 seconds with an 85 mA deposition current prior to the analysis. A Field Emission Scanning Electron Microscope FE-SEM (Zeiss

Sigma 500, Carl Zeiss, Germany) was used for morphology characterization. An Apreo SEM (Thermo Scientific, Oregon, USA) was used for EDS analysis. EDS analysis was performed with Pathfinder X-ray microanalysis software (Thermo Scientific, USA).

6.4   Results

6.4.1   Single particle analysis of incidental particles in two occupational settings

The morphology of the particles was characterized, and five nano-MOUDI stages collected during Day 1 at the machining center, were selected for SEM analysis: Stage 3 (3.2 to 5.6 µm), Stage 5 (1.0 to 1.8 µm), Stage 7 (320 to 560 nm), Stage 9 (100 to 180 nm) and Stage 11 (32 to 59 nm). However, due to the diminished amount of the nanoparticles little data were obtained for Stage 11.

Fig. 6.1a shows SEM images of the Stages 3, 5, 7 and 9. Low magnification images display the substrate homogeneity in Fig. 6.2. Spherical micron-sized particles are observed on Stage 3. These large spherical particles have smaller particles deposited onto their surface. Smaller spheres with similar morphology are also observed in Stage 5. The expected sub-micrometer fractal-like agglomerates densely pack Stages 7 and 9. The shapes of small agglomerates are distinguishable in Stage 7 but not in Stage 9, due to the fact that an iridium thin film covered a very compact bed of nanoparticles.

Fig. 6.1b shows higher magnification SEM images to closely observe the morphology of the collected particles. Similar to the other site, these micron-sized particles observed in stages 3 and 5 have coagulated smaller particles on their surface, which have different shapes and sizes. On Stage 7, three different kinds of particles are clearly detected:

167

spheres with diameters around 150 nm, quasi-spherical nanoparticles with diameters around 30 nm and cubes with around 100 nm edges. On Stage 9, like in the previous site, the SEM images provide no morphology insights due to the iridium thin layer covering a very compact bed of nanoparticles.
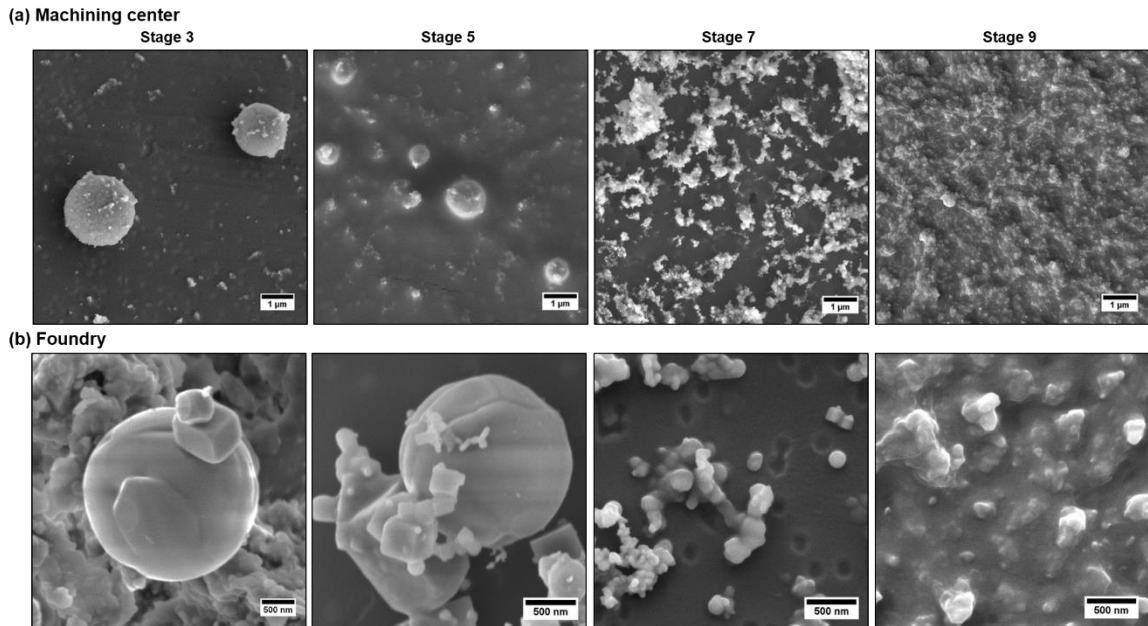
Figure 6.1: SEM images of particles found at the machining center and foundry sites for different size ranges including for particles collected by the nano-MOUDI stages 3 (3.2-5.6µm), 5 (1-1.8µm), 7 (320-560nm) and 9 (100-180nm) at the machining center (a) and foundry (b).
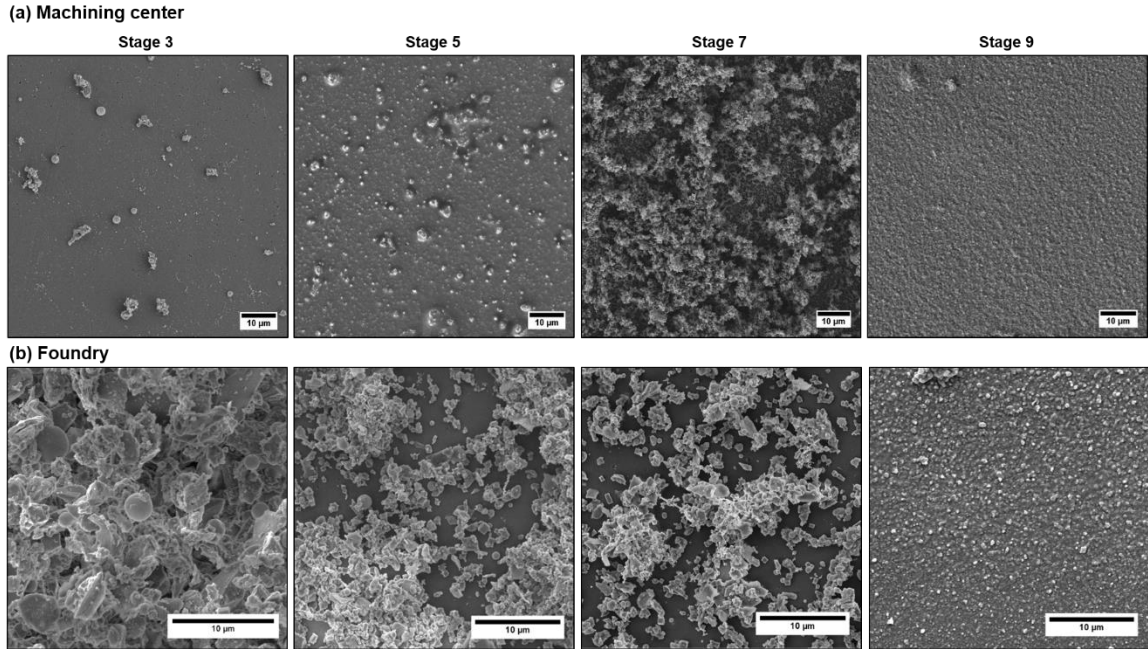
Figure 6.2: Low magnification SEM images of particles found at the machining center and the foundry for different size ranges including for particles collected by the nano-MOUDI stages 3 (3.2-5.6µm), 5 (1-1.8µm), 7 (320-560nm) and 9 (100-180nm) at machining center (a) and the foundry (b).

For the foundry, Day 2 was selected for imaging due to the detection of metals in the stages collecting nanoparticles. Fig. 6.2 shows low magnification SEM images of the Stages 3, 5, 7 and 9 from iron foundry to display the substrate homogeneity. Highly irregular agglomerates are present in stages 3 to 7. Images obtained for Stage 7, where their concentration diminishes, show that these agglomerates are partially formed by a few hundred nanometers prisms. The images of stages 3 and 5 show that spherical micron-sized particles are embedded in a dense layer of irregular agglomerates. In addition, in stages 5 and 7 few fractal-like agglomerates are observed connecting some distant isolated particles.

To further understand the composition of the samples, SEM/EDS was carried out. Fig. 6.3a shows the elemental mapping of some Fe-based micron-sized spheres found in Stage 3. The high association of O indicates these particles are Fe (hydroxy-)oxides, which

is in agreement with previous reports for ambient, super-micrometer Fe-containing spheres possible from steel production.[47] The Mn mapping shows higher intensities for the fractal-like agglomerates located on the surface of the micron-sized spheres. Cu mapping provides little information since Cu concentrations are lower than 1%, which is below the detection limit of EDS.[48] Fig. 6.4a shows a similar analysis for the particles collected in Stage 7, where large agglomerates (320 to 560 nm) of small nanoparticles are collected. In this case, the figure is less clear as the nanoparticles are smaller than the pixel size (40 nm), making the analysis less precise. However, key information is provided: i) all nanoparticles contain oxygen, ii) even when the Mn and Fe are easiest to be seen in the larger agglomerates, the areas with high intensity for each of these elements do not overlay and; iii) although Cu mapping is not very clear, there are a few points with high intensity. These observations allow the following conclusion: most of the nanoparticles are either Mn, Fe or Cu oxides, but are probably not mixed metals oxides.

(a) Machining center

(b) Foundry

Figure 6.3: SEM-EDS of select micron-sized particles found in the machining center and foundry. SEM images are compared to the Fe, O, Mn, and Cu elemental mappings for both sites. Zn, Mg, Al and Ca were also found and mapped in the foundry.
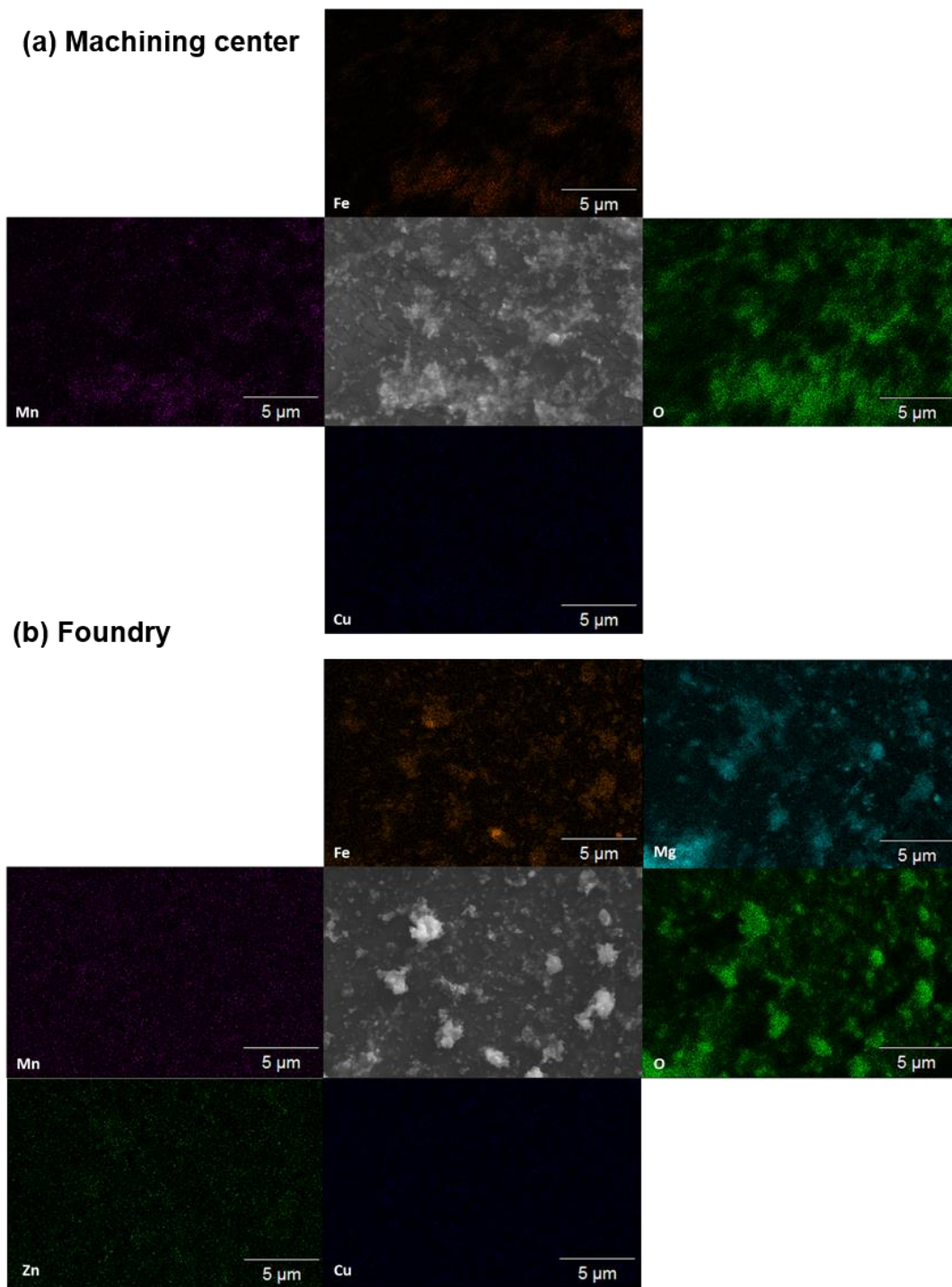
Figure 6.4: SEM-EDS of particles found on the machining center and the foundry. The SEM image is compared to the Fe, O, Mn, and Cu elemental mappings for both sites in nano-MOUDI stage 7 (320-560nm). Zn, and Mg were also found and mapped in the foundry.

Fig. 6.3b shows the elemental mapping of particles collected on Stage 3 in the foundry. For this stage, micron-sized spheres are seen to be composed of Fe and O whereas Mn, Cu, and Zn mappings do not show much signal and suggest their mass concentrations were below the limit of detection of EDS.[48] Aluminum is detected for the larger irregular agglomerates. Mg and Ca were also detected. In particular, Ca was observed when high Al was present. The presence of Ca, Al and Si (not measured) is possibly related to the use of clay materials for the casting process.[49] MgO seems to be the main component of the micron-sized well-defined prisms, due to the presence of only Mg and O in those particles. The detection of Mg can also be attributed to clay materials but another source of Mg is as an additive in the preparation of ductile iron.[50] Fig. 6.4b shows similar results for particles collected on Stage 7. Despite the fact that some nanoparticles are smaller than the pixel size (40 nm), key information can still be obtained: i) most particles are oxides, as O it is observed in all the area where the SEM image shows particles; ii) Mn and Cu are not observed as expected from the elemental analysis by ICP-MS; iii) Mg is observed in large amount but is present on the agglomerates with a smooth surface; iv) Fe is observed when small nanoparticles are observed; and v) Zn mapping is not very clear, but there are a few points with high intensity which may indicate that some small particles are ZnO.

In general, metal oxide INPs were observed occurring with two distinct and specific morphologies: fractal-like agglomerates and NP-collectors, referring to the micron-sized spheres decorated with nanoparticles on their surface. The term NP-collector is inspired by the analogous deposition of nanoparticles on grains during their transport through porous media.[51]
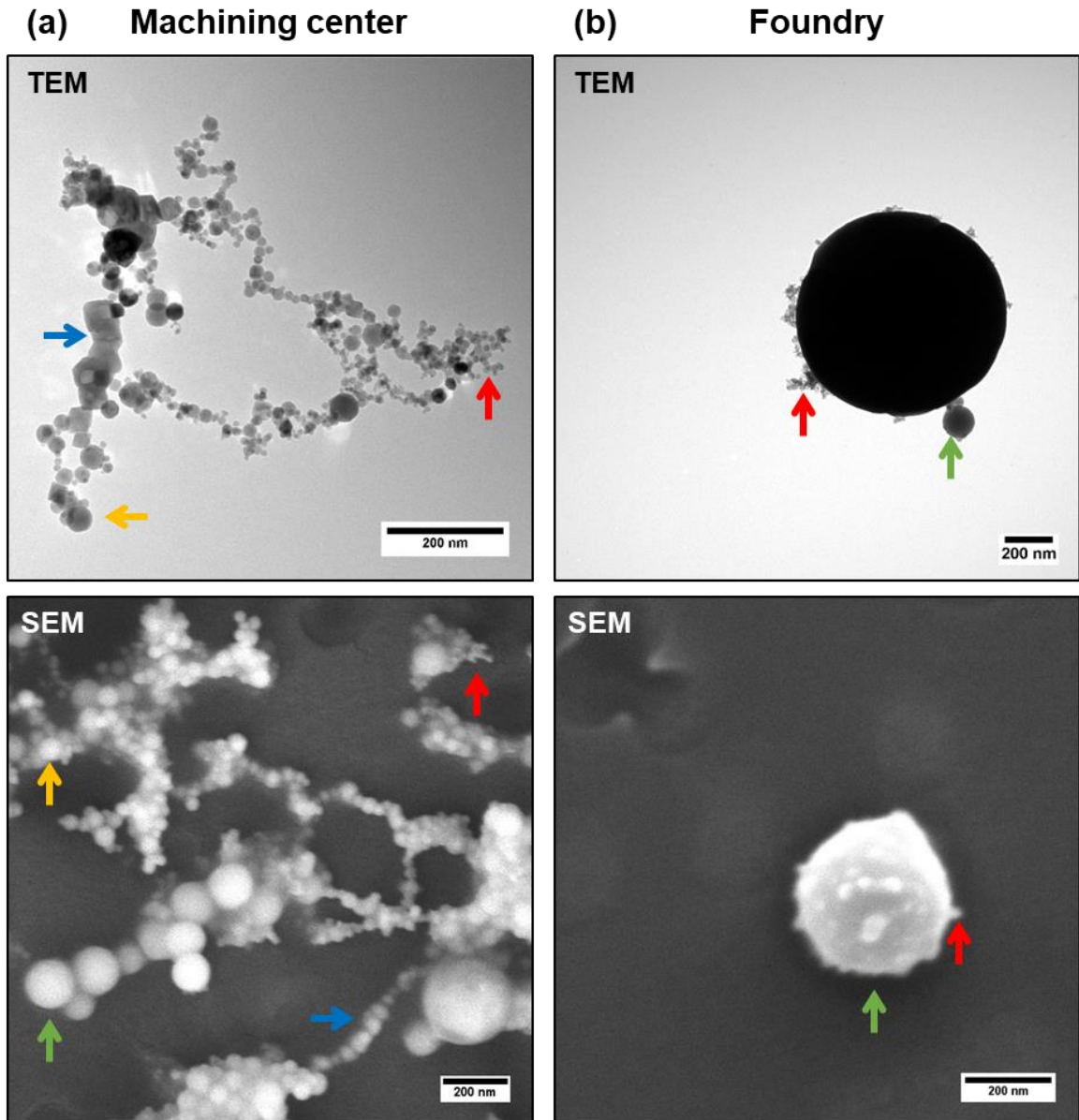
Figure 6.5: TEM (top) and SEM (bottom) images of particles detected at the machining center (a) and foundry (b) sites. For both sites, particles with different morphologies are observed including spherical and cubic (blue arrows) nanoparticles. At least four populations of spherical particle are observed including: very small nanoparticles, less than 10 nm (red arrows); small nanoparticles, less than 100 nm (yellow arrows); larger nanoparticles, approximately 100nm (green arrows) and very larger particles which are hundreds of nanometers in size or micrometers in size (purple arrows).

Fig. 6.5 shows both morphologies observed with TEM (top) and SEM (bottom) in both sites. In the machining center, fractal-like agglomerates were more common and were formed by four kinds of nanoparticles: spherical particles with diameters ~200 nm (green arrows), ~50 nm (yellow arrows) and ~10 nm (red arrows); and cubic particles with edges ~70 nm edges (blue arrows). This kind of agglomerates is the main component of the PM found in the machining center, but the NP-collectors significantly contribute to the micron-sized particles. In contrast, in the foundry the fractal-like agglomerates were observed in a minor proportion, due to the small amount of mass found for nanoparticles. The NP-collector architecture was not only found in micron-sized spheres as shown in the top of Figure 5b, but also in ~200 nm particles shown at the bottom. The NP-collector architecture is in agreement with what had been modeled for the first stages of coagulation in particles where the size distribution is highly polydispersed.[52] However, these agglomerates are composed by two different size distributions of primary particles. These agglomerates will likely follow the self-conserving size distribution observed for other aerosols,[53] including the fractal-like agglomerates observed in this work.

6.5   Discussion

A recent inhalation exposure study indicated that the sizes of both the agglomerates and the primary particles are important in terms of pulmonary effects,[54] but our study suggest that composition and morphology of agglomerates might play a role in the route of deposition and translocation. Both fractal-like agglomerates and NP-collectors are inhalable particles, however the NP-collectors will have different penetration range and

mechanism for deposition than the fractal-like agglomerates, and therefore, potentially very different locations, types, and severities of health effects.

Small micron-sized particles (1-10 µm), such as the NP-collectors, have a high deposition efficiency in the nasal area.[55] This is of particular importance as the olfactory route is one of the proposed mechanisms for nanoparticle translocation to the brain.[36] Despite that in the studies modeling nasal deposition only a few micron-sized particles deposit on the olfactory region,[56] the NP-collectors could play an important role in nanoparticles translocation to the brain as their surface is enriched with multiple INPs. In addition, the translocation is expected to only occur for individual or a few nanoparticles agglomerates; which in both cases implies a de-agglomeration process. This de-agglomeration process could be promoted by the presence of biomolecules,[57] which are in high concentration and of diverse nature in the olfactory mucosa.[58]

On the other hand, the sub-micron fractal-like agglomerates are more likely to reach the alveolar region of the lungs. To estimate the deposition of those particles, the NPM criterion was developed: it represents the fraction of particles smaller than 300 nm that would deposit in the respiratory system of an average adult under light exercise and nose-breathing conditions.[59] The NPM criterion, designed to represent deposition of near-spherical nanoparticles, can be adjusted for different particle morphologies using an appropriate dynamic shape factor.[54] Tables 6.2 and 6.3 summarize the total concentrations collected by the nano-MOUDI, by element and day, and the corresponding respirable and dynamic NPM fractions for the machining center and the foundry, respectively. A significant proportion of the INPs found in the fractal-like agglomerates contribute to the NPM fraction. This means that the NPM fraction provides a good estimation of the fractal-

like agglomerates that deposits in the respiratory system and may better reflect their

adverse health effects.

Table 6.2: Concentrations of metals for total, respirable and NPM fractions of the collected particles in the machining center. The concentrations were calculated by adding concentration multiplied by the corresponding fraction of each of the nanoMOUDI stages.

Element	Day 1			Day 2			Day 3		
	Collected, µg/m³	Respirable, µg/m³	NPM, µg/m³	Collected, µg/m³	Respirable, µg/m³	NPM, µg/m³	Collected, µg/m³	Respirable, µg/m³	NPM, µg/m³
Mn	28.9	27.3	7.8	24.7	23.9	6.8	18.4	17.3	4.8
Fe	190.4	159.4	45.1	151.2	135.3	36.9	137.8	112.4	32.1
Cu	3.1	3.0	0.9	5.1	4.4	1.0	1.3	1.2	1.0
Total	222.4	189.8	53.8	181.1	163.6	44.7	157.4	134.9	37.3

NPM = nanoparticulate matter

Table 6.3: Concentrations of metals for total, respirable and NPM fractions of the collected particles in the foundry. The concentrations were calculated by adding concentration multiplied by the corresponding fraction of each of the nanoMOUDI stages.

Element	Day 1			Day 2			Day 3		
	Collected, µg/m³	Respirable, µg/m³	NPM, µg/m³	Collected, µg/m³	Respirable, µg/m³	NPM, µg/m³	Collected, µg/m³	Respirable, µg/m³	NPM, µg/m³
Al	7.4	1.5	0.1	14.7	2.6	0.2	14.0	2.1	0.1
Mn	2.3	0.3	0.0	3.6	0.8	0.1	16.1	8.2	1.3
Fe	326.1	35.2	2.2	156.3	29.5	3.2	444.9	101.3	10.9
Cu	0.5	0.0	0.0	0.9	0.7	0.1	1.2	0.6	0.1
Zn	0.3	0.0	0.0	8.8	6.9	2.4	7.4	4.3	0.6
Total	336.6	36.9	2.3	184.3	40.5	5.9	483.6	116.5	13.1

NPM = nanoparticulate matter

Another important feature to consider is the heterogeneous composition of these agglomerates. Our EDS results suggest that both kinds of agglomerates are composed of single metal oxide particles; which is explained by the fact that each metal condenses at a different temperature.[60] Recent studies have shown that heterogeneous aggregation changes the fate of nanoparticles in the environment, as aggregation can change the reactivity of the nanoparticles including their ROS generation capabilities and photocatalytic properties.[61-63] Furthermore, the presence of Mn in Fe-rich PM has shown to change the proportion of the different oxidation states of Fe oxides.[40] This can have a significant effect on the inflammatory responses that the agglomerates will generate in the lung as each oxide dissolves at different rates.[64, 65] In addition, the transport of the same INPs to different parts of the respiratory tract may generate different health effects.[66] For example, ZnO and Cu/CuO nanoparticles have shown to dissolve in the lung mostly by macrophage action,[64, 67] but there is no indication that dissolution will occur if transported directly to the brain by the olfactory system. Previously, the generation of Fe and Mn nanoparticles was simulated to have a close model to characterize the materials and their behavior under contact with biological solutions.[65, 68] However, from this study, it is concluded that new models that include heterogeneous agglomerates of incidental nanoparticles (Fe-Mn-Cu and Fe-Mn-Zn) with both architectures are required to better understand the health implications that these incidental nanoparticles will have.

6.6   Conclusions

In this work, an on-site technique to analyze substrates deposited particulate matter recently reported on[43] was used successfully for metal analysis in PM characterization. The

same substrates can then be later used in off-site analysis to obtain more information of the collected particles, including morphology using SEM. Two types of agglomerates were found: fractal-like agglomerates, typically observed in INPs generating activities such as welding, and NP-collectors. Similar NP-collectors were recently observed in factories conducting MIG welding[46] and in PM collected from air pollution,[37] which indicates that they might be as common as the fractal-like agglomerates and should be studied in detail since they transport incidental nanoparticles on their surface.

6.7   Acknowledgments

Chapter 6, in full, is reproduced with permission from Taylor & Francis: Gonzalez-Pech, N. I.; Stebounova, L. V.; Ustunol, I. B.; Park, J. H., Renee Anthony, T.; Peters, T. M.; Grassian, V. H. Size, Composition, Morphology, and Health Implications of Airborne Incidental Metal-Containing Nanoparticles. *J. Occup. Environ. Hyg.* **2019,** 16, 6, 387-399.

The dissertation author was the investigator and author of this paper. The dissertation author conducted electron microscopy and energy dispersive X-Ray analyses.

6.8   References

(1)   Yokel, R.A., and R.C. MacPhail: Engineered nanomaterials: exposures, hazards, and risk prevention. *Journal of Occupational Medicine and Toxicology* 6(2011).

(2)   Boyes, W.K., B.L.M. Thornton, S.R. Al-Abed, C.P. Andersen, D.C. Bouchard, R.M. Burgess et al.: A comprehensive framework for evaluating the environmental health and safety implications of engineered nanomaterials. *Critical Reviews in Toxicology* 47(9): 767-810 (2017).

(3)   Mattsson, M.O., and M. Simko: The changing face of nanomaterials: Risk assessment challenges along the value chain. *Regulatory Toxicology and Pharmacology* 84: 105-115 (2017).

(4)   Grassian, V.H., A.J. Haes, I.A. Mudunkotuwa, P. Demokritou, A.B. Kane, C.J. Murphy et al.: NanoEHS - defining fundamental science needs: no easy feat when the simple itself is complex. *Environmental Science: Nano* (2015).

(5)   Hendren, C.O., G.V. Lowry, J.M. Unrine, and M.R. Wiesner: A functional assay-based strategy for nanomaterial risk forecasting. *Science of the Total Environment* 536: 1029-1037 (2015).

(6)   Brouwer, D.: Exposure to manufactured nanoparticles in different workplaces. *Toxicology* 269(2-3): 120-127 (2010).

(7)   Curwin, B., and S. Bertke: Exposure characterization of metal oxide nanoparticles in the workplace. *Journal of Occupational and Environmental Hygiene* 8(10): 580-587 (2011).

(8)   Kuhlbusch, T.A.J., C. Asbach, H. Fissan, D. Gohler, and M. Stintz: Nanoparticle exposure at nanotechnology workplaces: A review. *Particle and Fibre Toxicology* 8(2011).

(9)   Ding, Y., T.A.J. Kuhlbusch, M. Van Tongeren, A.S. Jimenez, I. Tuinman, R. Chen et al.: Airborne engineered nanomaterials in the workplace-a review of release and worker exposure during nanomaterial production and handling processes. *Journal of Hazardous Materials* 322: 17-28 (2017).

(10)   Park, J.H., I.A. Mudunkotuwa, L.W.D. Mines, T.R. Anthony, V.H. Grassian, and T.M. Peters: A granular bed for use in a nanoparticle respiratory deposition sampler. *Aerosol Science and Technology* 49(3): 179-187 (2015).

(11)   Mines, L.W.D., J.H. Park, I.A. Mudunkotuwa, T.R. Anthony, V.H. Grassian, and T.M. Peters: Porous polyurethane foam for use as a particle collection substrate in a nanoparticle respiratory deposition sampler. *Aerosol Science and Technology* 50(5): 497-506 (2016).

(12)   Asbach, C., C. Alexander, S. Clavaguera, D. Dahmann, H. Dozol, B. Faure et al.: Review of measurement techniques and methods for assessing personal exposure to airborne nanomaterials in workplaces. *Science of the Total Environment* 603: 793-806 (2017).

(13)   Ham, S., S. Kim, N. Lee, P. Kim, I. Eom, P.J. Tsai et al.: Comparison of nanoparticle exposure levels based on facility type-small-scale laboratories, large-scale manufacturing workplaces, and unintended nanoparticle-emitting workplaces. *Aerosol and Air Quality Research* 15(5): 1967-1978 (2015).

(14)   Berlinger, B., N. Benker, S. Weinbruch, B. L'Vov, M. Ebert, W. Koch et al.: Physicochemical characterisation of different welding aerosols. *Analytical and Bioanalytical Chemistry* 399(5): 1773-1780 (2011).

(15)   Baker, M.G., S.R. Criswell, B.A. Racette, C.D. Simpson, L. Sheppard, H. Checkoway et al.: Neurological outcomes associated with low-level manganese exposure in an inception cohort of asymptomatic welding trainees. *Scandinavian Journal of Work Environment & Health* 41(1): 94-101 (2015).

(16)   Thomassen, Y., W. Koch, W. Dunkhorst, D.G. Ellingsen, N.P. Skaugset, L. Jordbekken et al.: Ultrafine particles at workplaces of a primary aluminium smelter. *Journal of Environmental Monitoring* 8(1): 127-133 (2006).

(17)   Weinbruch, S., N. Benker, K. Kandler, M. Ebert, D.G. Ellingsen, B. Berlinger et al.: Morphology, chemical composition and nanostructure of single carbon-rich particles studied by transmission electron microscopy: source apportionment in workroom air of aluminium smelters. *Analytical and Bioanalytical Chemistry* 408(4): 1151-1158 (2016).

(18)   Santos, R.J., and M.T. Vieira: Assessment of airborne nanoparticles present in industry of aluminum surface treatments. *Journal of Occupational and Environmental Hygiene* 14(3): D29-D36 (2017).

(19)   Ono-Ogasawara, M., F. Serita, and M. Takaya: Distinguishing nanomaterial particles from background airborne particulate matter for quantitative exposure assessment. *Journal of Nanoparticle Research* 11(7): 1651-1659 (2009).

(20)   Elihn, K., and P. Berg: Ultrafine particle characteristics in seven industrial plants. *Annals of Occupational Hygiene* 53(5): 475-484 (2009).

(21)   Bemer, D., R. Regnier, I. Subra, B. Sutter, M.T. Lecler, and Y. Morele: Ultrafine particles emitted by flame and electric arc guns for thermal spraying of metals. *Annals of Occupational Hygiene* 54(6): 607-614 (2010).

(22)   Robertson, S., and M.R. Miller: Ambient air pollution and thrombosis. *Particle and Fibre Toxicology* 15(2018).

(23)   Araujo, J.A., and A.E. Nel: Particulate matter and atherosclerosis: role of particle size, composition and oxidative stress. *Particle and Fibre Toxicology* 6(2009).

(24)   Hoek, G., R.M. Krishnan, R. Beelen, A. Peters, B. Ostro, B. Brunekreef et al.: Long-term air pollution exposure and cardio- respiratory mortality: a review. *Environmental Health* 12(2013).

(25)   Rao, X.Q., J.X. Zhong, R.D. Brook, and S. Rajagopalan: Effect of particulate matter air pollution on cardiovascular oxidative stress pathways. *Antioxidants & Redox Signaling* (2017).

(26)   Vignal, C., M. Pichavant, L.Y. Alleman, M. Djouina, F. Dingreville, E. Perdrix et al.: Effects of urban coarse particles inhalation on oxidative and inflammatory parameters in the mouse lung and colon. *Particle and Fibre Toxicology* 14(2017).

(27)   Meldrum, K., C. Guo, E.L. Marczylo, T.W. Gant, R. Smith, and M.O. Leonard: Mechanistic insight into the impact of nanomaterials on asthma and allergic airway disease. *Particle and Fibre Toxicology* 14(2017).

(28)   Pope, C.A., and D.W. Dockery: Health effects of fine particulate air pollution: Lines that connect. *Journal of the Air & Waste Management Association* 56(6): 709-742 (2006).

(29)   Ruckerl, R., A. Schneider, S. Breitner, J. Cyrys, and A. Peters: Health effects of particulate air pollution: A review of epidemiological evidence. *Inhalation Toxicology* 23(10): 555-592 (2011).

(30)   Heal, M.R., P. Kumar, and R.M. Harrison: Particles, air quality, policy and health. *Chemical Society Reviews* 41(19): 6606-6630 (2012).

(31)   Cheng, H., A. Saffari, C. Sioutas, H.J. Forman, T.E. Morgan, and C.E. Finch: Nanoscale particulate matter from urban traffic rapidly induces oxidative stress and inflammation in olfactory epithelium with concomitant effects on brain. *Environmental Health Perspectives* 124(10): 1537-1546 (2016).

(32)   Cassee, F.R., M.E. Heroux, M.E. Gerlofs-Nijland, and F.J. Kelly: Particulate matter beyond mass: recent health evidence on the role of fractions, chemical constituents and sources of emission. *Inhalation Toxicology* 25(14): 802-812 (2013).

(33)   Maher, B.A., I.A.M. Ahmed, V. Karloukovski, D.A. MacLaren, P.G. Foulds, D. Allsop et al.: Magnetite pollution nanoparticles in the human brain. *Proceedings of the National Academy of Sciences* 113(39): 10797-10801 (2016).

(34)   Calderon-Garciduenas, L., B. Azzarelli, H. Acuna, R. Garcia, T.M. Gambling, N. Osnaya et al.: Air pollution and brain damage. *Toxicologic Pathology* 30(3): 373-389 (2002).

(35)   Dorman, D.C., K.A. Brenneman, A.M. McElveen, S.E. Lynch, K.C. Roberts, and B.A. Wong: Olfactory transport: A direct route of delivery of inhaled manganese phosphate to the rat brain. *Journal of Toxicology and Environmental Health-Part A* 65(20): 1493-1511 (2002).

(36)   Oberdorster, G., Z. Sharp, V. Atudorei, A. Elder, R. Gelein, W. Kreyling et al.: Translocation of inhaled ultrafine particles to the brain. *Inhalation Toxicology* 16(6-7): 437-445 (2004).

(37)   Gonzalez, L.T., F.E.L. Rodriguez, M. Sanchez-Dominguez, A. Cavazos, C. Leyva-Porras, L.G. Silva-Vidaurri et al.: Determination of trace metals in TSP and PM2.5 materials collected in the metropolitan area of Monterrey, Mexico: A characterization study by XPS, ICP-AES and SEM-EDS. *Atmospheric Research* 196: 8-22 (2017).

(38)   Jelenska, M., B. Gorka-Kostrubiec, T. Werner, M. Kadzialko-Hofmokl, I. Szczepaniak-Wnuk, T. Gonet et al.: Evaluation of indoor/outdoor urban air pollution by magnetic, chemical and microscopic studies. *Atmospheric Pollution Research* 8(4): 754-766 (2017).

(39)   Yang, Y., M. Vance, F.Y. Tou, A. Tiwari, M. Liu, and M.F. Hochella: Nanoparticles in road dust from impervious urban surfaces: distribution, identification, and environmental implications. *Environmental Science-Nano* 3(3): 534-544 (2016).

(40)   Sanderson, P., S.S. Su, I.T.H. Chang, J.M.D. Saborit, D.M. Kepaptsoglou, R.J.M. Weber et al.: Characterisation of iron-rich atmospheric submicrometre particles in the roadside environment. *Atmospheric Environment* 140: 167-175 (2016).

(41)   Ashley, K.: "Elements by ICP (microwave digestion), method 7302". NIOSH Manual of Analytical Methods (NMAM), 2016.

(42)   Amaral, S.S., J.A. de Carvalho, M.A.M. Costa, and C. Pinheiro: An overview of particulate matter measurement instruments. *Atmosphere* 6(9): 1327-1345 (2015).

(43)   Park, J.H., I.A. Mudunkotuwa, K.J. Crawford, T.R. Anthony, V.H. Grassian, and T.M. Peters: Rapid analysis of the size distribution of metal-containing aerosol. *Aerosol Science and Technology* 51(1): 108-115 (2017).

(44)   Peters, T.M., S. Elzey, R. Johnson, H. Park, V.H. Grassian, T. Maher et al.: Airborne monitoring to distinguish engineered nanomaterials from incidental particles for environmental health and safety. *Journal of Occupational and Environmental Hygiene* 6(2): 73-81 (2009).

(45)   Stebounova, L.V., N.I. Gonzalez-Pech, J.H. Park, T.R. Anthony, T.M. Peters , and V.H. Grassian: Particle concentrations in occupational settings measured with a Nanoparticle Respiratory Deposition (NRD) sampler. *Annals of Work Exposure and Health* 65(6): 699-710(2018).

(46)   Stanislawska, M., T. Halatek, M. Cieslak, I. Kaminska, R. Kuras, B. Janasik et al.: Coarse, fine and ultrafine particles arising during welding - Analysis of occupational exposure. *Microchemical Journal* 135: 1-9 (2017).

(47)   Ault, A.P., T.M. Peters, E.J. Sawvel, G.S. Casuccio, R.D. Willis, G.A. Norris et al.: Single-particle SEM-EDX analysis of iron-containing coarse particulate matter in an urban environment: Sources and distribution of iron within Cleveland, Ohio. *Environmental Science & Technology* 46(8): 4331-4339 (2012).

(48)   Friel, J.J., and C.E. Lyman: X-ray mapping in electron-beam instruments. *Microscopy and Microanalysis* 12(1): 2-25 (2006).

(49)   "Guide to casting and molding processes." Available at https://pdfs.semanticscholar.org/2fa7/9ad6d87450d1f12ffb718ed58199b1bc7240.pdf (accessed May 9, 2018).

(50)   Loizaga, A., J. Sertucha, and R. Suarez: Influence of treatments using different magnesium ferroalloys on the melt quality and the solidification processes of ductile irons. *Revista De Metalurgia* 44(5): 432-446 (2008).

(51)   Lecoanet, H.F., J.Y. Bottero, and M.R. Wiesner: Laboratory assessment of the mobility of nanomaterials in porous media. *Environmental Science & Technology* 38(19): 5164-5169 (2004).

(52)   Goudeli, E., M.L. Eggersdorfer, and S.E. Pratsinis: Coagulation of agglomerates consisting of polydisperse primary particles. *Langmuir* 32(36): 9276-9285 (2016).

(53)   Goudeli, E., M.L. Eggersdorfer, and S.E. Pratsinis: Coagulation-agglomeration of fractal-like particles: Structure and self-preserving size distribution. *Langmuir* 31(4): 1320-1327 (2015).

(54)   Kim, S.C., J. Wang, M.S. Emery, W.G. Shin, G.W. Mulholland, and D.Y.H. Pui: Structural property effect of nanoparticle sgglomerates on particle penetration through fibrous filter. *Aerosol Science and Technology* 43(4): 344-355 (2009).

(55)   Hofmann, W.: Modelling inhaled particle deposition in the human lung-A review. *Journal of Aerosol Science* 42(10): 693-724 (2011).

(56)   Calmet, H., C. Kleinstreuer, G. Houzeaux, A.V. Kolanjiyil, O. Lehmkuhl, E. Olivares et al.: Subject-variability effects on micron particle deposition in human nasal cavities. *Journal of Aerosol Science* 115: 12-28 (2018).

(57)   Tantra, R., J. Tompkins, and P. Quincey: Characterisation of the de-agglomeration effects of bovine serum albumin on nanoparticles in aqueous suspension. *Colloids and Surfaces B-Biointerfaces* 75(1): 275-281 (2010).

(58)   Ding, X., and F. Xie: 3. Olfactory mucosa: composition, enzymatic localization, and metabolism. In *Handbook of Olfaction and Gustation*, R.L. Doty (ed.). Hoboken, NJ, USA: John Wiley & Sons, Inc, 2015.

(59)   Cena, L.G., T.R. Anthony, and T.M. Peters: A personal nanoparticle respiratory deposition (NRD) sampler. *Environmental Science & Technology* 45(15): 6483-6490 (2011).

(60)   Byeon, J.H., J.H. Park, and J.H. Hwang: Spark generation of monometallic and bimetallic aerosol nanoparticles. *Journal of Aerosol Science* 39(10): 888-896 (2008).

(61)   Therezien, M., A. Thill, and M.R. Wiesner: Importance of heterogeneous aggregation for NP fate in natural and engineered systems. *Science of the Total Environment* 485: 309-318 (2014).

(62)   Hotze, E.M., J.Y. Bottero, and M.R. Wiesner: Theoretical framework for nanoparticle reactivity as a function of aggregation state. *Langmuir* 26(13): 11170-11175 (2010).

(63)   Jassby, D., J.F. Budarz, and M. Wiesner: Impact of aggregate size and structure on the photocatalytic properties of TiO2 and ZnO nanoparticles. *Environmental Science & Technology* 46(13): 6934-6941 (2012).

(64)   Pettibone, J.M., A. Adamcakova-Dodd, P.S. Thorne, P.T. O'Shaughnessy, J.A. Weydert, and V.H. Grassian: Inflammatory response of mice following inhalation exposure to iron and copper nanoparticles. *Nanotoxicology* 2(4): 189-204 (2008).

(65)   Stebounova, L.V., N.I. Gonzalez-Pech, T.M. Peters , and V.H. Grassian: Physicochemical properties of air discharge-generated manganese oxide nanoparticles: comparison to welding fumes. *Environ. Sci.: Nano* 5: 696-707 (2018).

(66)   Madl, A.K., and K.E. Pinkerton: Health effects of inhaled engineered and incidental nanoparticles. *Critical Reviews in Toxicology* 39(8): 629-658 (2009).

(67)   Adamcakova-Dodd, A., L.V. Stebounova, J.S. Kim, S.U. Vorrink, A.P. Ault, P.T. O'Shaughnessy et al.: Toxicity assessment of zinc oxide nanoparticles using sub-acute and sub-chronic murine inhalation models. *Particle and Fibre Toxicology* 11(2014).

(68)   Park, J.H., I.A. Mudunkotuwa, J.S. Kim, A. Stanam, P.S. Thorne, V.H. Grassian et al.: Physicochemical characterization of simulated welding fumes from a spark discharge system. *Aerosol Science and Technology* 48(7): 768-776 (2014).

Chapter 7   Conclusions and Future Directions

Metal oxide nanoparticles attract significant attention in many applications and are ubiquitous in the environments. There has been rising interest in their interactions with proteins and amino acids to improve the *in-situ* material performance and better understand biological component-surface interactions at the molecular level for human health and the environment. Despite their enhanced usage, adsorption dynamics and stability of many common molecules to metal oxide nanoparticles, particularly in heterogeneous aqueous matrices, are not fully understood.

This dissertation focuses on understanding protein and amino acid adsorption on metal oxide nanoparticle surfaces and the effects of various nanoparticle and environmental factors of complex media on biomolecule-nanoparticle surface interactions. Adsorption of biomolecules on the nanoparticle surfaces could play a critical role in determining their behavior in complex aqueous systems. By studying biomolecule interactions, an understanding of the persistence of such bio-essential compounds and predictive insight into how larger molecules might behave upon introduction to nanoparticle surfaces can be gained. Due to the complexity of the interactions at bio-nano interfaces, influencing factors including nanoparticle surface chemistry, pH, the presence of phosphate, and lipopolysaccharides were individually studied to investigate each aspect in detail.

Chapter 2 presents the experimental techniques used in elemental and morphological characterization of nanoparticles, biomolecule-nanoparticle surface interactions, aqueous phase protein and amino acid surface adsorption, protein structural analysis nanoparticle–nanoparticle interactions, and aggregation states were described. The

described techniques were helpful to characterize both the bulk biomolecules and nano-bio interface. They provided qualitative and quantitative analysis for protein and amino acid adsorption and surface-induced protein secondary structural change.

In Chapter 3, the effects of pH on amino acid adsorption onto TiO_2 nanoparticle surfaces were investigated. Results from the ATR-FTIR spectra and zeta-potential analyses evidence that solution pH significantly influences amino acid speciation and adsorption mechanisms. At acidic conditions, protonated surface species were present for all amino acids. High amount of adsorption was observed when amino acid speciation consists of zwitterion species. Moreover, glycine and lysine revealed a similar adsorption trend where their adsorption was increased with increasing pH. When considered together, the results provide valuable insights into the mechanisms of more complex aqueous biomolecule-surface interactions at different pH values and illuminate a detailed understanding of human and environmental exposure to TiO_2 nanoparticles.

In chapter 4, adsorption of arginine, aspartic acid, and lysine on α-Fe_2O_3 nanoparticles were investigated. The results of the pH-dependent adsorption of lysine and glutamic onto α-Fe_2O_3 were compared to those in Chapter 3. ATR-FTIR spectroscopy was used to probe the spectral changes. TiO_2 and α-Fe_2O_3 nanoparticles interacted distinctively with the amino acids as a function of pH. Amino acids showed a stronger amine group interaction and higher symmetry of carboxylate coordination on the α-Fe_2O_3 than TiO_2. Surface species were changing at different pH values, and a stronger H-bonding occurred when aspartic acid concentration increased. Overall, the results provide valuable insights into the mechanisms of biomolecule-nanoparticle surface interactions on different metal oxide nanoparticles.

In Chapter 5, the effects of pre-adsorbed phosphate and lipopolysaccharides on protein adsorption onto α-Fe_2O_3 nanoparticles were investigated. Phosphate occupied active sites and reduced the BSA and β-LG surface coverage, whereas LPS did not significantly impact the IgG surface coverage. Adsorption isotherms revealed that adsorption kinetics were protein-specific, as BSA exhibited Langmuir adsorption behavior, while β-LG showed sigmoidal-shape adsorption indicative of multilayer adsorption on α-Fe_2O_3. Upon adsorbed onto surfaces, proteins underwent unfolding or refolding. While BSA exhibits a loss of α-helices, β-LG was folding into α-helices in the presence and absence of phosphate. Likewise, β-LG, adsorbed IgG folded into α-helices when pre-adsorbed LPS was present.

Chapter 6 of this dissertation complemented our understanding of protein and amino acid adsorption studies onto metal oxide nanoparticles. In this chapter, microscopic analyses of airborne metal-containing nanoparticles were performed in different production sites in an occupational health study. EDX analyses and SEM/TEM images were used to identify the produced nanoparticles in these settings. The results showed that the airborne particles were in forms of agglomerates and differed in size and composition. Sub-micrometer fractal-like particulates and super-micrometer particles (named as nanoparticle collectors) were observed. Furthermore, we proposed that these agglomerates with nanoparticles coagulated on their surfaces would impact deposition mechanisms and transportation in the human respiratory system.

The interaction of amino acids and protein with metal oxide nanoparticle surfaces can be influenced by the chemistry of surrounding complex environments, the solid-liquid interface, nanoparticle composition and its surface chemistry, and the nature of the

biomolecule. The research presented in the dissertation contributes to a greater understanding of several influencing factors on amino acid and protein behaviors at the nano-bio interface. Although this dissertation opens doors to uncover some molecular-level details of these interactions, some unexplored investigation areas need to be addressed to fully understand and evaluate metal oxide nanoparticles' properties in complex environments. Some of the grand opportunities of the research areas include:

i.   Create a greater understanding of biomolecule-nanoparticle surface chemistry and morphology-dependent properties, which are essential in environmental and biological processes *by involving more species of metal oxide nanoparticles*.

ii. Expand the investigation and comparison of the toxicity of metal oxide nanoparticles *by including other proteins*. Probe possible correlations exist that could help us to understand complex nano-bio interactions and their role in toxicity.

iii. Create a systematic qualitative and quantitative evaluation of biomolecule-nanoparticle surface interactions as a function of biologically and environmentally relevant factors *by combining different experimental techniques* (2DCOS, HDX-MS, QCM-D, AFM-IR etc.).

To fulfill the gap in the existing literature on these open research areas, it is needed to combine computational, theoretical, and experimental efforts devoted to understanding nanoparticles and the critical properties in their physicochemical transformation, mobility, uptake, and toxicity in complex environmental and biological systems.

Appendix A Supporting Information for " pH-Dependent Adsorption of α-Amino Acids, Lysine, Glutamic Acid, Serine and Glycine, on TiO₂ Nanoparticle Surfaces

A.1   Supporting Information – Figures
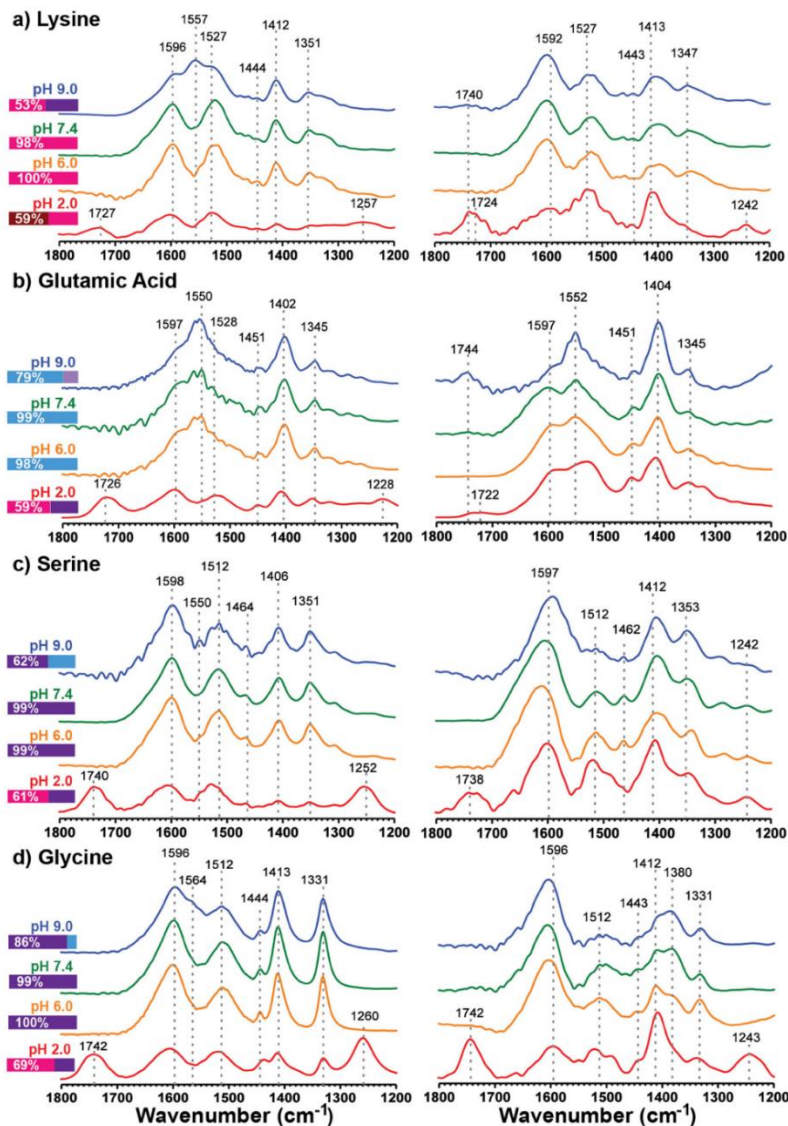
Figure A.1:   Solution (left) and normalized adsorbed ATR-FTIR spectra (right) of (a) lysine; (b) glutamic acid; (c) serine; and (d) glycine on TiO₂ NPs at different pH values as a function of time. The bars represent the speciation percentages at each pH.
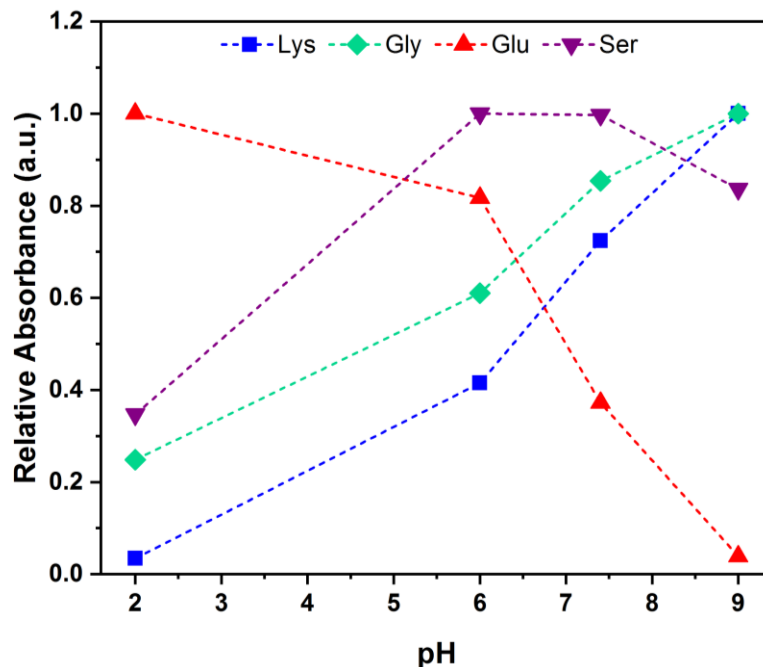
Figure A.2: The pH-dependent adsorption of amino acids onto TiO_2 nanoparticles. Absorbance intensities at 1600 cm^{-1} were normalized by the peak maximum at each pH. Lysine and glycine show similar adsorption trends with changing pH and the greatest adsorptions occur at pH 9; adsorption increases by increasing pH. Whereas for glutamic acid the greatest adsorption occurs at pH 2; adsorption decreases as pH increases. Serine shows a different trend; adsorption is the highest when pH is close to the pH$_{PZC}$ of TiO_2 nanoparticles.
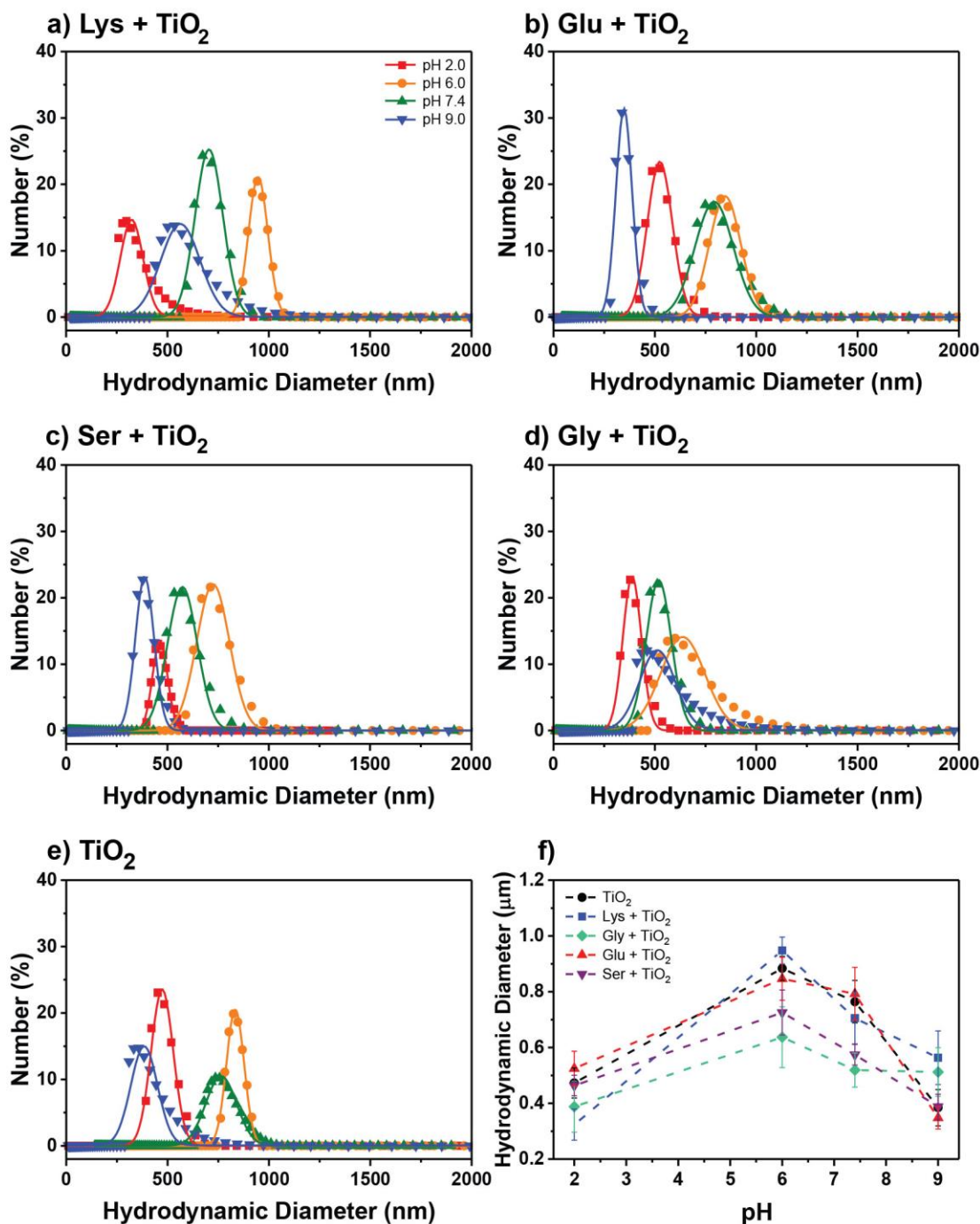
Figure A.3: The pH-dependent hydrodynamic sizes of bare and amino acids-coated TiO$_2$ nanoparticles. The size distribution of TiO$_2$ nanoparticles (30 mg/L) dispersed in 5 mM (a) lysine; (b) glutamic acid; (c) serine; (d) glycine solution; and (e) MilliQ water. (f) The summary of the pH-dependent hydrodynamic diameter shows that bigger aggregates form at pH 6.

A.2   Supporting Information – Tables

Table A.1: Changes in the wavenumber splitting of symmetric and asymmetric carboxylate stretches upon adsorption on TiO_2 nanoparticles.

Amino Acids	Frequency Shift (cm^{-1})							
	pH 2		pH 6		pH 7.4		pH 9	
	Solution Δv_{as-s}	Adsorbed Δv_{as-s}	Solution Δv_{as-s}	Adsorbed Δv_{as-s}	Solution Δv_{as-s}	Adsorbed Δv_{as-s}	Solution Δv_{as-s}	Adsorbed Δv_{as-s}
Lys	184	183/197	182	176/196	182	179/192	187	185/197
Glu α-carboxylate	187	174/193	196	174/195	196	172/194	194	194
Glu distal-carboxylate	-	123/142	146	128/149	148	128/150	151	150
Ser	185	182/192	192	187/209	193	188/206	191	183/204
Gly	185	178/218	183	182/217	185	182/215	184	184/215

($\Delta v_{as-s} = \Delta v_{as} - \Delta v_s$); v_{as}: asymmetric stretching and v_s: symmetric stretching vibrations.

Appendix A is reproduced with permission from Elsevier: Ustunol, I. B.; Gonzalez-Pech, N. I.; Grassian, V. H. pH-dependent Adsorption of α-Amino Acids, Lysine, Glutamic Acid, Serine, and Glycine, on TiO_2 Nanoparticle Surfaces. *J. Colloid Interface Sci.* **2019**, 554, 362-375. The dissertation author was the primary investigator and author of this paper.